



UNIVERSITY OF L'AQUILA
DEPARTMENT OF INDUSTRIAL AND INFORMATION ENGINEERING AND
ECONOMICS

Doctor of philosophy course on Industrial and Information Engineering and Economics:
Curriculum Ingegneria elettrica, elettronica e dell'informazione
XXXIII cycle

Title of the Thesis

Modelling and Design of High Speed Synchronous Reluctance Motors for Electric Vehicles

SSD ING/IND 32

Ph. D Student:
Andrea Credo

Coordinator of the course
Prof. Giuseppe Ferri

Tutor
Prof. Marco Villani

A.A. 2019/2020

Abstract

In recent years, the market of electric cars has been significantly growing compared to the previous period and this trend seems to be confirmed for the coming years, considering the policies adopted by several countries, the car manufacturers' new strategies, and the improvement of battery and power electronics technologies.

Nowadays, most of the Electric Machines (EM) used in the mobility sector are based on Rare-Earth (RE) Permanent Magnets (PMs). The high and volatile cost of raw materials for magnets makes their long-term availability uncertain, especially since the electric vehicle technology is going to be manufactured in mass production. Therefore, there is a growing attention in alternative solutions that include RE-free machines or reduced RE PM machines.

In this thesis, one of the most cost-effective solutions has been investigated: in particular, the Synchronous Reluctance Motor (SynRel) has been studied in-depth. Considering the torque capability of this type of machine, it can be stated that it depends only on the motor anisotropy due to the absence of permanent magnets, which cannot contribute to the torque production. Besides, the SynRel can have good performance, especially if it is compared to the Induction Motor (IM) one.

The Synchronous Reluctance Motor is an unusual solution for traction applications since it is characterized by a lower specific torque, a lower power density, and a lower power factor than the one of Permanent Magnet solutions.

This thesis aims to maximize the performance of this type of machine by proposing an innovative design procedure that can be applied to High Speed Synchronous Reluctance Motors that have to be adopted in the e-mobility in order sector. Different design procedures and technological solutions will be presented, analyzed, and discussed: in fact, robust designs, topology optimization, asymmetric rotors, and adhesive epoxy resin are the main topics that will be treated.

The proposed procedures have been applied for the design of the Synchronous Reluctance motors of the H2020 European Project ReFreeDrive that aims to reduce

the use of rare-earth materials in the next generation of electric drivetrains, facilitating the industrial feasibility for mass production at low manufacturing costs.

Two motor sizes have been optimized and, particularly, they are of 200 *kW* and 75 *kW*: their designs have the same stator and rotor shapes for scalability reasons and, hence, to give some benefits to electric vehicle manufacturers.

The prototypes have been realized and preliminarily tested for the verification of their mechanical integrity at high speeds, for the bearing running-in, and for the tuning of the control parameters. After that, the motors have been fully tested over their torque-speed range to verify their performance and to compare the experimental results with the simulation ones.

In the references, for better clarity, the papers authored or co-authored by me are reported at the beginning [1]-[12].

Table of Content

1 Introduction	1
2 Electric Vehicles	3
2.1 The market of electric cars	4
2.2 The market of raw materials.....	7
2.3 Motor solutions for electric vehicles	10
2.3.1 <i>H2020 ReFreeDrive project</i>	12
2.4 The electric car model	14
2.4.1 <i>Motional resistance forces</i>	15
2.5 Design Criteria for the Electric Motor	18
2.6 Comparison between different Light Drive Vehicle (LDV) categories.	21
2.7 Rare Earth-free motor solutions	29
2.7.1 <i>The Induction Motor</i>	29
2.7.2 <i>The Permanent Magnet-assisted-Synchronous Reluctance motor</i> .	30
2.7.3 <i>The pure Synchronous Reluctance motor</i>	32
3 The Synchronous Reluctance Motor	34
3.1 SynRel Modeling.....	35
3.1.1 <i>Integration of core, stray and mechanical losses</i>	38
3.1.2 <i>An example of an industrial SynRel</i>	40
3.2 The SynRel Rotor Geometry	42
3.2.1 <i>Axially-laminated rotor</i>	43
3.2.2 <i>U-Shaped Barriers</i>	44
3.2.3 <i>Circular Barriers</i>	45
3.2.4 <i>Fluid shaped barriers</i>	46
3.2.5 <i>Comparisons between the different shapes</i>	51

4 SynRel Motor Design Optimization	53
4.1 Preliminary design of the rotor core	54
4.2 Optimization of the SynRel.....	57
4.2.1 <i>The optimization algorithm</i>	57
4.2.2 <i>Optimization strategies</i>	60
4.3 An example of the application of the Optimization procedure..	64
4.3.1 <i>Results of the optimizations</i>	69
5 Robust Design Optimization	76
5.1 The Criteria of Robust Designs.....	77
5.2 Preliminary Design Optimization	80
5.2.1 <i>Sensitivity analysis</i>	82
5.2.2 <i>Individuation of different Local Minimums</i>	90
5.3 Statistical Performance Analysis	93
5.4 Worst-Case Analysis.....	99
5.5 Selection of the Robust Design.....	100
6 Asymmetric rotors for torque ripple reduction	104
6.1 Optimization with the symmetric rotor.....	105
6.2 Rotor with an asymmetry within the pole.....	107
6.3 Rotor with adjacent different poles.....	109
6.4 Combination of the two asymmetries	111
6.5 Comparison between the different solutions.....	112
7 High-Speed SynRel Design Criteria	116
7.1 Typical approach.....	117
7.2 Topology Optimization	121
7.3 Adhesive Epoxy Resin	128
7.4 Comparison of the proposed solutions.....	138
8 Two Case Studies: 200 and 75 kW SynRel Designs.....	143
8.1 Requirements	144
8.2 The Design Procedure	145
8.3 Rotor Skewing.....	153
8.4 The 75 kW Design	157
8.5 Prototyping.....	158

8.6	Experimental tests	164
8.6.1	<i>Maximum speed tests</i>	164
8.6.2	<i>Full load tests on the 200 kW machine</i>	166
8.6.3	<i>Full load tests on the 75 kW machine</i>	168
9	Conclusions and Future Developments	170
10	List of Figures	172
11	List of Tables	176
12	References	177

Chapter 1

Introduction

In recent years there has been a growing attention to air pollutants spreading all over industrialized cities: these harmful emissions are dangerous for people's health. Internal Combustion Engines (ICEs) are one of the main sources of air-borne pollutants: in fact, they are responsible for around 35% of atmospheric pollutants, even though their impact could be reduced if all cars were improved to Euro 6 [13]-[15]; therefore, the market of electric cars has been significantly growing if compared to the previous years, with a positive trend that seems to be confirmed for the coming years. This is supported by the policies of several countries, by the car manufacturers' new strategies, and by the improvement of battery and power electronics technologies. To reduce the cost of electric vehicles, an optimized design that aims to minimize the power needed by the electric machine is mandatory; this optimization can be carried out with the evaluation of the car model and of its requirements in terms of acceleration and maximum speed. Nowadays, the adopted motor solutions are mainly based on high performance permanent magnets, but the high and volatile cost of raw materials for magnets makes their long-term availability uncertain, especially since the electric vehicle technology is going to be manufactured in mass production. All these aspects are discussed in Chapter 2.

Therefore, there is a growing attention in alternative solutions such as Rare-Earth (RE) free machines: hence, the Synchronous Reluctance motor (SynRel) represents a valid alternative for electric and hybrid vehicles due to its simple and rugged construction.

The aim of this thesis is to design a High Speed Synchronous Reluctance motor for electric vehicles with a particular focus on the modelling and sizing procedures. A good modeling and an accurate analysis of the rotor shape of the Synchronous

Reluctance machine may be the key features for the maximization of the motor average torque and of its performance. These aspects are presented in Chapter 3.

Since this type of machine has a torque capability that is completely dependent on its anisotropy, specific optimization procedures are needed to maximize its performance. In order to correctly estimate the machine performance with the simulation tools, proper Finite Element (FE) analyses have been implemented, and some functions, whose derivatives are unknown, have been introduced. For this reason, derivative-free optimization algorithms are often preferred and, to reduce the number of optimization iterations, it is possible to use local optimizations. In order to have a good starting point for this type of algorithms a preliminary design procedure that is able to guarantee a good design is recommended. All these are the main topics of Chapter 4.

The machine performance strongly depends on its geometry, but the manufacturing processes introduce a deviation in each geometric variable, thus varying the performance of the simulated design. These deviations depend on the used manufacturing technology and their effects may affect more the optimal design than a generic one. All these mentioned concepts fall into the robust design aspects. The procedure for the evaluation of the most robust design is proposed in Chapter 5.

One of the most relevant design challenges of the Synchronous Reluctance machine consists of its high torque ripple: asymmetric solutions can be adopted to reduce the variation of the magnetic reluctance in relation to the rotor position. This solution is investigated in Chapter 6.

The electric car application requires high power density machines and this requirement can be fulfilled by the adoption of high speed motors; however, the Synchronous Reluctance motor particular shape suffers at high speed and, hence it requires the insertion of structural elements that also reduce the machine performance. In Chapter 7, different solutions are proposed and then compared with one another to check if the mechanical integrity at high speeds is guaranteed.

To demonstrate the design procedure discussed in this thesis, in Chapter 8 two case studies, which are part of the European H2020 ReFreeDrive project, are presented. The design procedure includes the definition of the preliminary design, the design optimization, and the introduction of the asymmetric rotor and of structural elements to sustain the rotor yokes at high speed. Finally, two prototypes are manufactured and tested.

Chapter 2

Electric Vehicles

In the last few years there has been a growing attention towards the air quality of the cities that results, when high and dangerous levels are reached, in a traffic stop to the Internal Combustion Engine (ICE) [14]. In fact, ICE vehicles are still one of the most relevant sources of air pollutants such as carbon monoxide (CO), black carbon (BC), fine particulate matter, and nitrogen oxides (NO_x); these emissions are dangerous for people's health. The use of Electric Vehicles (EVs) may be beneficial for the pollutant reduction, but not as much for the current state of the global climate change solution. It is true that EVs, during their operation, do not produce air pollutants and Green House Gases (GHG), but the electricity used to charge their storage systems is produced by thermal power stations, which in turn are supplied by fossil sources. If the production of electric energy maintains the fossil sources in the scenario and the number of EVs reaches a significant value, the emission of air pollutants will increase near the power production plants, which are typically low-density areas in terms of people, and will decrease in the urban cities: this is an advantage for the public health. The small reduction of GHG with the adoption of electric vehicles compared to the ICE use is due to the higher efficiency of the system thermal power station-transmission-electric vehicle than the one of the system involving the ICE. This higher efficiency is mainly due to the possibility of recovering the braking energy of the vehicles, which is one of the main advantages of Plug-in Hybrid Electric Vehicles (PHEVs) and of EVs.

In the coming years, the development and the increase of clean energies will guarantee the reduction of the emission of GHG during the production of electric energy, hence enhancing the advantages of the use of EVs. The strong limitations to the development of EVs are due to their high costs, to the difficulties in recycling, to the charging infrastructure, and to the short life of the energy storage system. Nowadays, the research is going towards the development of new typologies of battery systems and other kinds of energy storage systems in order to facilitate the growth of the EV market.

2.1 The market of electric cars

The Global EV Outlook, an annual publication on the developments in the electric mobility, is a useful document that gives the main information on the market of electric vehicles, on the recent developments across the globe, on the charging infrastructure deployment, and on many other aspects of the transportation electrification [15]. Although the 2019 report shows a reduction in the global sales of passenger cars, the sales increase of electric cars confirms a positive trend (2.1 million sales on a global scale compared to 1.5 million sales of 2018). In fact, in 2019 electric cars account for about 2.6% of global car sales compared to 1% of global car stock in 2018 this means that the electric car market has been having a high increase in the sales compared to the ones of ICE cars: indeed, it has been registered a 40% year-on-year increase. This increase is mainly due to two aspects: the first one regards the ambitious policy announcements of several countries that have encouraged car manufacturers to invest more in the electric mobility; the second one is related to the development of new technologies for energy storage systems (at the moment, the most critical aspect of electric vehicle) and power electronics. The trend of the electric vehicles sales in the last five years [15] is reported in Figure 2.1.

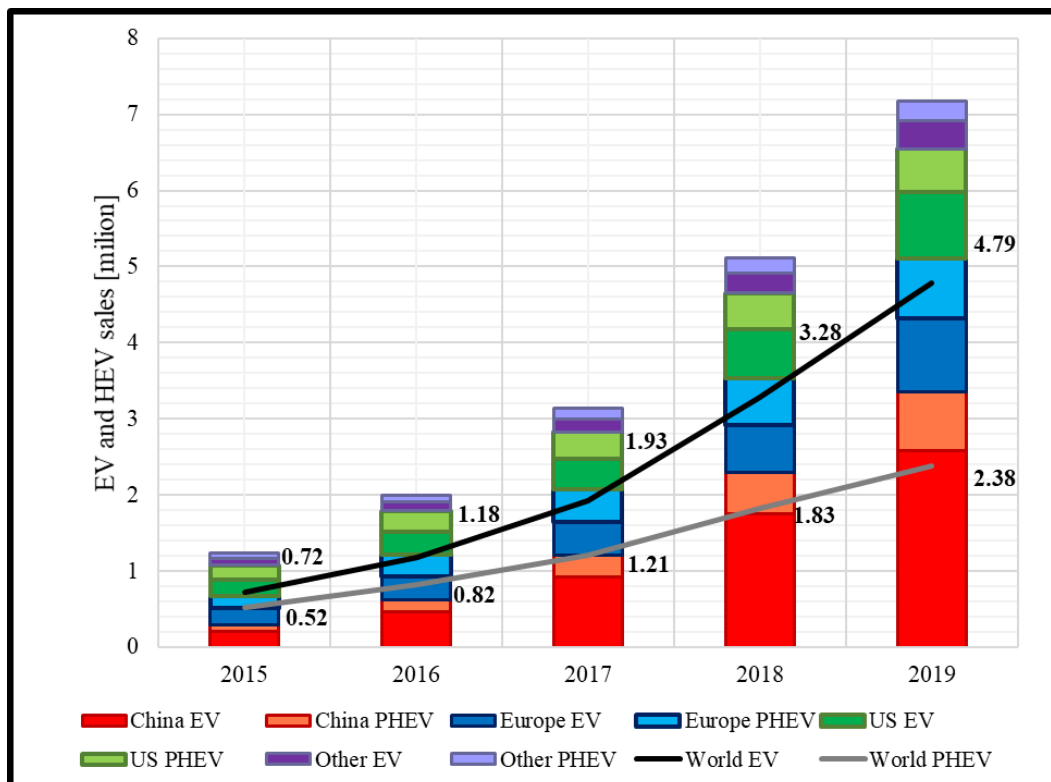


Figure 2.1: Global electric car sales trends.

The number of full Electric Vehicles (EVs) is higher than the Plug-in Hybrid Electric Vehicle (PHEV) one and each country has its own behavior in terms of sales of different electric vehicle typologies. China has the highest ratio between EV and PHEV sales while Europe, in contrast, has similar sales numbers for these two car typologies. The differences between those countries can be explained by the adoption of different policies and incentives, by the car use to satisfy average commuting needs (number of km per day), and by the availability of electric vehicle chargers and, hence, of charging infrastructures.

The increase in electric car demand also requires a growth of the infrastructures for electric vehicle charging, both for fast and slow charging. According to [15], in 2019 there were about 7.3 million chargers worldwide: most of them were private, like light-duty vehicle slow-chargers in private houses, others were installed in multi-dwelling buildings and workplaces. The main reasons for the prevalence of private charging must be sought in its convenience, its cost-effectiveness and in a variety of support policies. Figure 2.2 shows the rates of the different countries in terms of private electric vehicle slow-chargers in 2019 (the total number is about 6.5 million). This distribution reflects the number of sales of electric car: China is the country with both the highest number of electric cars and of slow-chargers, followed by the United States [15].

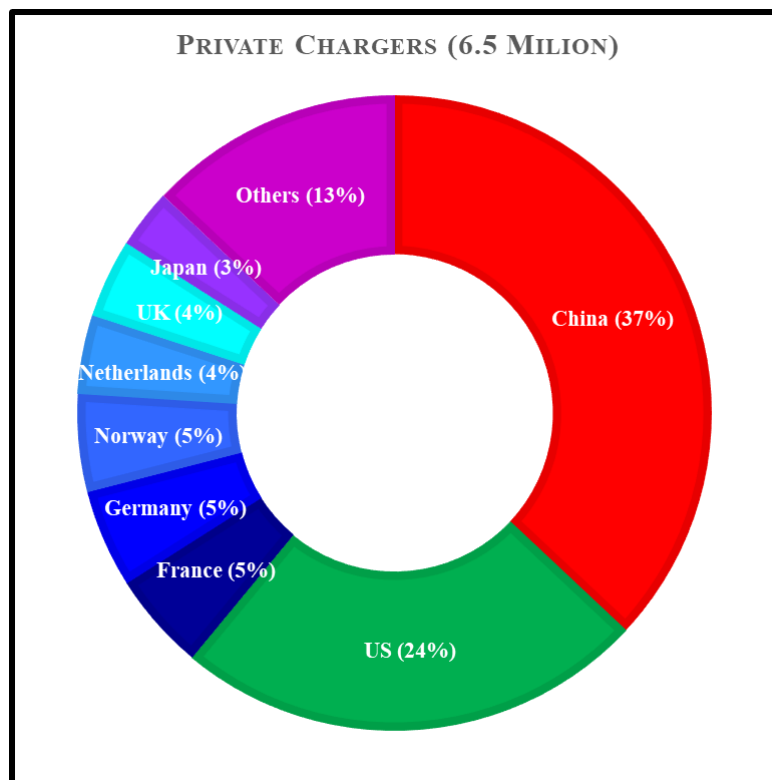


Figure 2.2: Private electric vehicle slow-chargers, 2019.

Figure 2.3 and Figure 2.4 show the rates of different countries in terms of public electric vehicle slow-chargers and public electric vehicle fast-chargers (the total number is almost the same, of about 600 thousand), respectively, in 2019 [15]. The rates are different from the ones in Figure 2.2 and show the different policies implemented by those countries. The United States have adopted support policies for private chargers avoiding, in that way, the adoption of public chargers; the rate of fast-chargers is very low compared to the number of sales of electric cars. China is the country that adopts a massive number of fast chargers and this explains why the ratio between EVs and PHEVs is so high.

The high utilization of EVs requires high investments in infrastructures for electric vehicle chargers (slow and fast) and, as a result, an upgrade of the power of electric distribution and transmission; this consideration justifies the higher sales of EVs in China. Other countries preferred to facilitate the sales of PHEVs in order to have a slow transition from ICE cars to EVs. Another important data is the increase, in 2019, in the public accessible chargers compared to the ones of the previous year (+60%): in fact, this data increase is higher than the one of electric car sales. This last data is an indicator of the government choice to invest in the electric car development together with the increase in the number of charges. Probably, this investment would be followed by another important investment to increase the number of the stock of electric cars.

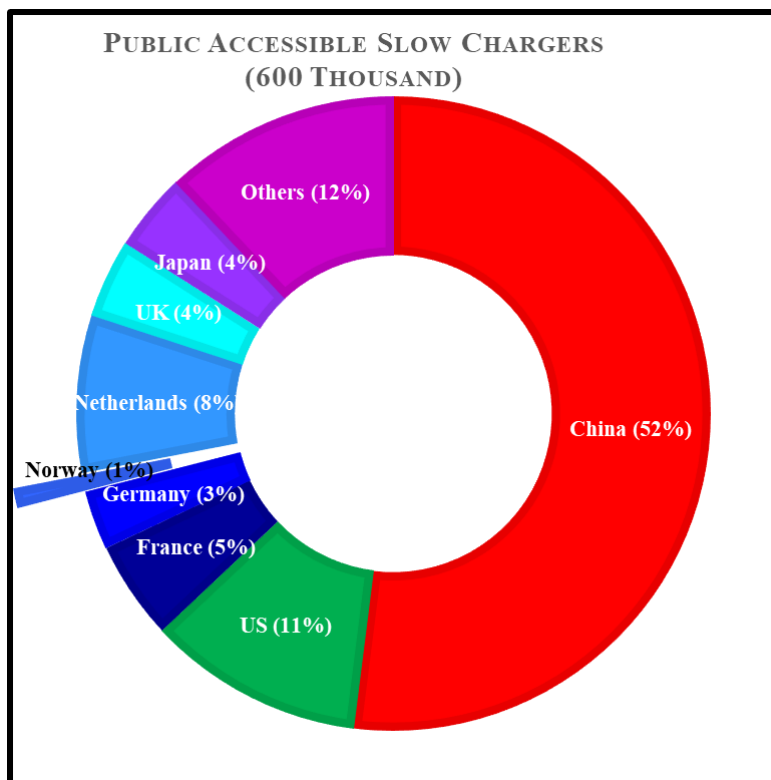


Figure 2.3: Public electric vehicle slow-chargers, 2019.

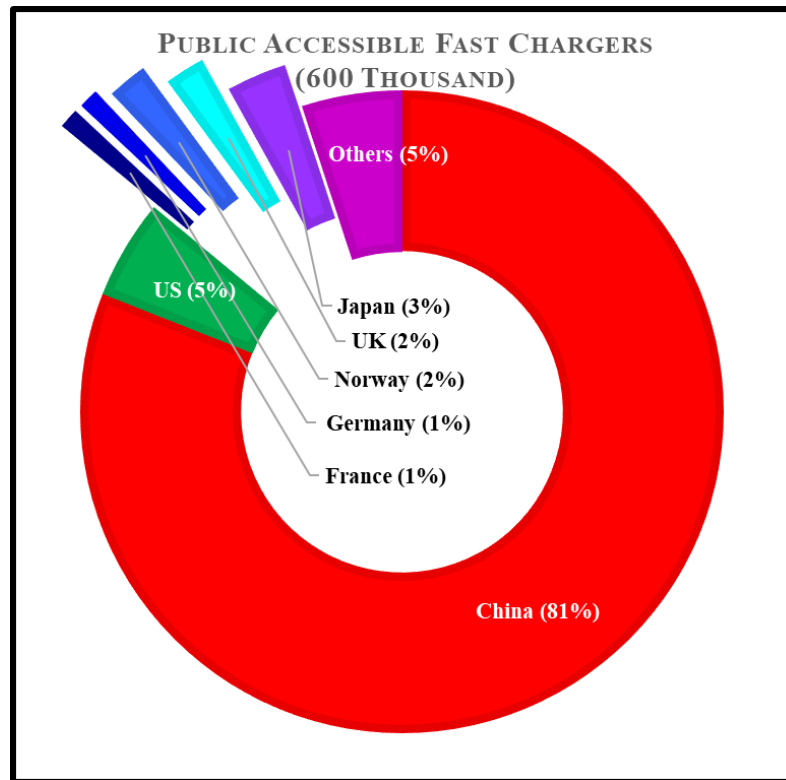


Figure 2.4: Public electric vehicle fast-chargers, 2019.

2.2 The market of raw materials

Another important aspect for the development of electric cars is the electric machine technology. Nowadays, the most common solution for electric vehicles consists of Permanent Magnet motors. These motors offer the best performance for traction applications thanks to their high power density, high specific torque, high power factor, high efficiency, and good flux-weakening capability. All these characteristics are important for this type of application in order to minimize the material mass (thus increasing the acceleration performance), to reduce the apparent power needed by the motor (the size of the power electronics can be reduced), and to reduce the energy losses (the vehicle can have a higher km range or a reduced battery energy). However, these advantages have to face some drawbacks, such as: the high and volatile price of raw materials, their supply risk, and their sustainable extraction since the motors that can guarantee this good performance are the ones that use Rare Earth (RE) Permanent Magnets.

Another important aspect that has to be considered is the dependences from other countries for the supply of raw materials because only a few countries have the reserves and extract the RE materials. The available amount of RE materials is abundant on the Earth's crust, but minable concentrations are less common than for

most other ores (from this the adjective “Rare”) Figure 2.5 and Figure 2.6 show the world mine production and reserves respectively in the last decade [16].

From the figures, it is clear that the production and the reserves are in the hands of a few countries. For instance, China has been producing over half of the RE materials for the last decade and it owns around 50% of these raw material reserves. This could be one of the main reasons of the great development of EVs in China: the companies based right there have advantages for what concerns the raw material supply, besides the fact that the country itself has invested a lot in infrastructures for the battery charge. The reserves of the “Other” countries in Figure 2.6 are mainly located in Russia, South Africa, Tanzania, and Vietnam. This situation creates a supply risk because there is a relevant dependence on very few countries and this makes the market very uncertain: in a few years, the material price could significantly change.

Figure 2.7 shows the behavior of the Neodymium (one of the most used RE materials for the magnet production) price over the last decade [17]. In 2011, there has been a high increase in its price caused by political reasons. In September 2010, China reduced RE exports to Japan because of a maritime incident between these two countries. This export reduction raised significantly the price of REs because Japan was one of its main importers [18].

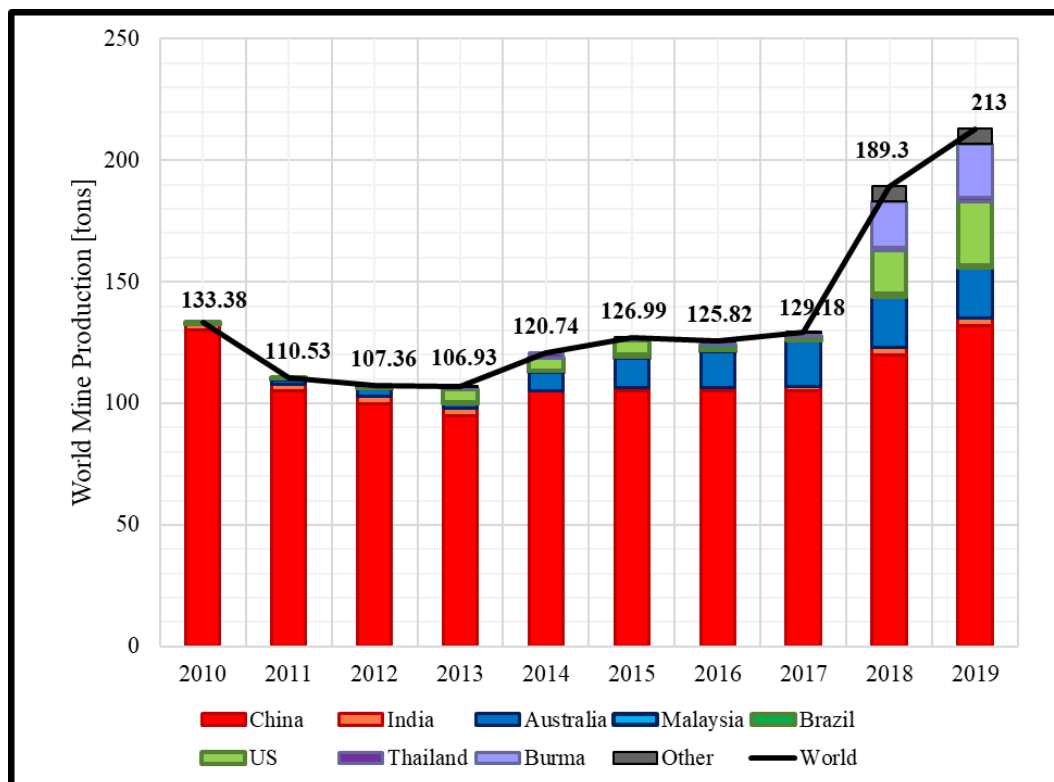


Figure 2.5: World mine production of Rare Earth materials over the last decade in tons.

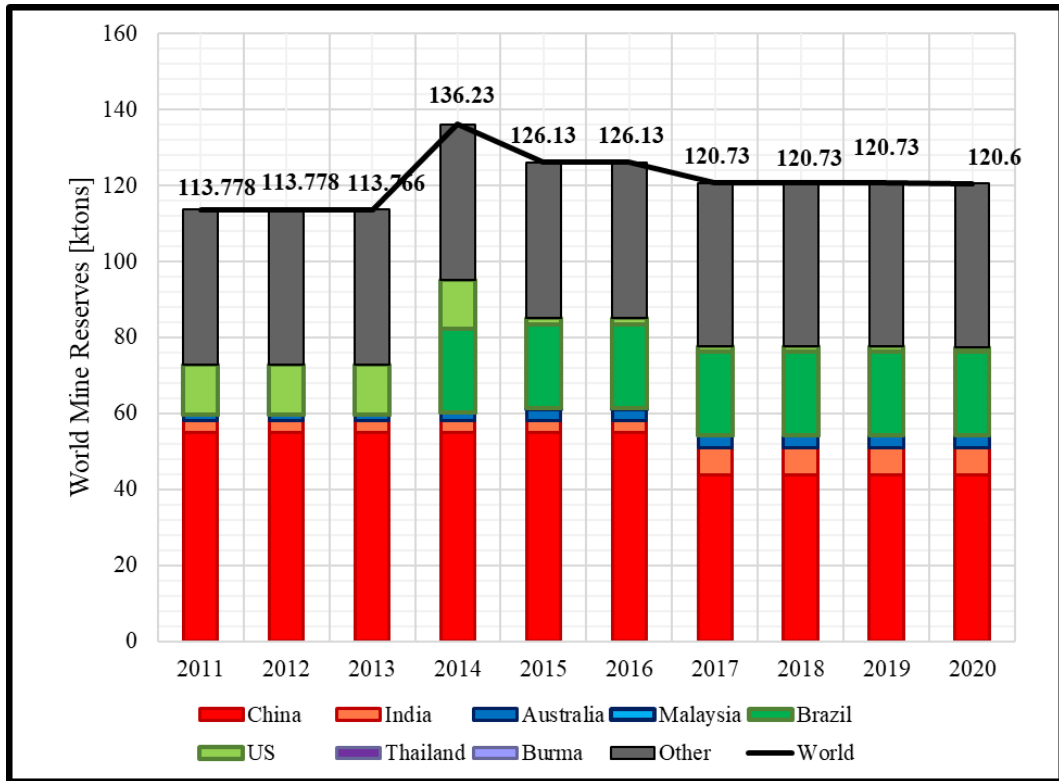


Figure 2.6: World mine reserves of Rare Earth materials over the last decade in ktons.

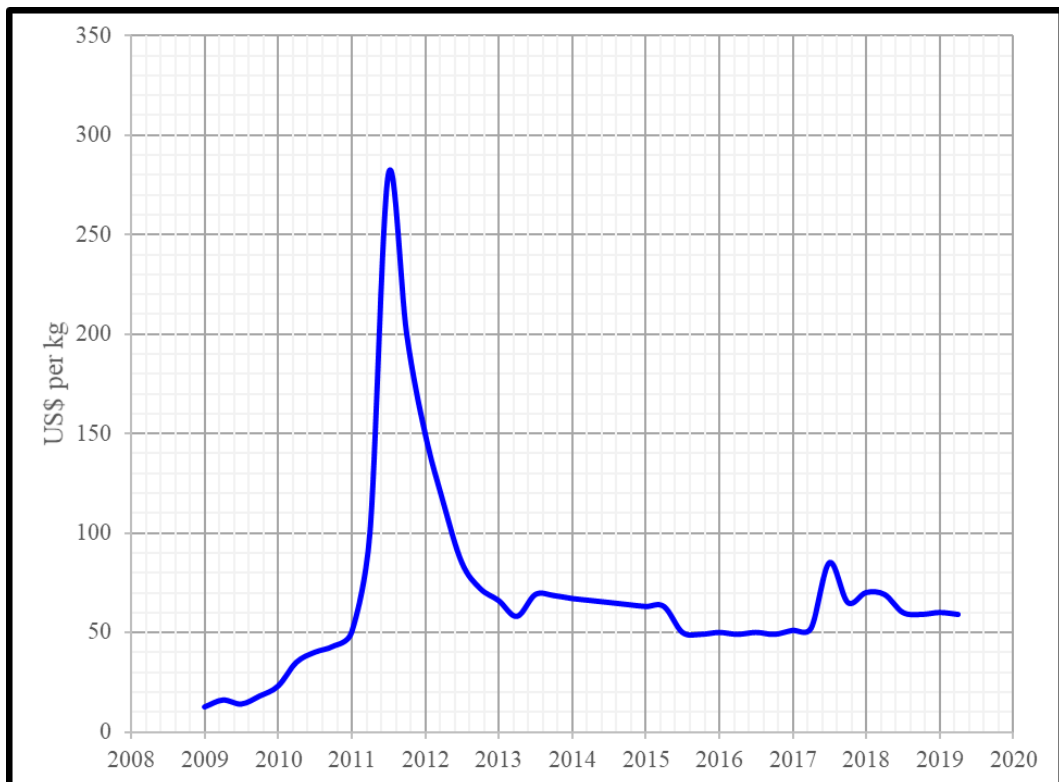


Figure 2.7: Neodymium price over the last decade in US\$ per kg.

The automotive industry has long-term investments as well as planning; when a strategic decision is made, it will reflect the activity of the companies of this sector for many years to come. Considering the fluctuations in the price of RE materials and the monopoly of certain countries on their reserves and on their mining resources, some countries and automotive companies began to invest in the study of RE-free solutions for electric vehicle applications.

A recent JRC study [19] specifies that the EU could become vulnerable for the supply of several key materials needed for photovoltaic, wind, and electric vehicle technologies: if mitigation measures are not taken, the EU reliance on potential power supply issues will harm the investments.

2.3 Motor solutions for electric vehicles

Table 2.1 presents the motor types, the maximum power, the maximum vehicle speed, the time to accelerate from 0 to 100 *km/h*, the gear ratio and the maximum speed of the electric machines of the main EVs sold in the EU & US markets [20]-[21]. When not available, the maximum electric machine speed has been estimated.

The RE machines have higher power density, specific torque, and power factor compared to the one of RE-free machines [22]-[24]; in order to improve the performance of these last machine typologies, the design engineers are pushed to increase the maximum operating speed, as shown in the table. Between the listed motors, the ones that reach the highest speeds are the Tesla model electric motors, which are based on Induction Motor (IM) solutions and on Permanent Magnet-assisted-Synchronous Reluctance (PM-a-SynRel) ones. The IM is RE-free, while the PM-a-SynRel motor uses a reduced amount of RE magnets compared to the amount employed for PM Synchronous Motor (PMSM) solutions; for PM-a-SynRel machines, it is possible to use RE-free permanent magnets such as ferrite magnets.

Despite the use of RE-free solutions, Tesla vehicles still have the highest maximum power, the top speed and the minimum acceleration time; that clearly means that using RE-free solutions does not necessarily correspond to low vehicle performance. The RE solution with the maximum motor speed is the one of the Jaguar I-Pace (13000 *rpm*): its maximum speed is lower than the one of the Tesla Model 3 (20000 *rpm*), which uses an IM for the front wheels and a PM-a-SynRel motor for the rear ones.

Up to 2017, only two companies (Tesla and Renault) were using RE-free solutions for their electric vehicles, but in the last years other companies have

decided to switch to RE-free motors (Audi and BMW [25]); however, on the market there are no solutions that use the pure Synchronous Reluctance motor (SynRel). Renault has chosen the Wound Rotor Synchronous Motor (WRSM), which needs the usage of slip rings and brushes, hence implying maintenance requirements.

Table 2.1: Traction motors for electric vehicles (2018-2019) [21].

Vehicle Model	Motor type Front / Rear	Max Power (kW) Front / Rear	Top speed (km/h)	Acceleration 0-100 km/h (s)	Gear ratio	EM Max speed (rpm)
Audi e-tron 55	IM / IM	125 / 140	200	6.6	9.2	13000
Audi Q4 e-tron	IM / PMSM	75 / 150	180	6.3	9.2	12000
BMW i3S 42	- / PM-a-SynRel	- / 135	160	6.9	9.66	11500
BMW i3S 33	- / PM-a-SynRel	- / 135	160	6.9	9.66	11500
Chevrolet Bolt	PMSM / -	150 / -	145	6.9	7.05	8600
FIAT 500e	PMSM / -	83 / -	141	-	9.59	12000
Hyundai e-Kona 64	PMSM / -	150 / -	167	7.6	7.98	10500
Jaguar I-Pace	PMSM / PMSM	147 / 147	200	4.8	9.04	13000
KIA Soul EV	PMSM / -	81 / -	145	11.5	8.21	9600
KIA e-Niro 39	PMSM / -	100 / -	155	9.8	8.21	10000
KIA e-Niro 64	PMSM / -	150 / -	167	7.8	8.21	11000
Nissan Leaf SL Plus	PMSM / -	160 / -	159	-	8.19	10500
Nissan Leaf SL	PMSM / -	110 / -	144	7.9	8.19	9700
Renault Zoe R110	WRSM / -	80 / -	135	11.4	9.3	11000
Renault Zoe Q90	WRSM / -	65 / -	135	13.2	9.3	11000
Tesla Model X	IM / IM	193 / 375	250	3.7	9.7	17000
Tesla Model X SR	PM-a-SynRel / IM	193 / 375	250	2.9	9.7	17000
Tesla Model 3	IM / PM-a-SynRel	147 / 211	250	3.4	9.7	20000
Tesla Model S P100D	IM / IM	193 / 375	250	2.4	9.7	18000
Volkswagen e- Golf	PMSM / -	100 / -	150	9.6	9.7	12000
Volkswagen e-up!	PMSM / -	60 / -	130	12.4	8.16	10000

PMSM = PM Synchronous Motor; IM = Induction Motor; WRSM = Wound Rotor Synchronous Motor; PM-a-SynRel = Permanent Magnet-assisted-Synchronous Reluctance Motor.

The SynRel solution is a particular motor type that has neither the magnets nor the windings inside the rotor, making it the potentially cheapest solution; its torque production depends only on the rotor anisotropy. The SynRel motor has lower costs

compared to other solutions, both for the raw materials that it uses (the rotor is only made of steel) and for the manufacturing process, since it does not require the insertion of Permanent Magnets, windings, or a cage.

The reasons why this typology is not used in the automotive sector are its low power density, specific torque, and power factor, but these disadvantages can be partially overcome with an accurate design procedure.

2.3.1 H2020 ReFreeDrive project

Besides car manufacturers, the European Union has also funded the H2020 project ReFreeDrive (Rare Earth Free e-Drives featuring low-cost manufacturing). The aim of this project is to avoid the use of RE magnets for the development of electric drivetrains, ensuring the industrial feasibility for mass production while focusing on the low cost of the manufacturing technologies. The ReFreeDrive Consortium is composed of 13 partners in six European countries, including the University of L'Aquila. The project arises because diesel and gasoline-powered vehicles have been seriously questioned at EU level for air quality, CO₂, and energy efficiency.

The Clean Vehicles Directive has increasingly focused on higher ambition levels in terms of pollutant and CO₂ emissions and the energy efficiency directive comes with an impact assessment drafting a landscape of 39.8 million electric vehicles by 2030. Some states in the EU have begun to provide incentives for the purchase of electric cars and a resolution to ban the ICE vehicles starting in 2030. Moreover, car manufacturers are expressing their interest in electric vehicles (partly in response to the emission scandal of 2015) [25].

The choice of the RE-free solution can be explained by the high and volatile cost of raw materials for magnets, the uncertainty for their long-term availability, and the aspects treated in the previous subchapters.

The main target of this project is the development of RE-free traction machines with new designs and technologies in order to improve their performance while guaranteeing low-cost products both from a manufacturing and a material point of view for large mass production. In addition to the motor sizing, the design and the integration of the power electronics system have been carried out in order to obtain a full powertrain to be tested at the end of the project.

The following solutions have been investigated:

- an IM with fabricated and copper die-cast rotors;
- a PM-a-SynRel motor with ferrite magnets;
- a pure SynRel motor.

The team of the University of L'Aquila took in charge the design of the pure Synchronous Reluctance motor for the full-electric vehicles.

Within the project, an accurate analysis of mechanical, magnetic, and economic aspects of different electrical steels has been made in order to select the best material for the application.

Two different sizes have been designed: 75 kW and 200 kW of peak power. The two solutions share the same electrical steel, the stator and rotor shapes, and the housing in order to have a scalability and to reduce the manufacturing costs. The only differences consist in the DC voltage supply, in the stack length and in the winding configuration.

In order to increase the power electronics density and efficiency, the SiC power modules have been chosen. The motor and the power electronics have been integrated and they share the same cooling system.

The SiC power modules allow to reach higher switching frequencies, which is necessary since RE-free machines reach higher speeds than RE ones, leading to a higher fundamental frequency; these modules are expensive, going against the principle of low-cost applications. Many studies about this technology show that, nowadays, this solution cost is too high for mass production; on the other hand, when this technology will reach its full development, the price of these SiC modules may be comparable to the current technology. Even if at the moment these modules cost is not competitive, the power electronics of Tesla 3 is composed of custom SiC MOSFETs produced by STMicroelectronics.

The motor requirements have been set in terms of specific power, power density, and efficiency: these data have been compared to the ones of a current RE-free electric vehicle taken as a reference (Tesla Model S 60, 2012). The objective was to have a 30% increase in specific power with a 50% increase in maximum operating speed, a 50% energy losses reduction and the capacity to operate with the same cooling system used for the ICE in vehicles with a hybrid configuration.

The increase of the motor speed (up to 20000 rpm) allows to reduce the maximum torque of the machine and, therefore, its weight: this in turn increases the power density of the machine. However, a higher speed requires a gearbox with a higher split ratio (higher losses and lower efficiency) to provide the adequate vehicle speed.

The specifications indicated above have required a complex optimization process for the SynRel design to match the desired performance whilst respecting the component cost target.

2.4 The electric car model

The car is a very complex system that can be difficult to represent with a simple model because several subsystems have to be considered, each of whom has a complex model. The aim of the modeling in this subchapter is to provide a simple model of the resistances to motion in order to evaluate the performance that the electric motor must have to satisfy the requirements of the vehicle [27].

The electric machine is typically connected to the wheels through a transmission system, with its own torque and energy losses. The torque of the motor is converted to the forces of the vehicle by using the contact between the wheel and the road. The transmission of these forces is guaranteed by a perfect adhesion between the wheel and the road.

Figure 2.8 shows the distribution of the pressure between the wheel and the road, the deformation (h) of the wheel, and the forces and the torque applied to it. The pressure (p) can be computed as a derivative of the gravity force (W) with respect to the contact surface (A). Simplifying the model, the average pressure is the ratio between the gravity force and the wheel contact area. The contact area depends on the inflation pressure of the tires: in fact, the higher the pressure, the lower the area and, as a consequence, the adherence and the resistance force.

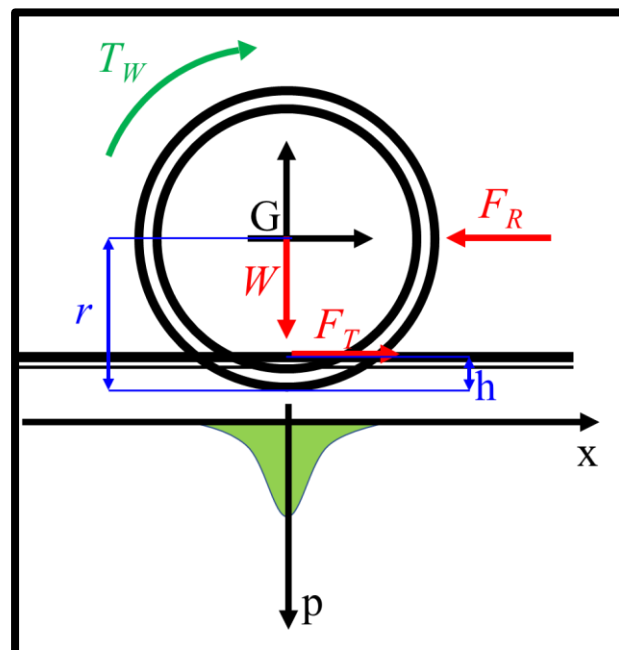


Figure 2.8: Wheel-road kinematic pair in stationary conditions.

Neglecting the deformation of the wheel ($h \ll r$) and considering the balance of the forces and of the torque respect to the contact point, it is possible to write the following equations:

$$\begin{cases} \mathbf{F}_T - \mathbf{F}_R = m_{eq} \frac{d\mathbf{v}}{dt} \\ \mathbf{T} - \mathbf{F}_R r = J_{eq} \frac{d\omega}{dt} \end{cases} \quad (2.1)$$

where \mathbf{F}_T is the traction force exchange at the contact surface, \mathbf{F}_R is the resistance force, \mathbf{T} is the motion torque, r is the radius of the wheel, \mathbf{v} is the linear speed, ω is the angular speed, m_{eq} is the equivalent mass, and J_{eq} is the equivalent inertia.

The equivalent mass includes, besides the mass of the vehicle, the reported mass of all the rotating elements inside the car.

The adherence condition is verified if the wheel has a pure rolling motion, without relative sliding, and the speed of the contact point of the wheel is zero; in this condition, the linear speed and the angular one are linked by this expression:

$$\mathbf{v} = \omega r \quad (2.2)$$

The higher the motion torque, the higher the traction force; but this last term has a limit due to the adherence. Therefore, it is possible to define a traction force limit:

$$\mathbf{F}_T \leq \mu_{ad} \mathbf{W} \quad (2.3)$$

where μ_{ad} is the adhesion coefficient and \mathbf{W} is the gravity force.

In the next analyses, only the perfect adhesion condition will be evaluated.

2.4.1 Motional resistance forces

The first motional resistance force that will be analyzed is the resistance due to the friction between the bearing and the spindle at the wheel axes; in fact, there are a relative motion and a dynamic friction coefficient that have to be considered.

Figure 2.9 shows the forces and the torque generated from the friction between the spindle and the bearing at the wheel axis.

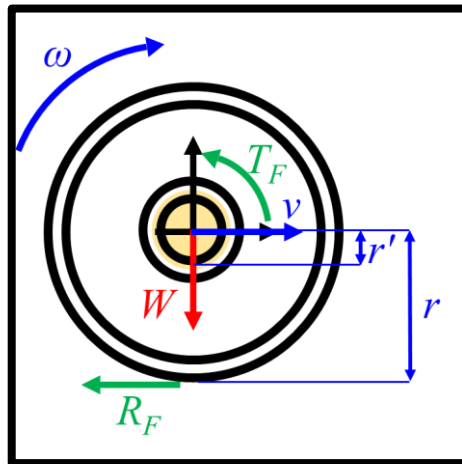


Figure 2.9: Friction between the spindle and the bearing.

The resistance torque (T_F) is generated by the resistive force due to friction, while the frictional resistive force (R_F) is a consequence of this torque since it balances out the torques on the wheel. The expression of the resistive force can be calculated with the following expression:

$$T_F = \mu_{dyn} G r' = R_F r \Rightarrow R_F = \mu_{dyn} G \frac{r'}{r} \quad (2.4)$$

where μ_{dyn} is the dynamic friction coefficient and r' is the inner radius of the bearing.

Another resistive force is due to the rolling friction between the wheel and the road. When the vehicle has a non-zero speed, the distribution of the contact pressure (visible in Figure 2.8) changes and the pressure resultant moves to the right of the axis passing through the gravity center, hence creating a resistance torque that has to be balanced by another tangential force acting on the contact point between the road and the wheel, as shown in Figure 2.10.

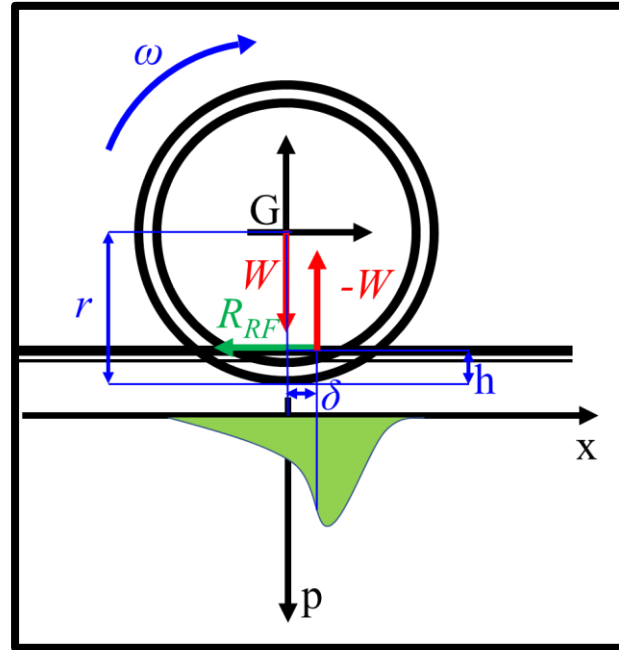


Figure 2.10: Rolling friction between the wheel and the road.

From the figure, it is possible to carry out the balance of the momentum in order to obtain the expression of the rolling frictional resistive force (R_{RF}).

$$W \delta = R_{RF} r \Rightarrow R_{RF} = W \frac{\delta}{r} \quad (2.5)$$

where δ is the distance between the equivalent contact point in stationary conditions and during motion. This term depends on the inflation pressure of the tires (the higher the pressure, the lower the δ), on the conditions of the tires, and on

the condition of the road. The sum of the rolling frictional resistive force and the frictional resistive force gives the rolling resistive force (R_R); using (2.4) and (2.5), it is possible to write:

$$\mathbf{R}_R = \mathbf{R}_{RF} + \mathbf{R}_F = \mathbf{W} \frac{\delta}{r} + \mathbf{W} \mu_{dyn} \frac{r'}{r} = \frac{\mathbf{W}}{r} (\delta + \mu_{dyn} r') = k_R \mathbf{W} \quad (2.6)$$

where k_R is the rolling friction coefficient:

$$k_R = \frac{(\delta + \mu_{dyn} r')}{r} \quad (2.7)$$

The aerodynamic drag is due to the motion of a vehicle in a fluid (air) and depends on the geometry of the vehicle, on the properties of the fluid and on the relative speed between the fluid and the vehicle according to:

$$\mathbf{R}_A = \frac{1}{2} \rho A_f \gamma (\mathbf{v} - \mathbf{v}_a)^2 = c_x (\mathbf{v} - \mathbf{v}_a)^2 \quad (2.8)$$

where ρ is the fluid density (air), A_f is the frontal area of the vehicle, γ is the drag coefficient of the vehicle (a typical value ranges from 0.2 to 0.3), v is the vehicle speed, v_a is the fluid speed, and c_x is the aerodynamic coefficient. This term does not include the additional resistance due to the roughness of the vehicle lateral surface, to the turbulence of the air between the bottom of the car and the road, and to the suction that is present at the back of the vehicle. The aerodynamic force does not depend on the mass of the vehicle, it only depends on its shape and on its length, on its frontal air, and on the relative speed. At high speeds, this term has a predominant weight compared to the other resistances.

The gradient force (R_G) occurs when there is a road slope: this force can be a resistance (if the slope is greater than zero) or it can help the vehicle motion (if the slope is lower than zero), as shown in Figure 2.11.

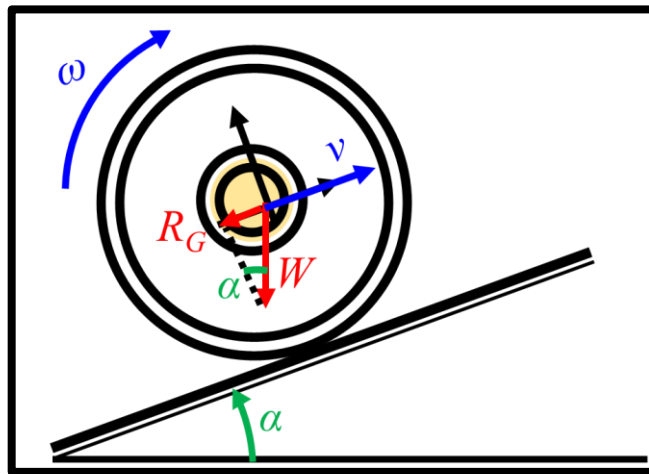


Figure 2.11: Gradient resistive force.

This resistive force is accidental and not always present, therefore, for the calculation of the acceleration it can be neglected; on the other hand, for the computation of the maximum force that is required at the maximum speed, a constant value of the slope, equal to its maximum admissible value, will be considered. From Figure 2.11, it is possible to calculate the expression of the gradient resistive force:

$$R_G = G \sin(\alpha) = G \frac{\tan(\alpha)}{\sqrt{1 + \tan^2(\alpha)}} \quad (2.9)$$

where $\tan(\alpha)$ is the typical value indicated for the slope. Considering that the slope is lower than 30%, it is possible to make the following simplification:

$$R_G \cong G \tan(\alpha) \quad (2.10)$$

The inertial force (F_i) is opposed to the speed variation and, therefore, to the acceleration; this term depends on the value of the mass. The motion of the vehicle is not a simple linear motion because there are many parts inside of it that are characterized by a rotation. For this reason, the value of the mass is increased by a constant (k_{eq}), which takes into account the equivalent mass of all the rotating parts.

$$F_i = k_{eq} m \frac{dv}{dt} = m_{eq} a \quad (2.11)$$

where m is the mass of the vehicle, m_{eq} is the equivalent mass, and a is the vehicle acceleration.

2.5 Design Criteria for the Electric Motor

The linear motion of the vehicle is due to the rotating movement of the electric motor and of the wheels. The motor is connected to the wheels through a transmission system and, under the assumption of perfect adhesion between the wheels and the road and considering the equations (2.1) and (2.2) carried out earlier, the motor torque can be linked to the driving force applied to the vehicle wheels through the following expression:

$$T_\omega = T_e \eta_t i \Rightarrow F_T = \frac{T_e \eta_t i}{r} \quad (2.12)$$

where T_e is the torque of the electric machine, η_t is the efficiency of the transmission system, and i is the gear ratio.

Considering the expressions of all the resistive forces (2.6), (2.8) and (2.10), of the inertial force (2.11), and of the traction force (2.12), it is possible to write the dynamic model of the vehicle:

$$\frac{dv}{dt} = \frac{1}{m_{eq}} \left(\frac{T_e \eta_t i}{r} - k_R W - \tan(\alpha) W - c_x (v - v_a)^2 \right) \quad (2.13)$$

The electric machine is typically able to supply a constant torque up to the point corresponding to its base speed; from this point forward, the machine works in the flux-weakening region with constant power. The traction motor requirements, such as maximum speed, base speed, maximum torque, and maximum power at maximum speed, depend on the vehicle specifics, as described below.

The most important performance parameters of the vehicle are the maximum speed (v_{max}) and the acceleration time from 0 to 100 km/h (t_a). Other two performance parameters could be the acceleration time from 60 km/h to 100 km/h and the one from 0 to 120 km/h.

The parameters and the required performance of an electric car are listed in Table 2.2: these values have as a reference a high performance car, the Tesla Model 3 in Table 2.1. These data will be used for a numerical example of the computation of the electric motor requirements.

Table 2.2: Vehicle parameters and performance.

Parameter	Unit	Value	Parameter	Unit	Value
Mass (m)	kg	2500	Drag Coeff. (γ)		0.26
Mass Correction Factor (k_{eq})		1.04	Wheel Radius (r)	m	0.30
Air Density (ρ)	kg/m ³	1.225	Maximum speed (v_{max})	km/h	250
Rolling Resistance Coeff. (k_R)		0.0054	Time 0-100 km/h (t_a)	s	2.5
Frontal Area (A_f)	m ²	1.746	Maximum slope ($\tan(\alpha)$)	%	2.5

The first step to find the requirements of the electric motor for an electric car application consists in the selection of the gear ratio, which depends on the maximum vehicle speed, on the wheel radius (both imposed by the vehicle) and on the maximum rotating speed (ω_{max}) that the designer set for the motor according to:

$$i = \frac{\omega r}{v} = \frac{\omega_{max} r}{v_{max}} \quad (2.14)$$

The efficiency of the transmission system depends on the value of the gear ratio: the higher this ratio, the lower the efficiency. This downside limits the convenience in trying to increase the electric motor speed: in fact, according to Table 2.1, the range of maximum speeds that is feasible does not exceed 18000÷20000 rpm.

By imposing a maximum speed of the motor of 20000 rpm and using the expression (2.14), it is possible to calculate the gear ratio (i), which is equal to **9.05**. It is worth remarking that, for this computation and for the next ones, the rotating

speed has to be in *rad/s* and the vehicle speed in *m/s*. With this value of the gear ratio, it is possible to consider a transmission efficiency equal to **97%**.

For the computation of the maximum torque and of the base speed, the time to accelerate the car from 0 to 100 *km/h* will be considered; the gradient resistive force and the fluid speed will be neglected because the acceleration is requested with a null slope and a null air speed. In order to calculate the speed, the differential equation (2.13) is used as starting point and a null speed is imposed as initial value.

$$v(t_a) = \sqrt{\frac{\frac{T_e(\omega)\eta_t i}{r} - k_R W}{c_x}} \tanh\left(\sqrt{\left(\left(\frac{T_e(\omega)\eta_t i}{r} - k_R W\right) c_x\right) \frac{t_a}{m_{eq}}}\right) \quad (2.15)$$

If the base speed matches the rotating speed of the motor that corresponds to the vehicle speed of 100 *km/h*, the motor torque is therefore constant and equal to its maximum value ($T_{e,max}$) throughout the entire acceleration period of the vehicle from 0 to 100 *km/h*. This consideration allows to minimize the value of the maximum torque, while also reducing the mass of the electric machine but admitting a slightly increase of the peak power.

Considering the expression (2.15), the only unknown term is the electric machine torque since the other terms (except for i , which has already been calculated) are imposed by the vehicle data. However, it is not possible to analytically solve the equation respect to the term $T_{e,max}$: for this reason, the solution has to be obtained numerically.

The maximum torque of the electric machine is equal to **624 Nm**; a vehicle with those requested performance has generally two electric machines, so the torque of each motor is equal to **312 Nm**, while the base speed (ω_b) is equal to **8000 rpm**. This last value has been obtained considering that at the base speed the vehicle car is equal to 100 *km/h*. In this condition, the maximum power at the base speed (P_b) is equal to **260 kW**.

After that the maximum torque has been evaluated, it is possible to calculate the power at the maximum speed. In this condition, the inertial force can be neglected because of steady state conditions. Moreover, the gradient resistive force is set to its maximum value for those routes where it is possible to reach the maximum speed.

$$\frac{T_e(\omega)\eta_t i}{r} = k_R W + \tan(\alpha_{lim}) W + c_x v^2 \quad (2.16)$$

Multiplying each term by the vehicle speed:

$$\frac{T_e(\omega)\eta_t i}{r} v = k_R W v + \tan(\alpha) W v + c_x v^3 \quad (2.17)$$

Using (2.14) and considering that the product of the torque and of the motor rotating speed gives the motor power (P_e), it is possible to write:

$$P_e(\omega_{max}) = \frac{k_R W v_{max} + \tan(\alpha_{max}) W v_{max} + c_x v_{max}^3}{\eta_t} \quad (2.18)$$

The only unknown term is the power of the motor at the maximum speed, whose value can now be computed. Solving the expression (2.15) numerically and using (2.18), it is possible to define the limit performance of the motor.

In addition, through the expression (2.18) it is possible to calculate the power at the maximum speed ($P_{\omega,m}$), which is equal to **145 kW**: although, considering that there are two motors, each one should guarantee a power of **77.5 kW** and a torque at the maximum speed ($T_{\omega,m}$) equal to **37 Nm**.

2.6 Comparison between different Light Drive Vehicle (LDV) categories

Figure 2.12 shows a possible torque-speed curve (in blue) and a power-speed curve (in red) that an electric machine should have in order to satisfy the vehicle requirements. It is sufficient to maintain a constant power beyond the point of the motor base speed in correspondence of a vehicle speed of **120 km/h** in order to maximize the acceleration performance up to that speed. Above **120 km/h**, there are no requirements for the acceleration performance, then the output power of the motor should only guarantee the motion at that speed. Obviously, the higher the power, the higher the performance of the vehicle. The curves are very interesting because they show that the electric machine does not need a large constant-power section in the flux-weakening region; for this reason, it is also possible to choose solutions without a good flux-weakening behavior (this justifies, for example, the use of the SynRel motor).

In order to evaluate the efficiency of the vehicle, a driving cycle has to be considered. In this thesis, the WLTP cycle 3 has been chosen as reference cycle. It is characterized by three main routes: the first route is in the urban city with frequent accelerations and decelerations and with a speed always lower than **50 km/h**; the second one is on an extra-urban road with a speed always lower than **100 km/h**; the third route is on the highway with a maximum speed of **130 km/h**. The cycle is shown in Figure 2.13.

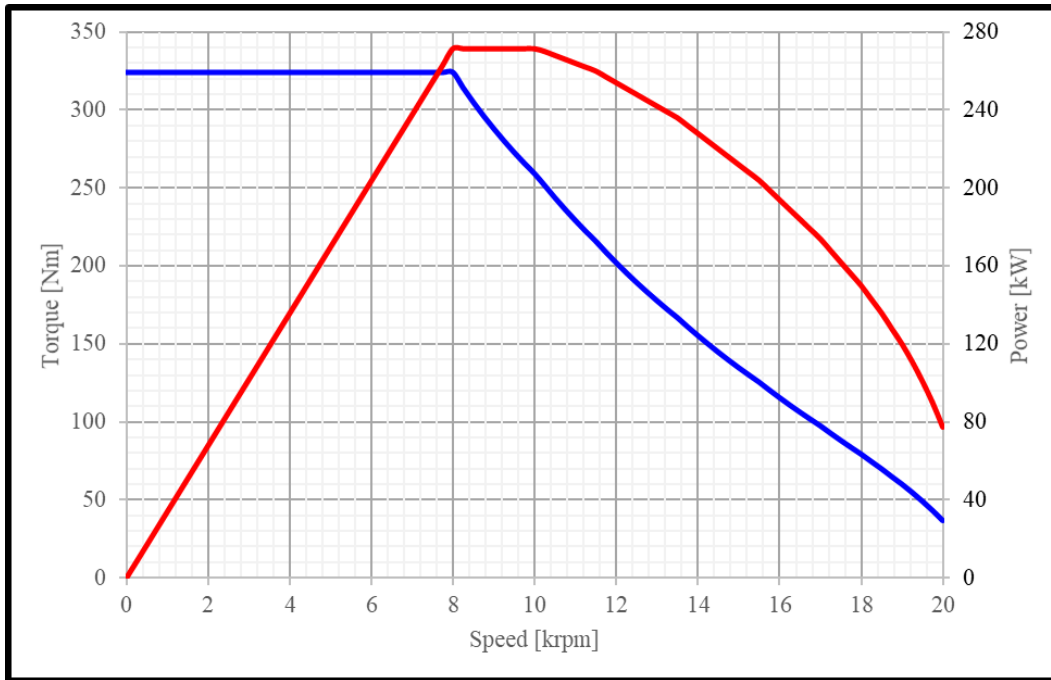


Figure 2.12: Torque (blue) and power (red) vs speed.

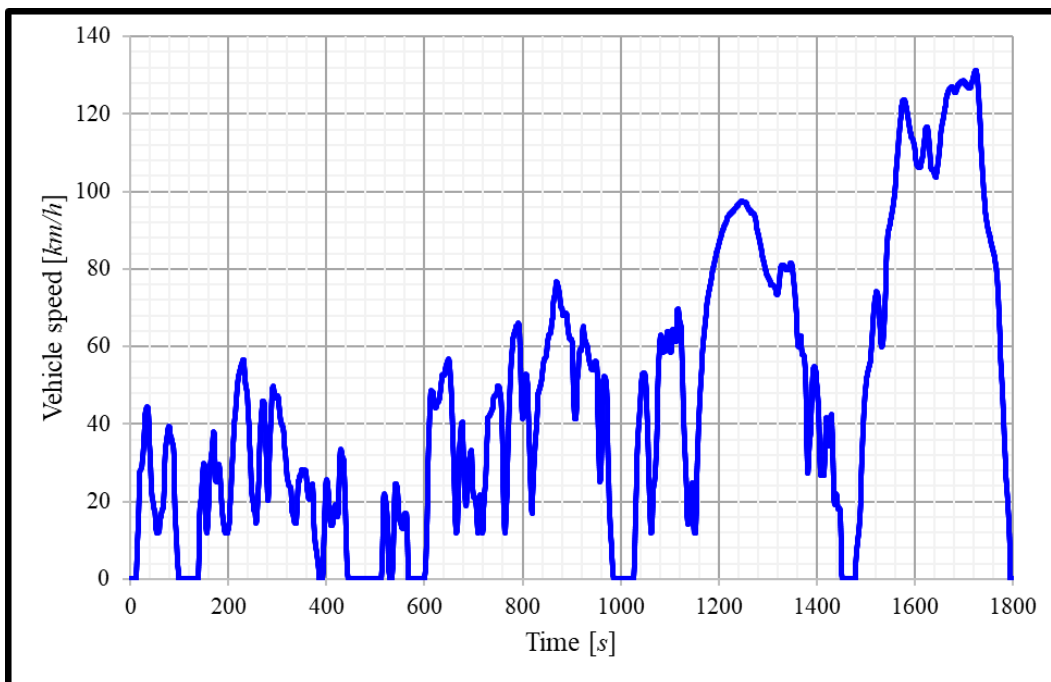


Figure 2.13: WLTP cycle 3.

Thanks to the model (2.13) and to the expression (2.14), it is possible to calculate the torque and the speed of the motor for the whole driving cycle. The torque (in red) and the speed (in blue) are shown in Figure 2.14.

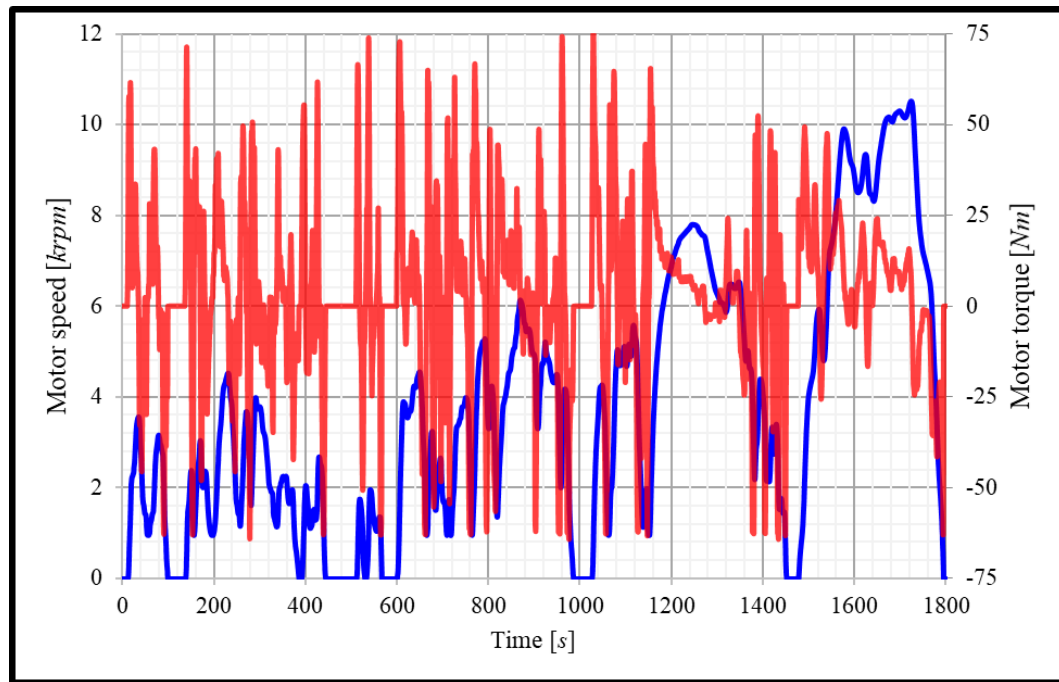


Figure 2.14: Torque and speed during the WLTP cycle 3.

During the deceleration steps, the electric machine works as a generator and the regenerative braking energy can be recovered in the energy storage system. This is one of the main advantages of the use of electric vehicles; by recovering the braking energy, it is possible to increase the efficiency of the car: this energy retrieval can also be done by hybrid vehicles but not by ICE vehicles.

Figure 2.15 shows the torque-speed points during the WLTP cycle 3. It is worth noting that the green points are in the area of low torque and speed. In order to guarantee a higher cycle efficiency, the electric machine should have a good efficiency in that area. A typical design of electric machines leads to obtain their maximum efficiency within the medium torque-speed area (around 100 Nm and 10krpm): an example is shown in Figure 2.16. For this reason, a particular design procedure has to be used in order to move the maximum efficiency points towards the driving cycle points, so that the overall cycle efficiency can be increased.

According to [28], the vehicles can be classified among the segments obtained by the common features of each vehicle, according to the classification of the European Light Drive Vehicle (LDV). From this study, it is possible to evaluate the use of electric machines in each segment to calculate their performance. The parameters of the segments are calculated for the ICE motors, hence, in order to consider the energy storage system of the EV, an additional mass must be included. The study has been made in 2016 using the commercial vehicle of 2013. It is useful to include the table of this study in order to have an idea of the typology of the different segments and of the reference parameters. This is reported in Table 2.3.

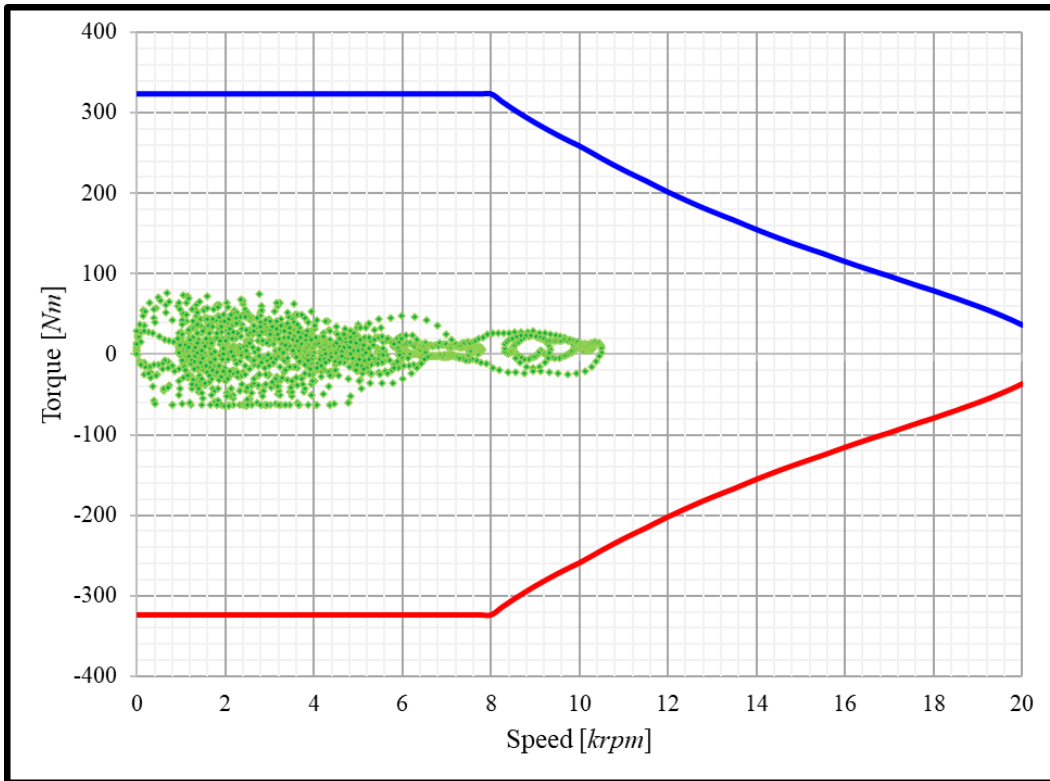


Figure 2.15: Torque-speed points (green) in the WLTP cycle 3 and their limits (blue and red).

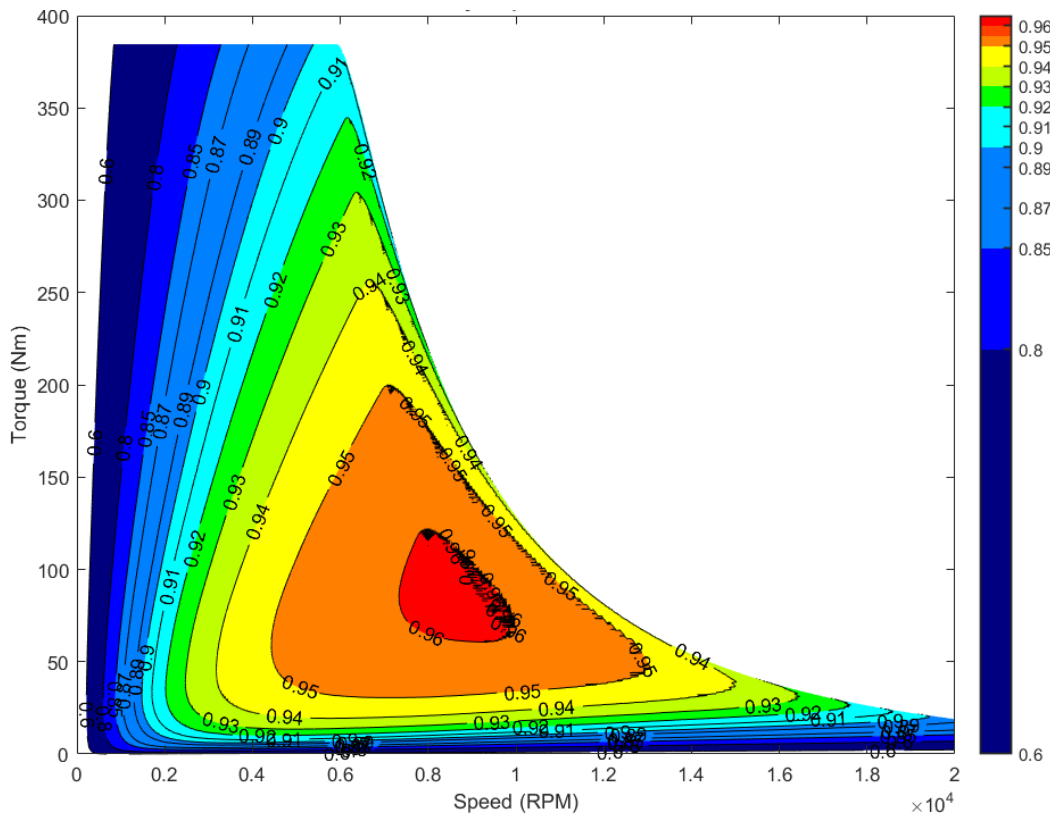


Figure 2.16: Example of an efficiency map.

Table 2.3: European Light Drive Vehicle (LDV) categories and parameters.

LDV segment	Euro Car specification	Top speed (km/h)	t_a (s)	Mass (kg)	k_R	c_x (kg/m)
A	Mini	160	13.0	1550	0.01167	0.4655
B	Small	180	11.7	1800	0.01171	0.4594
C	Mediums	200	10.0	2100	0.01123	0.4716
D	Larges	220	8.8	2300	0.01139	0.4410
E	Executives	250	6.2	2500	0.01163	0.4594
J	Sport Utility	190	9	2350	0.01224	0.6003

Using the same procedure shown before, it is possible to calculate the performance of the electric machines and the torque-speed points for the WLTP cycle 3. For each case, the maximum rotating speed of the electric machine is imposed equal to 20000 rpm, the mass correction factor is set to 1.04, the number of the electric machines is equal to 1, the maximum slope is imposed equal to 2.5%, and the wheel radius is considered equal to 0.3 m. Table 2.4 shows the electric machines performance in the different LDV segments.

Table 2.4: Electric machines performance in the different LDV segments.

LDV segment	i	η_t (%)	$T_{e,max}$ (Nm)	ω_b (rpm)	P_b (kW)	$P_{\omega,m}$ (kW)	$T_{\omega,m}$ (Nm)
A	14.14	96	82.78	12500	108.36	65.65	31.35
B	12.57	96.25	118.36	11111	137.72	89.84	42.9
C	11.31	96.5	176.51	10000	184.84	122.33	58.41
D	10.28	96.75	238.93	9091	227.46	150.82	72.01
E	9.05	97	412.01	8000	345.16	216.24	103.25
J	11.91	96.38	208.72	10526	230.07	133.56	63.77

For all the segments, the power at the maximum speed is around the 60% of the power at the base speed; therefore, also in these cases, the constant power area requested by the electric machine is small and the electric machine itself does not have good flux-weakening capabilities.

Figures from Figure 2.17 to Figure 2.22 show the torque-speed points during the WLTP cycle 3 for the LDV segments A, B, C, D, E, and J, respectively. When the requirements of the electric vehicle increase in terms of top vehicle speed and acceleration time, the points of the driving cycle move away from the limit torque curves. This results in a departure of the driving cycle operating points from the area of maximum efficiency of the electric machine. Therefore, the electric vehicle has the maximum efficiency during the cycle when the required vehicle performance is similar to the one of the LDV segment A, but it is always possible to reach higher requirements, such as the ones imposed by the segment E.

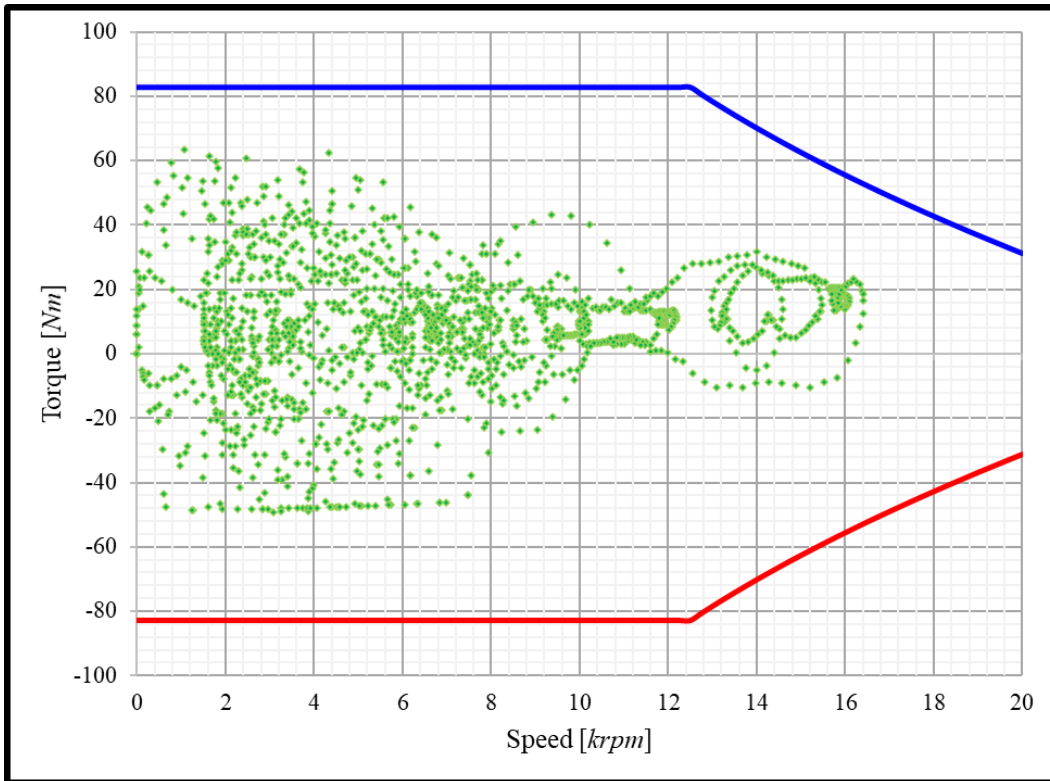


Figure 2.17: Torque-speed points (green) in the WLTP cycle 3 and their limits (blue and red) for the LDV segment A.

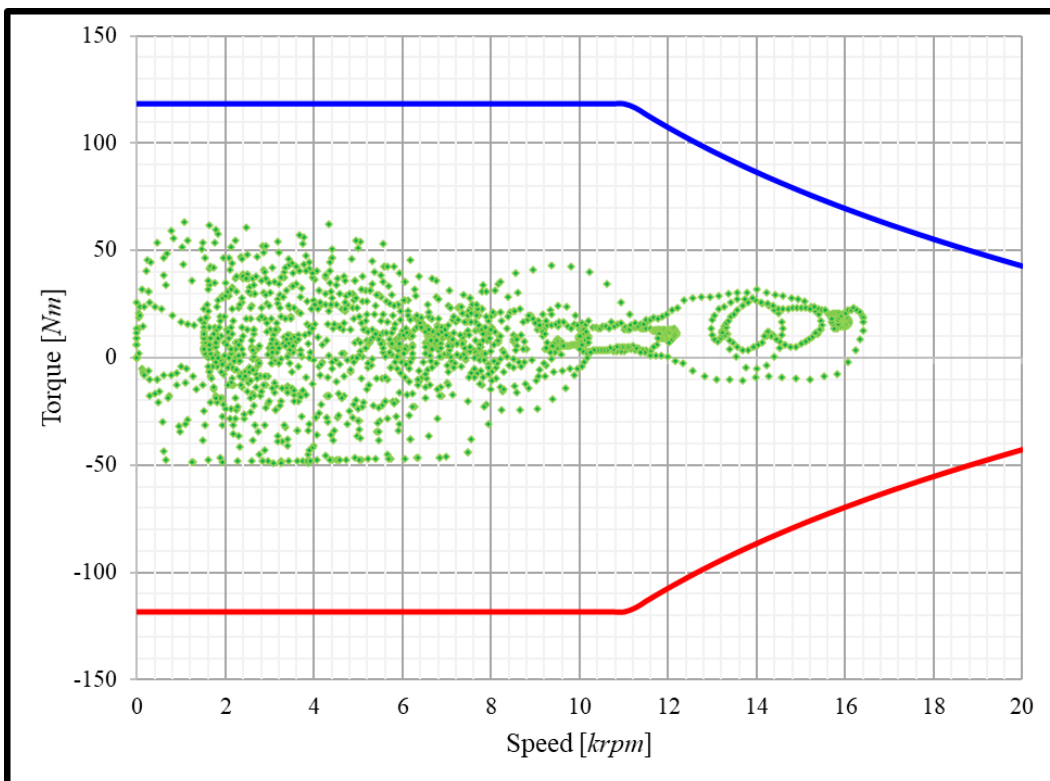


Figure 2.18: Torque-speed points (green) in the WLTP cycle 3 and their limits (blue and red) for the LDV segment B.

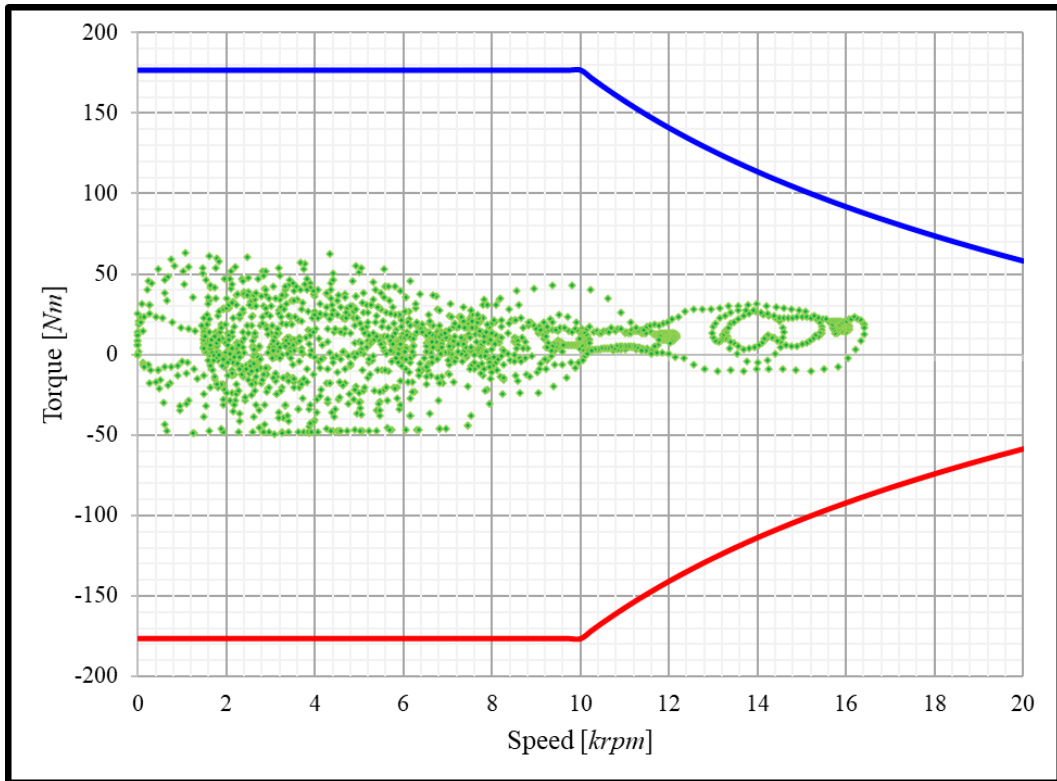


Figure 2.19: Torque-speed points (green) in the WLTP cycle 3 and their limits (blue and red) for the LDV segment C.

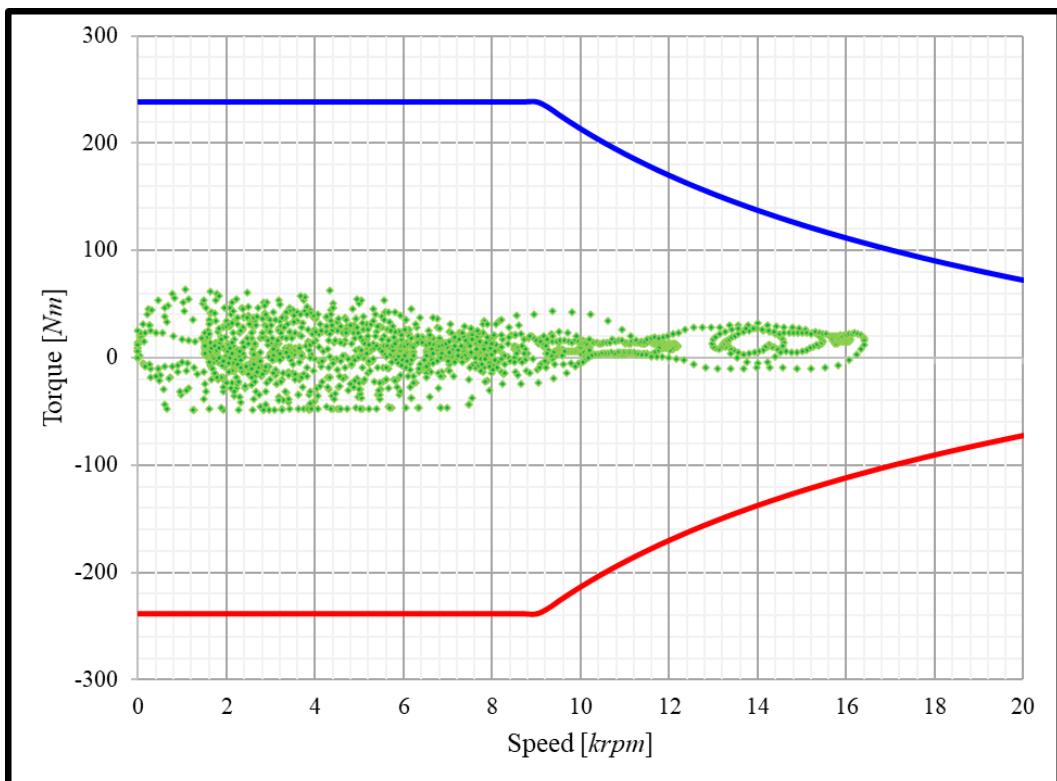


Figure 2.20: Torque-speed points (green) in the WLTP cycle 3 and their limits (blue and red) for the LDV segment D.

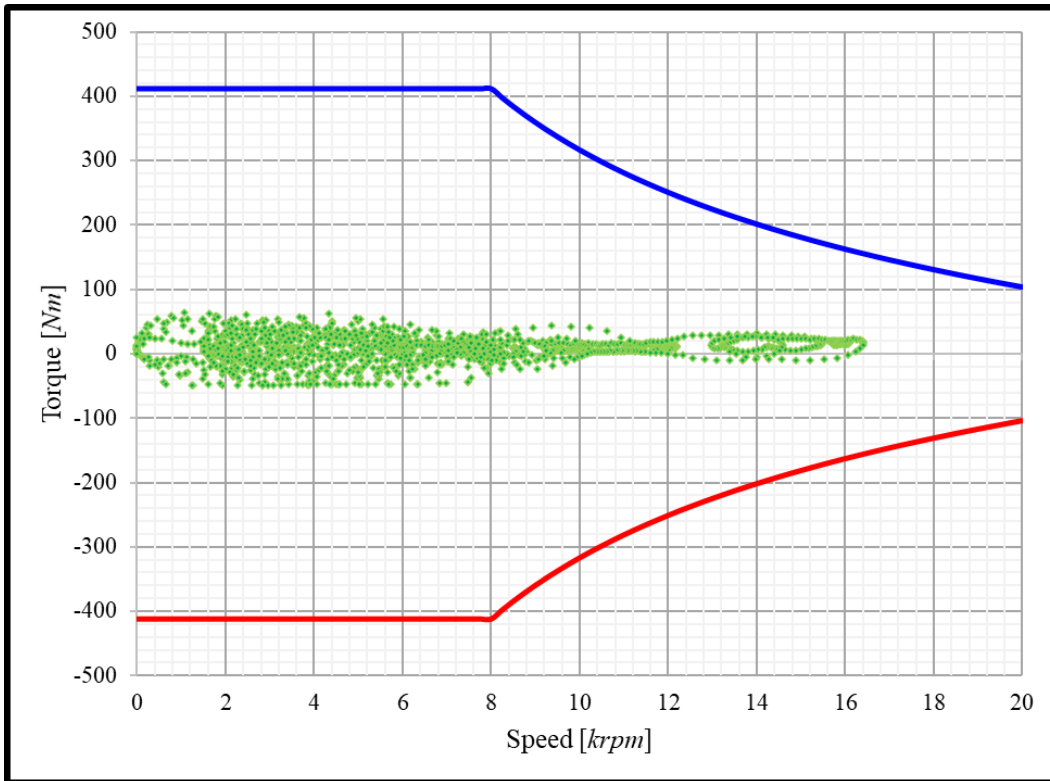


Figure 2.21: Torque-speed points (green) in the WLTP cycle 3 and their limits (blue and red) for the LDV segment E.

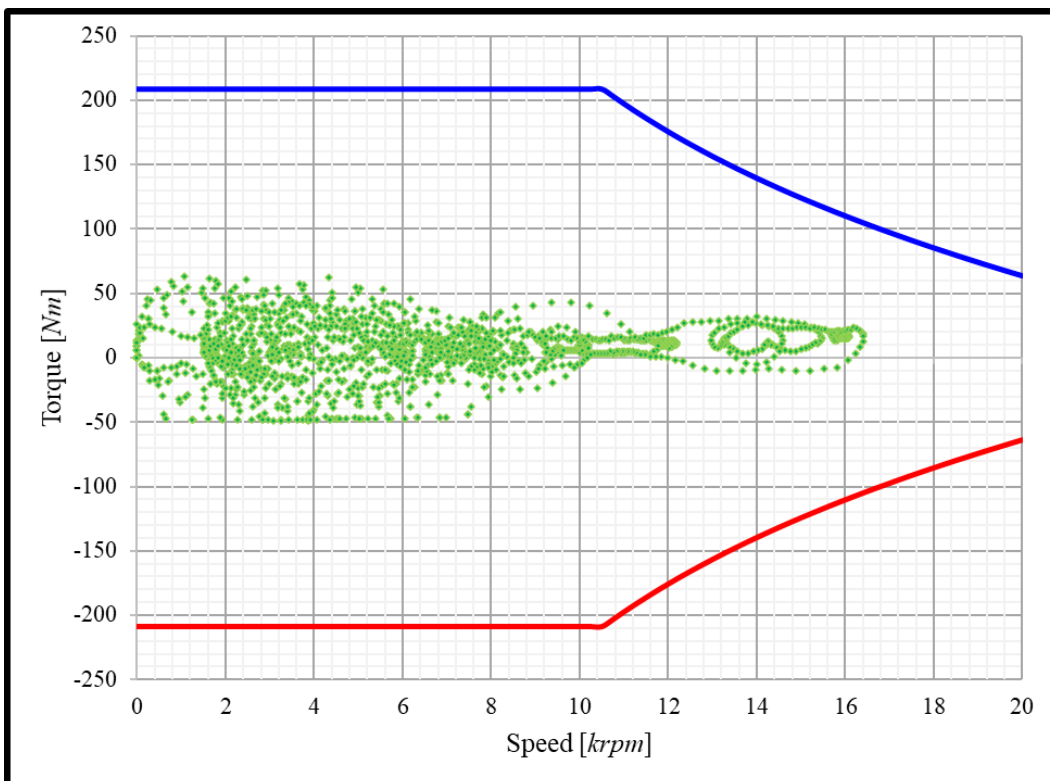


Figure 2.22: Torque-speed points (green) in the WLTP cycle 3 and their limits (blue and red) for the LDV segment J.

2.7 Rare Earth-free motor solutions

In this subchapter, different RE-free solutions will be discussed and compared with one another, focusing on their main advantages and drawbacks. The proposed solutions are the same ones that have been analyzed for the ReFreeDrive project and, particularly: the Induction Motor, the Permanent Magnet-assisted-Synchronous Reluctance motor, and the Pure Synchronous Reluctance motor.

2.7.1 The Induction Motor

The Induction Motor (IM) is the most used typology among the electric motors used for industrial applications; this motor type is characterized by a stator distributed winding and a squirrel cage rotor. An example of IM is shown in Figure 2.23 [29].



Figure 2.23: Induction Motor: examples of squirrel cage rotors.

For electric vehicle applications, the aluminum cage can be replaced with a copper one in order to increase the bars conductivity and therefore to reduce the rotor losses.

During the flux-weakening operation of the IM, the slip between the rotor and the stator magnetic fields is higher than the one corresponding to the constant torque area (considering the same power): this causes an increase in the rotor losses, both in the rotor cage and in the steel laminations.

The losses generated by the rotor cannot be neglected since they are responsible for a significant temperature raise within the rotor, hence limiting the rated power of the machine. For this reason, for high power density motors for EV applications it is better to adopt a liquid cooling system for the IM rotor in order to avoid critical operating temperatures.

The die-casted copper rotor requires a high technological level because the copper melting temperature is high, especially if compared to the aluminum one. For this reason, the fabricated copper bars can represent an alternative solution.

Both the fabricated and the die-casted copper rotors require a technology that implies a high investment cost, which is justified for large mass productions.

Despite the drawbacks of the high investment costs and the need to use a liquid cooled rotor, the induction motor is the most used RE-free solution for EVs, as it has been shown in Table 2.1.

The reason of this large use must be sought in the robustness of the rotor, in the absence of the open-circuit back electromotive force (bemf) (that could be very dangerous in the flux-weakening region), in the simplicity of the design (thanks to its simple geometry) and in the simulation (thanks to the goodness of the well-developed model for this type of machine).

Another key aspect consists in the simplicity of the control of this machine when the power supply is a power converter. Differently from the synchronous machine, the IM does not require an accurate measurement of the rotor position because the optimal control can be done only by using an observer in order to estimate the position of the rotor field.

2.7.2 The Permanent Magnet-assisted-Synchronous Reluctance motor

The Permanent Magnet-assisted-Synchronous Reluctance motor (PM-a-SynRel) is becoming extremely interesting to study for high-efficiency applications thanks to its reduced use of RE Permanent Magnets. In fact, for this type of machine it is possible to use ferrite magnets, thus obtaining a RE-free motor.

The stator of the PM-a-SynRel has the same configuration used for the IM one: therefore, its stator is also characterized by a distributed winding. The torque of this

type of machine is generated both by the anisotropy of the motor and by the permanent magnets; the ratio of these two contributions depends on the quantity of magnets that are used. In Figure 2.24, a typical rotor geometry is shown.



Figure 2.24: Permanent Magnet-assisted-Synchronous Reluctance motor: one rotor pole.

The magnets used for this type of machine are typically low-power density PMs, such as ferrites.

Despite the ferrite has a low energy density, the PM-a-SynRel still presents a b_{emf} , which can be critical at very high speeds in the flux-weakening region; for this reason, during the design procedure, the b_{emf} corresponding to the maximum speed must be limited under the value of the DC voltage.

This consideration can be very useful during the machine flux-weakening operation so that it is not necessary to apply a demagnetization current through the machine control, hence avoiding unnecessary losses; moreover, there is no risk for the phase voltage to reach critical values whether the control could be lost for possible fault reasons.

The low cost magnets inside the machine allow to slightly increase the power density and the efficiency of the machine, compared to the ones of a pure SynRel; the main advantage consists in the improvement of the power factor. In the flux-weakening region, the SynRel has to be controlled with a high current angle, which may be critical to set up (a small error in the position measurement could be dangerous for the control), while the PM-a-SynRel needs a lower control angle that avoids this problem.

The manual insertion of the magnets is expensive in the motor manufacturing process and requires the use of adhesive in order to avoid the detachment of the magnets from the steel: once again, the costs are justified for mass production.

Another key aspect that must be considered for this machine is the demagnetization problem. Since the magnets have a low power density, they are also characterized by a low coercive force with a consequent high risk of damaging them in case of a short circuit fault at sufficient operating speeds: this aspect must be considered during the first design steps. Furthermore, the magnets performance depends on the temperature of the machine; the electric mobility applications have a large working temperature range ($-40^{\circ}\text{C} \div +50^{\circ}\text{C}$) and the maximum temperature that the rotor typically reaches can go over 140°C . If the motor uses Neodymium magnets, the Intrinsic Coercivity (H_{ci}) of Nd magnets is reduced by a temperature increase; on the contrary, ferrite magnets have the opposite behavior. The machine must guarantee the rated performance for all the operating ranges of the temperature.

2.7.3 The pure Synchronous Reluctance motor

The Synchronous Reluctance motor (SynRel) is one of the most promising solutions to obtain a low-cost motor with a good efficiency. The limited use of this type of machine for industry applications is due to the absence of line-start capabilities (this aspect can be overcome with the insertion of a rotor cage), to the use of a hard to calibrate control algorithm (the torque-current behavior is non-linear and the control law used in this case depends on the flux curves of the machine), to low power density and power factor if compared to the ones of the PM solutions.

The capabilities of this machine in terms of torque production depend only on the machine anisotropy, which is obtained with the use of flux barriers in the rotor core. In Figure 2.25, two rotors of SynRel motors are shown.



Figure 2.25: Pure Synchronous Reluctance motors.

Considering the manufacturing processes, the SynRel machine requires the same procedures of the other machine typologies for the realization of the stator and for its assembly, meanwhile the rotor manufacturing requires just the punching process followed by the assembly of the rotor electrical steel laminations.

The rotor core is easy to manufacture and it is less expensive than the one of the IM motor due to the absence of the cage or of the windings in the rotor. Moreover, the absence of windings or magnets allows the rotor to have lower mass and inertia. Considering the losses, the only ones present in the rotor are those generated by the harmonics of the flux and, fortunately, their value is typically low. The absence of other types of rotor losses avoids the use of a rotor cooling system, thus having a low cost-benefit ratio and making this type of machine a good low-cost solution.

Chapter 3

The Synchronous Reluctance Motor

In the recent years, there has been an increasing interest in the design of SynRel motors for industrial applications in order to replace the IMs; many companies are adding this type of machine in their catalogues since it is able to reach a higher efficiency compared to the one of the IM.

The aim of this thesis is to analyze the SynRel motor for automotive applications since it is potentially the less expensive solution and could be proposed for those applications that do not require a high vehicle performance. This activity has been carried out within the European H2020 ReFreeDrive project.

This chapter presents the modeling of the SynRel machine starting from the voltage equations and introducing the core, the strain, and the mechanical losses in the dynamic model (subchapter 3.1). Then, in subchapter 3.2, a review of the common shape used for the design of the SynRel is presented and discussed. A further discussion about the fluid shape barriers is carried out in section 3.2.4. In section 3.2.5, there is a brief comparison between different rotor shapes and the reasons of the choice of the fluid one are presented.

3.1 SynRel Modeling

The voltage equations of three-phase synchronous machines are based on the voltage balance between the power supply, the resistive voltage drop and the induced back electromotive force, according to the following equations:

$$\begin{cases} v_a = R_s i_a + \frac{d\psi_a}{dt} \\ v_b = R_s i_b + \frac{d\psi_b}{dt} \\ v_c = R_s i_c + \frac{d\psi_c}{dt} \end{cases} \quad (3.1)$$

where v_a , v_b , and v_c are the phase voltages; i_a , i_b , and i_c are the phase currents; ψ_a , ψ_b , and ψ_c are the phase flux linkage; R_s is the phase resistance.

The equations can be written considering a stationary reference system (the stator one) (3.2) or a rotating reference system (the rotor one) (3.3). When a rotating reference system is used the motional term, proportional to the rotating speed of the system (3.3), has to be added.

$$\mathbf{v}^s = [R_s] \mathbf{i}^s + \frac{d\boldsymbol{\psi}^s}{dt} \quad (3.2)$$

$$\mathbf{v}^r = [R_s] \mathbf{i}^r + \frac{d\boldsymbol{\psi}^r}{dt} + [J] \omega_e \boldsymbol{\psi}^r \quad (3.3)$$

where the superscript s and r indicate the stator and rotor references, respectively; ω_e is the speed of the reference system and $[J]$ is the motional matrix, equal to the imaginary unit expressed in matrix form.

These equations can be rearranged considering an equivalent two-phase system: it can be the stationary (α - β), obtained using the Clarke's transformation, or it can be rotating at the synchronous speed (with the rotor reference d - q), obtained using the Park's transformation. With this last one, it is possible to obtain:

$$\mathbf{v}^r = R_s \mathbf{i}^r + \frac{d\boldsymbol{\psi}^r}{dt} + [J] \omega_e \boldsymbol{\psi}^r = R_s \mathbf{i}^r + \frac{d\boldsymbol{\psi}^r}{dt} + \begin{bmatrix} 0 & -1 \\ 1 & 0 \end{bmatrix} \omega_e \boldsymbol{\psi}^r \quad (3.4)$$

Using the axis equations:

$$\begin{cases} v_d = R_s i_d + \frac{d\psi_d}{dt} - \omega_e \psi_q \\ v_q = R_s i_q + \frac{d\psi_q}{dt} + \omega_e \psi_d \end{cases} \quad (3.5)$$

The $abc \rightarrow dq$ transformation used in this thesis is the one in which the amplitudes of the phase currents in the d - q reference system are the same of the ones in the abc reference system.

Pre-multiplying (3.4) by the transposed vector of the currents and by the constant $3/2$, it is possible to have the active input power and the power balance.

$$P_i = \frac{3}{2} \mathbf{i}^{rT} \mathbf{v}^r = \overbrace{\frac{3}{2} \mathbf{i}^{rT} [R_s] \mathbf{i}^r}^{P_j} + \overbrace{\frac{3}{2} \mathbf{i}^{rT} \frac{d\boldsymbol{\psi}^r}{dt}}^{P_{mag}} + \overbrace{\frac{3}{2} \omega_e \mathbf{i}^{rT} [\mathbf{J}] \boldsymbol{\psi}^r}^{P_m} \quad (3.6)$$

where the active input power is:

$$P_i = \frac{3}{2} \mathbf{i}^{rT} \mathbf{v}^r = \frac{3}{2} [i_d \quad i_q] \begin{bmatrix} v_d \\ v_q \end{bmatrix} = \frac{3}{2} (v_d i_d + v_q i_q) \quad (3.7)$$

The expression of the Joule losses is the following one:

$$P_j = \frac{3}{2} \mathbf{i}^{rT} [R_s] \mathbf{i}^r = \frac{3}{2} [i_d \quad i_q] \begin{bmatrix} i_d \\ i_q \end{bmatrix} = \frac{3}{2} R_s (i_d^2 + i_q^2) = \frac{3}{2} R_s i^2 \quad (3.8)$$

The magnetization energy variation per unit of time is:

$$P_{mag} = \frac{3}{2} \mathbf{i}^{rT} \frac{d\boldsymbol{\psi}^r}{dt} = \frac{3}{2} [i_d \quad i_q] \begin{bmatrix} \frac{d\psi_d}{dt} \\ \frac{d\psi_q}{dt} \end{bmatrix} = \frac{3}{2} \left(\frac{d\psi_d}{dt} i_d + \frac{d\psi_q}{dt} i_q \right) \quad (3.9)$$

The mechanical output power is equal to:

$$P_m = \frac{3}{2} \omega_e \mathbf{i}^{rT} [\mathbf{J}] \boldsymbol{\psi}^r = \frac{3}{2} \omega_e [i_d \quad i_q] \begin{bmatrix} 0 & -1 \\ 1 & 0 \end{bmatrix} \begin{bmatrix} \psi_d \\ \psi_q \end{bmatrix} = \frac{3}{2} \omega_e (\psi_d i_q - \psi_q i_d) \quad (3.10)$$

Dividing (3.10) by the mechanical speed, it is possible to obtain the expression of the electromagnetic torque of the motor:

$$T_e = \frac{P_m}{\omega_m} = p \frac{P_m}{\omega_e} = \frac{3}{2} (\psi_d i_q - \psi_q i_d) \quad (3.11)$$

where p is the number of pole pairs.

Pre-multiplying (3.4) by the transposed vector of the currents, by the transpose of the motional matrix, and by the constant $3/2$, it is possible to have the reactive input power:

$$Q_i = \frac{3}{2} \mathbf{i}^{rT} [\mathbf{J}]^T \mathbf{v}^r = \overbrace{\frac{3}{2} \mathbf{i}^{rT} [\mathbf{J}]^T [R_s] \mathbf{i}^r}^0} + \overbrace{\frac{3}{2} \omega_e \mathbf{i}^{rT} [\mathbf{J}]^T [\mathbf{J}] \boldsymbol{\psi}^r}^{Q_{mag}} + \overbrace{\frac{3}{2} \mathbf{i}^{rT} [\mathbf{J}]^T \frac{d\boldsymbol{\psi}^r}{dt}}^{\frac{1}{p} \frac{dT}{dt} |_{i_d, i_q = const}} \quad (3.12)$$

where the reactive input power is:

$$Q_i = \frac{3}{2} \mathbf{i}^{rT} [\mathbf{J}]^T \mathbf{v}^r = \frac{3}{2} [i_d \quad i_q] \begin{bmatrix} 0 & 1 \\ -1 & 0 \end{bmatrix} \begin{bmatrix} v_d \\ v_q \end{bmatrix} = \frac{3}{2} (v_q i_d - v_d i_q) \quad (3.13)$$

From the balance of the reactive power, two terms can be defined; the first one is the reactive power needed to maintain the axis fluxes at the electrical speed:

$$\begin{aligned} Q_{mag} &= \frac{3}{2} \omega_e \mathbf{i}^{rT} [\mathbf{J}]^T [\mathbf{J}] \boldsymbol{\psi}^r = \frac{3}{2} \omega_e [i_d \quad i_q] \begin{bmatrix} 0 & 1 \\ -1 & 0 \end{bmatrix} \begin{bmatrix} 0 & -1 \\ 1 & 0 \end{bmatrix} \begin{bmatrix} \psi_d \\ \psi_q \end{bmatrix} \\ &= \frac{3}{2} \omega_e (\psi_d i_d + \psi_q i_q) \end{aligned} \quad (3.14)$$

The second term can be associated to the derivative of the torque per pole when the axis currents have constant values.

$$\left. \frac{1}{p} \frac{dT_e}{dt} \right|_{i_d, i_q = \text{const}} = \frac{3}{2} \left(\frac{d\psi_d}{dt} i_q - \frac{d\psi_q}{dt} i_d \right) = \frac{3}{2} \mathbf{i}^{rT} [\mathbf{J}]^T \frac{d\boldsymbol{\psi}^r}{dt} \quad (3.15)$$

The terms of this last equation can be associated to the torque ripple because: the variation of the axis flux, considering a constant value of the axis current, is due to the harmonics inside the machine that produce the oscillation of the torque; the torque ripple is associated to the reactive power because it has a zero average value, hence causing only oscillations.

In order to complete the dynamic equations that describe the machine, it is necessary to add the mechanical equation for the computation of the speed:

$$\frac{d\omega_m}{dt} = \frac{1}{p} \frac{d\omega_e}{dt} = \frac{1}{J_m} (T_e - T_l) \Rightarrow \frac{d\omega_e}{dt} = \frac{p}{J_m} \left(\frac{3}{2} (\psi_d i_q - \psi_q i_d) - T_l \right) \quad (3.16)$$

where ω_m is the mechanical speed, J_m is the inertia of the system and T_l is the load torque.

Rearranging (3.5) and adding (3.16) to it, it is possible to write the complete dynamic system equations of the machine:

$$\begin{cases} \frac{d\psi_d}{dt} = v_d - R_s i_d + \omega_e \psi_q \\ \frac{d\psi_q}{dt} = v_q - R_s i_q - \omega_e \psi_d \\ \frac{d\omega_e}{dt} = \frac{p}{J_m} \left(\frac{3}{2} (\psi_d i_q - \psi_q i_d) - T_l \right) \end{cases} \quad (3.17)$$

The inputs of this system are the axis voltages and the load torque. The number of state variables is five with only three equations. In order to solve the system, it is necessary to introduce the magnetic model, which links the fluxes to the currents:

$$\begin{cases} \psi_d(i_d, i_q) = f_d(i_d, i_q) \\ \psi_q(i_d, i_q) = f_q(i_d, i_q) \end{cases} \quad (3.18)$$

where f_d and f_q are two non-linear functions that describe the behavior of the axis fluxes respect to the axis currents. Introducing the apparent axis inductances L_d and L_q and the cross-saturation terms L_{dq} and L_{qd} , it is possible to rearrange the general magnetic model in order to obtain the model of the SynRel:

$$\begin{cases} \psi_d(i_d, i_q) = f_d(i_d, i_q) = L_d(i_d)i_d + L_{dq}(i_d, i_q)i_q \\ \psi_q(i_d, i_q) = f_q(i_d, i_q) = L_{qd}(i_d, i_q)i_d + L_q(i_q)i_q \end{cases} \quad (3.19)$$

Using (3.19) in (3.17), it is possible to obtain:

$$\begin{cases} v_d = R_s i_d + \left(L_d + \frac{dL_d}{di_d} i_d + \frac{\partial L_{dq}}{\partial i_d} i_q \right) \frac{di_d}{dt} + \\ \quad + \left(L_{dq} + \frac{\partial L_{dq}}{\partial i_q} i_q \right) \frac{di_q}{dt} - \omega_e (L_{qd} i_d + L_q i_q) \\ v_q = R_s i_q + \left(L_q + \frac{dL_q}{di_q} i_q + \frac{\partial L_{qd}}{\partial i_q} i_q \right) \frac{di_q}{dt} + \\ \quad + \left(L_{qd} + \frac{\partial L_{dq}}{\partial i_d} i_d \right) \frac{di_d}{dt} + \omega_e (L_d i_d + L_{dq} i_q) \\ \frac{d\omega_e}{dt} = \frac{p}{J_m} \left(\frac{3}{2} \left((L_d - L_q) i_d i_q + L_{dq} i_q^2 - L_{qd} i_d^2 \right) - T_l \right) \end{cases} \quad (3.20)$$

This last dynamic model considers both the saturation and the cross-coupling effects, but the only losses that are taken into account are the Joule losses. In order to have a complete model, also the other losses (e.g. core losses, stray losses caused by the presence of leakage fields, and mechanical losses) should be considered.

3.1.1 Integration of core, stray and mechanical losses

In literature, different models have been proposed to include core, stray and mechanical losses; most of them take into account these losses with an equivalent resistance in parallel to the main inductances while a few models consider these losses as a reduction of the motor produced torque.

This thesis proposes a model in which the core and the stray losses are included as additional voltages, while the mechanical losses are considered as an additional load torque.

These losses are present in both the static and the dynamic models: for the computation of the additional voltage terms, it is useful to start from the static model in which all the derivative terms are equal to 0. From the expressions (3.6), (3.12), and (3.20), the following equations can be written:

$$\left\{ \begin{array}{l} v_d = R_s i_d + -\omega_e (L_{qd} i_d + L_q i_q) \\ v_q = R_s i_q + +\omega_e (L_d i_d + L_{dq} i_q) \\ \frac{d\omega_e}{dt} = \frac{p}{J_m} \left(\frac{3}{2} \left((L_d - L_q) i_d i_q + L_{dq} i_q^2 - L_{qd} i_d^2 \right) - T_l \right) \\ P_i = \frac{3}{2} (v_d i_d + v_q i_q) = P_j + P_m \\ Q_i = \frac{3}{2} (v_q i_d - v_d i_q) = Q_{mag} \end{array} \right. \quad (3.21)$$

Adding to (3.21) the additional voltage terms (v_d^* , v_q^*), the additional load torque (T_l^*) and the additional powers for the core, the stray, and the mechanical losses (P_{core} , P_{stray} , $P_{l,m}$), it is possible to obtain the following system:

$$\left\{ \begin{array}{l} v_d = R_s i_d + -\omega_e (L_{qd} i_d + L_q i_q) + v_d^* \\ v_q = R_s i_q + +\omega_e (L_d i_d + L_{dq} i_q) + v_q^* \\ \frac{d\omega_e}{dt} = \frac{p}{J_m} \left(\frac{3}{2} \left((L_d - L_q) i_d i_q + L_{dq} i_q^2 - L_{qd} i_d^2 \right) - (T_l + T_l^*) \right) \\ P_i = \frac{3}{2} (v_d i_d + v_q i_q) = P_j + P_m + P_{core} + P_{stray} + P_{l,m} \\ Q_i = \frac{3}{2} (v_q i_d - v_d i_q) = Q_{mag} \end{array} \right. \quad (3.22)$$

This model has been obtained considering that the losses do not introduce an additional reactive power term.

Using the expressions (3.8), (3.10) and (3.14) in the obtained system (3.22):

$$\left\{ \begin{array}{l} T_l^* = p \frac{P_{l,m}}{\omega_e} \\ P_{core} + P_{stray} = \frac{3}{2} (v_d^* i_d + v_q^* i_q) \\ 0 = \frac{3}{2} (v_q^* i_d - v_d^* i_q) \end{array} \right. \quad (3.23)$$

From the last two equations in (3.23), it is possible to calculate the expressions of the two additional terms of the core and stray losses:

$$\left\{ \begin{array}{l} v_d^* = \frac{2}{3} (P_{core} + P_{stray}) \frac{i_d}{i_d^2 + i_q^2} \\ v_q^* = \frac{2}{3} (P_{core} + P_{stray}) \frac{i_q}{i_d^2 + i_q^2} \end{array} \right. \quad (3.24)$$

All terms of the system (3.22) are defined and, therefore, the static model is:

$$\begin{cases} v_d = R_s i_d + -\omega_e (L_{qd} i_d + L_q i_q) + \frac{2}{3} (P_{core} + P_{stray}) \frac{i_d}{i_d^2 + i_q^2} \\ v_q = R_s i_q + +\omega_e (L_d i_d + L_{dq} i_q) + \frac{2}{3} (P_{core} + P_{stray}) \frac{i_q}{i_d^2 + i_q^2} \\ \frac{d\omega_e}{dt} = \frac{p}{J_m} \left(\frac{3}{2} ((L_d - L_q) i_d i_q + L_{dq} i_q^2 - L_{qd} i_d^2) - (T_l + p \frac{P_{lm}}{\omega_e}) \right) \end{cases} \quad (3.25)$$

while the dynamic model is the following one:

$$\begin{cases} v_d = \left(R_s + \frac{2(P_{core} + P_{stray})}{3(i_d^2 + i_q^2)} \right) i_d + \left(L_d + \frac{dL_d}{di_d} i_d + \frac{\partial L_{dq}}{\partial i_d} i_q \right) \frac{di_d}{dt} + \\ + \left(L_{dq} + \frac{\partial L_{dq}}{\partial i_q} i_q \right) \frac{di_q}{dt} - \omega_e (L_{qd} i_d + L_q i_q) \\ v_q = \left(R_s + \frac{2(P_{core} + P_{stray})}{3(i_d^2 + i_q^2)} \right) i_q + \left(L_q + \frac{dL_q}{di_q} i_q + \frac{\partial L_{qd}}{\partial i_q} i_d \right) \frac{di_q}{dt} + \\ + \left(L_{qd} + \frac{\partial L_{dq}}{\partial i_d} i_d \right) \frac{di_d}{dt} + \omega_e (L_d i_d + L_{dq} i_q) \\ \frac{d\omega_e}{dt} = \frac{p}{J_m} \left(\frac{3}{2} ((L_d - L_q) i_d i_q + L_{dq} i_q^2 - L_{qd} i_d^2) - (T_l + p \frac{P_{lm}}{\omega_e}) \right) \end{cases} \quad (3.26)$$

In the model above, the core and the stray losses can be seen as an additional phase resistance whose value depends on the loss value and on the current amplitude. If the losses were considered as a parallel resistance (thus introducing an additional current), when the speed and, as a consequence, the losses increase, the value of the current control angle should be changed; however, the values of the currents do not change together with the speed (until the base speed is reached), thereby justifying the use of the model (3.26).

3.1.2 An example of an industrial SynRel

Using as an example the parameters of an industrial SynRel [1]-[3] (Table 3.1), it is possible to compute the behavior of the d - q fluxes respect to the d - q currents and to the constant torque loci, as presented in Figure 3.1, Figure 3.2 and Figure 3.3.

Table 3.1: The commercial SynRel parameters.

Parameter	Unit	Value	Parameter	Unit	Value
Base Voltage (V_B)	V	280	Base Flux Linkage	Wb	0.977
Base Current (I_B)	A	10.34	Number of pole pairs (p)		2
Rated d -current	A	5.74	Phase resistance (R_s)	s	2.5
Rated q -current	A	8.85	Direct inductance (L_d)	mH	186
Base Electrical Speed	rad/s	314	Quadrature inductance (L_q)	mH	34.1
Rated Torque	Nm	20	Salency ratio		5.45

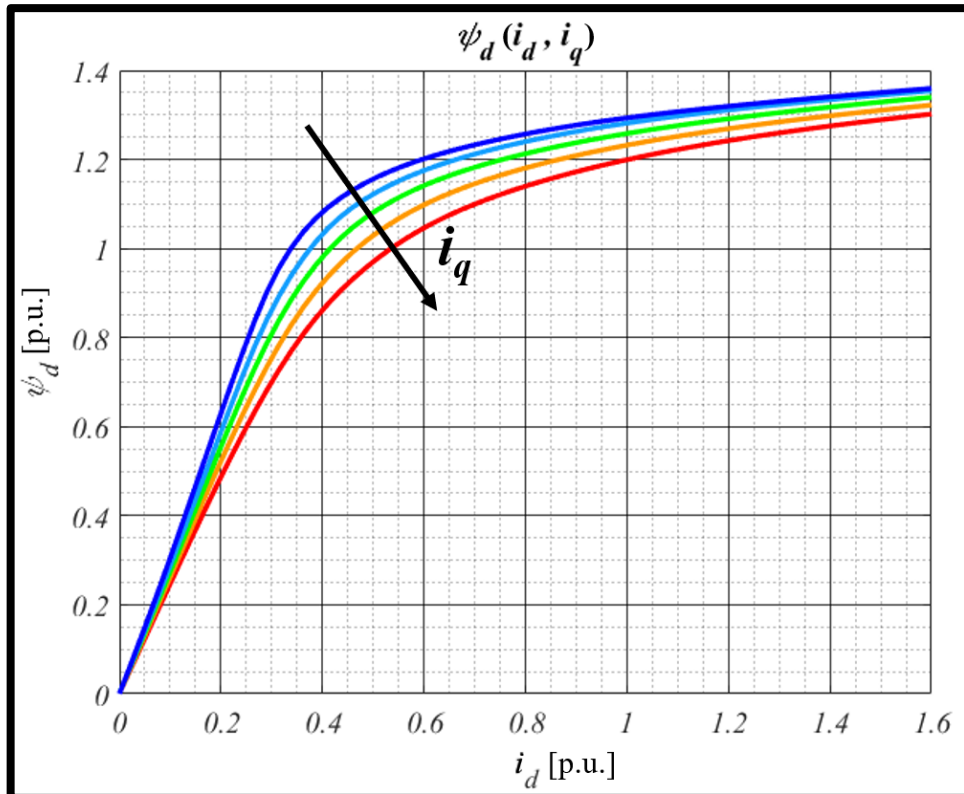


Figure 3.1: Direct-axis flux vs d-q currents in p.u.

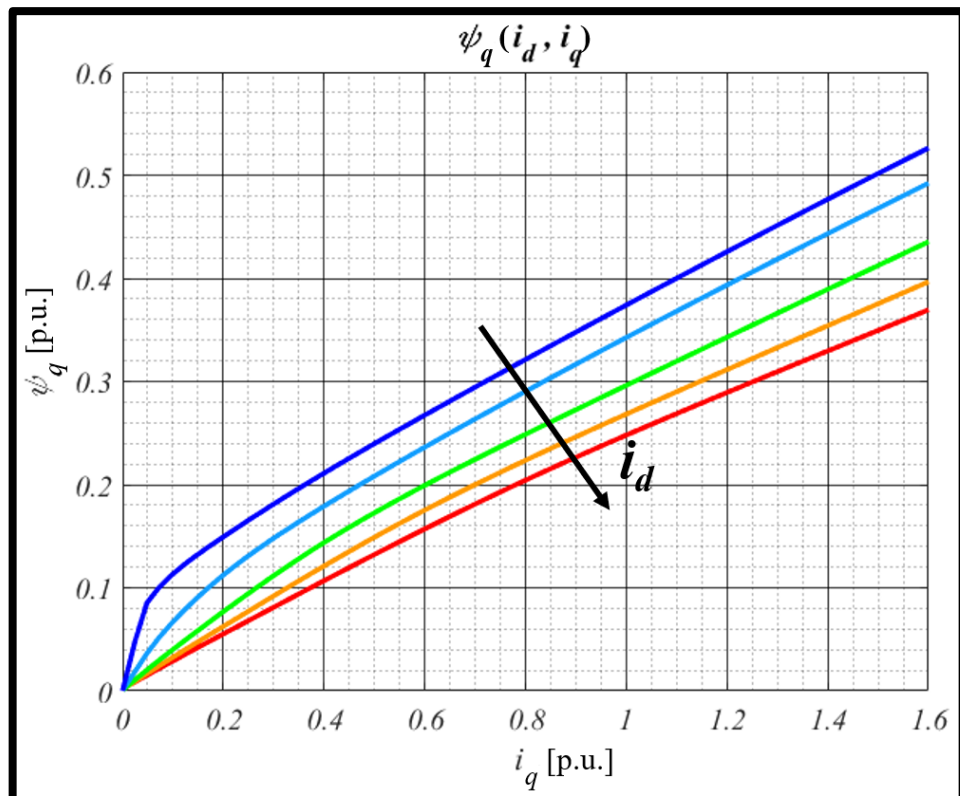


Figure 3.2: Quadrature-axis flux vs d-q currents in p.u.

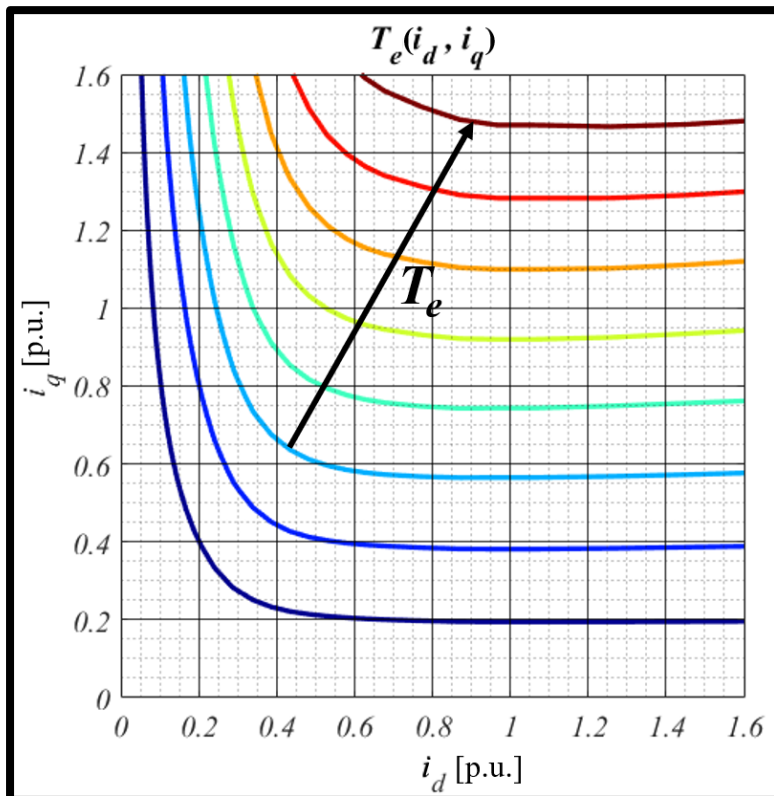


Figure 3.3: Constant Torque loci vs d - q currents.

These figures point out both the cross-coupling and the saturation effects. In Figure 3.1, after that the d -current reaches its rated value, the slope of the d -flux is reduced as well as the d -inductance. The cross-coupling effect is higher when the machine reaches higher values of saturation.

In Figure 3.2, the slope of the q -flux is high only when the q -current and the d -current have low values. This is justified by the saturation of the tangential ribs: in fact, before they saturate, the q -flux path has a lower reluctance. After the saturation of the tangential ribs, the flux-current behavior is linear and the q -inductance is constant.

In Figure 3.3, the effects of the saturation are visible for high values of the d -current: in fact, even though the d -current increases (with a constant value of the q -current), the torque value stays the same.

3.2 The SynRel Rotor Geometry

The performance of the SynRel can be maximized with the improvement of the saliency ratio of the machine; the rotor shape could facilitate the path of the d -flux while obstructing the one of the q -axis. In the following section, different rotor configurations are presented and analyzed.

3.2.1 Axially-laminated rotor

The most promising solution for the maximization of the saliency ratio of the SynRel consists in the adoption of the axially-laminated rotor that guarantees a very high value of the saliency ratio (greater than 10).

When the electrical steel is axially laminated, there are no ribs that connect the q -flux path, thus maximizing the q -reluctance (and minimizing the q -inductance) and increasing the saliency ratio. In this way, the electrical steel can be Grain Oriented (GO) because the flux inside the machine takes only one direction; the GO electrical steel has a higher magnetic permeability and lower losses than the Non-Grain Oriented (NGO) one, thus increasing the performance of the machine.

From a manufacturing point of view, this solution is much more complex for two main reasons: the first one is due to the different dimensions of the electrical steel that composes the machine; the second one is due to the use of a strong adhesive between the electrical steel laminations since they have to guarantee the machine integrity at high speeds. The centrifugal forces, for this type of machine, tend to detach the electrical steel laminations, which are kept together only by the adhesive or by the bolts. A schematic design of a 4-pole axially laminated rotor is shown in Figure 3.4.

This type of machine is susceptible to the harmonics of the flux, which generate a variable flux in the rotor, hence producing eddy currents in the electrical steel. These currents, and the resulting losses, are higher than the ones generated in the transversally-laminated rotor because the currents can flow through the electrical steel laminations in the axial direction.

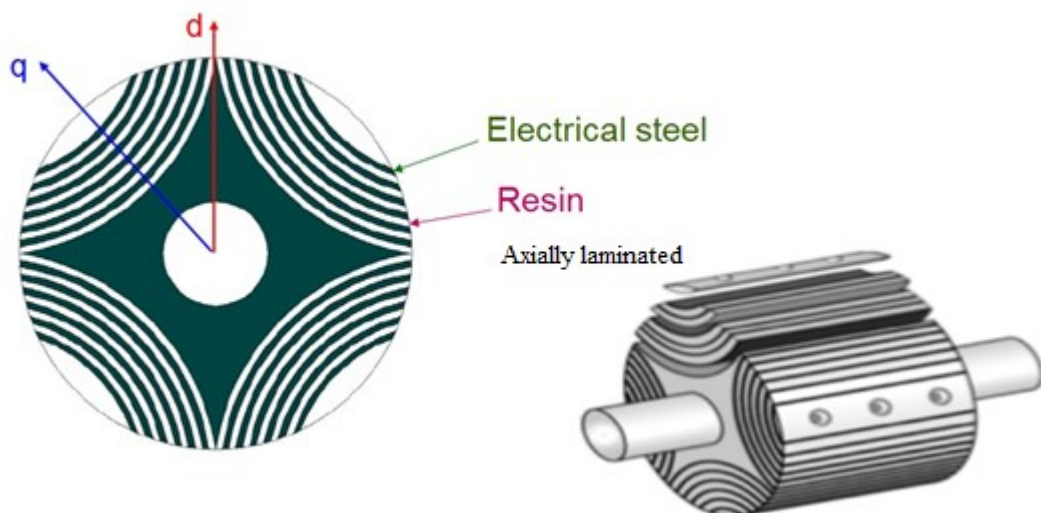


Figure 3.4: 4-pole axially-laminated rotor [23].

3.2.2 U-Shaped Barriers

The other typology of the SynRel rotor is the transversally-laminated one, which is the most used solution for the manufacturing of SynRel rotors. The electrical steel laminations are punched with the desired shape and then assembled in the axial direction. There are different types of shapes for the SynRel rotor: the most used one is with U-shaped barriers; an example of this rotor shape is shown in Figure 3.5.

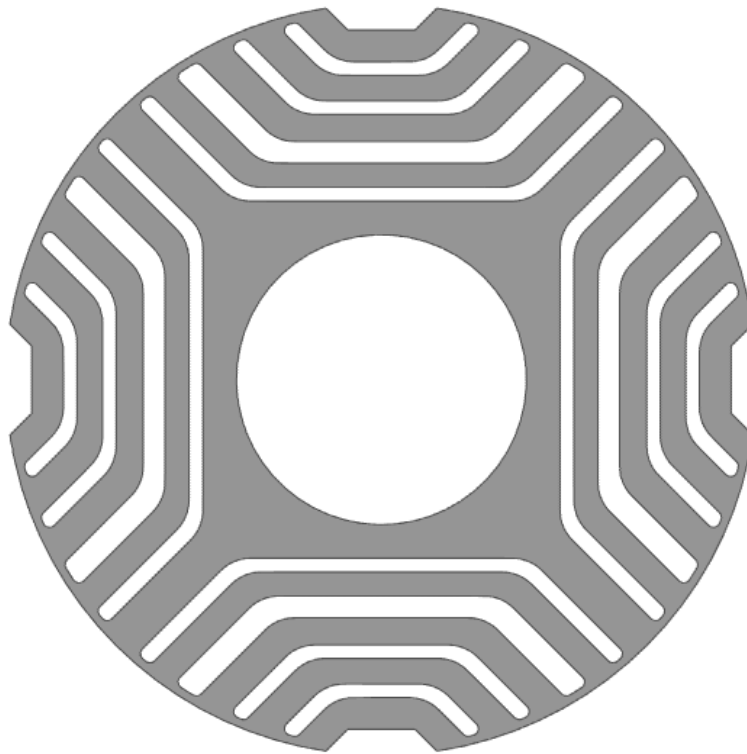


Figure 3.5: 4-pole transversally-laminated rotor (U-shaped).

The minimum number of variables that are needed to define this shape is of two for each barrier and of one for the notch, which is the last part of the rotor. The key design parameters are the width of the barriers and the angle between the last part of the barriers and the q -axis. It is possible to use more variables for each barrier in order to have more flexibility in the design and to improve the performance of the machine.

Using only two variables per barrier, the shape of the barriers is fixed as well as the performance of the motor. The magnetic flux in the U-shaped rotor could drastically change its direction near the bending of the barrier; this is a variation of the magnetic vector potential that can be seen as an addition to the path reluctance or as a seat of additional losses. This hypothesis derives from the analogy between the magnetic flux and the fluid, which will be discussed in the next section. This effect can increase the reluctance of the d -axis flux, thus reducing the d -inductance and the saliency ratio.

3.2.3 Circular Barriers

Another possible shape for the rotor barriers is the circular one. Also in this case, the number of variables to define the shape is of two for each barrier and of one for the notch. The variables are the position of the flux barriers from the origin of the circles and their width.

It is possible to use another variable for each barrier, which is the position of the center of the circumference that generates the barrier, to improve the performance of the machine. According to [30], a good choice for the center of the circles that generate the flux barriers is represented by the crossing point between the two lines that are tangent to the outer rotor circumference. A possible shape for this rotor geometry is shown in Figure 3.6.

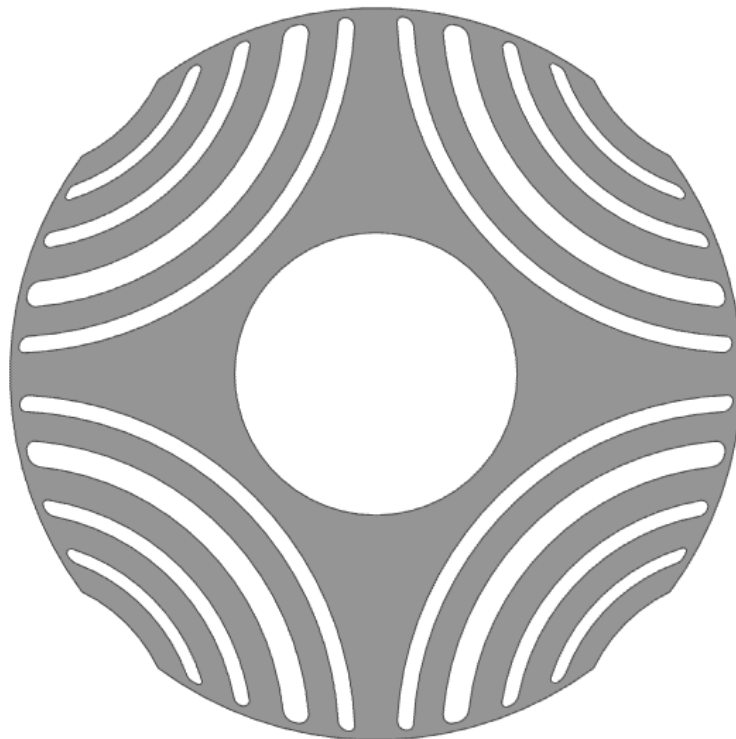


Figure 3.6: 4-pole transversally-laminated rotor (Circular Shape).

The circular barrier shape is a reasonable choice if the number of poles is four; instead, when the number of poles increases, the path of the flux tends to move towards the outer part of the rotor laminations. In order to better approximate the flux path to the one created by the barriers, different circle centers have to be considered. Respect to the U-shaped barriers, the flux path is regular within the steel laminations, but not near the shaft: the steel between the two inner barriers has a lower width in correspondence of the d -axis if compared to the one in correspondence of the q -axis and of the other parts of the rotor. Therefore, these

thin parts can easily saturate and, as a consequence, reduce the d -inductance (the width between the inner barriers of different poles could be reduced in order to increase the reluctance of the q -axis).

3.2.4 Fluid shaped barriers

The idea of the fluid shaped barrier comes from the analogy between the magnetism and the mechanical field. The magnetic flux within the rotor of the SynRel can be associated to the flow around the cylinder with radius ϱ_0 . The equation of these equipotential lines can be computed according to a specific model, which is described below [31]. Figure 3.7 shows the flow that passes around a cylinder under the condition that, far from the cylinder, the flow is unidirectional and uniform.

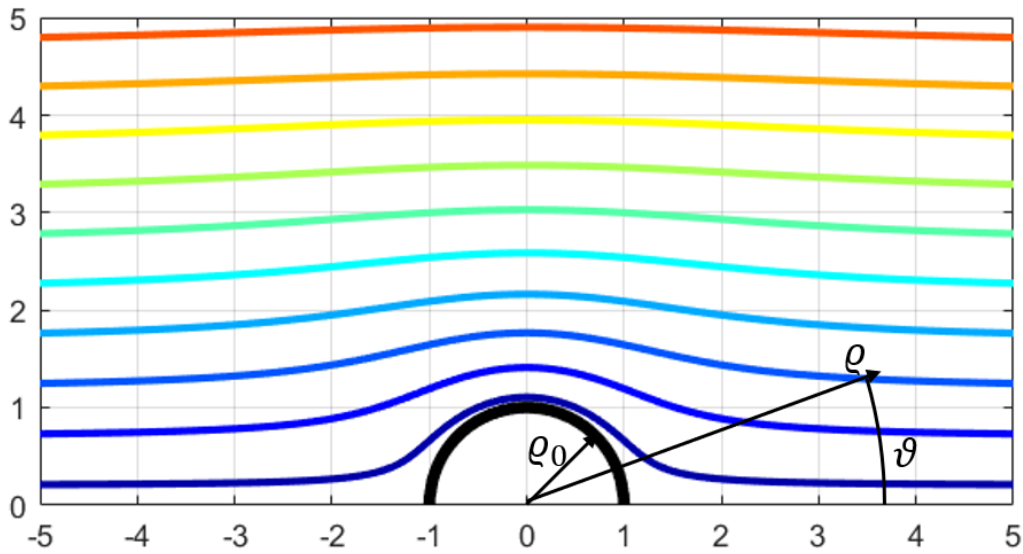


Figure 3.7: Flow around a cylinder.

The boundary condition of this system, considering an incompressible and inviscid fluid in correspondence of the cylinder border, is the following one:

$$\mathbf{v} \cdot \hat{\mathbf{n}} = 0 \quad (3.27)$$

where \mathbf{v} is the vector of the speed and $\hat{\mathbf{n}}$ is the vector normal to the cylinder's surface.

This condition means that the flow is tangential to the surface of the cylinder and that it cannot cross the cylinder itself. Considering that the flow has a constant mass density, it is inviscid, incompressible and irrotational, it is possible to write:

$$\nabla \cdot \mathbf{v} = 0 \quad (3.28)$$

$$\nabla \times \mathbf{v} = 0 \quad (3.29)$$

If the flow is irrotational, there must exist a velocity potential ϕ defined as:

$$\mathbf{v} = \nabla\phi \quad (3.30)$$

Using the expressions (3.29) and (3.30), it is possible to write:

$$\nabla^2\phi = 0 \quad (3.31)$$

The Laplace equation seen above can be written in polar coordinates:

$$\frac{1}{\varrho} \frac{\partial}{\partial \varrho} \left(\varrho \frac{\partial \phi}{\partial \varrho} \right) + \frac{1}{\varrho^2} \frac{\partial^2 \phi}{\partial \vartheta^2} = 0 \quad (3.32)$$

The solution of this second order partial differential equation, considering the boundary condition of the expression (3.27), is shown below:

$$\phi(\varrho, \vartheta) = v_0 \rho \left(1 + \frac{\varrho_0^2}{\varrho^2} \right) \quad (3.33)$$

It is now possible to define the stream function (ψ) for an incompressible flow through the curve between the points A and B :

$$\psi = \int_A^B (v_x dy - v_y dx) \quad (3.34)$$

In differential terms, the expression becomes:

$$\delta\psi = v_x dy - v_y dx \quad (3.35)$$

Considering that the flow is incompressible, it is possible to write:

$$\frac{\partial v_x}{\partial x} + \frac{\partial v_y}{\partial y} = 0 \quad (3.36)$$

$$\delta\psi = \frac{\partial \psi}{\partial x} dx + \frac{\partial \psi}{\partial y} dy \quad (3.37)$$

Therefore, the flow velocity components in relation to the stream function have to be the following ones:

$$\begin{cases} v_x = \frac{\partial \psi}{\partial y} \\ v_y = -\frac{\partial \psi}{\partial x} \end{cases} \quad (3.38)$$

The result of the system in terms of streamline function is:

$$\psi = v_0 \left(\varrho - \frac{R^2}{\varrho} \right) \sin \vartheta \quad (3.39)$$

Under the hypothesis that the speed is related to the induction field (B), the streamline can be related to the magnetic vector potential, which is defined according to the following equation:

$$\mathbf{B} = \nabla \times \mathbf{A} \quad (3.40)$$

Considering a 2-D problem, the relation between the induction field and the magnetic vector potential is:

$$\begin{cases} B_x = \frac{\partial A_z}{\partial y} \\ B_y = -\frac{\partial A_z}{\partial x} \end{cases} \quad (3.41)$$

The expression form of the system (3.41) is the same one of the system (3.38) but considering the induction field and the magnetic vector potential. Therefore, considering a magnetic field that flows horizontally through a surface with the condition of the tangential field or using the boundary condition of the magnetic vector potential equal to zero, the behavior of the equipotential magnetic lines is the same one described by the result obtained with the mechanical model in (3.39):

$$A = B_0 \left(\varrho - \frac{R^2}{\varrho} \right) \sin \vartheta \quad (3.42)$$

From this equation, it is possible to define the expression of the shape of the equipotential lines:

$$\varrho = R \frac{\frac{A}{B_0 R} + \sqrt{\left(\frac{A}{B_0 R} \right)^2 + 4 \sin^2 \vartheta}}{2 \sin \vartheta} = R \frac{C_k + \sqrt{C_k^2 + 4 \sin^2 \vartheta}}{2 \sin \vartheta} \quad (3.43)$$

where C_k is the coefficient of the k -th line.

The expression (3.43) would give a good estimation of the flux path if the induction field could be represented as a horizontal field: this could be true if the distribution of the conductors in the stator were sinusoidal and if the permeability of the electrical steel were much higher than the one of the shaft. These conditions are typically satisfied in the SynRel machine, thereby it is possible to draw the barriers according to the expression (3.43).

The (3.43) is defined for a 2-pole machine because the induction field is only horizontal. In order to define the expression for a generic $2p$ -pole machine, it is necessary to use the conformal mapping [32].

The variation in the number of pole pairs can be seen as a reduction of the available plane in terms of angles. In a 2-pole machine, the induction field can be seen as horizontal and the angle varies from 0 to π ; in a 4-pole machine, the north

and the south poles have a distance of $\pi/2$ between each other and the angle of the field varies from 0 to $\pi/2$; in a generic $2p$ -pole machine, the north and the south poles have a distance of π/p between each other. The reduction of the angle can be seen as a fractional power and a root of a complex number:

$$\frac{1}{z^p} = (\rho e^{i\vartheta})^{\frac{1}{p}} = \rho^{\frac{1}{p}} \left(\cos \frac{\vartheta}{p} + i \sin \frac{\vartheta}{p} \right) \quad (3.44)$$

Applying the conformal map to the expression of the equipotential lines in (3.43):

$$\varrho = R \sqrt[p]{\frac{C_k + \sqrt{C_k^2 + 4 \sin^2(p\vartheta)}}{2 \sin(p\vartheta)}} \quad (3.45)$$

This is the generic expression, for a $2p$ -pole machine, of the equipotential lines considering a perfect distribution of the input induction field, according to the d -axis, and a permeability of the steel much higher than the one of the shaft.

Figure 3.7 also presents the flux lines of a 2-pole machine while Figure 3.8 shows in sequence the flux lines of 4-pole, 6-pole, 8-pole, and 10-pole machines.

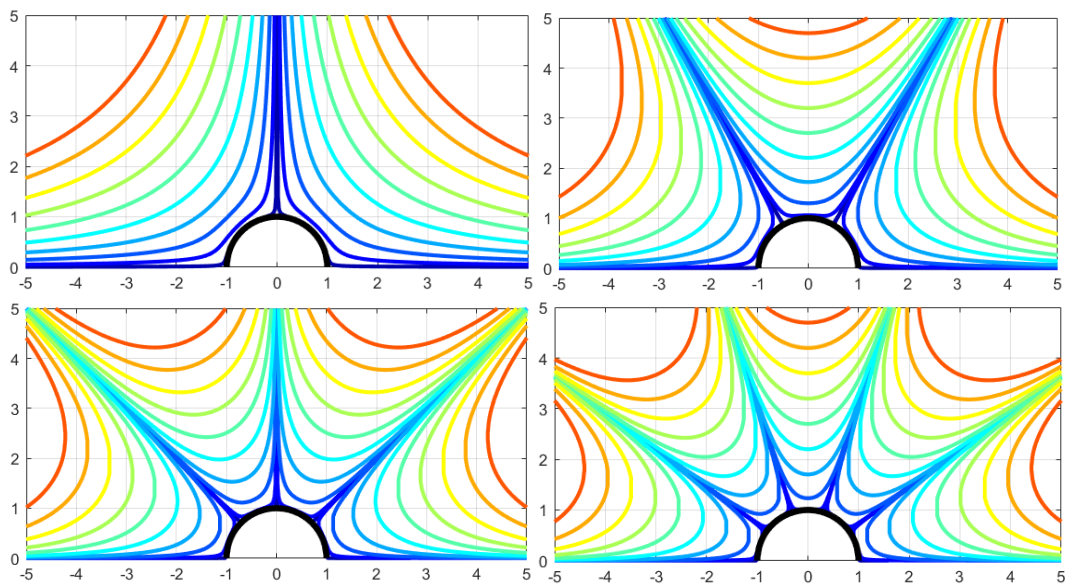


Figure 3.8: Flux lines of 4-pole, 6-pole, 8-pole and 10-pole machines.

With the increase in the number of poles, the curves are more closed, in particular near the shaft. It is useful to increase the number of poles if the value of the shaft diameter becomes close to the one of the outer diameter. If the shaft radius is small compared to the rotor outer one, it is better to use a low number of poles in order to better exploit the available machine volume.

The next step consists in the drawing of this particular shape and, according to Figure 3.9, in defining the variables of the fluid shaped barriers.

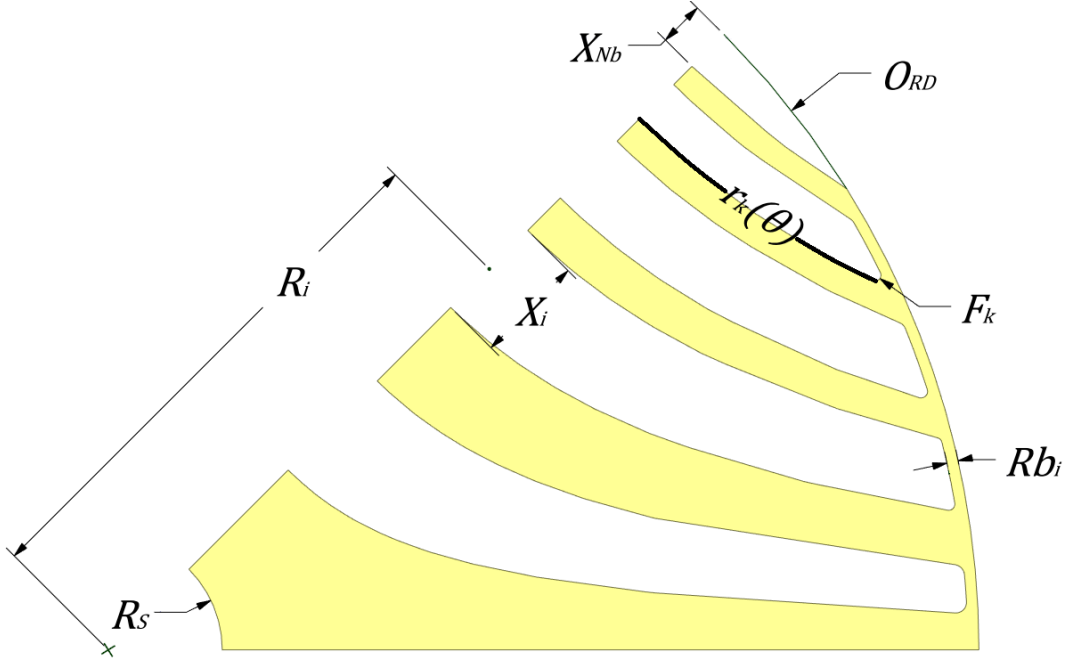


Figure 3.9: Variables of a fluid shaped rotor.

For each flux barrier, it is necessary to define 2 variables: the position of the barrier (R_i) and its width (X_i) in correspondence of the q -axis. The only variable that is necessary to define for the notch is its width. The expression of the k -th curve line of the barrier, where k is equal to $2i-1$ for the lower curve line in the i -th barrier and to $2i$ for the upper curve line in the i -th barrier, is equal to:

$$r_k = R_s \sqrt[p]{\frac{C_k + \sqrt{C_k^2 + 4 \sin^2(p\vartheta)}}{2 \sin(p\vartheta)}} \quad (3.46)$$

where R_s is the shaft radius and the constant C_k can be expressed in function of the width and position of the i -th barrier.

$$C_{(2i-1)}(X_i, R_i) = \frac{\left(\frac{R_i - X_i}{R_s}\right)^{2p} - 1}{\left(\frac{R_i - X_i}{R_s}\right)^p} \quad (3.47)$$

$$C_{(2i)}(X_i, R_i) = \frac{\left(\frac{R_i + X_i}{R_s}\right)^{2p} - 1}{\left(\frac{R_i + X_i}{R_s}\right)^p} \quad (3.48)$$

The fluid shaped rotor is the most promising solution that aims to maximize the saliency ratio of the SynRel because the flux barriers have the same shape of the equipotential magnetic lines. Under ideal conditions, the magnetic flux does not

change its direction within the rotor, thus minimizing the d -reluctance. This solution does not require additional variables because it is optimized with the flux path.

3.2.5 Comparisons between the different shapes

In this section, an example of a schematic 4-pole solution with either circular barriers or fluid shaped ones is presented in order to verify if the circular barriers represent a good approximation of the flux path. This evaluation has also been made for a 6-pole solution for a better comprehension of the shape differences.

Figure 3.10 shows the comparison between the circular and the fluid shapes in a 4-pole machine. The circular barrier approximation is good at halfway between the shaft and the rotor outer diameter but, in correspondence of the two extremities, the flux behavior has a different shape respect to the barrier one. When the radius of the shaft is bigger than the one in the figure, the circular barrier shape can be a good solution for the design of the SynRel.

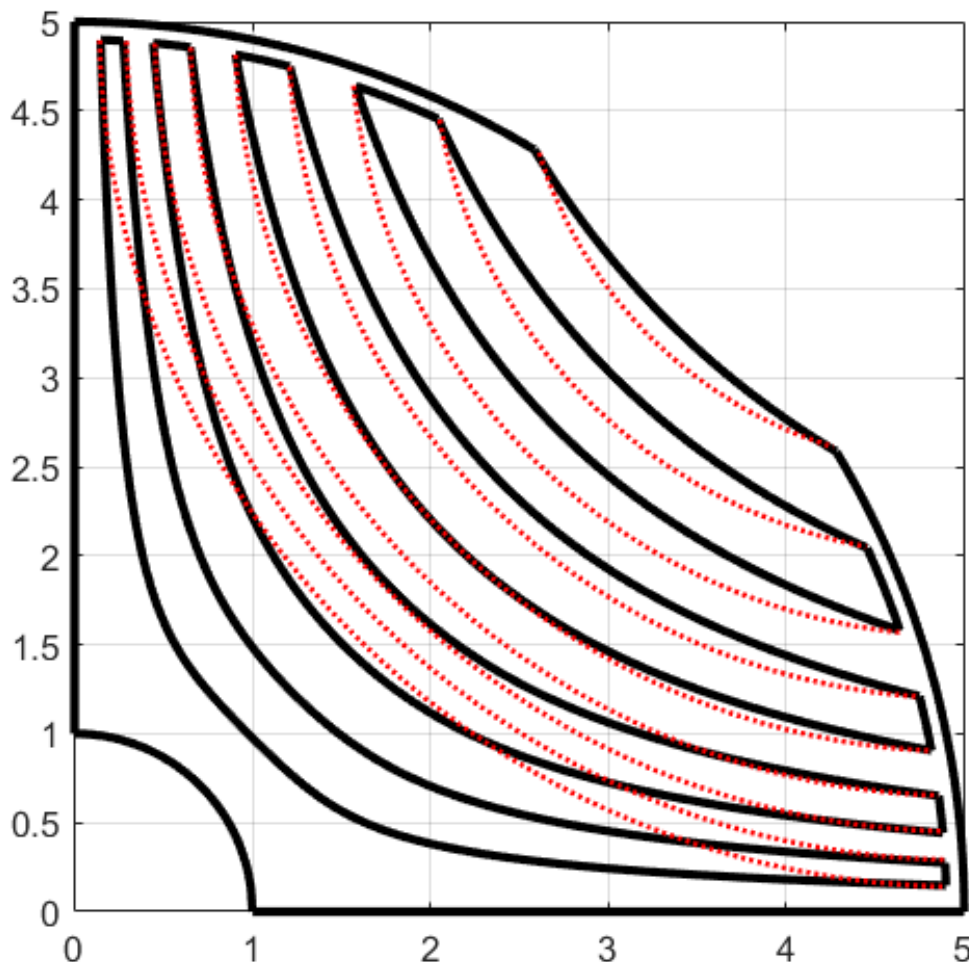


Figure 3.10: Comparison between the circular (red dotted line) and the fluid (black line) shapes in a 4-pole machine.

Figure 3.11 shows the comparison between the circular and the fluid shapes in a 6-pole machine. In this case, the circular barrier approximation is not as good as in the 4-pole machine, both at the extremities of the machine and in the middle.

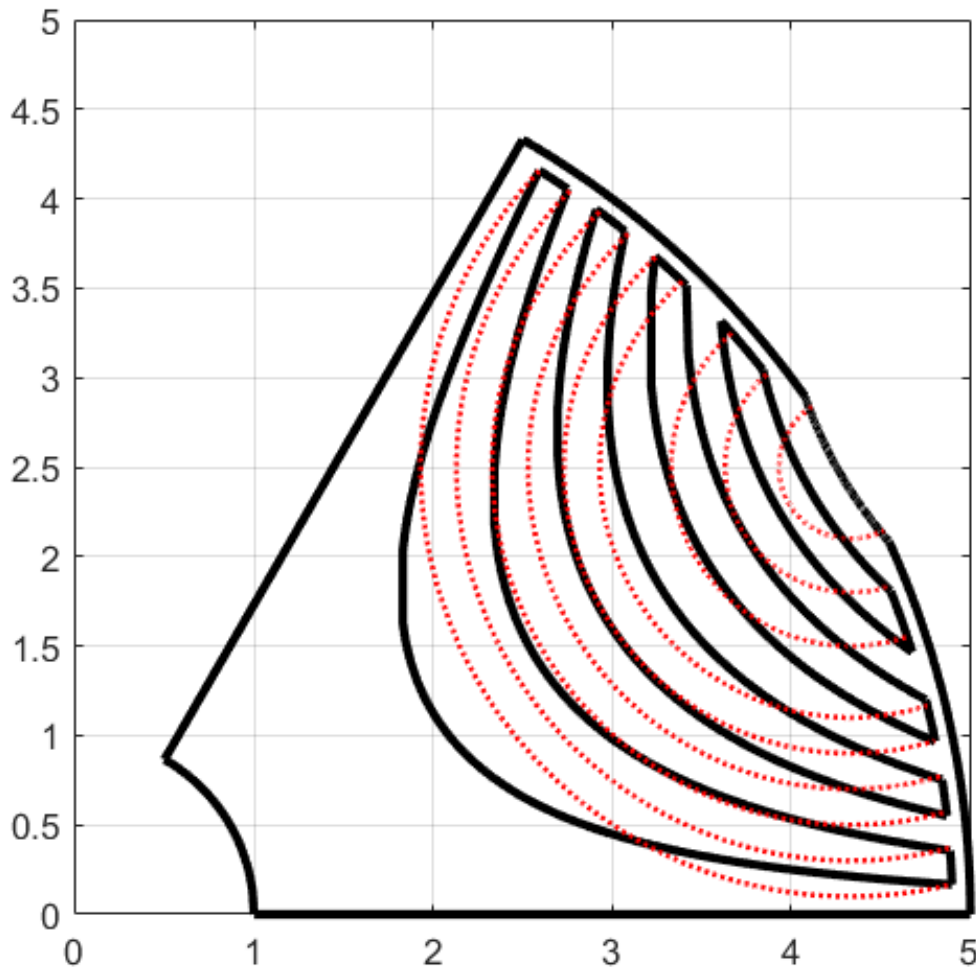


Figure 3.11: Comparison between the circular (red dotted line) and the fluid (black line) shapes in a 6-pole machine.

Increasing the number of poles, the circular shaped barriers get away from the fluid shaped ones and, for this type of machine, if the fluid shaped barriers cannot be used, it is better to use the U-shaped ones rather than the circular shaped ones. Varying the center of the circles of the different barriers, it is possible to better approximate the fluid shape.

Chapter 4

SynRel Motor Design Optimization

Part of the work presented in this chapter has been previously published in [4],[11]

The design of electrical machines requires the use of advanced methods for the computation of their performance. In order to achieve high performance, the use of optimization procedures is mandatory; however, these procedures require a lot of iterations to reach the convergence and, hence, the best solution.

In order to reduce the computational burden, it is possible to use analytical models augmented by Finite Element analyses either to reduce the time for each iteration or to use appropriate optimization algorithms to reduce the number of iterations.

In this chapter, the machine preliminary design of the SynRel is discussed in subchapter 4.1: starting from the typical procedure for IMs for the design of the stator [33], a procedure to calculate the width and the position of the fluid shaped barriers has been defined. Subchapter 4.2 deals with the optimization algorithm and with the strategies that can be used for the electrical machine design and, in particular, for the SynRel one. Finally, in subchapter 4.3, an example of the application of the mentioned methods for the design of a SynRel, which works in a particular operating cycle, is presented and discussed.

4.1 Preliminary design of the rotor core

In this subchapter, a preliminary design for the placement and the width calculation of each barrier is discussed and analyzed. The procedure starts with the hypothesis that the barriers are distributed within the pole according to the magnetomotive force of the d -axis. Under ideal conditions, the barrier magnetomotive force distribution is proportional to the cosine of the electrical angle while the distribution of the equipotential lines is proportional to the sine of the same angle [34].

According to (3.46), the C_k term can be associated to the value of the magnetic vector potential of the equipotential lines; defining A_0 as the value of the magnetic potential vector in the equipotential lines that are in the outer rotor diameter and in the q -axis, B_0 as the induction field at the airgap and R_S as the shaft radius, it is possible to calculate the term C_0 :

$$C_0 = \frac{A_0}{B_0 R_S} = \frac{\left(\frac{R_{e,r}}{R_S}\right)^{2p} - 1}{\left(\frac{R_{e,r}}{R_S}\right)^p} \quad (4.1)$$

where $R_{e,r}$ is the value of the outer rotor radius.

Considering the distribution of the equipotential flux lines, the term $C_{0,i}$, associated to the position of each barrier, can be calculated according to:

$$C_{0,i} = \frac{\sin\left(\frac{(2i-1)\pi}{4(N_b+1)}\right) A_0}{B_0 R_S} = \sin\left(\frac{(2i-1)\pi}{4(N_b+1)}\right) \frac{\left(\frac{R_{e,r}}{R_S}\right)^{2p} - 1}{\left(\frac{R_{e,r}}{R_S}\right)^p} \quad (4.2)$$

where i represents the i -th flux barrier and N_b is the number of the barrier.

Using (4.2) in the expression (3.46) and considering that the value of the position of the barrier is computed in correspondence of the q -axis, where the electrical angle is equal to $\pi/2$, and that its sine is equal to 1, the following expression is obtained:

$$R_i = R_S \sqrt{\frac{C_{0,i} + \sqrt{C_{0,1}^2 + 4}}{2}} \quad (4.3)$$

The width of each barrier can be calculated considering the distribution of the magnetomotive force of the q -axis, which is proportional to the sine of the electrical angle, and the hypothesis of a uniform force distribution between the steel and the air.

The procedure for the calculation of the barrier widths starts with the calculation of the differential magnetic voltage [35]. This calculation can be made in per units because it is important to calculate the ratio between the differential magnetic voltage and the total magnetic voltage.

The expression of the p.u. magnetic voltage of the q -axis can be calculated according to the distribution of the magnetomotive forces:

$$f_q = \sin(p\vartheta) \quad (4.4)$$

$$V'_{mq,i} = \frac{1}{\vartheta_m} \int_{\frac{2i-1}{2}\vartheta_m}^{\frac{2i+1}{2}\vartheta_m} \sin(p\vartheta) = \frac{\cos\left(p\frac{2i-3}{2}\vartheta_m\right) - \cos\left(p\frac{2i-1}{2}\vartheta_m\right)}{p\vartheta_m} \quad (4.5)$$

$$V'_{mq,N_b} = \frac{1}{\vartheta_m} \int_{\frac{2i+1}{2}\vartheta_m}^{\frac{\pi}{2p}} \sin(p\vartheta) = \frac{\cos\left(p\frac{2i+1}{2}\vartheta_m\right)}{p(\vartheta_m + \vartheta^*)} \quad (4.6)$$

$$\vartheta_m = \frac{\pi}{2p(N_b + 1)} \quad (4.7)$$

where ϑ_m is the mechanical angle between the N_b flux barriers and ϑ^* is the angular distance between the q -axis and the last barrier. A good initial value for this distance is the half of ϑ_m .

$$\vartheta^* = \frac{\vartheta_m}{2} \quad (4.8)$$

It is possible to calculate the expression of the differential magnetic voltage in the flux barriers according to the following expressions:

$$\Delta V'_{mq,1} = V'_{mq,1} = \frac{\cos\left(\frac{p\vartheta_m}{2}\right) - \cos\left(\frac{3p\vartheta_m}{2}\right)}{p\vartheta_m} \quad (4.9)$$

$$\begin{aligned} \Delta V'_{mq,i} &= V'_{mq,i} - V'_{mq,i-1} \\ &= \frac{2 \cos\left(p\frac{2i-3}{2}\vartheta_m\right) - \cos\left(p\frac{2i-1}{2}\vartheta_m\right) - \cos\left(p\frac{2i-5}{2}\vartheta_m\right)}{p\vartheta_m} \end{aligned} \quad (4.10)$$

$$\begin{aligned} \Delta V'_{mq,N_b} &= V'_{mq,N_b} - V'_{mq,N_b-1} \\ &= \frac{(2\vartheta_m + \vartheta^*) \cos\left(\frac{pN_b\vartheta_m}{2}\right) - (\vartheta_m + \vartheta^*) \cos\left(p\frac{2N_b-3}{2}\vartheta_m\right)}{p\vartheta_m(\vartheta_m + \vartheta^*)} \end{aligned} \quad (4.11)$$

Using (4.8) in (4.11), it is possible to write:

$$\Delta V'_{mq,N_b} = \frac{5 \cos\left(\frac{pN_b\vartheta_m}{2}\right) - 3 \cos\left(p\frac{2N_b-3}{2}\vartheta_m\right)}{3p\vartheta_m} \quad (4.12)$$

In order to minimize the q -axis flux, the width of each barrier (X_i) has to follow a specific distribution rule, which can be summarized by this expression [36]-[38]:

$$\frac{X_i}{X_j} = \frac{\Delta V'_{mq,i}}{\Delta V'_{mq,j}} \sqrt{\frac{L_i}{L_j}} \quad (4.13)$$

where L_i is the width of the steel between two barriers in the q -axis direction, and i is equal to 1 and it is the distance between the shaft and the first inner barrier.

Considering a homogeneous anisotropic structure in which the ratio between the steel and the air widths is constant in each part of the rotor, the ratio is expressed by the following expression:

$$\frac{X_i}{X_j} = \frac{L_i}{L_j} \quad (4.14)$$

It is also possible to write the following expression:

$$\frac{X_i}{X_j} = \left(\frac{\Delta V'_{mq,i}}{\Delta V'_{mq,j}}\right)^2 \quad (4.15)$$

In order to solve the system obtained in (4.15), it is useful to define the following vector:

$$\Lambda(j) = \left(\frac{\Delta V'_{mq,j}}{\Delta V'_{mq,j+1}}\right)^2 \quad \{j = 1, 2 \dots N_b - 1\} \quad (4.16)$$

$$\Lambda(N_b) = \sum_{i=1}^{N_b} X_i \quad (4.17)$$

The term in (4.17) has to be fixed by the designer: a typical value is of (40÷45) % of the total q -length of the rotor. This term strongly depends on the saturation level of the machine: in fact, if the machine works in high saturation conditions, this term decreases.

Using the vector defined in (4.16) and in (4.17), it is possible to solve the system (4.15) with the following expression:

$$X_i = \frac{\prod_{j=i}^{N_b} \Lambda(j) (-1)^{i+1}}{\left\{ \sum_{r=1}^{N_b-1} \left[\prod_{m=r}^{N_b-1} (\Lambda(m) (-1)^{r+1}) \right] \right\} - 1} \quad (4.18)$$

With the expressions (4.3) and (4.18), it is possible to obtain the preliminary rotor design: the inputs of this procedure are the outer rotor radius, the shaft radius and the sum of the flux barrier length. The outer rotor radius can be calculated with the same procedure used for the other machine types (e.g. the IM) [39]-[40].

4.2 Optimization of the SynRel

The SynRel is a particular kind of machine that requires the use of Finite Element (FE) analyses to correctly simulate the behavior of the performance of the machine. In literature, several approaches have been presented and they show a good approximation for a few working points: this is due to the strong dependence on the core saturation and on the high torque oscillations caused by the saliency of the machine. The use of only analytical models can be helpful to define a good preliminary design, but for the final design the integration with the FE model and with the optimization algorithm is mandatory.

In order to reduce the computational time of the FE models, it is possible to use analytical models augmented with FE analyses; according to [41], this method is able to reduce the computational effort up to 80% for the optimization procedure, with an error in the average torque of 2%. The other aspect that is not considered consists in the torque ripple computation error with the use of the analytical method integrated with FE analyses. This method can be used and can give optimal results for those applications that do not require a minimization of the torque ripple or for which a preliminary design is needed to be further optimized with the aim to reduce the torque oscillations.

In this thesis, the full FE model has been used to calculate the performance of the machine; therefore, the functions that describe the motor performance related to the motor parameters cannot formally be expressed, but they can only be computed by complex simulations. Since the functions are unknown, their derivatives are also unknown and, as a result, derivative-free algorithms have to be employed.

The typical approach in the optimization procedure of electrical machines, and particularly of SynRels, consists in the minimization of the torque ripple and in the maximization of the torque average value. Hence, the optimization procedure involves a multi-objective problem.

4.2.1 The optimization algorithm

In literature, there are several multi-objective derivative-free algorithms that match with the problem of the electrical machine optimization [42]-[43]. Some of these methods take into account the preferences of the decision maker in relation to

the choice of the targets: for example, they consider if an objective function should be preferred respect to another one. In the electrical machine context, there usually is a trade-off between a small torque profile variance (minimization of the torque ripple) and a high value of the mean torque.

For electrical machines, and in particular for SynRels, the minimization of the torque ripple is in conflict with the maximization of the mean torque and a proper compromise has to be chosen, even if a slight increase in the mean torque can be obtained with a high increase of the torque ripple (the Pareto front is “flat”).

The motor input variables can be expressed through a vector v , while the mean torque and the torque ripple can be expressed as $T(v)$ and $\zeta(v)$, respectively. A possibility to properly take into account the torque ripple in the maximization of the mean torque is given by the minimization of a proper combination of the two objectives according to the following expression, which can be called “risk-sensitive” objective function:

$$f(v) = -T(v) + \gamma\zeta(v) \quad (4.19)$$

The parameter γ in the expression is called risk-aversion parameter (since the objective is the minimization of the torque ripple $\gamma \geq 0$).

The higher the risk-aversion parameter, the higher the influence of the torque ripple in the minimization problem; this value should be chosen in function of the weight and normalized respect to the estimated mean torque and torque ripple at the end of the optimization, according to the following expression:

$$\gamma = \frac{W\hat{T}}{\hat{\zeta}} \quad (4.20)$$

where W is the weight in per unit of the torque ripple, $\hat{\zeta}$ is the torque ripple estimated final value (or desired) and \hat{T} is the estimated final value of the mean torque (or desired).

The optimization problem can be summarized by the following integer non-linear minimization problem:

$$\left\{ \begin{array}{l} \min f(v) \\ g(v) \leq 0 \\ l \leq v \leq u \\ v_i \in \mathbb{Z}, \quad i \in I_z \\ v_i \in \mathbb{R}, \quad i \in I_c = \{1, 2, \dots, n\} \setminus I_z \end{array} \right. \quad (4.21)$$

where $g(v)$ is the constraint function; l and u are the lower and upper constraints of the variables of the electric motor; I_z is the index set of integer variables and I_c is the index set of continuous variables. It is possible to add these other conditions:

$$\begin{cases} f: \mathbb{R}^n \rightarrow \mathbb{R} \\ g: \mathbb{R}^n \rightarrow \mathbb{R}^m \\ v \in \mathbb{R}^n \\ l \in \mathbb{R}^n \\ u \in \mathbb{R}^n \end{cases} \quad (4.22)$$

where n is the number of variables and m is the number of constraints.

Considering the high computational burden that is needed to correctly evaluate the motor behavior with a full FE analysis, the application of a global optimization algorithm could be impractical due to the high iterations required when only a limited number of function evaluations is available. Therefore, a good practice to solve the problem is the employment of a local derivative-free algorithm that uses, as starting point, the preliminary design obtained with the expressions in subchapter 4.1.

The local derivative-free algorithm used in this thesis, which has been developed by the colleagues of the Operative Research group of the University of Rome ‘La Sapienza’, is the DFL Algorithm that is proposed in [44].

The algorithm is based on a sequential penalty approach, the non-linear constrained problem (4.21) is approximated by a sequence of box-constrained problems in the following form:

$$\begin{cases} \min[P(v, \varepsilon_k)] = f(v) + \frac{1}{\varepsilon_k} \sum_{i=1}^m \max\{0, g_i(v)\}^r \\ l \leq v \leq u \\ v_i \in \mathbb{Z}, \quad i \in I_z \\ v_i \in \mathbb{R}, \quad i \in I_c = \{1, 2, \dots, n\} \setminus I_z \end{cases} \quad (4.23)$$

where $\varepsilon_k > 0$ and $r > 1$.

The DFL algorithm generates a sequence $\{\varepsilon_k\}$ such that, for any given ε_k , the function $P(v, \varepsilon_k)$ is reduced with respect to v along all the coordinate directions by means of suitable derivative-free line searches. Then, if the violation of the constraint at the new point is not sufficiently decreased, the penalty parameter ε_k is updated.

The main steps of the method are highlighted in Figure 4.1, which shows a scheme of the DFL algorithm.

From the scheme, it is possible to see that the method is based on a suitable sampling strategy along a specific set of search directions $D = \{\pm e_i\}$, where e_i is a vector with 1 in the i -th entry and zeros for all the other elements, for $i=1, \dots, n$. By exploring a given direction, the algorithm moves in a component-wise fashion. Now it is possible to use a specific search strategy, discrete or continuous, according to the nature of the variable; therefore, it depends on the direction (or component) that the algorithm is evaluating. When a continuous variable is evaluated, the goal of

the optimization is to guarantee both a sufficient movement along the search direction and a good decrease in the objective function. When a discrete variable is evaluated, the goal is to sample the objective function in such a way that the integrality is always satisfied.

The sampling strategy can get, with some limits, a sufficient knowledge of the problem function both for the continuous and for the discrete search and it can make a sort of local optimality for the discrete variables and recover first order information for the continuous ones.

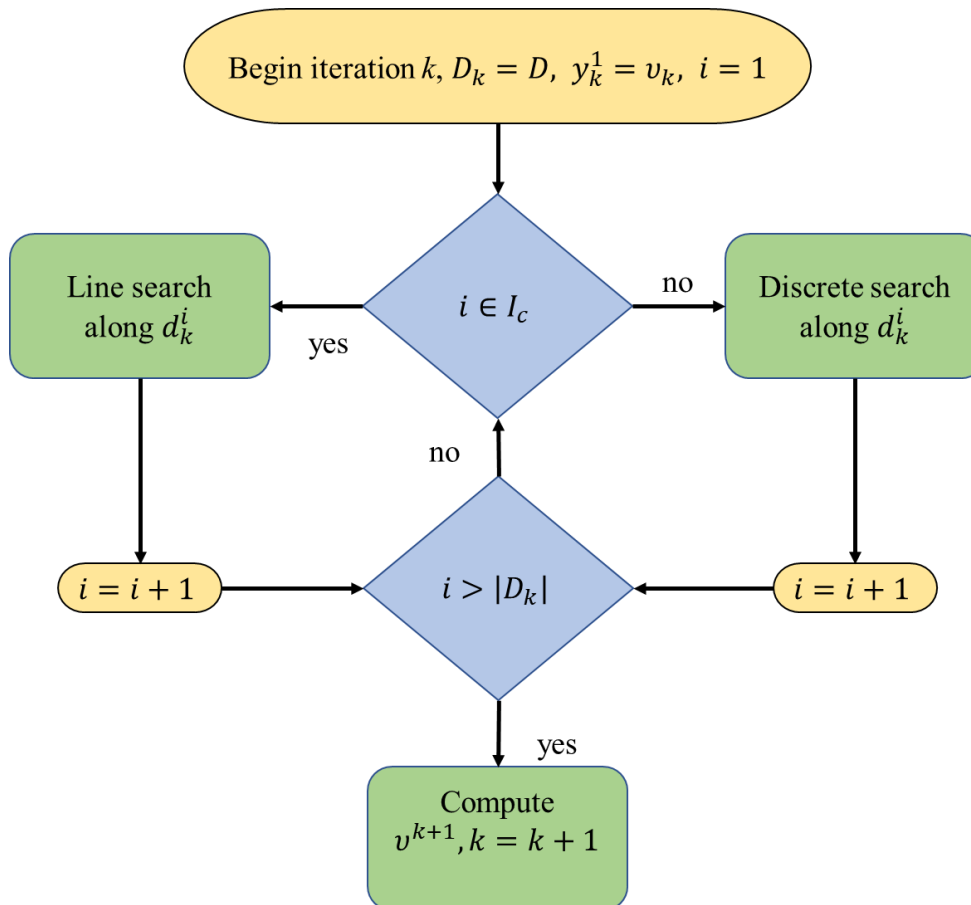


Figure 4.1: Simplified scheme of the DFL algorithm.

4.2.2 Optimization strategies

The typical approach in the optimization of electrical machine for industrial applications consists in the maximization of the efficiency at the rated working point with a reasonable torque ripple (or the minimum possible) since the machines will likely work, for most of the time, at their rated speed and torque.

Once that the rated working point, the variables and the constraints (maximum ripple, maximum phase voltage, maximum inertia or torque to start, etc.) have been

assigned, it is possible to set the lower and upper constraints of the variables and to start the optimization of the efficiency in correspondence of the rated working point.

Conversely, since the synchronous machines are typically employed for variable speed drives, they can work with a more complex working cycle profile, which includes speed and torque variations.

The optimization procedure should consider this working cycle profile so that all those points can be computed. These further calculations require more computational burden because of the performance evaluation, and this depends on the number of the considered working points. If the application requires the evaluation of a high number of working points (the electric vehicles application is one of those), there are two possible strategies for the computation of the performance of the machine:

- Identifying a low number of significant working points (typically four or five) to properly represent the working cycle and to evaluate the machine performance for those points;
- Using an analytical model augmented by the FE analysis and evaluating the machine performance in every point of the working cycle, admitting a higher error in the torque/losses estimation and especially in the torque ripple calculation.

As an example, it is possible to use the working cycle obtained by the analyses of the driving cycle in subchapter 2.4.

Considering only the motor operation, from Figure 2.15 it is possible to define four working areas, which are represented by 4 equivalent points.

The selection of the areas can be made in two main ways:

- The areas can be divided according to the concept of low, medium, and high speeds and of low and high torque. By making that, it is possible to define a maximum of six representative points; however, since for electric car applications at medium and high speeds the motor has a low torque, for these applications there are four representative points, which have to be weighted in function of the total points that represent (Figure 4.2);
- The areas can be divided considering that in each area there is the same number of working points (Figure 4.3).

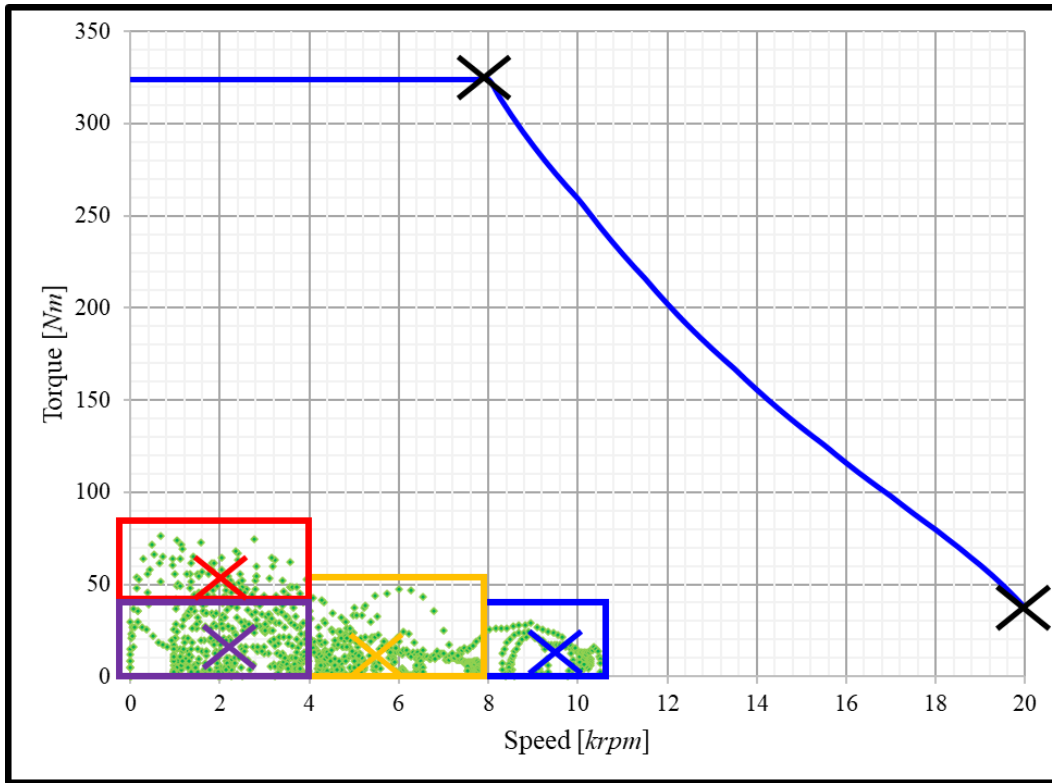


Figure 4.2: Division of the cycle in working areas (Case 1).

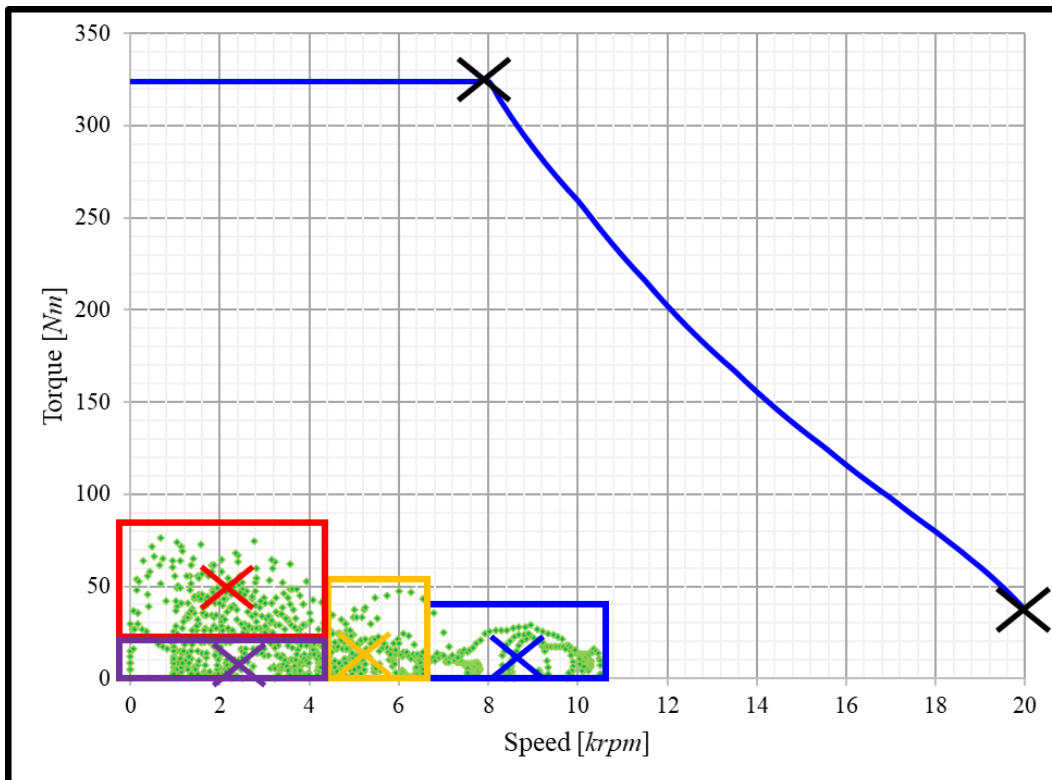


Figure 4.3: Division of the cycle in working areas (Case 2).

The following table highlights the values and the weights of the efficiency computation for the selected representative points for the two cases. The two cases have the same constraint points, which are the maximum torque at base speed and the maximum torque at maximum speed.

Table 4.1: Comparison between the representative points.

	Case 1			Case 2		
	Torque [Nm]	Speed [rpm]	Weight [%]	Torque [Nm]	Speed [rpm]	Weight [%]
Pt 1 (Purple)	16.45	2222	35.8	8.92	2406	25
Pt 2 (Red)	52.00	2014	11.6	40.04	2139	25
Pt 3 (Yellow)	11.67	5744	37.8	12.24	5215	25
Pt 4 (Blue)	11.98	9511	14.8	10.81	8642	25
Pt 5 (Black)	312.00	8000	0	312.00	8000	0
Pt 6 (Black)	37.00	20000	0	37.00	20000	0

For the SynRel, the points Pt1, Pt3, and Pt4 have similar torque values; since the machine is far from working in the flux-weakening region, its current control angles, phase currents and distributions of the induction field inside the machine are very similar for these working points. From a simulation point of view, it is possible to simulate only one of these points and then to calculate the core and stray losses at different speeds according to the Bertotti equation and by varying the value of the frequency. The points Pt5 and Pt6 have not a weight in the efficiency calculation during the cycle because they are only used for the acceleration performance and to reach the maximum speed of the vehicle. In the optimization context, these points must be simulated and used as constraints.

In conclusion, in order to correctly simulate the maximum performance in terms of acceleration and maximum speed and to have an estimation of the efficiency during the driving cycle, it is necessary to compute four points with FE analyses. Once that these points have been simulated, it is possible to use either in the objective function or as constraints the torque ripple values in order to reduce or to minimize the noise and vibrations at the bearings.

This is only an example of the possible selection of representative points of the driving cycle; in fact, it is also possible to use more regions, hence obtaining more simulation points. In this way, the efficiency computation for each optimization step is more accurate as well as the computational burden is more time-consuming.

Thanks to the constant development of the computational power and to the possibility of parallelization of FE analyses of different points, this approach is preferable to use an analytical model augmented by FE analyses if all the representative points can be simulated at the same time.

4.3 An example of the application of the Optimization procedure

The presented procedure has been applied to a SynRel that has been designed to work with the S8 duty cycle (continuous-operation periodic duty cycle with related load/speed). This duty cycle is defined as a repeated sequence of different conditions of torque and speed, which are both applied for a defined time; this could be associated to the driving cycle of EVs when it is divided in its representative working points. Despite the difference in terms of power (the output rate for this motor is around 1000 W), this example can simplify the design issue due to the mechanical integrity of the SynRel at high speeds by only focusing on the design and considering more than one working point.

The inputs for the designer are the torque-speed specifications, the maximum stack length and the maximum stator outer diameter. The duty cycle of the machine is shown in Figure 4.4 in terms of torque and speed. It is simple to define, from this duty cycle, four working points and the duration of their application times:

- 1) Torque= 2.26 Nm , Speed= 4000 rpm , Application time= 3.4 min (overloading)
- 2) Torque= 1.60 Nm , Speed= 6000 rpm , Application time= 13.8 min (rated)
- 3) Torque= 0.86 Nm , Speed= 8000 rpm , Application time= 55.2 min
- 4) Torque= 0.22 Nm , Speed= 8000 rpm , Application time= 27.6 min

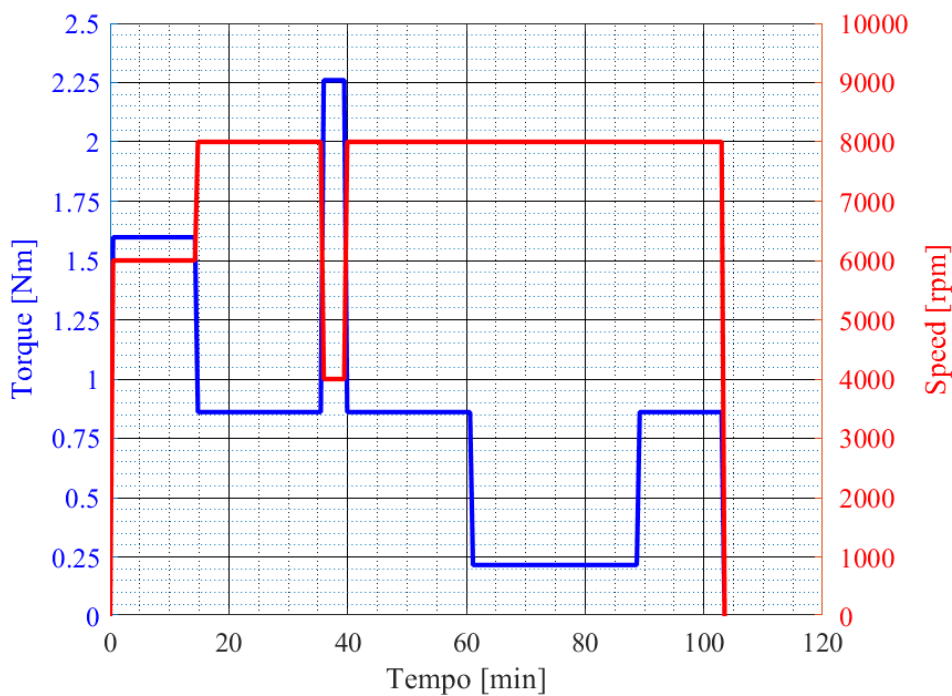


Figure 4.4: Duty cycle in terms of torque and speed.

The next step consists in the computation of the rotor outer radius after that the maximum current density at the rated point has been fixed (which is lower than 4 A/mm^2 in this case). For this application, the maximum frequency is imposed and, therefore, the number of poles is equal to four. The choice of the number of slots and barriers has been made according to the best practice explained in [45]. The number of slots is 36 and the number of barriers is 4 plus a notch. After the computation of the rotor outer radius, it is possible to define the flux barrier variables according to (4.3) and (4.18). The values of all the variables are reported in the following Table 4.2. The shapes of the rotor and of the stator of the Preliminary Design (PrD) are shown in Figure 4.5.

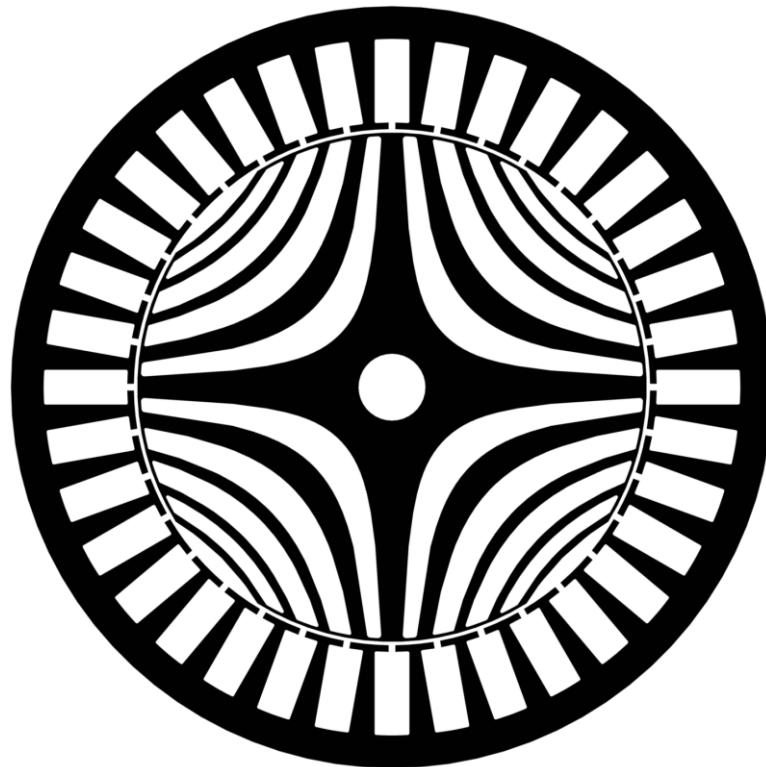


Figure 4.5: Stator and rotor shapes of the preliminary design.

Starting from this preliminary design, it is possible to define the upper and lower constraints for the optimization procedure. In this step, it is worth to analyze the effect of the optimization procedure on the results. For this reason, in this subchapter the preliminary design is compared with three optimizations:

- 1) OPT1 is the optimization that uses all the points of the cycle for the optimization, as explained in section 4.2.2;
- 2) OPT2 is the typical optimization of industrial motors that uses only the rated working point (P2);
- 3) OPT3 is a combination of OPT1 and OPT2 and uses a single point for the optimization: the most frequent one (P3).

In Table 4.2, the design variables, the starting values for the optimization, their upper and lower limits, the constraints and the objective functions used for the different strategies of the optimization are reported.

Table 4.2: Design variables, constraints and objective functions.

Variable	Preliminary (Starting point)	Lower limit	Upper limit
I_{SD}	77.2 mm	68 mm	88 mm
S_W	5.2 mm	4 mm	7 mm
S_H	12.5 mm	9.5 mm	15.5 mm
X_1	5.5 mm	2.5 mm	8.5 mm
R_1	13.9 mm	10.9 mm	16.9 mm
X_2	4.8 mm	1.8 mm	7.8 mm
R_2	23.6 mm	20.6 mm	26.6 mm
X_3	3.5 mm	0.5 mm	6.5 mm
R_3	29.7 mm	26.7 mm	32.7 mm
X_4	2.1 mm	0.5 mm	5.1 mm
R_4	33.9 mm	30.9 mm	36.9 mm
X_5	1.0 mm	0.5 mm	4 mm

Optimization	Objective Function	Constraint 1	Constraint 2
OPT1	Efficiency (Cycle)	Torque Ripple (Cycle) <15%	Current density (P2) <4 A/mm ²
OPT2	Efficiency (P2)	Torque Ripple (P2) <15%	Current density (P2) <4 A/mm ²
OPT3	Efficiency (P3)	Torque Ripple (P3) <15%	Current density (P2) <4 A/mm ²

In this example, for different optimizations, there is a single objective function in order to simplify the optimization problem, without losing in generality and by focusing on the results obtained by the use of several working points. For the computation of the efficiency, each working point is simulated considering a transient analysis in order to compute the induction field within the machine and its variation in terms of frequency; therefore, using the Bertotti equation, the core losses are computed. The stray losses are included as percentage of the mechanical output power (around the 0.5%).

Another important variable, especially for the reduction of the torque ripple, is the slot opening, which is not included as a design variable in order to minimize the number of variables and to reduce the computational burden. In this case, since the reduction of the slot opening reduces the torque ripple, the minimum value imposed by the manufacturing constraints has been set.

An important constraint is the maximum current density because its value strongly affects the maximum temperature in the windings, which has to be compatible with the application. The value of the OPT3 is lower than the ones of the other optimizations because the evaluated points have a lower torque; with a value of $2.6 A/mm^2$ in P3, a current density lower than $4 A/mm^2$ should be guaranteed in P2.

The optimizations require different numbers of iterations and different computational burdens. This depends on the number of computed points with a full FE analysis (four in OPT1 and one in the others) and on the different saturation levels, which affect the time of the analyses.

Figure 4.6, Figure 4.7 and Figure 4.8 show the behavior of the objective functions in the three optimizations OPT1, OPT2, and OPT3, respectively. The points that do not satisfy the constraints are the red dots in the figures, while the blue dots represent the ones that satisfy the constraints. When a point does not satisfy the constraints, the equivalent value of its objective function is forced to a higher value in order to discard that point from the optimization results, but in the figures its original value is used.

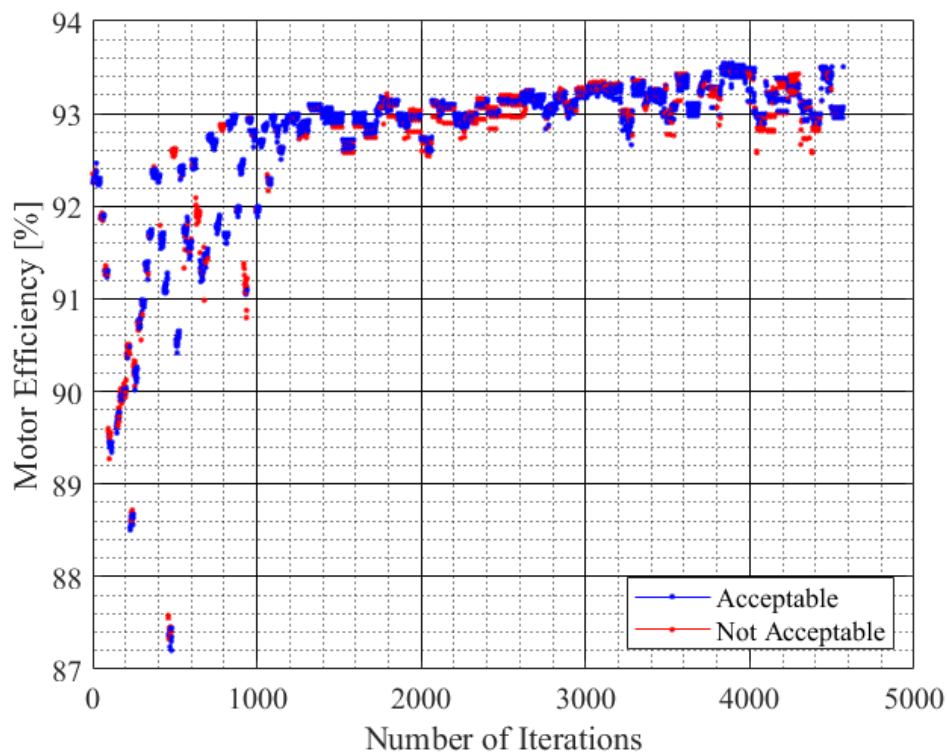


Figure 4.6: Behavior of the objective function (efficiency during the cycle) in the optimization OPT1.

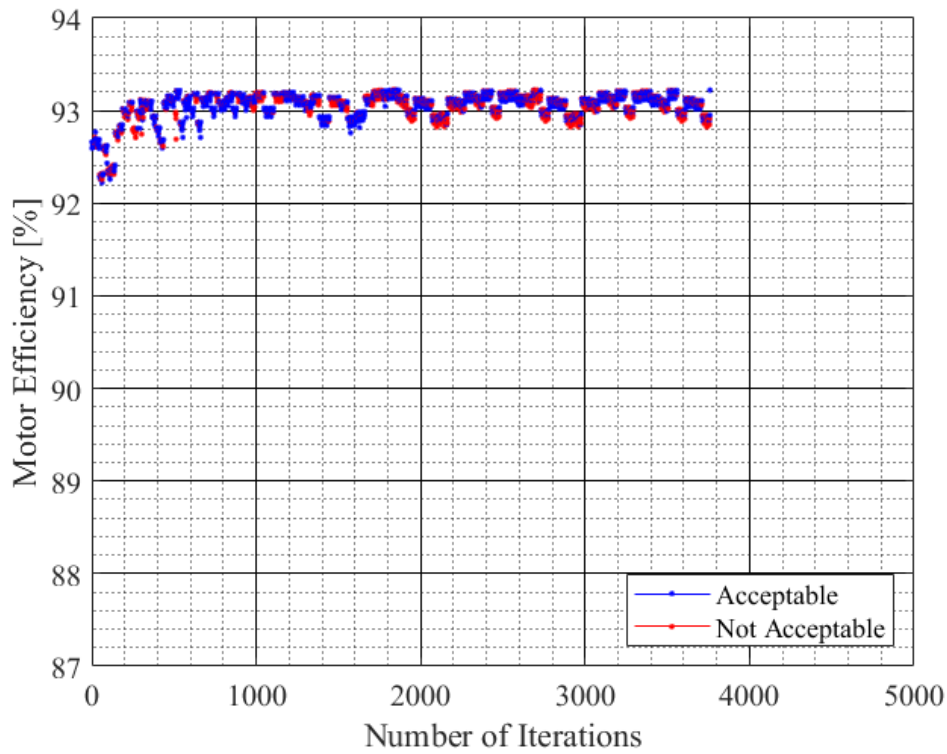


Figure 4.7: Behavior of the objective function (efficiency in P2) in the optimization OPT2.

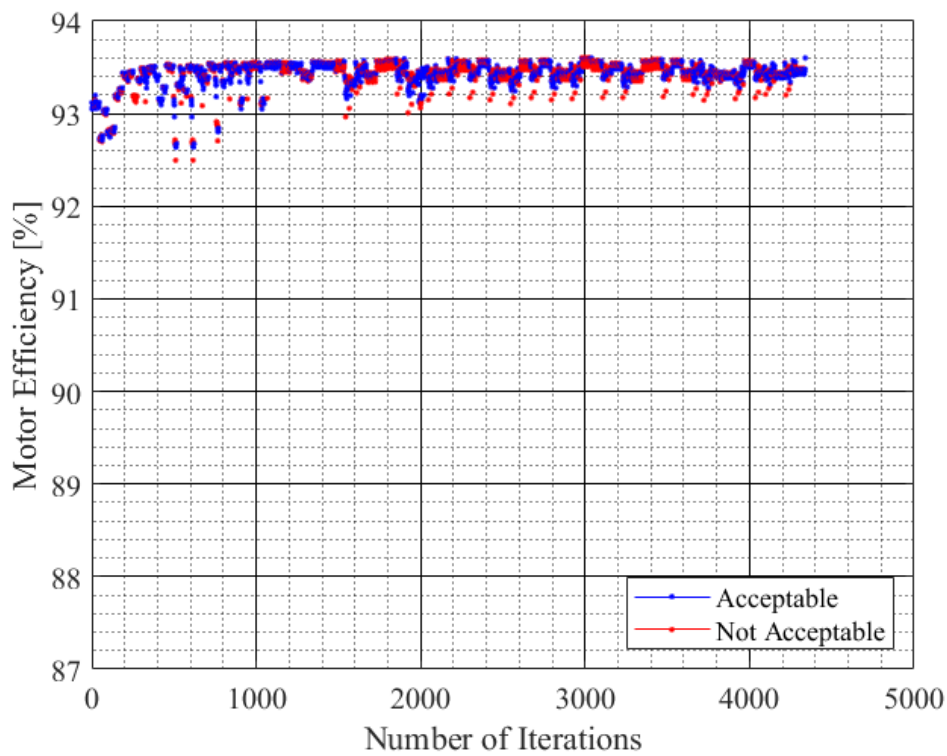


Figure 4.8: Behavior of the objective function (efficiency in P3) in the optimization OPT3.

The maximum number of iterations for each optimization has been set to 4600 in order to correctly compare the three strategies. Another possibility could have been to limit the computational burden for each optimization.

4.3.1 Results of the optimizations

It is worth noting that the optimization OPT1, the one that considers the full working cycle, requires more iterations to achieve a good value of efficiency compared to the other procedures, but the optimization has been stopped before it could reach the convergence because it has overcome the maximum number of iterations. In the first phase, the optimization reaches very low values of efficiency; this can be justified by the introduction of the overloading point. A little deviation from the preliminary design can really affect the performance when a high saturation level is reached. Only after 3000 iterations, the optimization reaches a good value of efficiency respect to the final one.

The optimization OPT2, which uses the rated point for the optimization procedure, is the first one to reach the convergence after 3800 iterations, even if the final value is not different from the one obtained after 600-800 iterations. The value of the efficiency is always close to the maximum one and this can be justified by the use of a good preliminary design as a starting point.

The optimization OPT3, which uses the most frequent point of the cycle, reaches the convergence after 4400 iterations; during the optimization procedure, the obtained efficiency values have a bigger difference than the OPT2 ones. In this case, a good value of efficiency is achieved after 800-1000 iterations. The remaining points are necessary to refine the results and to reach the optimal design.

The next step consists in the comparison of the stator and rotor cores, of the induction field for the different working points and of the losses for each working point and during the cycle: this must be done for the different optimizations and for the preliminary design.

Figure 4.9 shows the different stator and rotor cores obtained by the different optimization methods. The project OPT1 is the only design that considers the overloading point P1. In order to minimize the losses in that point, the width of the rotor and stator yokes are greater compared to other designs, thus reducing the saturation and the induction field in those elements, other than the phase current and the losses.

On the other side, the project OPT3, which only considers the most frequent point P3, has the thinnest rotor and stator yokes because the considered point needs a low level of induction field because it is characterized by a torque lower than the rated one: hence, it is possible to reduce the machine steel. Therefore, the current and the losses in the overloading working point P1 for the OPT3 will be much higher than the ones for the OPT1 design.

The rotor and stator yokes of the project OPT2 are in the middle of the projects OPT1 and OPT3, as well as the level of saturation, the losses and the phase currents. All these considerations are confirmed by the figures of the magnetic flux density in the working points P1 (Figure 4.10), P2 (Figure 4.11), P3 (Figure 4.12), and P4 (Figure 4.13).

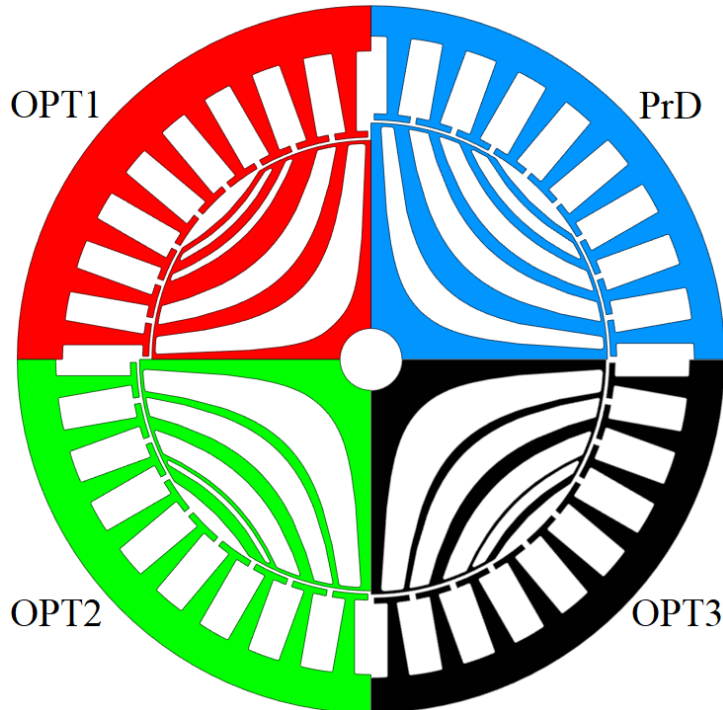


Figure 4.9: Stator and rotor geometries of the Preliminary Design (PrD) and of the optimizations during the cycle (OPT1), in P2 (OPT2), and in P3 (OPT3).

Figure 4.10 shows the magnetic flux density of the preliminary design and of each optimized design for the overloading working point P1. As it can be supposed by analyzing the stator and rotor shapes, the design OPT1 has the lowest saturation levels both in the stator and rotor yokes. This allows to have the best performance in that point compared to the one of the other designs. The preliminary design has the highest value of magnetic flux density; OPT 2 and OPT3 show similar values but the first one has a slightly lower magnetic flux density. Figure 4.11 shows the magnetic flux density in every design for the rated working point P2. The level of magnetic flux density in the rotor and stator yokes of the project OPT1 is low compared to the one of the other projects, while the projects OPT3 and PrD show that the yokes are lightly saturated. These two aspects lead to a lower value of the saliency ratio, thus reducing the motor torque capability and efficiency. Figure 4.12 shows the magnetic flux density in every design for the most frequent working point P3. The project OPT3 has the best levels of saturation, guaranteeing the best performance in correspondence of this point. Figure 4.13 shows a very low level of magnetic flux density for the working point P4.

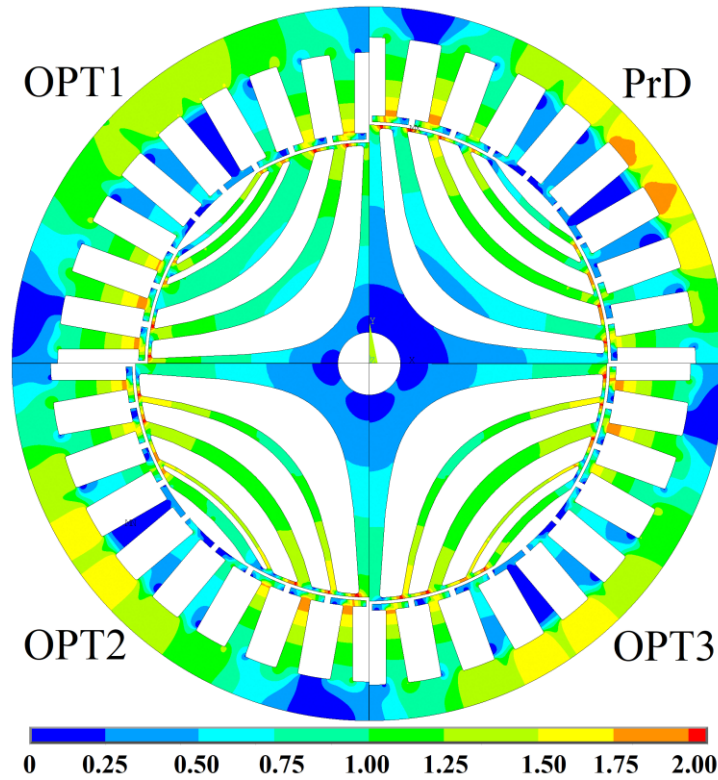


Figure 4.10: Magnetic flux density [T] for the working point P1 of the Preliminary Design (PrD) and of the optimizations during the cycle (OPT1), in P2 (OPT2), and in P3 (OPT3).

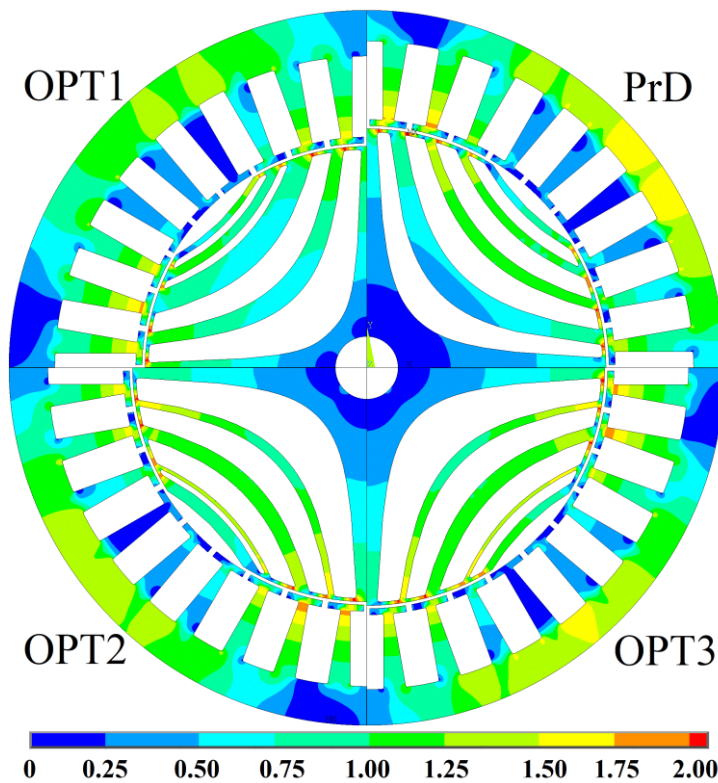


Figure 4.11: Magnetic flux density [T] for the working point P2 of the Preliminary Design (PrD) and of the optimizations during the cycle (OPT1), in P2 (OPT2), and in P3 (OPT3).

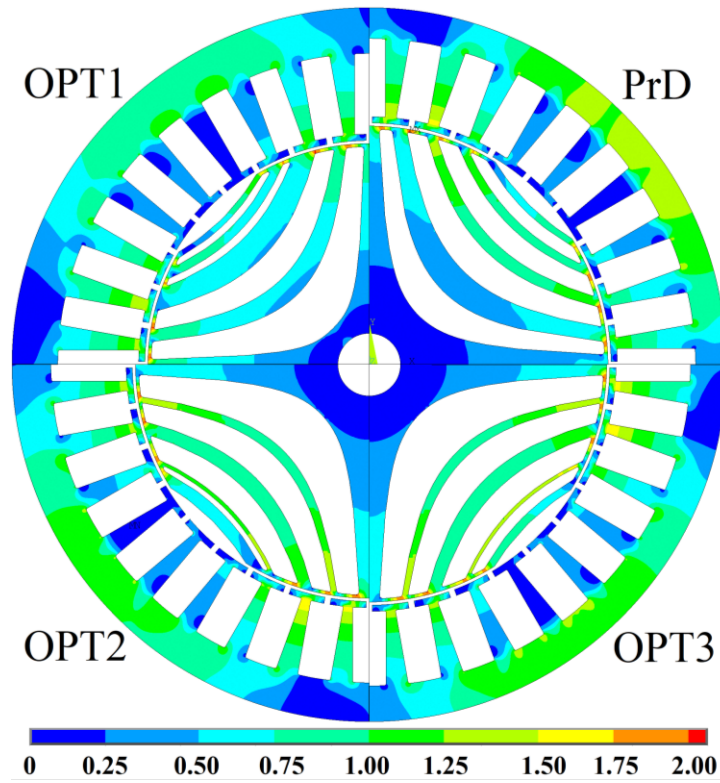


Figure 4.12: Magnetic flux density [T] for the working point P3 of the Preliminary Design (PrD) and of the optimizations during the cycle (OPT1), in P2 (OPT2), and in P3 (OPT3).

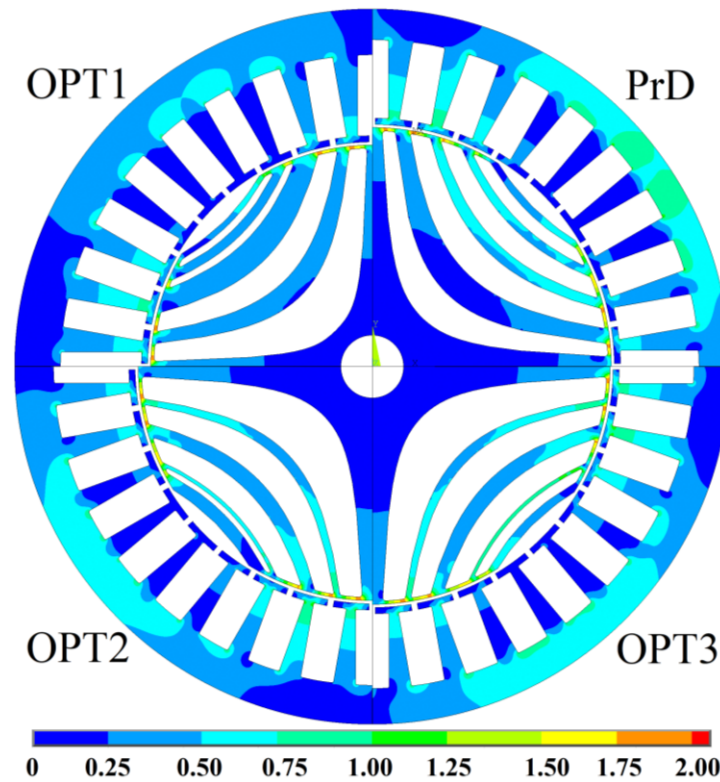


Figure 4.13: Magnetic flux density [T] for the working point P4 of the Preliminary Design (PrD) and of the optimizations during the cycle (OPT1), in P2 (OPT2), and in P3 (OPT3).

Every optimized project can guarantee the best performance in correspondence of the working points used for their optimization procedures in terms of saturation levels.

The results of all the designs for each working point and during the cycle are reported in Table 4.3. The numerical results confirm the considerations based on the shape of the project designs and on the evaluation of the magnetic flux density and of the saturation levels.

It is worth noting that the project OPT1 has the lowest current and losses and the highest efficiency for the overloading point P1. The projects OPT2 and OPT3 have the best performance for the rated point (P2) and for the most frequent point (P3), respectively. As expected, the project that has the best performance during the whole operating duty cycle of the machine is OPT1, but it is also more expensive from the computational burden point of view. In order to reduce the computation burden, it is possible to realize the optimization considering the most frequent working point (P3) while still guaranteeing a good efficiency during the cycle.

Table 4.3: Performance of the preliminary design and of the optimized ones.

	Current [<i>Arms</i>]			
Working point	PrD	OPT1	OPT2	OPT3
1	50.9	39.4	43.5	45.3
2	37.5	32.6	31.2	32.3
3	23.0	22.5	22.8	22.4
4	11.4	11.3	11.4	11.3
Cycle	23.9	21.38	21.52	21.48
	Efficiency [%]			
Working point	PrD	OPT1	OPT2	OPT3
1	87.06	90.83	89.76	89.37
2	91.51	93.06	93.22	92.80
3	93.00	93.47	93.26	93.60
4	91.03	91.28	91.11	91.26
Cycle	92.15	93.03	92.86	92.97
	Energy Losses [<i>Wh</i>]			
Working point	PrD	OPT1	OPT2	OPT3
1	7.97	5.42	6.12	6.38
2	21.45	17.24	16.82	17.94
3	49.89	46.31	47.90	45.32
4	8.35	8.10	8.27	8.12
Cycle	87.66	77.07	79.11	77.76

The optimization that uses all the working points of the cycle (OPT1) has been capable of reducing the energy losses during the cycle by only 0.7 *Wh* with an increase in the efficiency of $\approx 0.06\%$ compared to the values of the project obtained

by the optimization that uses the most frequent working point (P3). If the best design is compared to the one that used the rated point for the optimization (OPT2), there has been a reduction in the energy losses of 2.04 *Wh* with an increase in the efficiency of $\approx 0.17\%$.

The importance of using all the working points for the optimization consists in the possibility of guaranteeing that the value of the torque ripple is within the constraints for every working point. This aspect is not automatically satisfied by the optimizations that use a single working point.

This is visible in Figure 4.14, Figure 4.15, and Figure 4.16, in which the behavior of the torque is shown in relation to the mechanical angle for all the working points of the optimized designs OPT1, OPT2, and OPT3, respectively; the torque behavior is also compared to the torque ripple limits. In the figures, the working points from 1 to 4 are presented from the top to the bottom, respectively. The only project that satisfies the torque ripple constraint of 15% is the design OPT1 because it has been imposed as a constraint during the optimization procedure. When just one point is considered during the optimization (OPT2 and OPT3), the torque ripple is satisfied only for the considered working point. Therefore, for these projects, a post-processing step is necessary to make further verifications for the other working points in order to verify the satisfaction of the constraint.

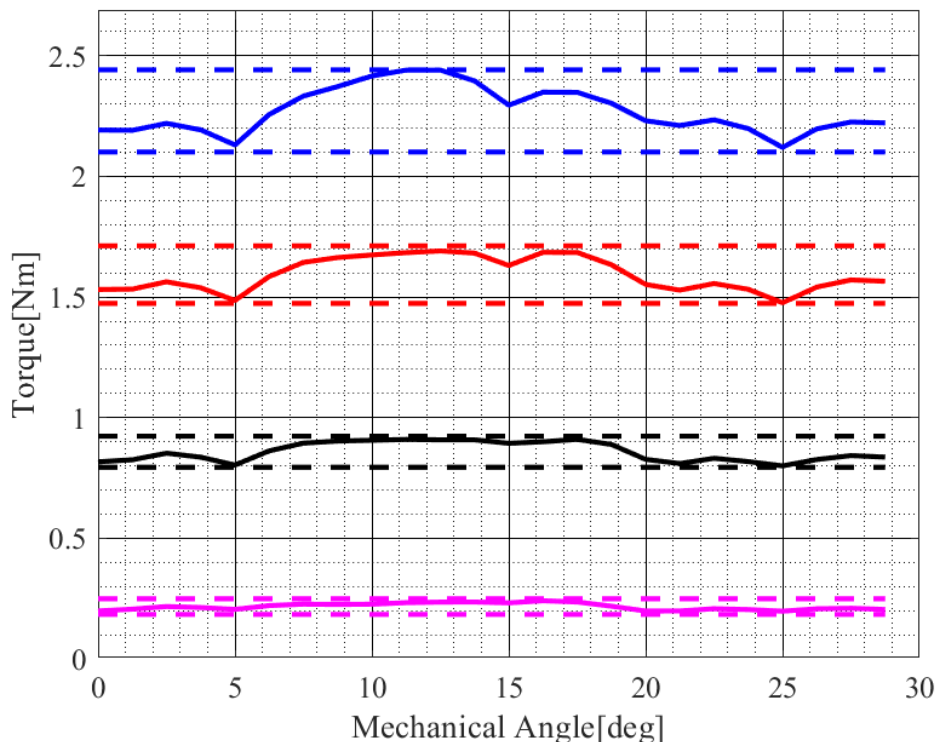


Figure 4.14: Behavior of the torque in relation to the mechanical angle for all the working points of the project OPT1.

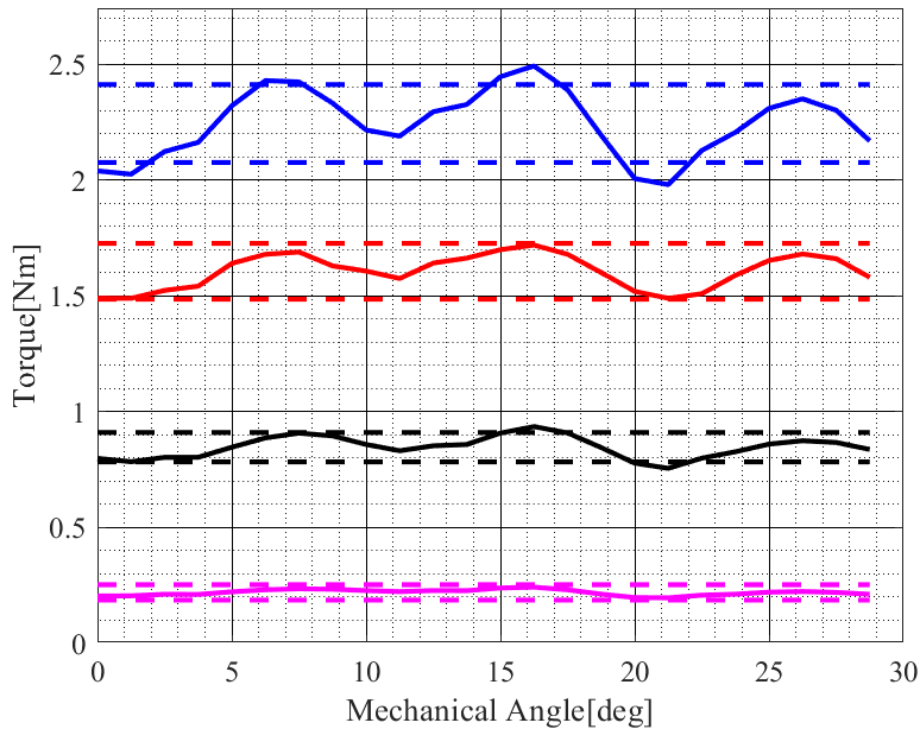


Figure 4.15: Behavior of the torque in relation to the mechanical angle for all the working points of the project OPT2.

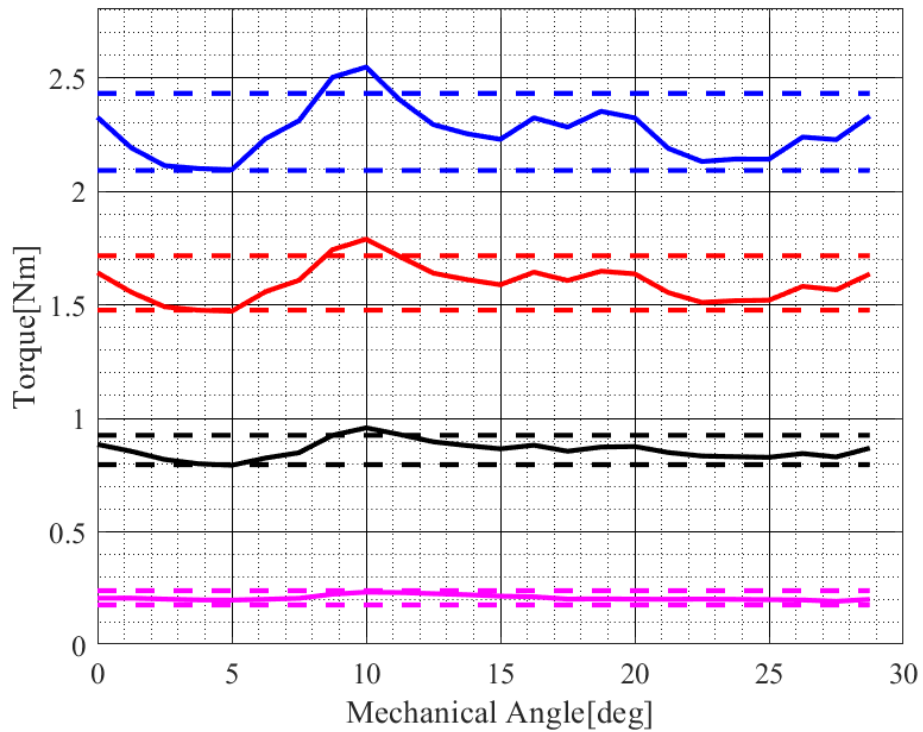


Figure 4.16: Behavior of the torque in relation to the mechanical angle for all the working points of the project OPT3.

Chapter 5

Robust Design Optimization

Part of the work presented in this chapter has been previously published in [10].

The improvement of the robustness of the performance of electrical machines in presence of neglected features, such as manufacturing tolerances and deviations in material properties and parameters, is increasingly demanded.

The typical design steps rarely take into account the Manufacturing Tolerances (MTs) or the deviations of the material properties due to the manufacturing processes of the machine [46]-[48]. The manufactured machine will have a different performance compared to the one of the ideal design obtained by the design procedures.

The tolerances of the material properties have been mainly taken into account in Permanent Magnet (PM) motors [49]-[50]. Robust design methods, accounting for PM property deviations, are proposed in [51]-[53].

Bianchi et al. propose a sensitivity analysis on SynRels focused on the evaluation of the effects of MTs on the torque ripple, highlighting the difficulty to obtain a robust motor geometry for the torque ripple containment [54]-[55].

Subchapter 5.1 introduces the principles of the statistical analysis and of the criteria for the robust design optimization. Subchapter 5.2 describes the method to obtain different candidates for the robust design and deals with the sensitivity analysis for the SynRel. The statistical tolerance analysis, the worst-case analysis and the items for the individuation of the most robust design are presented in subchapter 5.3 and subchapter 5.4, respectively. Finally, subchapter 5.5 presents the criteria for the selection of the most robust design (after the evaluation of the results of the previous analyses) and summarizes the entire proposed procedure.

5.1 The Criteria of Robust Designs

In the previous chapter, the optimization procedure for a SynRel has been presented and discussed. The result of this optimization was a project with the best performance in the neighborhood of the preliminary design; this can be defined as a Local Minimum (LM). Considering different starting points for the optimization procedure, it is possible to obtain different LMs. Therefore, the optimization procedure can be modified by the adoption of two different algorithms. A simulated annealing algorithm [56] has been used in order to find the neighbors of the LMs, which are used as starting points, and then the algorithm presented in the previous chapter has been adopted to perform a refined search of the LMs. Along with the LMs, the project that shows the best performance is defined as the Best Local Minimum (BLM).

The Manufacturing Tolerances (MTs) affect the geometry of the realized machine, which will have a deviation from the rated one. These deviations vary the performance of the design and, in particular, if the design has been obtained by an optimization procedure, they reduce it.

The effect of the MTs depends on the considered design: two different projects can be differently affected by them and the design that has the best performance, considering also the effect of the MTs, will be the most robust. As discussed in [57]-[60], the LMs could be more robust than the BLMs when the MTs are introduced and, for this reason, an accurate analysis on all the LMs must be carried out.

The MTs affect both the stator and the rotor cores and they are strictly related to the manufacturing process (i.e. punching, laser cutting, etc.). The manufacturers typically declare the maximum boundary condition for the tolerance of the process and it can be considered the same for all the dimensions. It can be represented as a bilateral deviation from the rated value of a dimension expressed as $x \pm g$, where g is the deviation.

Each variable, each dimension and each part of the machine may have, within the maximum boundary of the MTs, a different deviation from the declared value. Therefore, it is challenging to quantify or to estimate the impact of the process on each dimension, especially if considering the complex geometry of the SynRel.

In literature, different distributions of the MTs are proposed in the field of statistical tolerance analysis to represent these phenomena [61]. From these distributions, it is possible to select, in order to best approximate the behavior of the MTs, the normal (Gaussian) distribution $N(\mu, \sigma^2)$, where the probability that the dimension x is within the range $[\mu - 3\sigma, \mu + 3\sigma]$ is of 99.7% [61].

The expression of this distribution is the following one:

$$D_x = \frac{1}{\sigma\sqrt{2\pi}} e^{-\frac{(x-\mu)^2}{2\sigma^2}} \quad (5.1)$$

where D_x is the probability density distribution, x is the value of the random variable, μ is the mean value, and σ^2 is the variance.

The probability that the variable x assumes a value in the range $[x_1, x_2]$ can be calculated with the integral of the probability density distribution D_x in that range:

$$\%P_x(x_1, x_2) = 100 \int_{x_1}^{x_2} \frac{1}{\sigma\sqrt{2\pi}} e^{-\frac{(x-\mu)^2}{2\sigma^2}} \quad (5.2)$$

Another definition useful for further analyses is the cumulative distribution function $Q_x(x^*)$, which represents the probability that the variable x assumes a value less than or equal to a specific one [62]:

$$Q_x(x^*) = \int_0^{x^*} \frac{1}{\sigma\sqrt{2\pi}} e^{-\frac{(x-\mu)^2}{2\sigma^2}} \quad (5.3)$$

A good choice for the selection of the equivalent distribution parameters that approximate the behavior of the MTs is the one that uses as mean value the rated value obtained from the optimization of the variable ($\mu = x_r$) and as standard deviation one third of the maximum value of the tolerance ($\sigma = g/3$).

The deviation of each variable is different along the electrical steel laminations of the electrical machine. The performance of the machine is typically computed with the use of 2D models in order to reduce the computational burden, but with this type of analysis it is possible to simulate the effect of the MTs on only one electrical steel lamination: the effect of the stacked core must be considered.

Instead of using complex 3D FE models, it is possible to approximate the effect of the MTs on the stacked core by means of multiple 2D FE models. If the distribution D_{MT} is assumed for the laminations, the performance of a machine that considers all the laminations affected by the same MTs is D_p . Considering the real machine made by N_L laminations, it will present a performance distribution D_{p,N_L} . This last distribution will have a reduced variance with the same mean value compared to D_p : this is due to the averaging effects of the N_L samples.

If the number of laminations tends to infinity, or it is very large, the distribution D_{p,N_L} tends to be the mean value of D_p with a null variance.

All the distributions obtained by the different LMs have to be numerically compared between each other: for this purpose, it is useful to refer the results to a meaningful single value, but this is not easy to accomplish.

In order to achieve that, the cumulative distribution functions of the different performance under evaluation (Average Torque, Torque Ripple, etc.) are considered. Let's assume that T_{avg}^* , ζ^* and V_{ph}^* are the desired performance values of the average torque, of the torque ripple and of the phase voltage, respectively, and that they represent the terms of comparison for the different LMs; therefore, using the cumulative distribution, it is possible to define:

$$\begin{aligned} Q_{T,N_L}(T_{avg}^*) &= 1 - C \\ Q_{T,N_L}(\zeta^*) &= C \\ Q_{T,N_L}(V_{ph}^*) &= C \end{aligned} \quad (5.4)$$

where the constant C represents the probability for an output to guarantee the specific performance. This is an example of the possible performance that can be evaluated according to this method, but the designer can use other performance for the comparison of different LMs: this depends on the optimization strategy and on its constraints and objective functions.

By defining C as the Degree of Confidence (*DoC*) and claiming that the computed performance has a *DoC* equal to C , this indicates that the desired value is guaranteed for at least C cases over 100 (if it is expressed as a percentage). Therefore, if a C value is imposed, each cumulative distribution returns a numerical value for the performance (i.e. T_{avg}^* for the average torque) and this can be easily compared among the different LMs. A typical value for the *DoC* is 99.7% in the engineering process (3-sigma rule).

Another method to compare and to evaluate the robustness of a design respect to the MTs is the worst-case analysis: this consists in the search of the worst performance W_p in the neighborhood of the design using as limits the MTs. In order to have a robust design, the worst case should be the closest possible to the expected performance when the MTs are neglected. When different designs have to be compared (i.e. BLM and LMs), the project with the best worst-case is the most robust.

For the selection of the most robust design the statistical approach is preferred, but the worst-case method can be an additional way to evaluate the robustness of the design.

Figure 5.1 shows a comparison between the performance of a BLM (in blue) and of a LM (in orange) considering their distributions respect to the MTs. Nevertheless, the BLM has a better performance in the rated condition and, when the MTs are considered, its distribution has a higher variance reaching very low performance: the LM is a more robust design. This is only an example: in fact, it is possible that the BLM is also the most robust design.

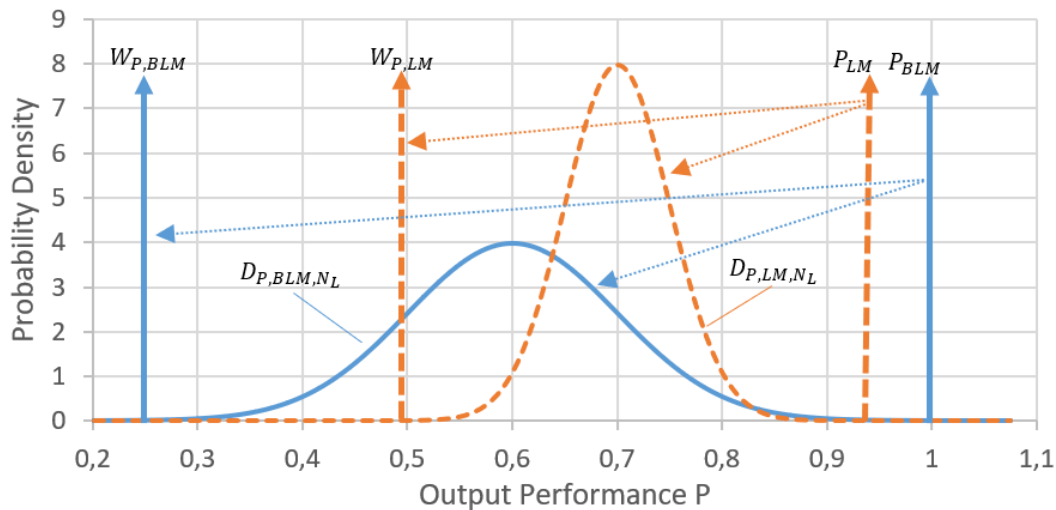


Figure 5.1: Effect of the MTs on the machine output performance P for the BLM design and for one LM design: design performance (P), distribution due to MTs (D) and worst-case due to MTs (W).

It is possible to better explain the described concepts with the help of a numerical example, which starts from the optimization of a SynRel and ends with the definition of the most robust design.

5.2 Preliminary Design Optimization

This example uses a reference SynRel with a fluid shaped rotor, which has been modeled in section 3.2.4. Table 5.1 presents the main motor data, the requirements used as constraints and the objective function for the optimization: these values will be used as base values for the rest of the discussion. The same number of poles, of slots and of rotor barriers of the example presented in subchapter 4.3 will be used, together with a similar power (around 800 W). This example will use a different motor type since the attention of the optimization will be focused on the minimization of the torque ripple, the output that is most affected by the MTs.

Table 5.1: Main motor requirements and data (Base values).

Requirements	Unit	Value	Requirements	Unit	Value
DC voltage	V	48	Actual length of steel in stack	mm	≤ 40
Rated power	W	800	Shaft diameter	mm	≥ 10
Rated torque	Nm	0.95	Airgap length	mm	≥ 0.5
Rated speed	rpm	8000	Pole pairs		2
Stator outer diameter	mm	≤ 115	Stator slots		36
Lamination thickness	mm	0.5	Lamination count max		≤ 80

The preliminary design has been obtained according to the equations presented in subchapter 4.1, the shape of the rotor is the same of Figure 3.9 while the stator variables are shown in Figure 5.2. The value and a brief description of the variables of the preliminary design are shown in Table 5.2.

Table 5.2: Independent design variables of the Preliminary Design (Base values).

Variable		Value	Variable		Value
D_F	Lower Slot Fillet	0.1 mm	F_8	Upper Fillet Fourth Barrier	3 mm
O_{SD}	Stator Outer Diameter	114 mm	O_{RD}	Rotor Outer Diameter	75.8 mm
S_L	Stack Length	41 mm	R_1	Position First Barrier	15.6 mm
S_H	Slot Height	11.5 mm	R_2	Position Second Barrier	23.5 mm
S_O	Slot Opening	1 mm	R_3	Position Third Barrier	30 mm
S_W	Slot Width	5.3 mm	R_4	Position Fourth Barrier	34 mm
T_{TA}	Tooth Tip Angle	3°	R_5	Shaft Radius	5 mm
T_{TD}	Tooth Tip Depth	1 mm	Rb_1	Rib Width First Barrier	0.5 mm
U_F	Upper Slot Fillet	0.1 mm	Rb_2	Rib Width Second Barrier	0.5 mm
δ	Airgap Length	0.5 mm	Rb_3	Rib Width Third Barrier	0.5 mm
F_1	Lower Fillet First Barrier	1.5 mm	Rb_4	Rib Width Fourth Barrier	0.5 mm
F_2	Upper Fillet First Barrier	0.5 mm	X_1	Width First Barrier	5.5 mm
F_3	Lower Fillet Second Barrier	0.5 mm	X_2	Width Second Barrier	4.75 mm
F_4	Upper Fillet Second Barrier	0.5 mm	X_3	Width Third Barrier	1.5 mm
F_5	Lower Fillet Third Barrier	0.5 mm	X_4	Width Fourth Barrier	1.35 mm
F_6	Upper Fillet Third Barrier	1 mm	X_5	Width Notch	1.3 mm
F_7	Lower Fillet Fourth Barrier	0.5 mm	I_{ph}	Phase Current	32 A

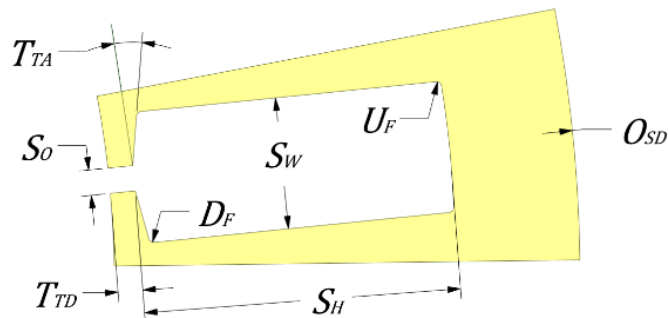


Figure 5.2: Stator slot geometry and related design variables.

Table 5.3 shows the performance of the preliminary design obtained by FE analyses. The preliminary design variables and its performance are used as base values for the presentation of further analyses.

Table 5.3: Preliminary design performance (Base values).

Performance		Value	Performance		Value
J_s	Current Density	2.1 A/mm ²	T_{avg}	Average Torque	0.9 mm
ζ	Torque Ripple	19%	V_{ph}	Phase Voltage	24 V

5.2.1 Sensitivity analysis

Before setting up the optimization, it is worth evaluating the impact of the tolerances on the preliminary design. It is possible to carry out a sensitivity analysis on all the independent variables in a range which is double the MTs one. For this case study, the maximum value for the MTs is set to 0.5 mm as representative of the different manufacturing processes for the size of the motor under analysis. The sensitivity analysis has two main advantages: firstly, it shows how the MTs, on each variable, affect the performance of the machine; secondly, it can help to select the independent design variables for the optimization. The following figures show the sensitivity analysis on each independent design variable and on the manufacturing factor, which affects the magnetic properties of the materials. The figures are displayed starting from the categories that are most affected by the MTs and ending with the least influenced ones.

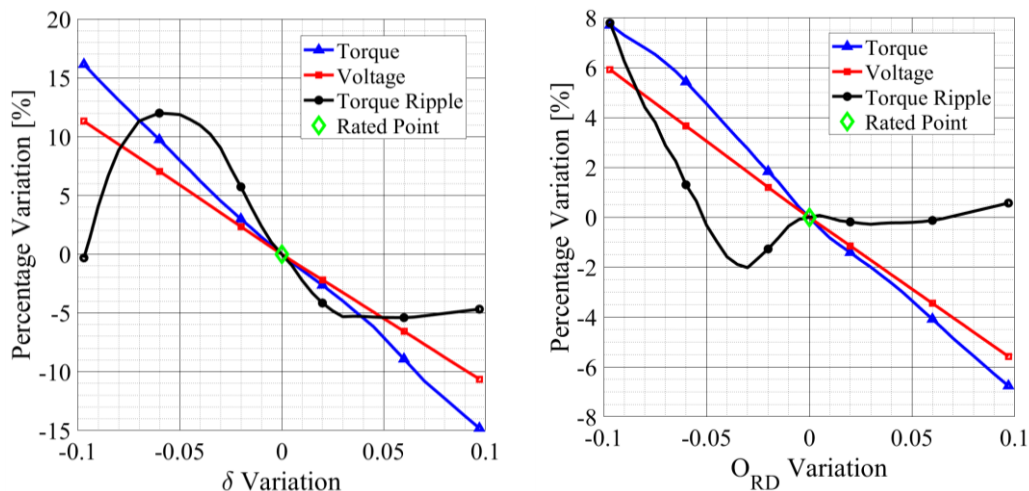


Figure 5.3: Sensitivity analysis on the airgap length (left) and the rotor outer diameter (right).

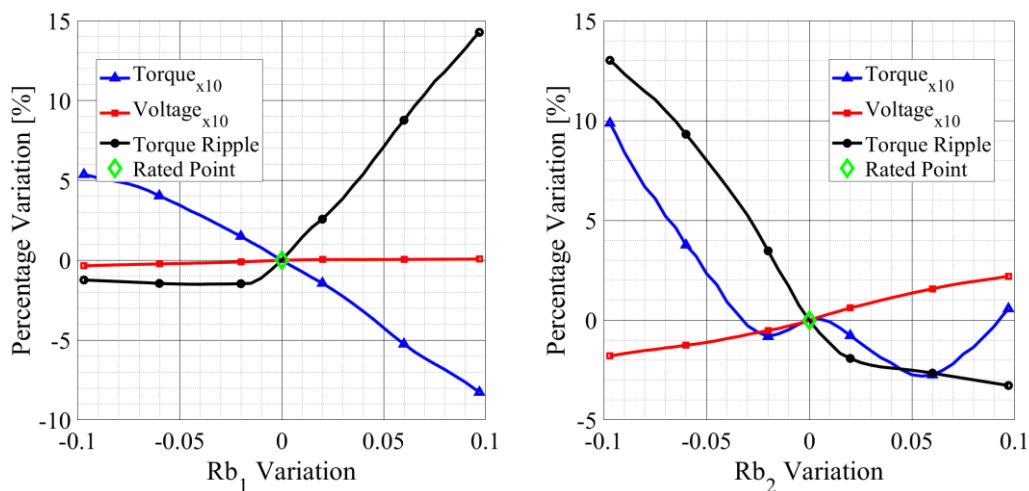


Figure 5.4: Sensitivity analysis on the ribs of the first (left) and of the second (right) barrier.

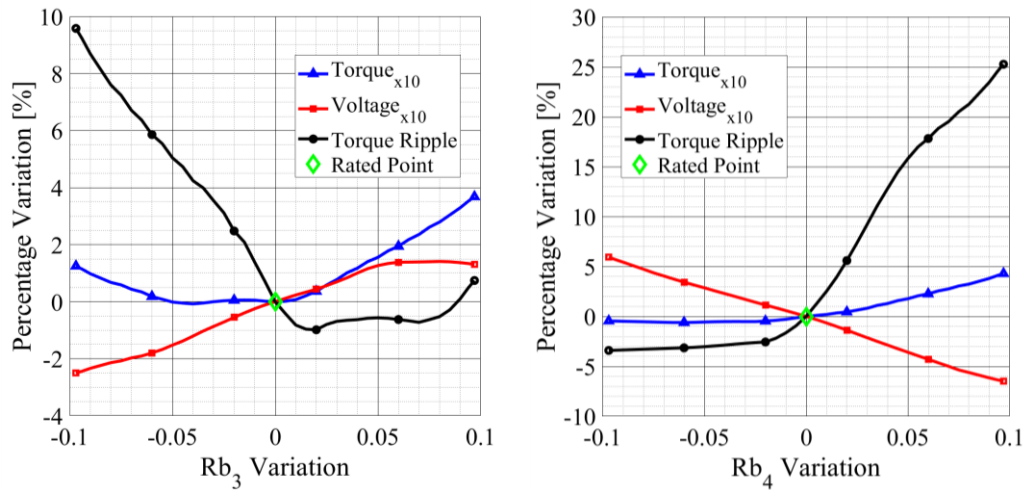


Figure 5.5: Sensitivity analysis on the ribs of the third (left) and of the fourth (right) barrier.

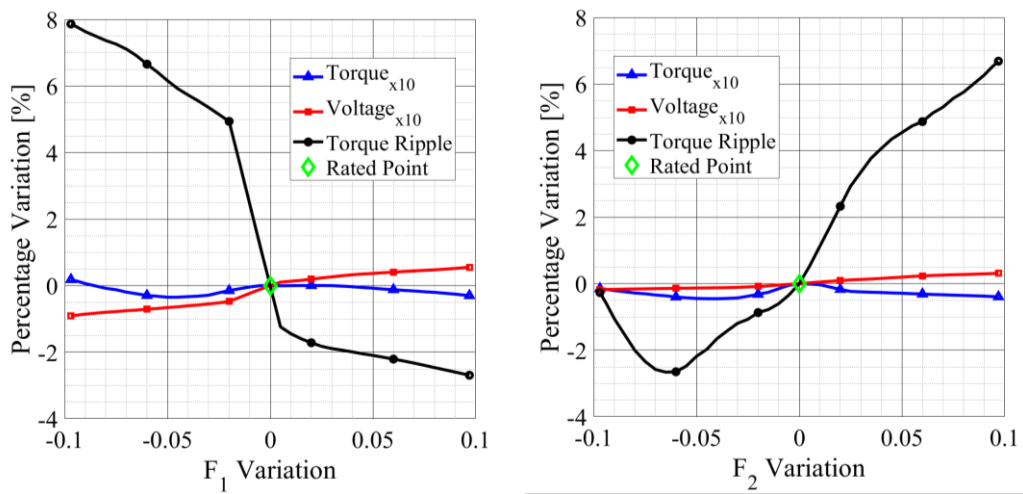


Figure 5.6: Sensitivity analysis on the lower (left) and on the upper (right) fillet of the first barrier.

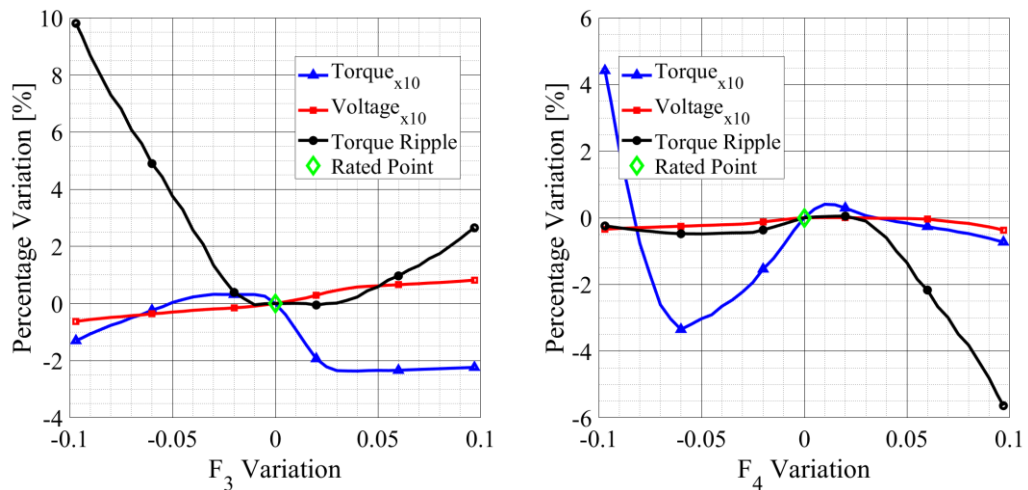


Figure 5.7: Sensitivity analysis on the lower (left) and on the upper (right) fillet of the second barrier.

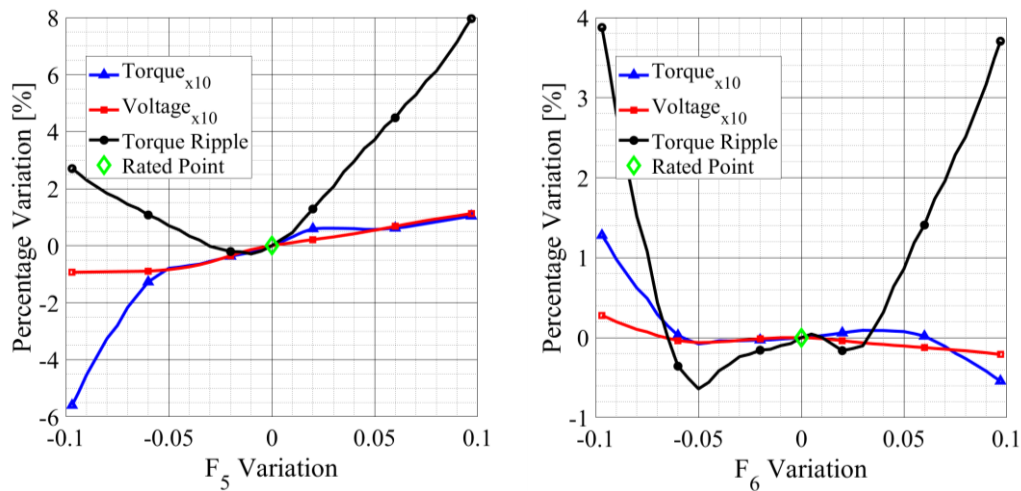


Figure 5.8: Sensitivity analysis on the lower (left) and on the upper (right) fillet of the third barrier.

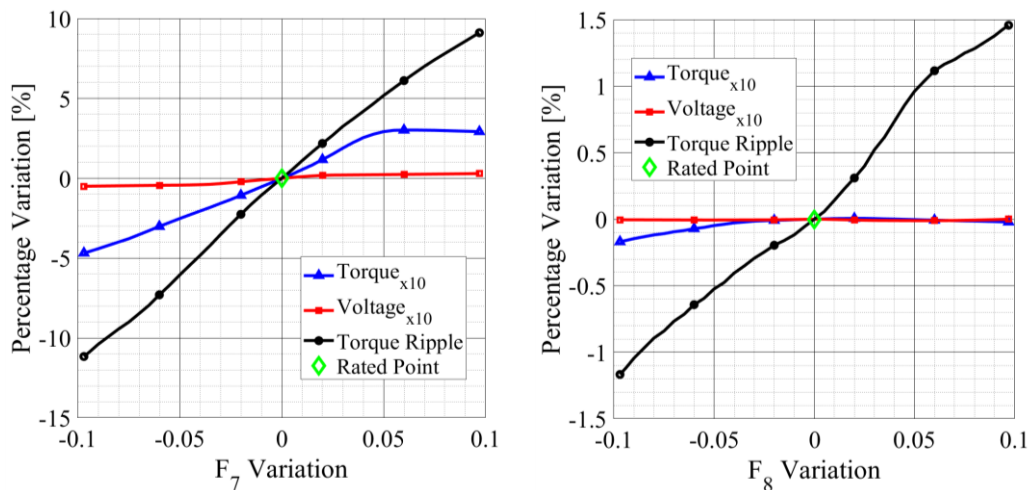


Figure 5.9: Sensitivity analysis on the lower (left) and on the upper (right) fillet of the fourth barrier.

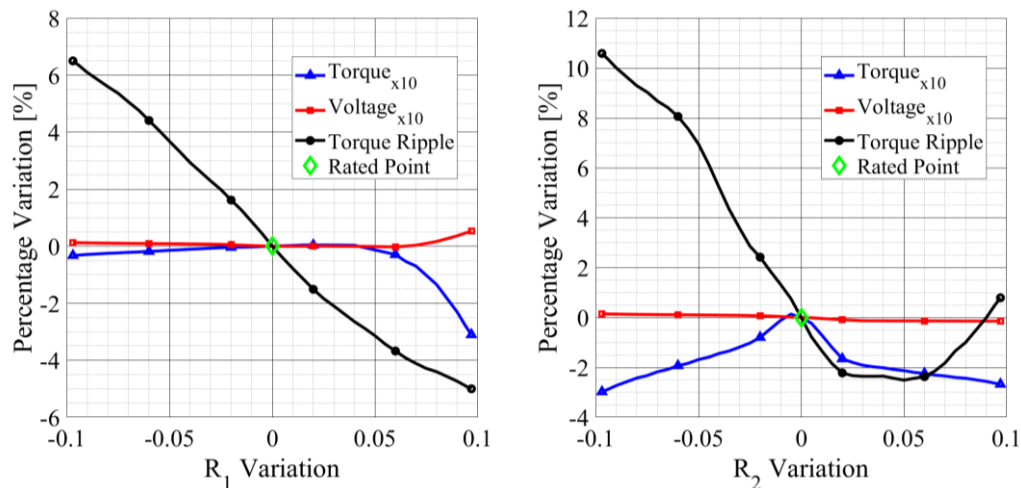


Figure 5.10: Sensitivity analysis on the position of the first (left) and of the second (right) barrier.

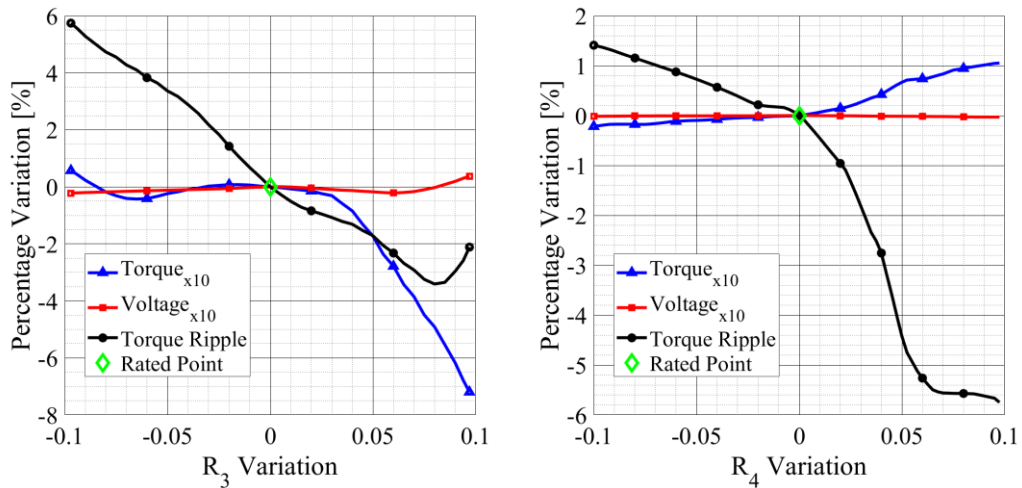


Figure 5.11: Sensitivity analysis on the position of the third (left) and of the fourth (right) barrier.

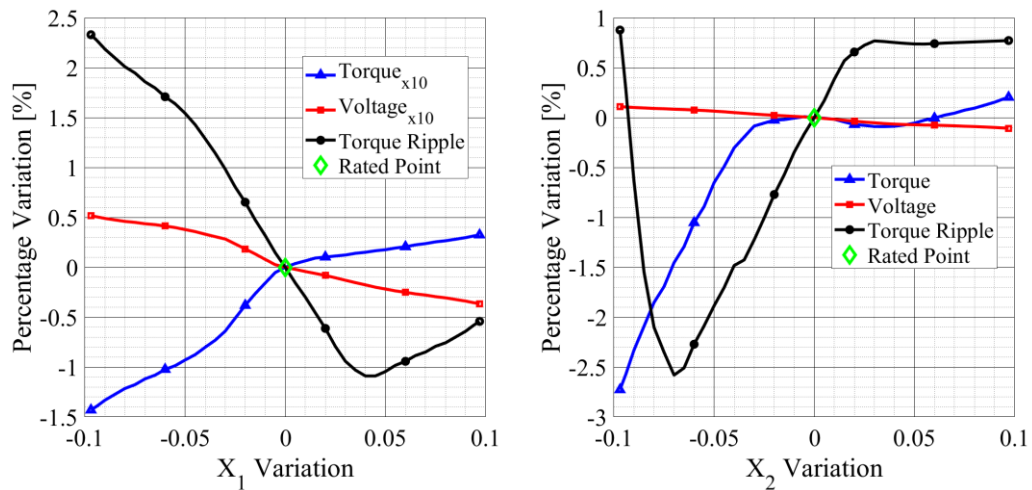


Figure 5.12: Sensitivity analysis on the width of the first (left) and of the second (right) barrier.

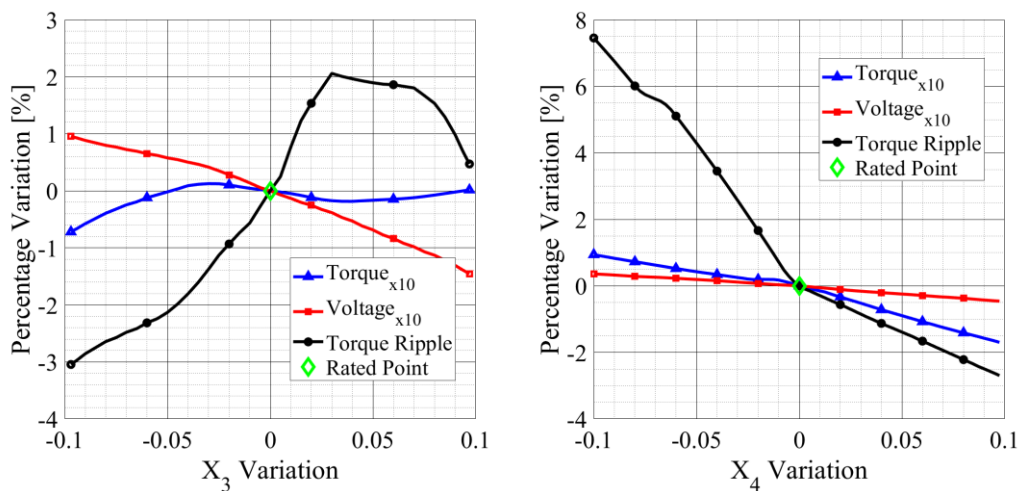


Figure 5.13: Sensitivity analysis on the width of the third (left) and of the fourth (right) barrier.

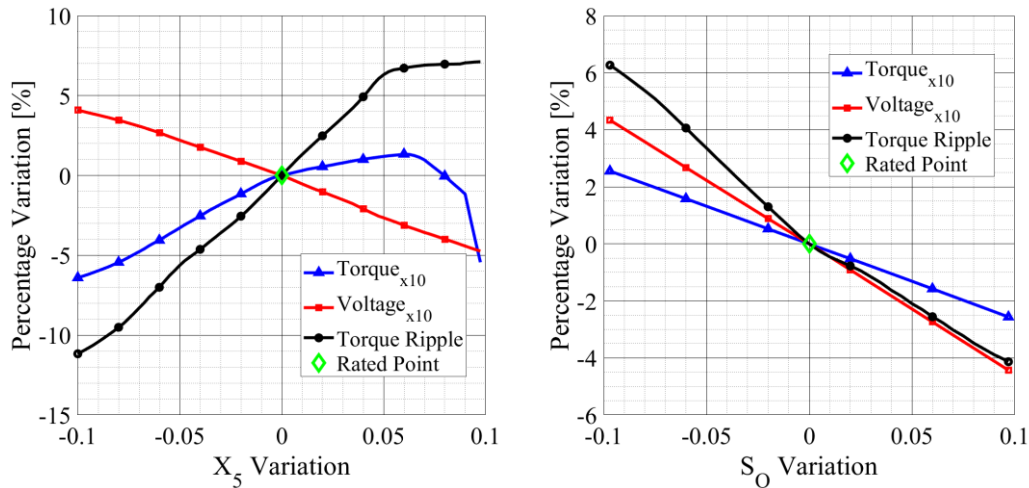


Figure 5.14: Sensitivity analysis on the width of the notch (left) and on the slot opening (right).

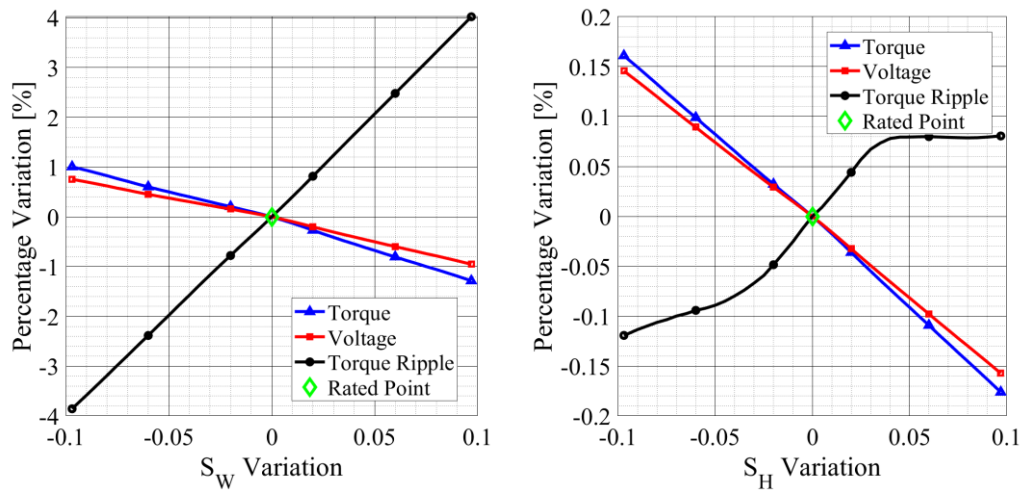


Figure 5.15: Sensitivity analysis on the slot width (left) and on the slot height (right).

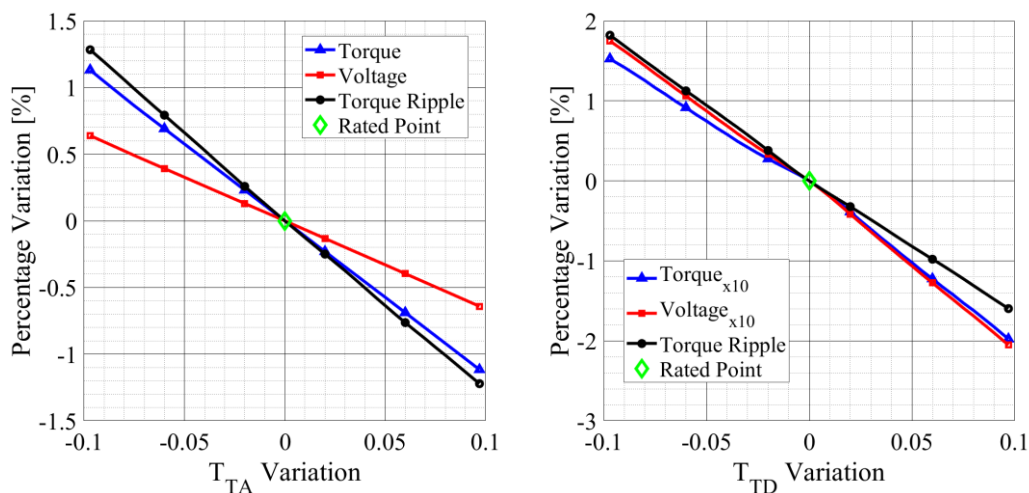


Figure 5.16: Sensitivity analysis on the tooth tip angle (left) and on the tooth tip depth (right).

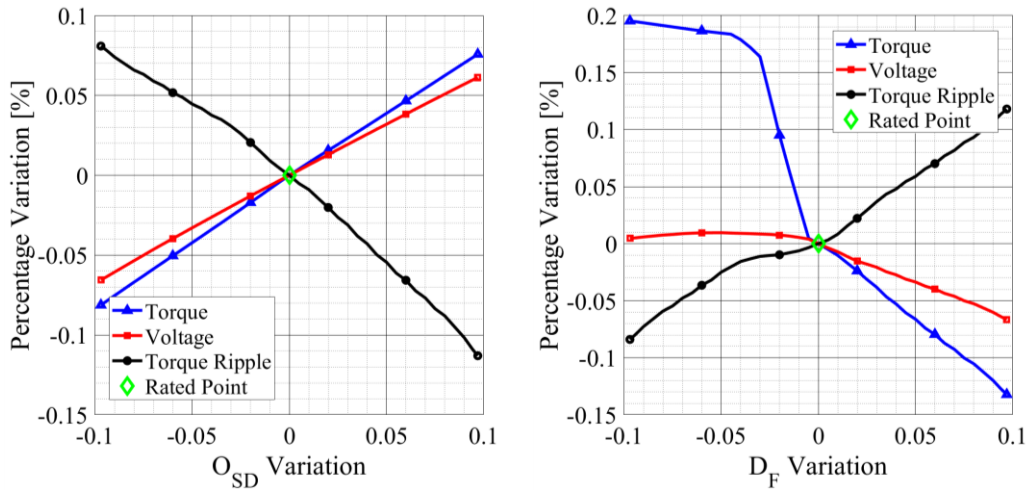


Figure 5.17: Sensitivity analysis on the stator outer diameter (left) and on the lower slot fillet (right).

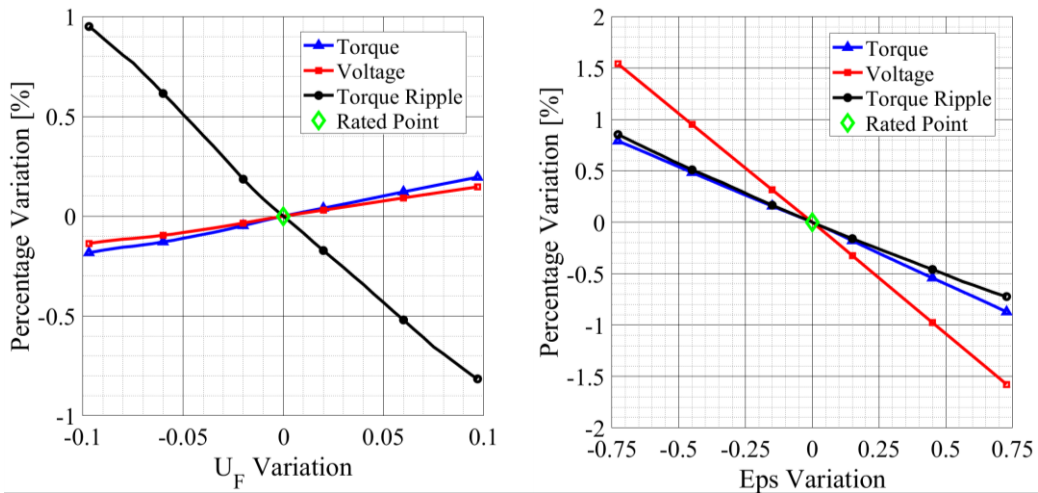


Figure 5.18: Sensitivity analysis on the upper slot fillet (left) and on the control angle (right).

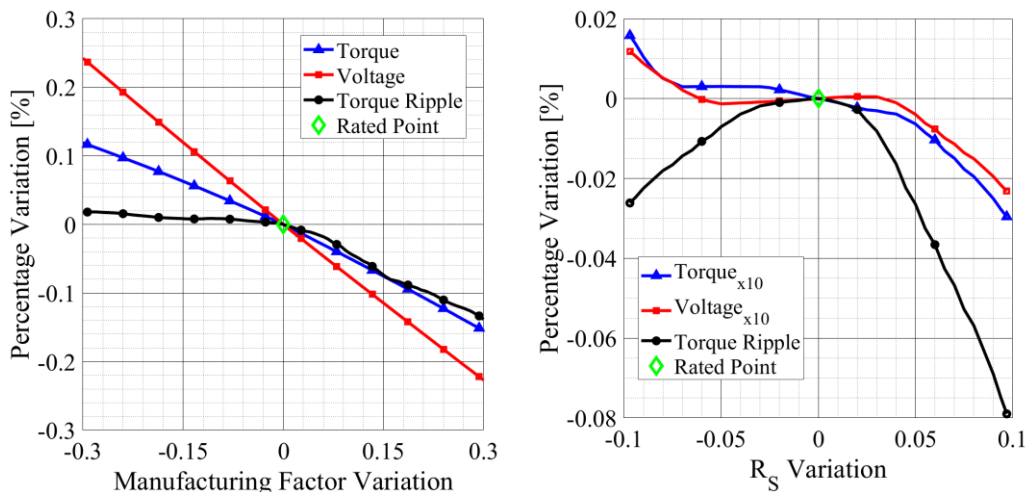


Figure 5.19: Sensitivity analysis on the manufacturing factor (left) and on the shaft radius (right).

The variables with the highest impact are the airgap length and the rotor outer diameter (Figure 5.3). The performance of the machine, in terms of phase voltage and average torque, decreases when the length of the airgap increases; therefore, this last variable can be fixed to the minimum possible, avoiding its use in the optimization. The same thing can be said for the rotor outer diameter, but this analysis is local and, with large variations of the rotor outer diameter, the performance of the machine can change a lot; moreover, the behavior of the performance is not decreasing, as shown in the figure. For this reason, the rotor outer diameter must be considered a design variable.

The second group of variables, in terms of sensitivity effects, are the ones of the radial ribs of each barrier (Figure 5.4 and Figure 5.5). The variation of the radial ribs, within a small range, mainly affect the value of the torque ripple of the machine. For large variations of these variables, it can be observed a reduction in the performance with the increase of their width caused by an increase of the q -axis inductance and by the cross-coupling. For this reason, these variables are set to the minimum possible according to the manufacturing process and to the mechanical integrity of the machine; hence, they are not used for the optimization. It is possible to carry out, after that the best project has been obtained, a new optimization with these types of variables, which affect the torque ripple in a local variation and that can be further minimized. The next group is composed by the lower and the upper fillets of the barriers (Figure 5.6, Figure 5.7, Figure 5.8, and Figure 5.9). The same goes for this group of variables. The fourth group is composed of the main variables of the rotor: the position (Figure 5.10 and Figure 5.11) and the width (Figure 5.12, Figure 5.13, and on the left in Figure 5.14) of the barriers. These variables, within a small range of variation, mainly affect the torque ripple of the machine, but with large variations they strongly influence the average torque and the torque ripple; therefore, they are selected for the design variables in the optimization.

The next group includes the stator and the control variables (on the right in Figure 5.14, Figure 5.15, Figure 5.16, Figure 5.17, and Figure 5.18). The slot opening is a very important variable in the optimization of the electrical machine, but if there is a strict limit imposed by the manufacturing process of the SynRel, the minimum value can be set in order to reduce the number of design variables. From the right in Figure 5.14 it is possible to see that, with the increase of the slot opening, the performance of the machine is reduced. The slot width (on the left in Figure 5.15) and the tooth tip angle (on the left in Figure 5.16), also within a small range variation, affect all the performance of the machine, while the slot height (on the right in Figure 5.15) and the current control angle (on the right in Figure 5.18) only influence the performance of the machine: these four variables are included in

the design variables. The tooth tip depth (on the right in Figure 5.16), the stator outer diameter (on the left in Figure 5.17) and the slot fillets (the lower is on the right in Figure 5.17 and the upper is on the left in Figure 5.18) have a lower influence compared to the one of the other variables: therefore, they are not selected for the optimization in order to reduce the variable number. To maximize the performance of the machine, the stator outer diameter has been set to the maximum value imposed by the constraints.

The last variables are the manufacturing factor (on the left in Figure 5.19) and the shaft radius (on the right in Figure 5.19). It is not possible to optimize with respect to the manufacturing factor because it only depends on the manufacturing process, while the impact of the variation of the rotor slot is minimum. However, the shaft radius is imposed according to the minimum value of the requirements in order to improve the performance of the machine.

Table 5.4 summarizes the results of the sensitivity analysis and it shows only the variables with a non-negligible sensitivity to the MTs.

Table 5.4: Summary of the sensitivity analysis.

Variable	Ripple	Torque	Voltage
δ	[-5÷12] % (M)	[-15÷16] % (H)	[-11÷11] % (H)
O_{RD}	[-2÷8] % (H)	[-6÷6] % (H)	[-7÷8] % (H)
Rb_1	[-2÷15] % (M)	[-0.8÷0.5] % (L)	[-0.05÷0.01] % (N)
Rb_2	[-3÷13] % (M)	[-0.3÷1] % (L)	[-0.2÷0.2] % (L)
Rb_3	[-1÷10] % (L)	[0÷0.4] % (N)	[-0.2÷0.16] % (L)
Rb_4	[-4÷25] % (H)	[-0.1÷0.5] % (L)	[-0.6÷0.6] % (M)
F_1	[-2.5÷8] % (L)	[-0.05÷0.02] % (N)	[-0.1÷0.05] % (N)
F_2	[-2.5÷7] % (L)	[-0.05÷0] % (N)	[-0.05÷0.05] % (N)
F_3	[0÷10] % (L)	[-0.25÷0.05] % (N)	[-0.05÷0.08] % (N)
F_7	[-11÷9] % (H)	[-0.5÷0.3] % (L)	[-0.05÷0.03] % (N)
R_1	[-5÷6.5] % (L)	[-0.3÷0] % (N)	[0÷0.05] % (N)
R_2	[-2÷10.5] % (M)	[-0.3÷0] % (N)	[-0.02÷0.02] % (N)
R_3	[-3.5÷6] % (L)	[-0.75÷0.05] % (L)	[-0.04÷0.05] % (N)
X_2	[-2.5÷1] % (N)	[-2.75÷0.25] % (M)	[-0.1÷0.1] % (N)
X_4	[-2.5÷7.5] % (L)	[-0.15÷0.1] % (N)	[-0.05÷0.05] % (N)
X_5	[-11÷7] % (H)	[-0.6÷0.1] % (L)	[-0.5÷0.4] % (L)
S_O	[-4÷6] % (L)	[-0.25÷0.25] % (L)	[-0.45÷0.45] % (L)
S_W	[-4÷4] % (L)	[-1.1÷1] % (M)	[-1÷0.8] % (M)
T_{TA}	[-1.25÷1.3] % (N)	[-1.1÷1.1] % (M)	[-0.6÷0.6] % (M)

The classification of the sensitivity of a design variable in function of its effects on the specific performance of the machine can be divided into: *High*, when the

specific performance is strongly affected by the MTs (H-red); *Moderate*, if the effect is relevant (M-blue); *Low*, if there is a minor effect, but this is still acceptable within the MTs (L-green); and *Negligible*, when there is not any relevant effect on the performance within the field of variation introduced by the MTs (N-black).

The sensitivity analysis will be useful in the search of the worst case in order to reduce the number of variables to be optimized; therefore, it is important to highlight the variables whose MTs have the highest impact on the torque ripple, on the average torque and on the phase voltage.

5.2.2 Individuation of different Local Minimums

In this example, a single-objective optimization has been adopted in order to simplify the optimization concept and investigate the aspects of the robust design; the objective consists in the minimization of the torque ripple δ . The average torque T_{avg} , the phase voltage V_{ph} and the current density J_s are set as constraints.

For each variable, a suitable range has been imposed and centered on the values of the preliminary design as a tradeoff between the design space and the number of iterations. Table 5.5 reports the design variables, their lower and upper limits and the chosen constraints for the optimization.

Table 5.5: Design Variables and Constraints (p.u.).

Variable	Limits (*)		Variable	Limits (*)	
	Lower Limit	Upper Limit		Lower Limit	Upper Limit
O_{RD}	0.9	1.1	X_3	0.5	1.5
S_W	0.6	1.4	R_3	0.8	1.2
S_H	0.65	1.35	X_4	0.5	1.5
X_1	0.5	1.5	R_4	0.85	1.15
R_1	0.7	1.3	X_5	0.5	1.5
X_2	0.5	1.5	T_{TA}	0.8	1.2
R_2	0.75	1.25	I_{ph}	0.85	1.25
			ε		
Constraints	Limits (*)		(*) All the quantities are referred to the preliminary design base values		
V_{ph}	<1				
J_s	<1				
T_{avg}	>1				

The optimization has been imposed with the use of seven starting points in order to have seven BLMs for further comparisons of the robustness of each design.

Table 5.6 reports the performance in terms of constraints and objective functions of the Preliminary Design and of seven Local Minimums (LMs); the project with the minimum value of the objective function is defined as Best Local Minimum (BLM).

Table 5.6: Constraints and Objective Function for the different projects (p.u).

Project	Ripple	Torque	Voltage	Current Density
Preliminary (P)	1.000	1.000	1.000	1.000
Best Local (BL)	0.2804	1.2031	0.9847	0.9777
Local 1 (L1)	0.2873	1.1852	0.9765	0.9896
Local 2 (L2)	0.2898	1.0859	0.9476	0.9422
Local 3 (L3)	0.2955	1.1417	0.9617	0.9708
Local 4 (L4)	0.3129	1.2072	0.9999	0.9993
Local 5 (L5)	0.3134	1.1385	0.9579	0.9708
Local 6 (L6)	0.3193	1.1285	0.9473	0.9708

All the optimized designs satisfy the constraints and, therefore, the requirements while having a reduced torque ripple compared to the preliminary design one. They also have a little higher average torque and similar values of current density and phase voltage. As an example, Figure 5.20 and Figure 5.21 show the cross section and the magnetic flux density of the preliminary design and of the BLM.

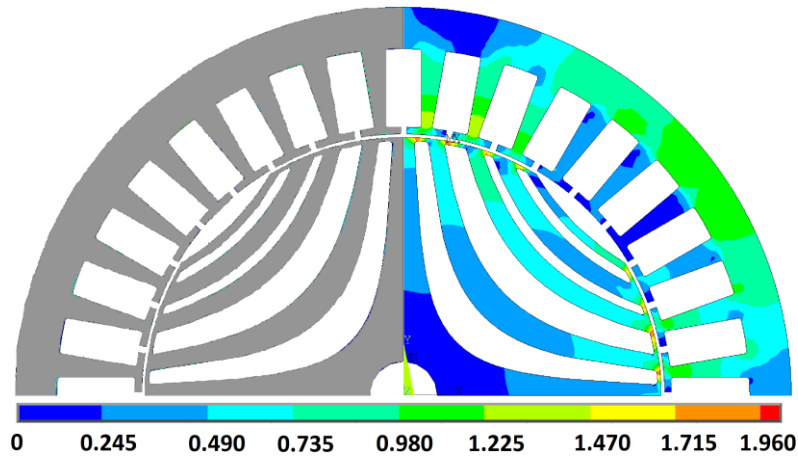
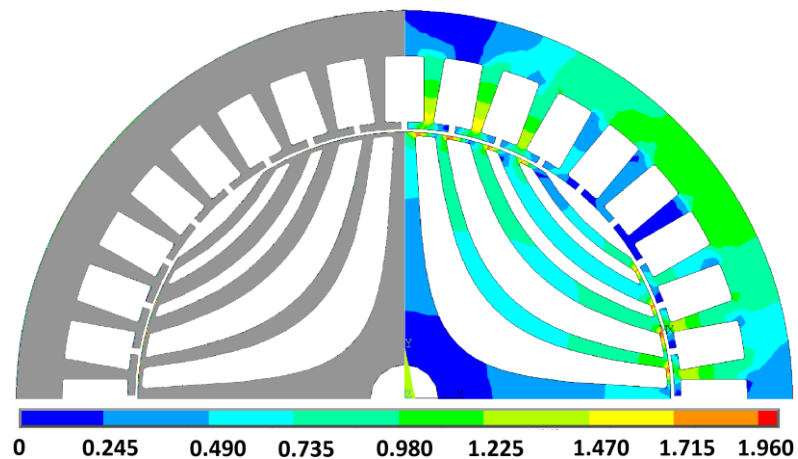
**Figure 5.20: Shape and magnetic flux density [T] at the rated power of the preliminary design.****Figure 5.21: Shape and magnetic flux density [T] at the rated power of the BLM.**

Figure 5.22 shows a comparison between the preliminary design and all the optimized ones in terms of rotor shape.

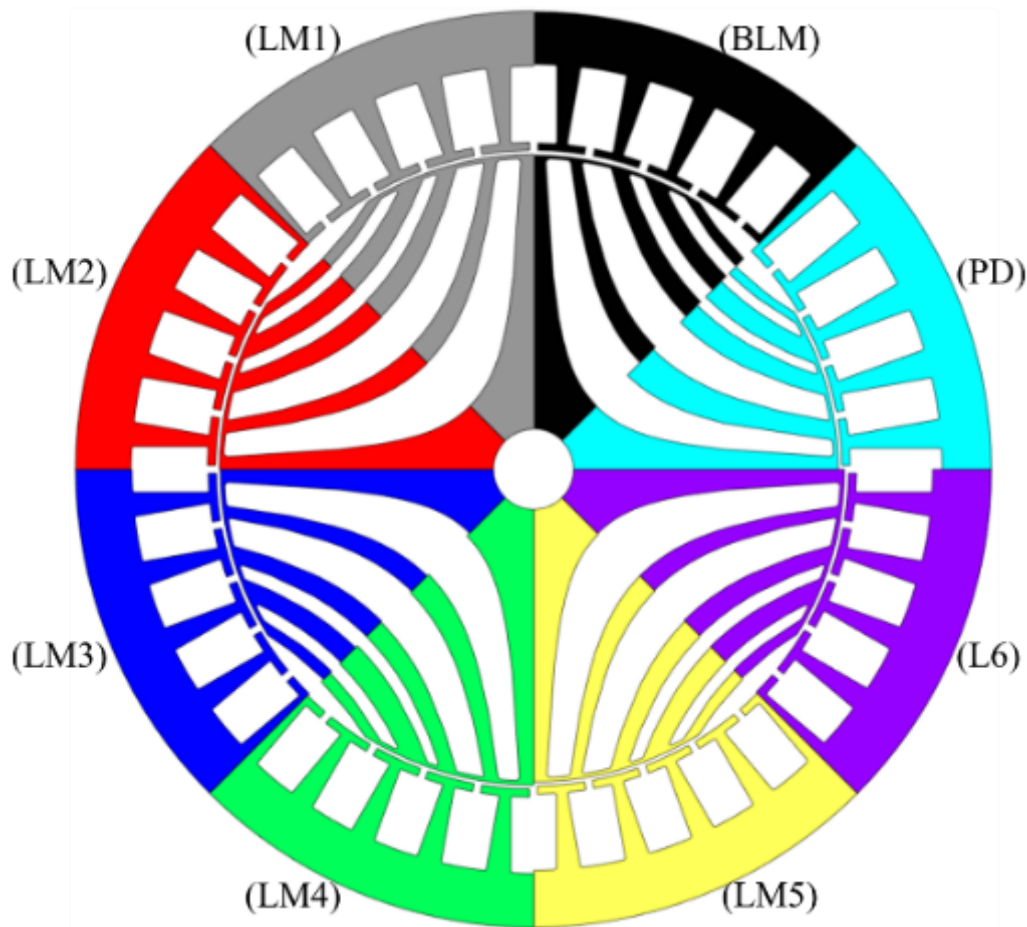


Figure 5.22: Comparison between the preliminary design (PD), the BLM design and the six LM designs (LM1, LM2, LM3, LM4, LM5, LM6).

After that the BLM has been identified and to conclude the optimization procedure (following the typical design flow), the performance validation has to be carried out; this includes the possible effects of the materials and of the manufacturing tolerances on the performance evaluation with the definition of proper coefficients aiming to improve the *DoC* of the project.

The experience of the designer is the key to the proper selection of the most suitable coefficients for a good approximation of the manufacturing effects.

The next subchapter presents and discusses a statistical method to take into account the effects of the MTs on the machine performance modification (typically, there is a degradation of the performance when an optimized design is considered).

5.3 Statistical Performance Analysis

In order to evaluate the effect of the MTs, a statistical tolerance analysis has been carried out with the adoption of the Monte Carlo method [63] coupled with a 2D FE analysis.

According to subchapter 5.1, the distribution of the MTs can be associated to a normal distribution: $D_{MT} = N(\mu, g/3)$; to perform the Monte Carlo method, the distribution is applied to each variable and, from this distribution, one value is carried out. After that each variable value is defined, it is possible to perform a FE analysis in order to evaluate the performance of the machine. The statistical distribution of each performance D_p due to the MTs is computed by repeating the procedure for a relevant number of samples. In this case, the procedure is repeated over a batch of 2000 machines and this requires the same number of FE calls.

The procedure is applied on each optimized design: the BLM and the LMs, for a total of 7x2000 FE analyses.

Since the dimensions are slightly modified by the MTs, the exact geometry of the BLM design is rarely achieved as well as its performance; therefore, the distribution presents a great variance. This large variation is mainly due to the performance computation of each FE analysis, considering that the machine is realized with identical laminations, each of which is affected by the MTs in the same way.

It follows that this distribution is not representative of the machine performance because the effect of the stacked core, in which the laminations are different and the effect of the MTs on each lamination is different, needs to be considered. The effect of the stacked core is an averaging effect that reduces the variance of the distribution.

In order to consider this effect, a subset of different machine performance equal to the motor lamination counts ($N = 80$ laminations) has been selected and the machine performance has been computed by averaging the performance of each lamination. This expedient is particularly useful to avoid the use of a complex 3D FE analysis, reducing a lot the computational burden.

Figure 5.23 shows the statistical distribution of the torque ripple, used as an example, of the BLM design affected by the MTs in a lamination and by the averaging effect of the laminated core. The resulting effect of the stacked core on the performance distribution is a reduction of the variance maintaining the same mean value.

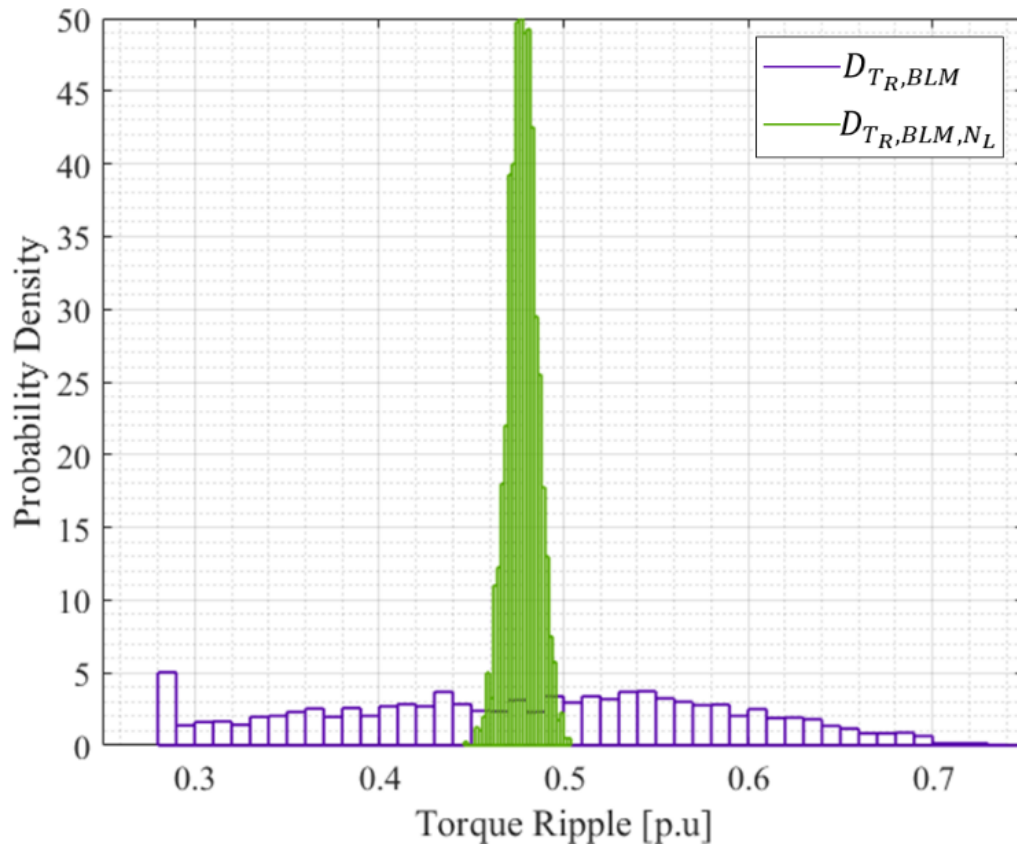


Figure 5.23: Statistical distribution of the torque ripple of the BLM design affected by the MTs in a lamination and the averaging effect of the stacked core.

This averaging effect, shown in Figure 5.23, has two meaningful results: the mean performance is quite different from the one computed in the rated condition ($\delta_{BLM}=0.28$) and the distribution of the stacked machine is representable as a normal distribution.

The same analysis has been carried out also for the LMs but, in Figure 5.24, only the results of the stacked core have been reported. For every optimized design, the mean value of the distributions is different from the rated one. Some projects have a value closer to the rated one (LM3 and LM5): these projects are probably the best candidates that could have the more robust design.

If a higher number of laminations is considered, the mean values of the distribution remain the same but the variance is reduced. Reducing the variance, it is simple to define the most robust candidates (LM3 and LM5); otherwise, the cumulative distribution has to be used. Figure 5.25 and Figure 5.26 show the statistical distribution of the average torque and of the phase voltage, respectively, for the optimized designs. In this performance, the mean value of the distribution is closer to the rated performance one: as shown in the sensitivity analysis, the MTs strongly affect the torque ripple instead of the average torque and of the phase voltage.

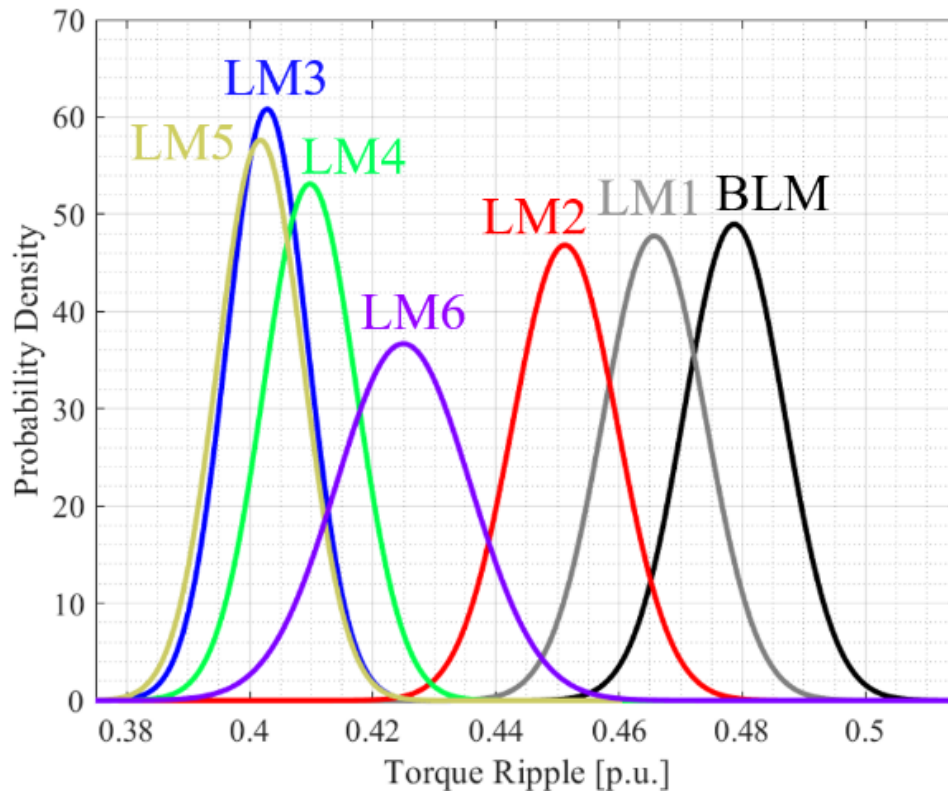


Figure 5.24: Statistical distribution of the torque ripple of the Best Local Minimum (BLM) and of the six Local Minima (LMs) considering the stacked machine affected by the MTs.

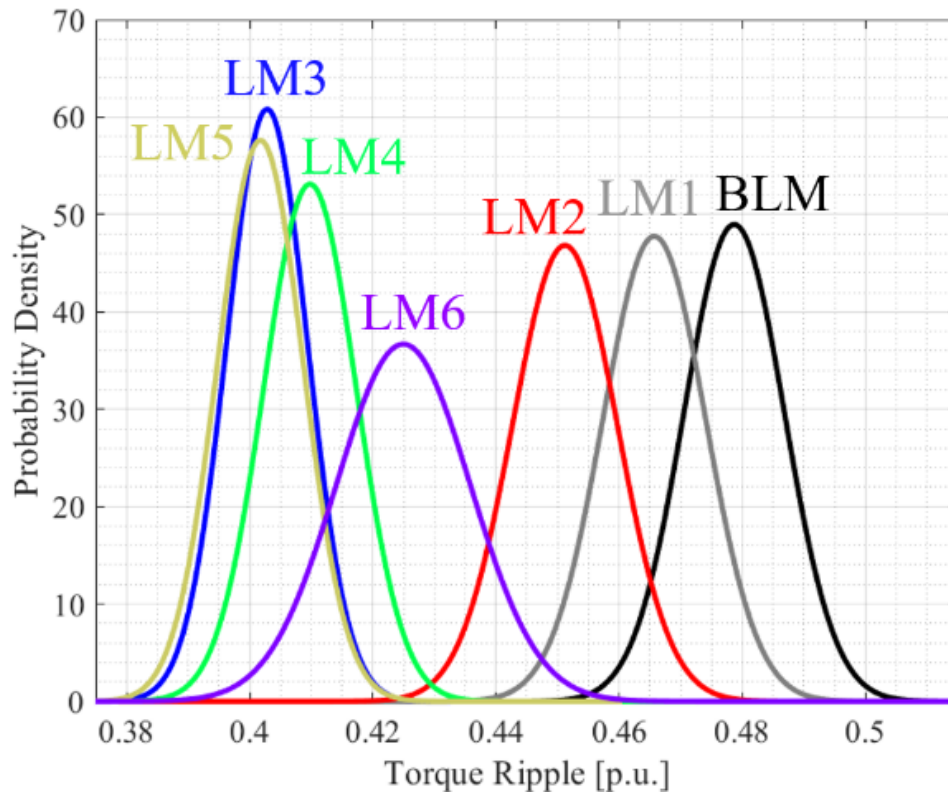


Figure 5.25: Statistical distribution of the average torque of the Best Local Minimum (BLM) and of the six Local Minima (LMs) considering the stacked machine affected by the MTs.

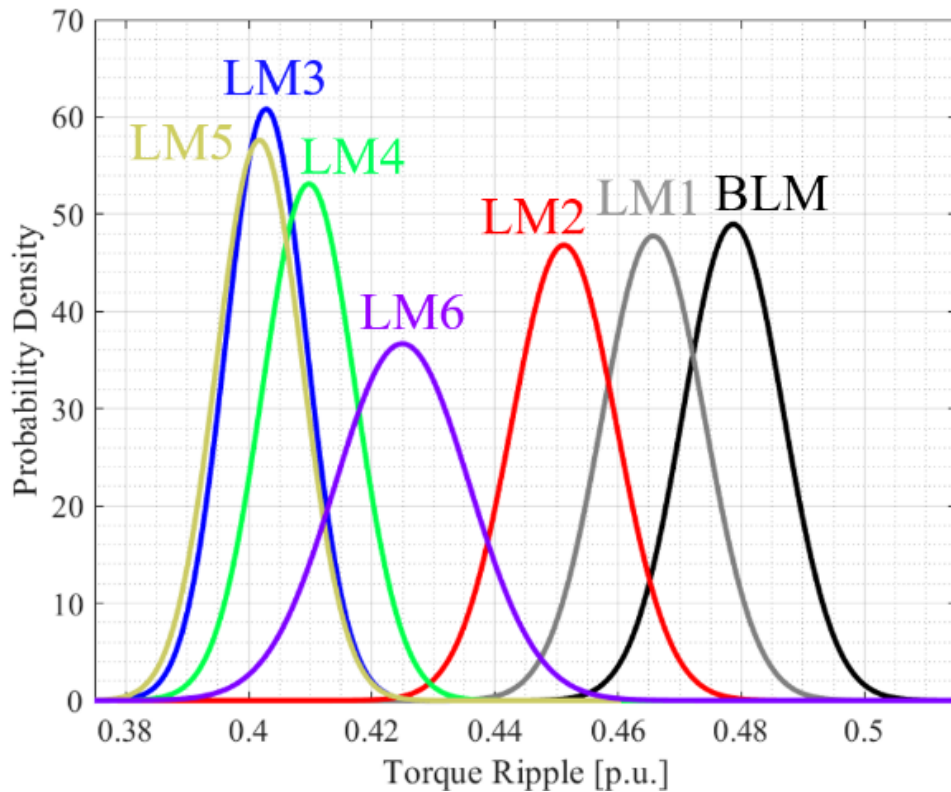


Figure 5.26: Statistical distribution of the phase voltage of the Best Local Minimum (BLM) and of the six Local Minimums (LMs) considering the stacked machine affected by the MTs.

As explained in subchapter 5.1, in order to compare the different distributions obtained by the different designs, the cumulative distribution and the degree of confidence DoC have to be introduced. The numerical comparison can be achieved through (5.4).

This expression can be graphically obtained with the interception of the horizontal line with a C value and the cumulative distribution.

The cumulative distribution functions of the torque ripple (Q_{ζ, N_L}), of the average torque ($Q_{\zeta, T_{avg}}$) and of the phase voltage ($Q_{V_{ph, N_L}}$) are reported in Figure 5.27, Figure 5.28, and Figure 5.29, respectively.

It is worth noting that the LM4 design does not satisfy the voltage constraint anymore (the rated value was of 0.9999) with a probability higher than 99.7% (3 sigma-rule) and that it can be therefore discarded. Furthermore, from the figures it appears clear that the most robust designs are LM3 and LM5 with a similar value. When this occurs, it is possible to refer to a value of a constraint (i.e. average torque) to guide the choice. Otherwise, a more rigorous approach featuring the adoption of a multi-objective optimization must be used.

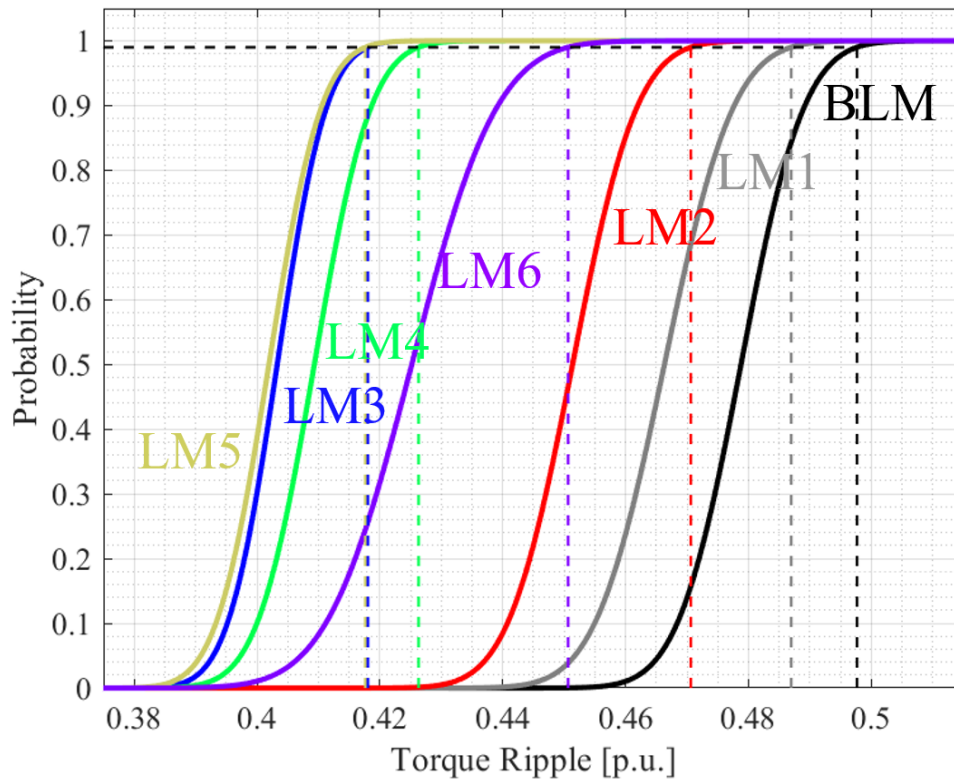


Figure 5.27: Cumulative distribution of the torque ripple of the Best Local Minimum (BLM) and of the six Local Minima (LMs) considering the stacked machine affected by the MTs.

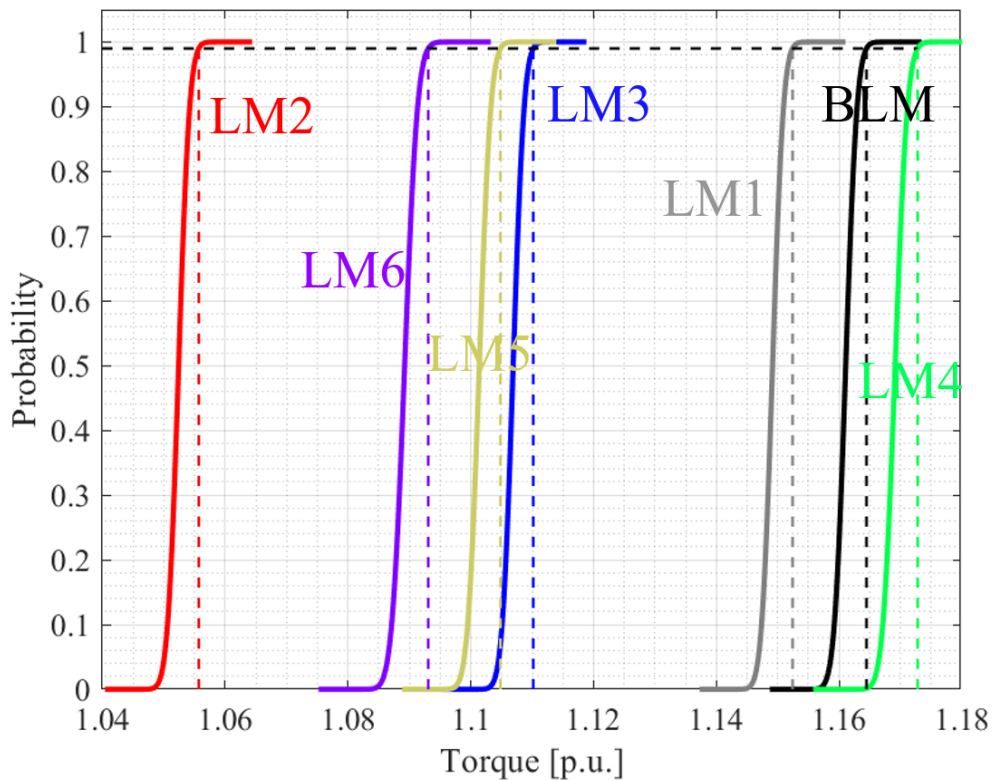


Figure 5.28: Cumulative distribution of the average torque of the Best Local Minimum (BLM) and of the six Local Minima (LMs) considering the stacked machine affected by the MTs.

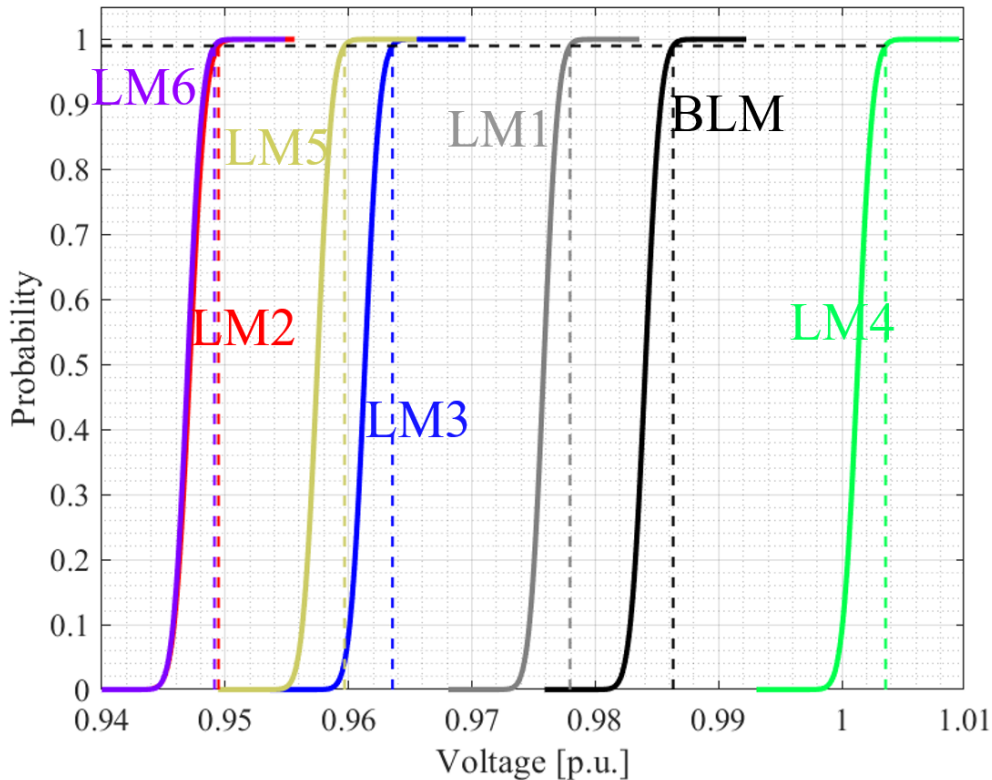


Figure 5.29: Cumulative distribution of the phase voltage of the Best Local Minimum (BLM) and of the six Local Minimums (LMs) considering the stacked machine affected by the MTs.

The numerical results of the statistical tolerance analysis of the different projects are shown in Table 5.7 to better compare the projects between each other.

Table 5.7: Results of the Statistical Tolerance Analysis of the different projects (p.u.).

Project	Ripple (ζ^*)	Torque (T_{avg}^*)	Voltage (V_{ph}^*)
Best Local (BL)	0.4973	1.1577	0.9862
Local 1 (L1)	0.4866	1.1460	0.9781
Local 2 (L2)	0.4705	1.0491	0.9494
Local 3 (L3)	0.4179	1.1037	0.9635
Local 4 (L4)	0.4281	1.1653	1.0025
Local 5 (L5)	0.4175	1.0979	0.9596
Local 6 (L6)	0.4505	1.0855	0.9490

From the numerical results and from the previous considerations, the project LM3 would be preferable to the LM5 one because they have a similar torque ripple but the first one has a higher average torque.

Therefore, the choice of the most robust design considering the statistical performance analysis is LM3, but both LM3 and LM5 are selected as robust candidates for a comparison in further analyses: in fact, the worst-case analysis is presented in the next subchapter.

5.4 Worst-Case Analysis

A further approach for the selection of the robust design candidates is the search of the worst-case performance: the candidate with the best one will be the most robust. In order to simplify the research, a sensitivity analysis on the BLM and on each LM has been carried out in order to obtain the information on the variable effects on the performance. The results are similar to the ones obtained by the preliminary design and, therefore, they are not presented.

In this case, the worst-case is verified when a constraint is not satisfied or in the point with the maximum torque ripple according to the criteria of the optimization.

From the independent design variables, only a set of meaningful ones has been chosen for the search of the worst-case: hence, the variables that have at least a performance with a high or a moderate impact or the ones with a low impact in all the performance have been chosen.

Table 5.8: Variables used in the search of the worst case and their limits.

Variable	Starting value	Lower limit	Upper limit
δ	Rated value	Rated value-0.5 mm	Rated value+0.5 mm
O_{RD}	Rated value	Rated value-0.5 mm	Rated value+0.5 mm
Rb_1	Rated value	Rated value-0.5 mm	Rated value+0.5 mm
Rb_2	Rated value	Rated value-0.5 mm	Rated value+0.5 mm
Rb_4	Rated value	Rated value-0.5 mm	Rated value+0.5 mm
F_7	Rated value	Rated value-0.5 mm	Rated value+0.5 mm
R_2	Rated value	Rated value-0.5 mm	Rated value+0.5 mm
X_2	Rated value	Rated value-0.5 mm	Rated value+0.5 mm
X_5	Rated value	Rated value-0.5 mm	Rated value+0.5 mm
S_O	Rated value	Rated value-0.5 mm	Rated value+0.5 mm
S_W	Rated value	Rated value-0.5 mm	Rated value+0.5 mm
T_{TA}	Rated value	Rated value-0.5 mm	Rated value+0.5 mm

The starting point of the worst-case search is the rated value of each minimum, while the limits are in the range of the MTs.

The total number of variables is twelve, lower than the one used in the optimization, and the range of variation is much lower; for this reason, the required number of iterations for the search of the worst-case is lower than the one for the optimization.

Table 5.9 shows the results obtained by the search of the worst-case for all the minimums. The worst torque ripple for each design is much higher than both the one computed for the rated condition (when the MTs are neglected) and for the indicator obtained by the statistical tolerance analysis. This is due to two main

reasons: first of all, the distribution of the torque ripple has a large variance and, in the worst-case search, the laminations of the stacked are supposed to be the same. Therefore, the worst-case is very unlikely: it practically never occurs, because the averaging effect of the stacked core improves the torque ripple performance.

It is worth noting that the value of the average torque is higher than the one obtained for the rated condition and for the indicator obtained by the statistical tolerance analysis; this can happen in the worst-case search because the target is the maximization of the torque ripple. The torque ripple and the phase voltage have an impact only if the constraints are not satisfied.

Table 5.9: Results of the Worst-case Analysis of the different projects (p.u).

Project	Ripple (ζ)	Torque (T_{avg})	Voltage (V_{ph})
Best Local (BL)	0.9979	1.2452	1.0299
Local 1 (L1)	0.6999	1.2624	0.9985
Local 2 (L2)	0.9046	1.1191	0.9923
Local 3 (L3)	0.9170	1.1949	1.0117
Local 4 (L4)	0.6975	1.2660	1.0401
Local 5 (L5)	0.7009	1.0402	0.9125
Local 6 (L6)	0.8555	1.1054	0.9488

Three projects (BLM, LM3, and LM4) no longer match the phase voltage constraint and they can be, as a consequence, discarded from the robust candidates. The projects LM1 and LM5 present the best worst-cases (their value is similar) and both of them are selected as robust candidates according to the worst-case analysis.

Even this method provides two projects with very similar torque ripples and the selection of one of them can be carried out considering the values of the constraints. LM1 ensures a higher value of the average torque compared to the one of LM5 and, for this reason, it is selected as the best design through this kind of analysis.

5.5 Selection of the Robust Design

The methods for the selection of the most robust design have been presented: they are the statistical tolerance analysis and the worst-case analysis. The candidates for these analyses have been obtained through an optimization procedure. The candidates, when the MTs are neglected, present similar values of the performance: the next step consists in the selection of the most robust design augmented by the obtained information.

The statistical tolerance analysis is able to compute the distribution of the performance for a batch of machines and, subsequently, it allows to obtain the value of the performance, which is guaranteed despite the presence of the MTs with a C

probability. Therefore, the designer accepts that, for a manufactured batch of machines, there is a probability equal to $(1-C)$ to have machines that do not satisfy the declared values $(\zeta^*, T_{avg}^*, V_{ph}^*)$.

The worst-case approach, differently, is a more severe evaluation in which the performance of the machine is computed for a very unlikely condition but, without considering the errors of the FE analyses, the manufactured machine will have performance values higher than or equal to the declared ones.

The choice of the preferred method depends on the application or on the designer considerations. The designers can adopt one of the presented methods depending on their specific needs. However, the best solution consists in the choice of a main method and in the use of the other one when the preferred method provides some robust design candidates with very similar performance.

From the discussion it appears that the most promising method, which better approximates the manufactured machine, should be the statistical approach, while the worst-case one could be useful for a last comparison between the designs with similar performance from the first method results.

Table 5.10 summarizes the results obtained by all the design steps; considering both the statistical analysis and the worst-case one, the project LM5 has been selected as the most robust design. The statistical analysis reports a torque ripple about 50% higher than the one of the BLM ideal design, but it is guaranteed for 99.7% of the manufactured machines.

Table 5.10: Results from all the design steps (p.u.).

Project	Ripple (ζ, ζ^*)	Torque (T_{avg}, T_{avg}^*)	Voltage (V_{ph}, V_{ph}^*)	Robust
Optimization				
Preliminary (P) (no tolerances)	1.0000	1.0000	1.0000	/
Best Local Minimum (BLM) (no tolerances)	0.2804	1.2031	0.9847	/
Statistical Analysis				
Local 3 (LM3)	0.4179	1.1037	0.9635	Best
Local 5 (LM5)	0.4175	1.0979	0.9596	Robust
Worst-case Analysis				
Local 1 (LM1)	0.6999	1.2624	0.9985	Best
Local 5 (LM5)	0.7009	1.0402	0.9125	Robust

Figure 5.30 summarizes the proposed procedure for the selection of the most robust design between the results of the optimization steps. The number of minimums of the first optimization can be changed reducing the computational burden of the procedure. It is worth noting that the sensitivity analysis could be carried out for the

local minimums or only for the preliminary design; in the last case, it can be executed in parallel to the first step of the optimization (which is the search of the starting points of the local minimums). The seven local optimizations can be carried out in a parallel way if the computer is able to start all these computations; this is also true for the statistical performance analysis and for the worst-case analysis.

The figure also shows the execution time for each method: the process is computationally intensive; however, by adopting a modern multicore desktop PC (i9-9980XE 18-cores processor, 3GHz 32GB RAM), a single FE call requires about 90 seconds (this strongly depends on the saturation conditions) and up to 7 FE analyses can be carried out in parallel within 120 seconds.

The entire method, considering the sensitivity analysis both for the preliminary design and for the minimum ones, requires a total time of about 240 hours (10 days).

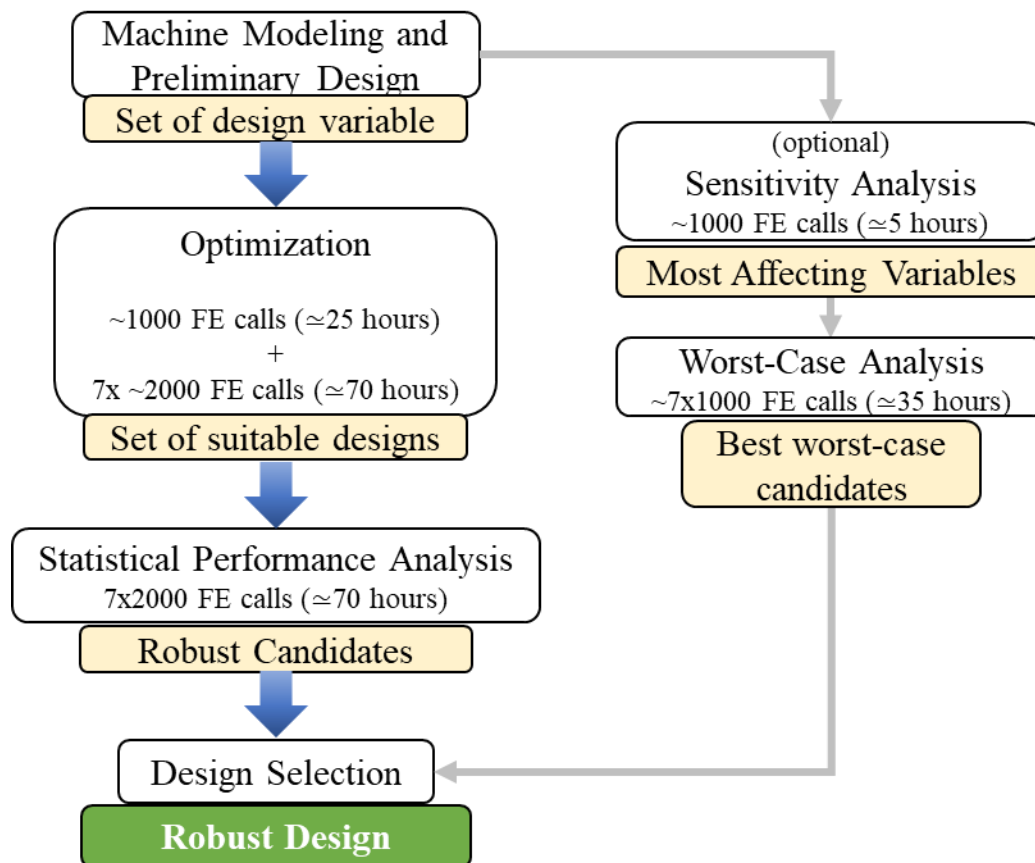


Figure 5.30: Proposed flow for the robust design selection.

The proposed procedure is generalizable towards different types of electrical machines referring to the related models and variables.

The problem that may arise is the following one: from the statistical tolerance analysis, in presence of the MTs and imposing the *DoC*, any design can satisfy the constraints. If the *DoC* is imposed as well as the manufacturing process (and the

MTs as a consequence), it is possible to make these constraints tighter before performing the first optimization step. The constraints may be iteratively changed until the statistical tolerance analysis is able to define at least one design that satisfies the constraints. Since the entire process is temporally intensive, the suggestion is to tighten up the constraints from the first optimization; if a constraint is satisfied with a limited deviation from the constraint itself (i.e. LM4 with a constraint of the phase voltage equal to 0.9999), after the statistical tolerance analysis it is almost certain that the constraints will not be satisfied.

The further step in order to improve the methodology is an effective integration of the statistical tolerance and worst-case analyses within the optimization algorithm, being this one a future development of the proposed procedure.

Chapter 6

Asymmetric rotors for torque ripple reduction

Part of the work presented in this chapter has been previously published in [7], [12]

The torque ripple is one of the major drawbacks of the SynRel and it causes additional stress on the bearings (reducing their lifetime), additional acoustic noise and vibrations.

In literature, there are some methods for the reduction of the torque ripple; the simplest one uses the skewing regardless of a mean torque reduction. Another technique consists in the minimization of the torque with an optimization procedure, which is discussed in subchapter 6.1. This solution has a limit in the minimization caused by the particular shape of the SynRel; this limit becomes more relevant in the flux-weakening region, where a high current control has to be used [64].

The other possibility for the reduction of the torque ripple is to use different electrical steels in the stack length and this technique has been named “Romeo and Juliet” by Bianchi et al.[65]; in the same paper, another method called “Machaon” has been presented: it consists in changing the span of two adjacent poles. This last solution is also discussed by Ferrari and Pellegrino in [66]. In the past years, the “Machaon” solution has changed and has turned into a solution composed by two poles of the first type and two other poles of another type [67]-[68]. In subchapter 6.2, a new solution with an asymmetry inside the pole is evaluated and compared to the new “Machaon” technique with two different adjacent poles, which is presented in subchapter 6.3. Subchapter 6.4 proposes a combination of the two asymmetries in order to further minimize the torque ripple. Finally, a comparison between the different solutions is carried out in subchapter 6.5.

6.1 Optimization with the symmetric rotor

After the optimization procedure, it is possible to further reduce the torque ripple of the machine with the use of an asymmetric rotor. In literature, there are a few methods that aim to reduce the torque ripple with asymmetric rotors and, in this subchapter, three types of asymmetries have been evaluated and compared between each other. As an example, this subchapter presents the study carried out on a design that has been optimized for an electric vehicle application.

This study starts with the definition of the stator geometry and of the windings; after that, it focuses on the rotor optimization. The first step is the optimization of the rotor considering the symmetric geometry: for this study, a 6-pole and 4-barrier plus a notch rotor has been used. The total number of variables for the optimization is nine: four for the barrier widths, four for the barrier positions and one for the width of the notch. The constraints for the optimization are based on two points: the base speed one and the maximum speed point. The constraints are the minimum torque at base speed and the minimum power at maximum speed, while the objective function of the optimization is the minimization of the torque ripple at the maximum speed operation. The design data with the information about the materials, the constraints and the stator are shown in Table 6.1. The motor presents 6-poles and the stator has 54 slots; Figure 6.1 shows the cross section of the stator.

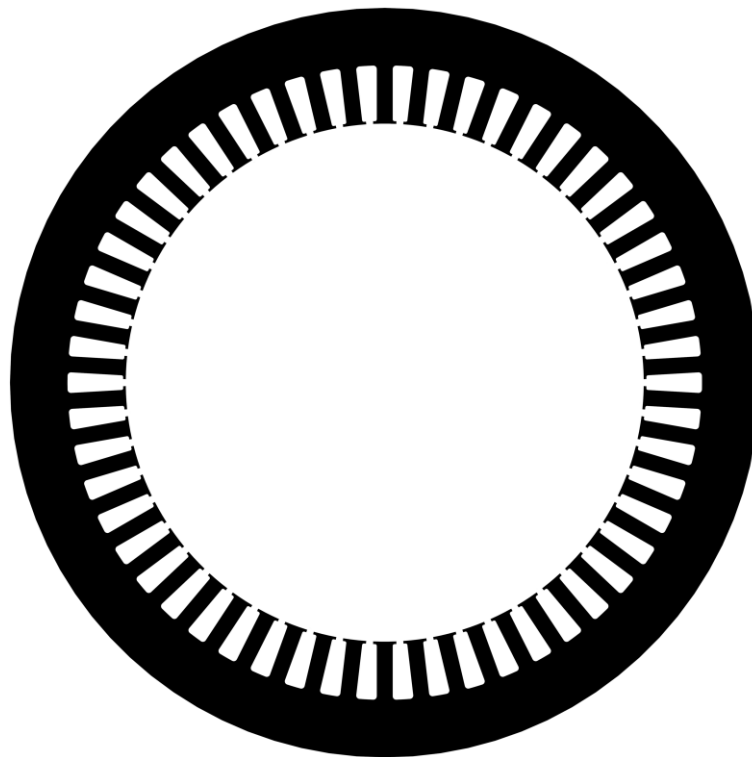


Figure 6.1: Cross section of the stator.

Table 6.1: Main motor requirements and data.

Requirements	Unit	Value	Stator data	Unit	Value
Base Speed	<i>rpm</i>	5000	Stator Outer Diameter	<i>mm</i>	220
Peak Torque @ Base Speed	<i>Nm</i>	≥ 380	Stack Length	<i>mm</i>	200
Maximum Speed	<i>rpm</i>	16000	Stator Inner Diameter	<i>mm</i>	152
Maximum Power @ Maximum Speed	<i>kW</i>	≥ 75	Electrical Steel		M235-35A
Torque Ripple @ Base Speed	%	≤ 15	Number of Conductors per Slot		7
Torque Ripple @ Maximum Speed	%	≤ 15	Slot Fill Factor		0.4
Motor Mass	<i>kg</i>	≤ 50	Airgap Length	<i>mm</i>	0.7

In this example, only the electromagnetic aspects have been considered; the issues due to the high speed have been neglected here, but considered and discussed in the next chapters.

The cross section of the symmetric solution (named M1) is shown in Figure 6.2.

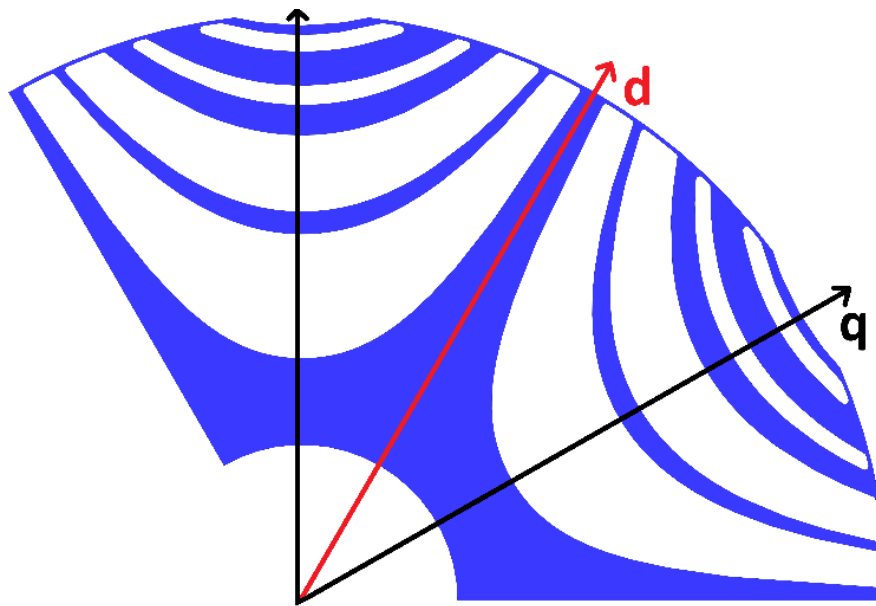


Figure 6.2: M1 design: cross section of the symmetric rotor (2 poles).

Since it is a symmetric solution, the behavior of the torque in the two rotating directions is the same. It is a 6-pole fluid shaped rotor, which is optimized according to the procedure explained in the previous chapters.

Figure 6.3 shows the torque versus the electric angle behavior, obtained by FE analyses, both for the peak torque at base speed and for the maximum torque at maximum speed. The average torque at base speed is over 380 *Nm* and the one at maximum speed is over 45 *Nm* (while the power is over 75kW), satisfying the values imposed by the constraints.

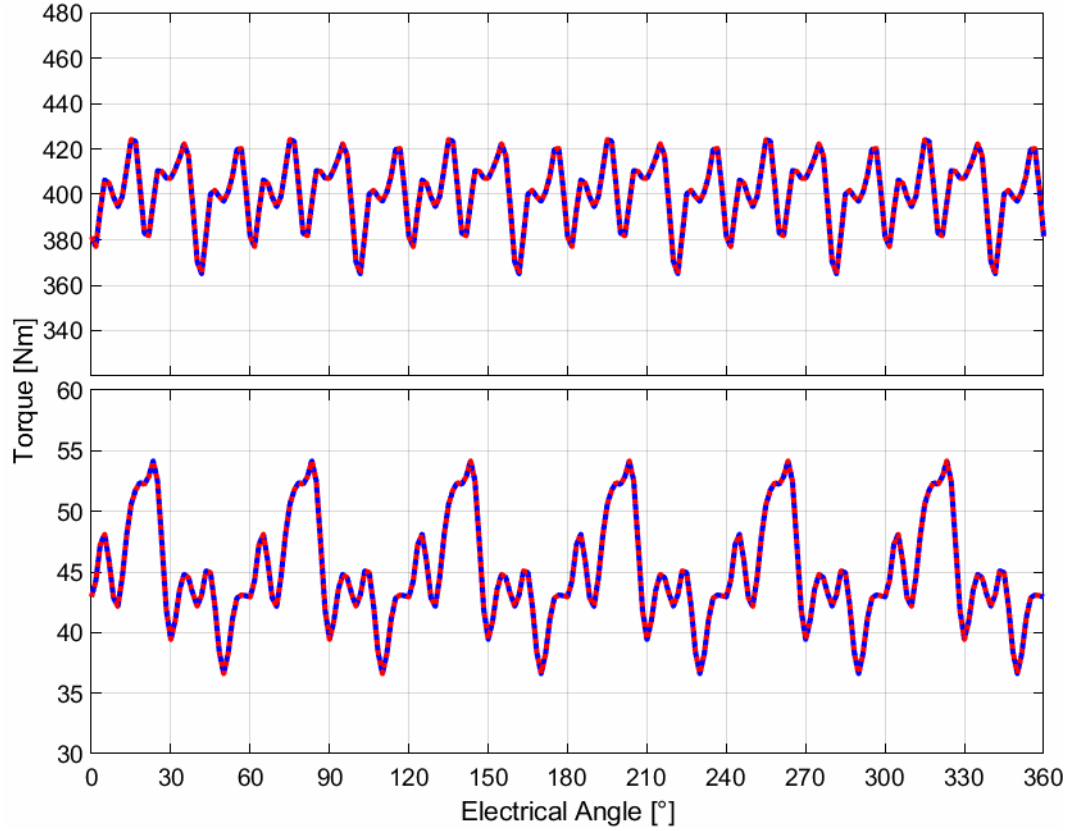


Figure 6.3: M1 design: Torque vs Electrical rotor position for peak torque and base speed (upper) and maximum torque and maximum speed (lower) operations.

6.2 Rotor with an asymmetry within the pole

Starting from the result obtained by the M1 design and in order to further reduce the torque ripple, an asymmetric solution has been evaluated. The rotor of this new optimized design, named M2, has been obtained by fixing the half pole of the one obtained for the M1 design introducing an asymmetry in the other half pole. The motor thus has an asymmetric pole structure to compensate the torque harmonics: particularly, the rotor shape is asymmetric in correspondence of the q -axis, but each pole is equal to the others.

In order to realize the asymmetry, the other half pole has a different expression for the rotor barrier respect to the (3.46) one. The new expression is:

$$r_k = R_s \sqrt{\frac{Ac_k(\vartheta) + \sqrt{[Ac_k(\vartheta)]^2 + 4 \sin^2(p\vartheta)}}{2 \sin(p\vartheta)}} \quad (6.1)$$

$$Ac_k = A_k - (A_k - C_k) \frac{1 - e^{-k_{a,k} \frac{2p\vartheta}{\pi}}}{1 - e^{-k_{a,k}}} \quad (6.2)$$

where A_k is an angle dependent term that substitutes C_k in (3.46), A_k is the parameter of the asymmetry and $k_{a,k}$ is a coefficient to vary the shape of the barriers. This term can be included in the optimization and it can be different for each curve. If A_k is equal to C_k , the rotor structure is symmetric.

The term A_k can be calculated according to the following expression:

$$A_k = \sin(p\theta_k) \left[\left(\frac{R_{e,r}}{R_s} \right)^p - \left(\frac{R_{e,r}}{R_s} \right)^{-p} \right] \quad (6.3)$$

where θ_k is the angle of the extremity (near the airgap) of the k -th curve of the barrier, $R_{e,r}$ is the rotor outer radius and R_s is the shaft radius.

The expressions (6.1) and (6.2) are obtained in order to create the asymmetry while maintaining the continuity of the function that describes the barriers in the contact point (q -axis). Fixing the value of $k_{a,k}$ to two, it is possible to use, for the optimization, only the θ_k angles (one for each curve) thus having a total of nine variables, the same number of the previous optimization. Using the same constraints, the same objective function and the obtained shape for the half pole of the first optimization (M1), it is possible to obtain the rotor shape shown in Figure 6.4.

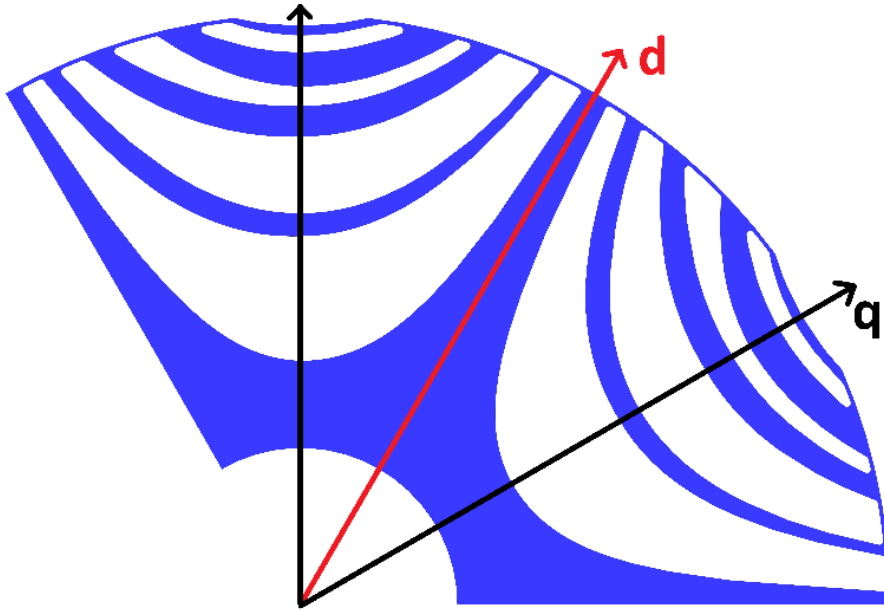


Figure 6.4: M2 design: cross section of the asymmetric rotor (2 poles).

The torque values have been calculated considering both positive values of the torque (in the traction mode with a clockwise motor rotation) and negative ones (in reverse gear with a counterclockwise rotation or in the regenerative braking mode with a clockwise rotation); this is due to the particular asymmetry of the rotor structure: Figure 6.5 points out a different trend on the torque profiles both for the

peak power operation and for the maximum speed operation. The torque ripple in the peak torque and base speed operation has increased compared to the one of the M1 design, while the torque ripple in the maximum torque and maximum speed operation is reduced; this is due to the optimization, which has worked on the minimization of the torque ripple for the maximum speed operation. The average torque values for the two conditions are higher than the M1 ones.

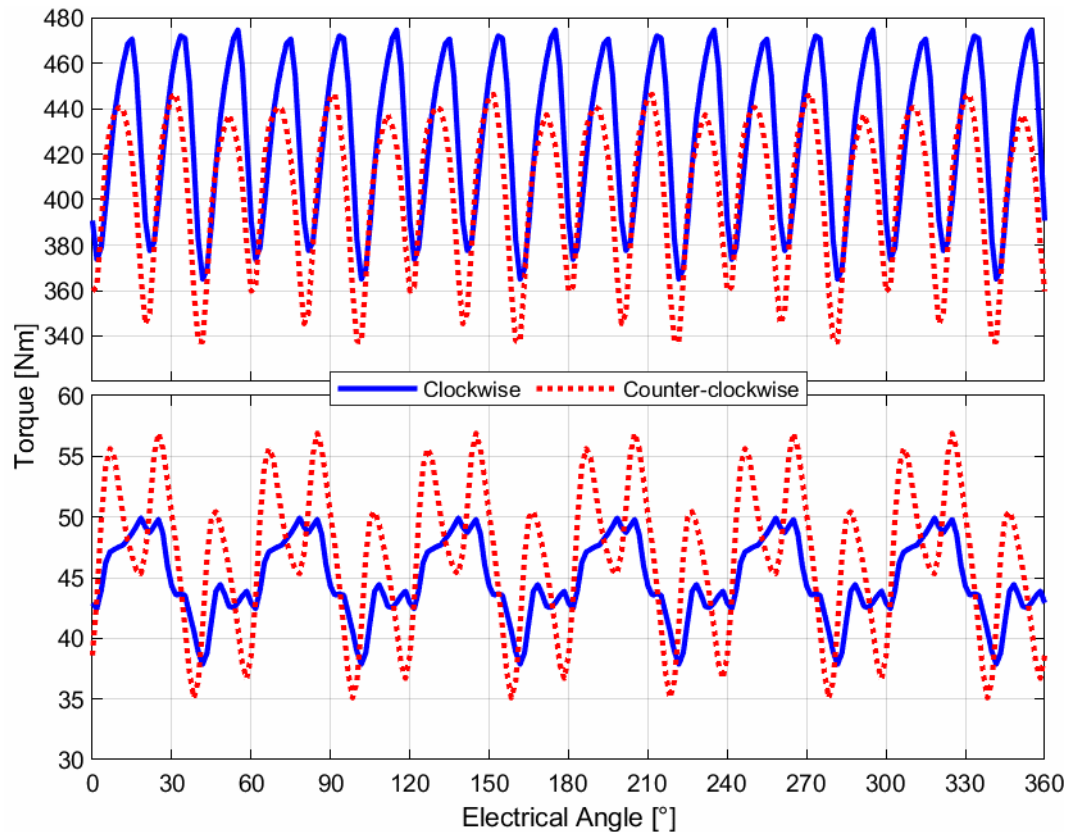


Figure 6.5: M2 design: Torque vs Electrical rotor position for peak torque and base speed (upper) and maximum torque and maximum speed (lower) operations.

6.3 Rotor with adjacent different poles

The other asymmetry that can be adopted for the reduction of the torque ripple uses two adjacent different poles. The rotor of this new optimization, named M3, has been obtained by setting the first pole to the one obtained for the M1 design and by carrying out a new optimization for the other pole. In this case, the variables, the objective function and the constraints are the same of the M1 design.

This new solution is shown in Figure 6.6, while the torque profiles are presented in Figure 6.7. In this case, the behavior of the torque both for the clockwise direction and for the counter-clockwise one is the same. This solution allows to strongly reduce the torque ripple at base speed, but the torque ripple at maximum speed is

slightly higher than the one of the M2 design, even though is still lower than the one of the M1 design.

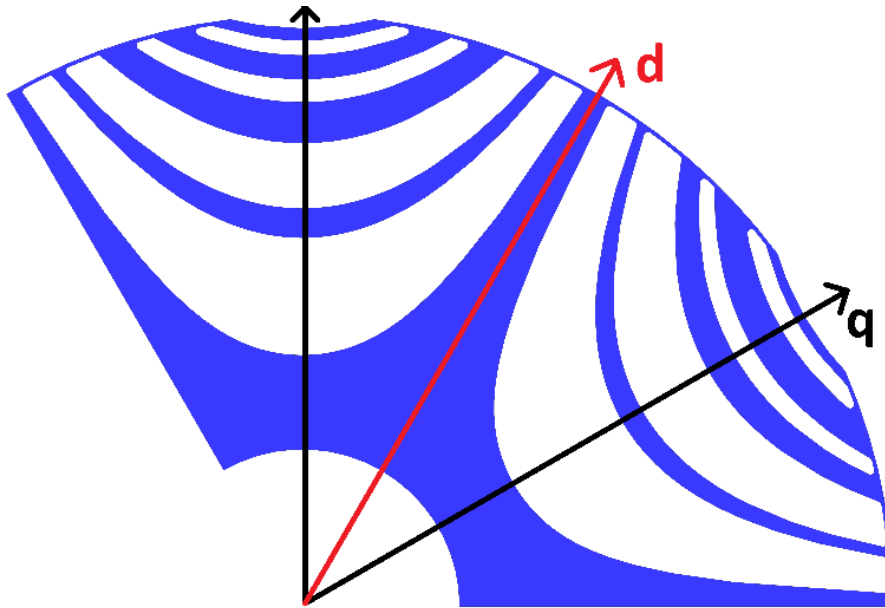


Figure 6.6: M3 design: cross section of the asymmetric rotor (2 poles).

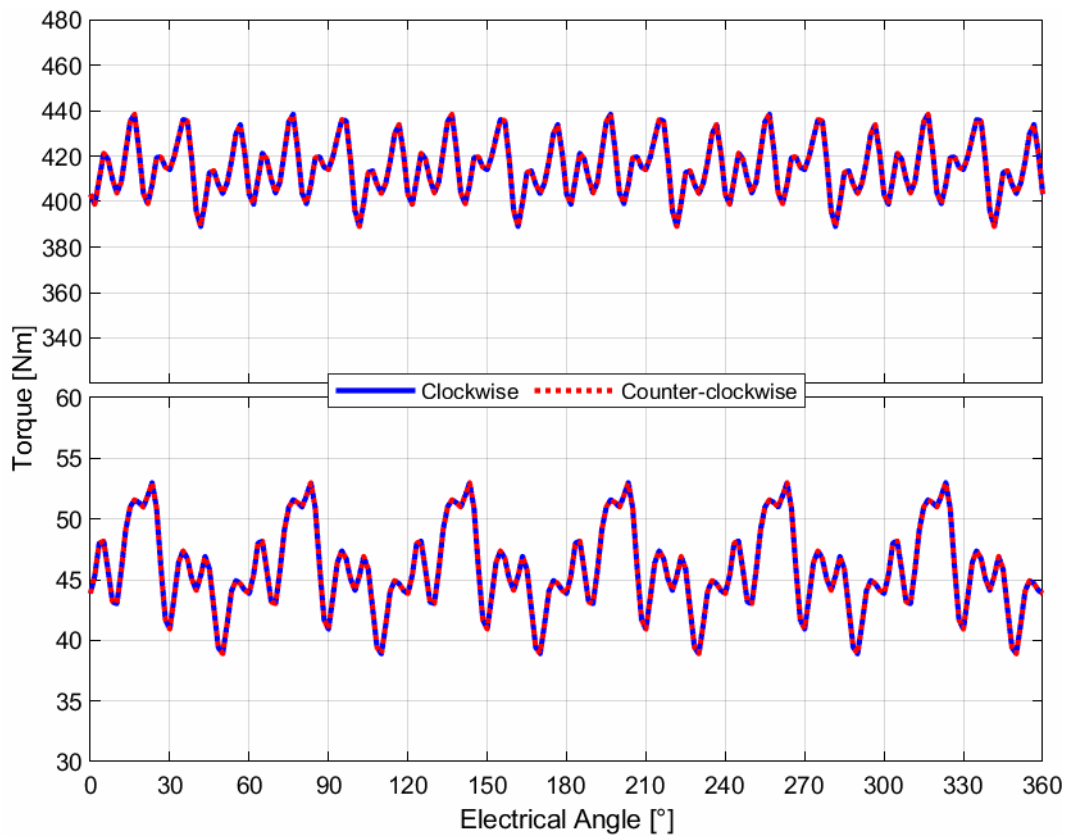


Figure 6.7: M3 design: Torque vs Electrical rotor position for peak torque and base speed (upper) and maximum torque and maximum speed (lower) operations.

6.4 Combination of the two asymmetries

The last asymmetry type that can be adopted for the reduction of the torque ripple consists in the combination of the other two asymmetries. The rotor of this new optimization, named M4, has been obtained by setting the first pole to the one obtained for the M2 design, by considering the second half pole equal to the second pole of the M3 design and by carrying out a new optimization for the last half pole. In this case, the variables, the objective function and the constraints are the same of the M2 design.

This last solution is shown in Figure 6.9, while the torque profiles are shown in Figure 6.9. As well as for the M2 design, the M4 one has different behaviors of the torque for the clockwise direction and for the counter-clockwise one. The reduction of the torque ripple, in this solution, is good both for the peak torque at base speed and for the maximum torque at maximum speed, even if the minimum oscillation at the first condition is in the M3 design.

The four solutions have been obtained by using the same number of variables for the optimization procedure in order to have a good basis for comparison between them. The same number of variables also means a similar number of iterations to reach the optimum design. Obviously, the best condition is the optimization of a solution similar to the M4 design, in which all the possible variables of the rotor are 36 if the $k_{a,k}$ is imposed, otherwise they are 54; however, this would require a much higher computational burden.

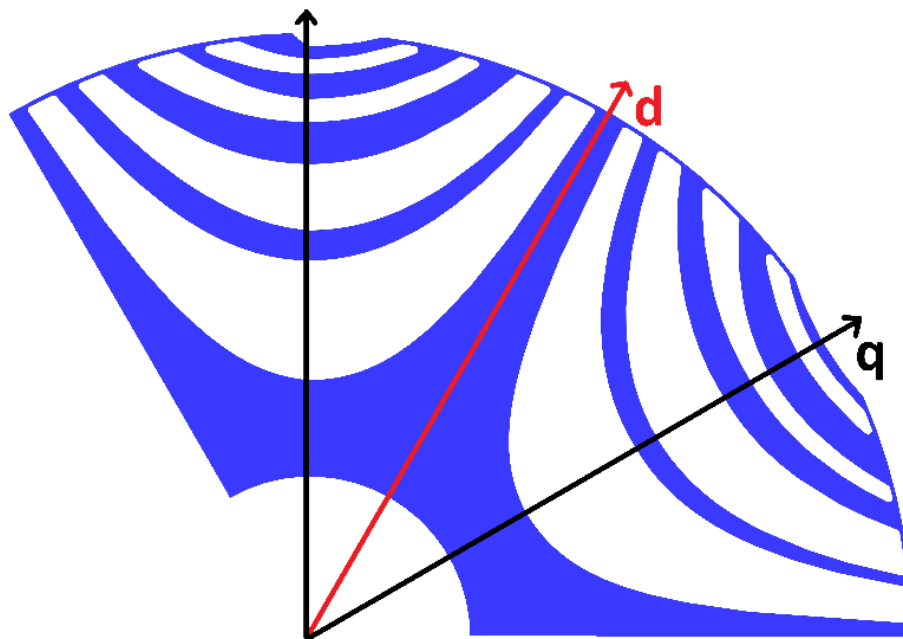


Figure 6.8: M4 design: cross section of the asymmetric rotor (2 poles).

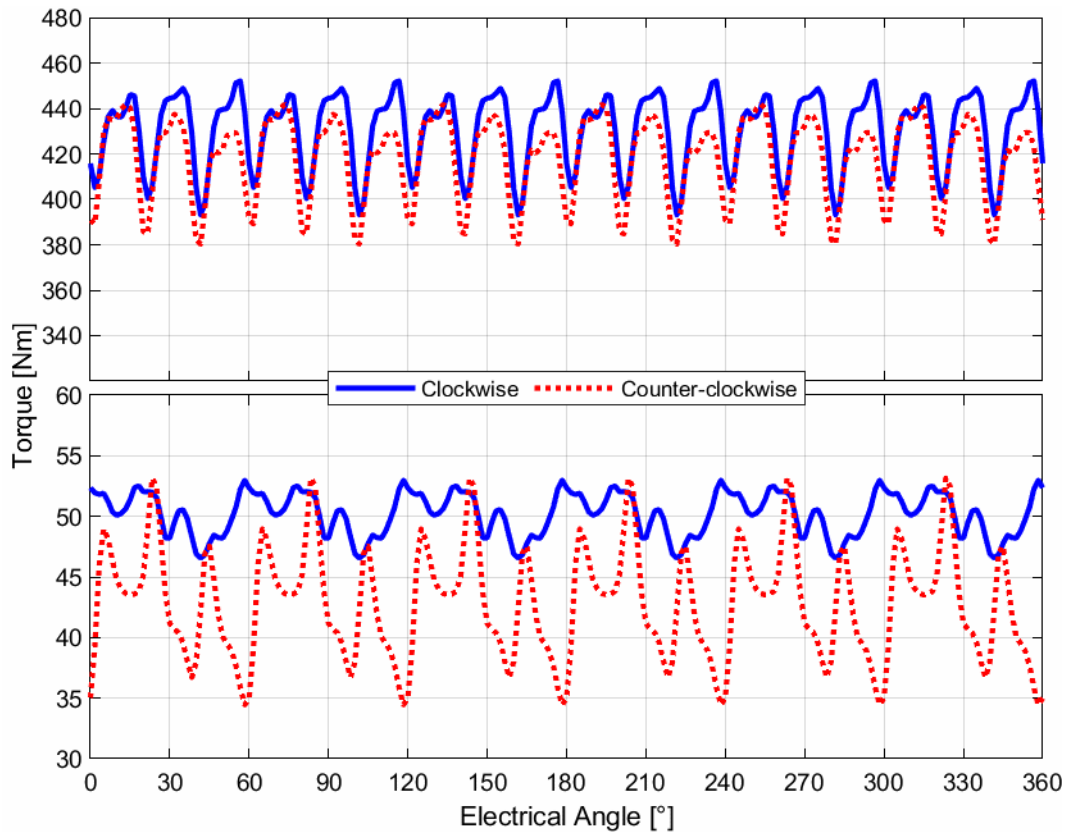


Figure 6.9: M4 design: Torque vs Electrical rotor position for peak torque and base speed (upper) and maximum torque and maximum speed (lower) operations.

6.5 Comparison between the different solutions

The performance of the proposed designs is compared in Table 6.2 the values that do not meet the requirements are in bold. The designs fully satisfy the peak torque at base speed and the maximum power at maximum speed. The M1 and M2 designs are not able to satisfy the torque ripple requirement, while the M3 one guarantees a good torque ripple only at base speed. The M4 design presents the best performance in terms of power at base and maximum speed with a reasonable torque ripple. The torque ripple has been computed through the following expression:

$$\zeta = \frac{T_{max} - T_{min}}{T_{avg}} \quad (6.4)$$

where T_{max} and T_{min} are the maximum and minimum torque in the electric period, respectively, and T_{avg} is the average torque.

The reduction of the torque ripple is important both at low speed and at high speed in order to reduce the noise and the vibrations in the vehicle, together with the stress on the bearings, even though the bearings have to endure the maximum stress at maximum speed.

Table 6.2: Optimized design comparison.

Performance	Unit	M1	M2	M3	M4
Peak Power @ Base Speed	<i>kW</i>	210	223	217	220
Peak Torque @ Base Speed (mean)	<i>Nm</i>	401	426	415	430
Peak Torque @ Base Speed (max)	<i>Nm</i>	424	475	438	452
Peak Torque @ Base Speed (min)	<i>Nm</i>	365	401	389	393
Torque Ripple @ Base Speed	%	14.7	25.7	11.9	13.7
Peak Power @ Maximum Speed	<i>kW</i>	75.4	78.4	76.9	84.1
Peak Torque @ Maximum Speed (mean)	<i>Nm</i>	45	46.8	45.9	50.2
Peak Torque @ Maximum Speed (max)	<i>Nm</i>	54.2	56.9	53.0	53.0
Peak Torque @ Maximum Speed (min)	<i>Nm</i>	36.6	35.1	38.9	46.6
Torque Ripple @ Maximum Speed	%	39.0	26.9	30.7	12.8
Motor Mass (Active Materials)	<i>kg</i>	47	47	47	47

The M2 and M3 designs have a quite similar torque ripple at maximum speed; therefore, the reduction of the flux harmonics in the deep flux-weakening region (the current control angle is the highest) is similar. Otherwise, the M3 design has a higher reduction of the torque ripple at peak power and base speed when the machine works in maximum saturation conditions; therefore, with the use of two different poles, it is possible to further reduce the flux harmonics within the high saturation region. Moreover, the average torque is also reduced. The M2 design specially works on the harmonics produced by a high current control angle without having any torque reduction, while the M3 design works on a general reduction of the flux harmonics with a reduction of the average torque as well. The M4 design, which combines the two asymmetries, can reach the lowest torque ripple in the flux-weakening region with also a good reduction in the high saturation region; furthermore, it guarantees the highest values of mean torque under each condition for the clockwise solution.

The particular asymmetric shape of the barriers of the M2 and M4 designs affects the performance of the motor in function of the rotating direction. This means that the motor must operate with the clockwise rotation in order to exploit the advantage of its rotor shape. This condition is not critical for electric vehicle applications, in which good performance is required during the traction (the clockwise rotation in this example) and lower performance is still acceptable for reverse gear or braking operations.

To obtain negative and positive values of the torque, it is necessary to change the sign of one of the axis currents and, therefore, to one of the axis fluxes. For the sake of simplicity, it has been supposed that the torque inversion is obtained by changing the sign of the d -flux. For the solutions in which the poles do not have an asymmetry

respect to the q -axis (M1 and M3 designs), the flux maintains the same path with an inversion of the d -flux; therefore the inductances are the same and also the torque is the same, but with a negative value. The torque ripple for the positive and negative values of the torque is the same. For the other solutions (M2 and M4 designs) in which the poles are asymmetric respect to the q -axis, the flux has a different path depending on the sign of the q -flux value: positive or negative; therefore, the inductances are different, the behavior of the torque is different together with the torque ripple, which changes for positive or negative values of the torque.

These aspects are visible in Figure 6.5 and in Figure 6.9 for the M2 and M4 designs, respectively, while in Figure 6.7 the torque has the same behavior in the M3 design despite the asymmetry.

As shown in Table 6.2, the M4 design is the only one that satisfies all the requirements and that appears to be a good solution with a smooth torque behavior for the clockwise rotation, where the torque ripple is of 12% at maximum speed and about 10% for peak torque and base speed operation.

Figure 6.10 shows the torque ripple map in the torque-speed plane: in order to obtain this map, the control angle that has been used is the one that maximizes the efficiency. The map considers both positive and negative values of the torque.

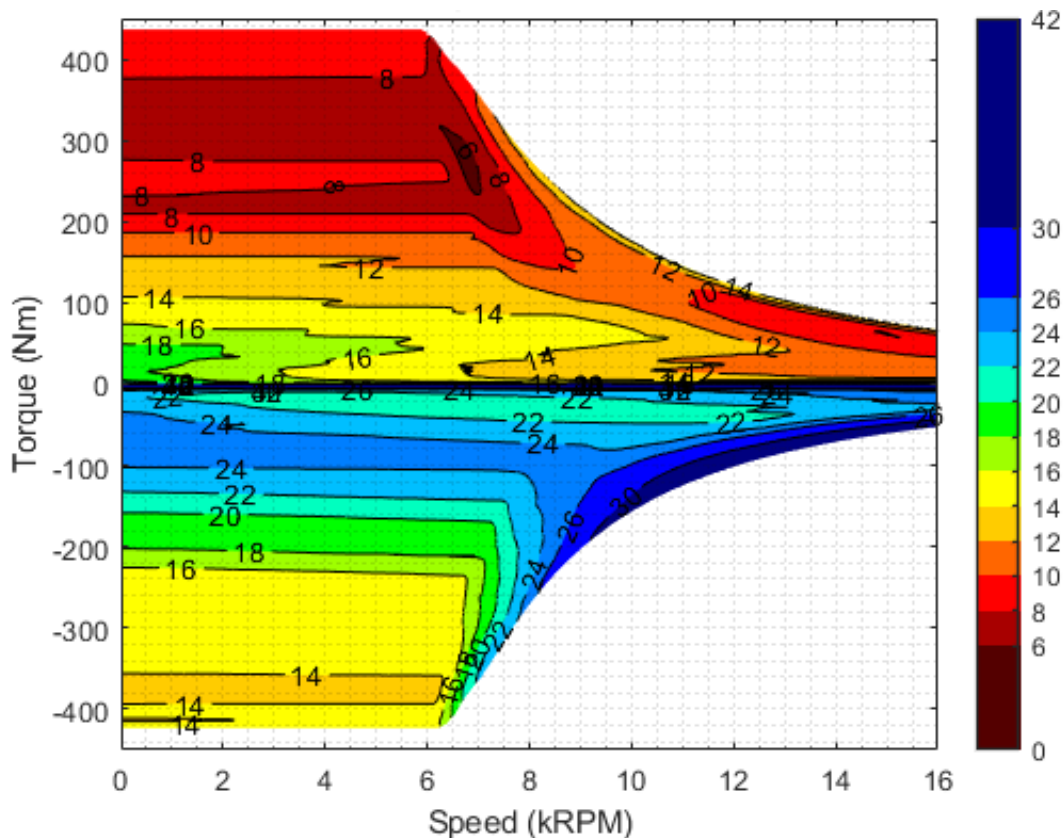


Figure 6.10: M4 design: Torque ripple map.

The use of the M4 design allows a significant reduction of the torque ripple for the clockwise direction (for positive torque values), but for the counter-clockwise direction the torque ripple is very high. This is in accordance with what has been imposed during the optimization steps, where only the main direction has been considered for the minimization of the torque ripple. Moreover, the area with the lowest torque ripple (about 6%) is close to the peak torque and base speed operation: this happens because, with a high current control angle and whenever the q -axis current is high, the reduction of the torque ripple is more difficult to achieve. The region with negative torque values (in the counter-clockwise direction) presents higher torque ripples, with a maximum value of about 40% at the maximum torque and from 10 $krpm$ to the maximum speed. Considering the electric vehicle applications, this condition is not critical because the duration of this operation is short. In fact, considering also the typical mass of a car and the respective resistance forces, during the braking operation the machine certainly goes from the maximum speed to 10 $krpm$ in less than 5 seconds; therefore, the additional oscillations caused by the high torque ripple and the consequent increasing acoustic noise do not impact on the normal operation.

However, if the application requires a lower torque ripple in the region with negative torque values, it is possible to skew the rotor core, to consider also the braking operation during the optimization steps or to use the M3 design, which shows a low torque ripple for both the operating directions. Regarding the possibility to skew the rotor, this option will be discussed in the next chapter.

Chapter 7

High-Speed SynRel Design Criteria

Part of the work presented in this chapter has been previously published in [5], [7], [8], [12]

After the electromagnetic optimizations discussed in the previous chapters, the rotor geometry needs to be refined from a mechanical point of view in order to guarantee the integrity of the rotor up to the machine maximum speed. The focus of this further refinement needs to be on the mechanical stresses and on the deformations at the airgap caused by centrifugal forces. As an example, the design displayed in Figure 6.2 is retained only for the very thin tangential ribs; the mass of the rotor steel and its position generate high centrifugal forces, especially at high speeds. In order to increase the maximum speed, different innovative approaches compared to the adoption of radial ribs along the q -axis (discussed in subchapter 7.1) have been adopted in literature; the main ones are:

- the adoption of high strength electrical steel [69], which usually has worse magnetic properties;
- the adoption of retaining sleeves [70]-[71], which requires a custom manufacturing process and leads to an increase of the magnetic airgap together with the mechanical one;
- novel rotor constructions [72], which need a custom manufacturing process and custom spare parts;
- the adoption of proper end plates connected to the rotor and of an interconnecting shaft (press fit versus dovetails) [73]; however, this solution is more effective for compact buried PM rotors;
- the adoption of optimized structural ribs [74]-[78], whose basic principles are discussed in subchapter 7.2;
- the adoption of structural non-magnetic ribs [80]-[82] (in titanium, carbon fiber, etc.) or the use of epoxy adhesive resin (this last approach is discussed in subchapter 7.3).

7.1 Typical approach

The typical approach consists in the use of radial ribs along the q -axis in order to improve the strength of the structure while guaranteeing the rotor integrity at higher speeds. This approach provides the variation in the width of the radial and tangential ribs and their fillets. After that the optimal electromagnetic shape has been frozen (M1 has been considered for this study), a further mechanical optimization of the width of the ribs under the effect of centrifugal forces has been carried out. In this particular phase, there are two main approaches: the first one is the adoption of mechanical FE analyses during the optimization steps, using the maximum stress inside the machine as a constraint and the minimization of the rib material as an objective function; the second one is the adoption of a multiphysics approach, using the same constraint of the previous approach but a different objective function: in this case, it is the maximization of the electromagnetic performance.

These two approaches allow to minimize the impact of the radial and tangential ribs on the machine performance. The total number of variables for this optimization is 24: in detail, one variable for each width and two variables for the fillets of each rib. The shape of the optimized solution is shown in Figure 7.1.

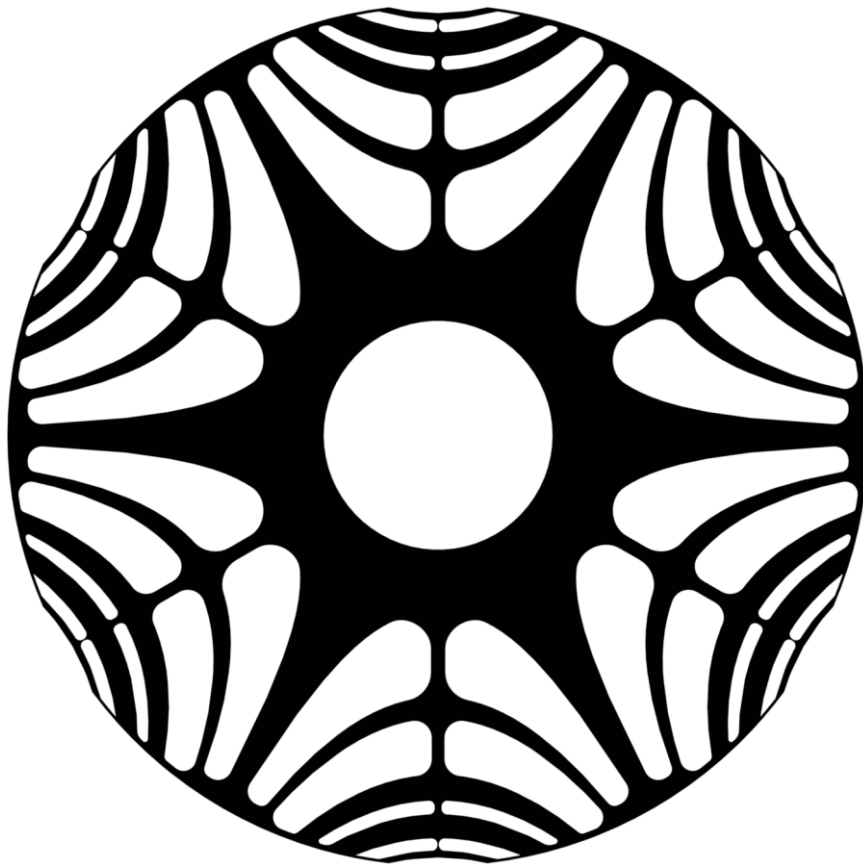


Figure 7.1: Radial rib solution shape.

The width of the ribs increases going from the shaft to the rotor outer diameter because the mass that each rib has to sustain increases.

Figure 7.2 shows the equivalent von Mises stress computed by the FE analysis. The maximum stress is on the rib of the first barrier; however, this rib has a very low average value of the stress but punctual high stress values. If the stress on this point reaches a critical value, there is the possibility of a crack raise: this crack can then propagate in the machine with a consequent rotor failure. The maximum admitted stress for a long time, considering that it is punctual, is the ultimate tensile strength of the steel reduced by a coefficient of 1.4. The ultimate tensile strength for the considered steel (M235-35A) is of 540 MPa; therefore, the maximum admitted stress is 385 MPa and the solution satisfies this constraint.

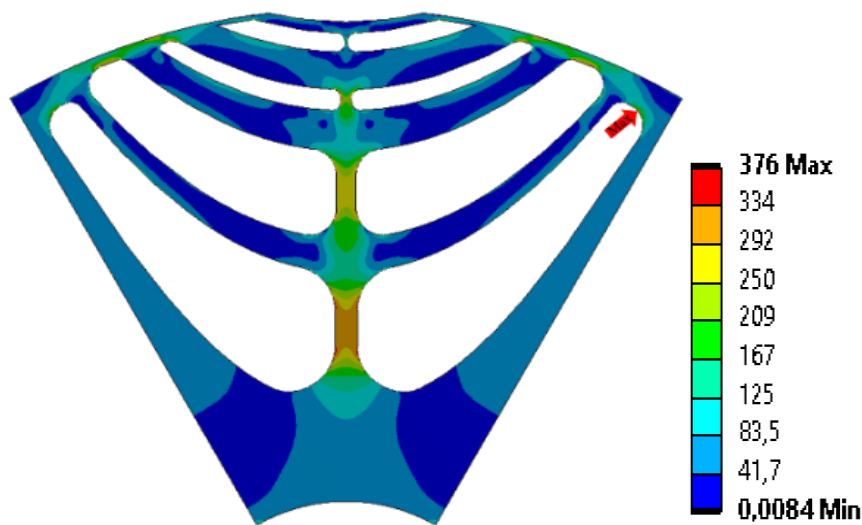


Figure 7.2: Equivalent von Mises stress [MPa] of the rotor with radial ribs.

Figure 7.3 points out the rotor deformations close to the airgap. Being the value of the airgap length (Table 6.1) equal to 0.7 mm, the maximum variation in the airgap length, according to the maximum speed and using commercial bearings for this application, must stay under 10%. From the figure it is clear that the maximum deformation of the notch at the airgap is of 47 μm , while the airgap deformation is lower than this value (in correspondence of the notch, the effective airgap is higher than the rated one) and it is acceptable for this type of application.

Figure 7.4 shows the direct and quadrature inductances and the saliency ratio over the speed range for the maximum torque points. Up to the base speed, the d - and q -inductances have low values due to the saturation, together with the saliency ratio; therefore, the saliency ratio increases whenever the machine works with an optimal control angle. When the speed further increases, the current control angle reaches its maximum value, the q -current reaches a very high value and the radial ribs reduce the saliency ratio and the performance of the machine.

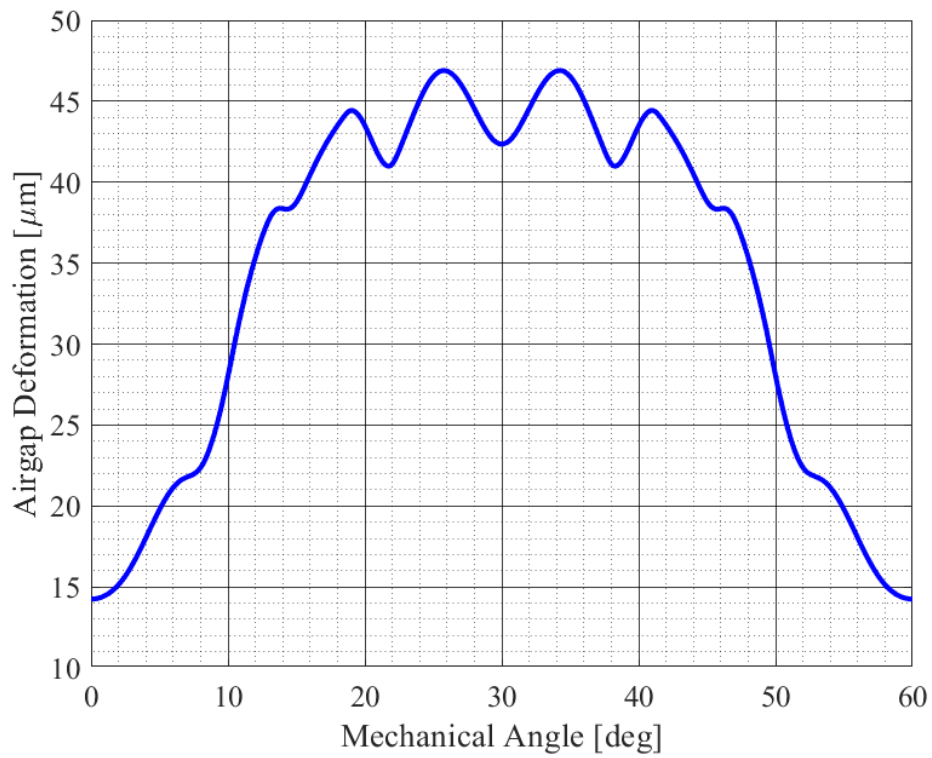


Figure 7.3: Airgap deformations [μm] of the rotor with radial ribs.

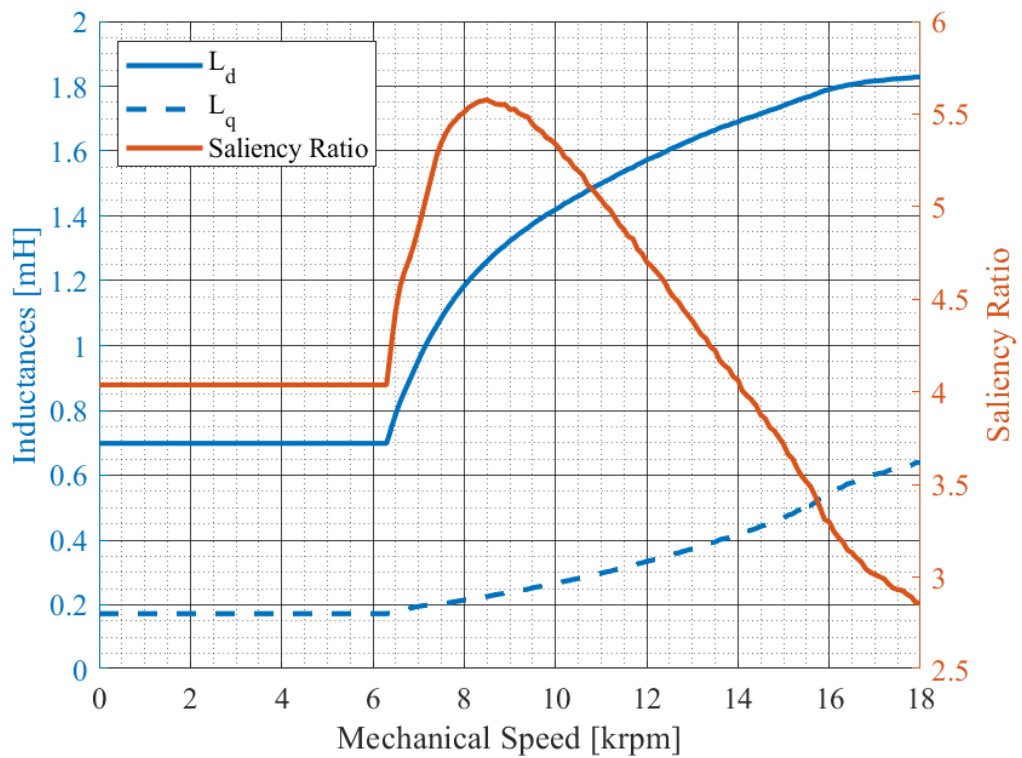


Figure 7.4: d - and q -axis inductances and saliency ratio over the speed range of the rotor with radial ribs.

Figure 7.5 reports the performance of the motor over the speed range in terms of maximum torque and power. The peak torque at base speed is reduced down to 350 Nm in the solution with radial ribs (12.5% reduction), while the maximum power at maximum speed is reduced down to 20 kW . The reduction that appears when the radial ribs are introduced is more important in the flux-weakening region because the main negative effect of the radial rib introduction is an increase in the q -inductance and a consequent increase in the voltage to sustain the q -flux at high speeds when the current control angle is high.

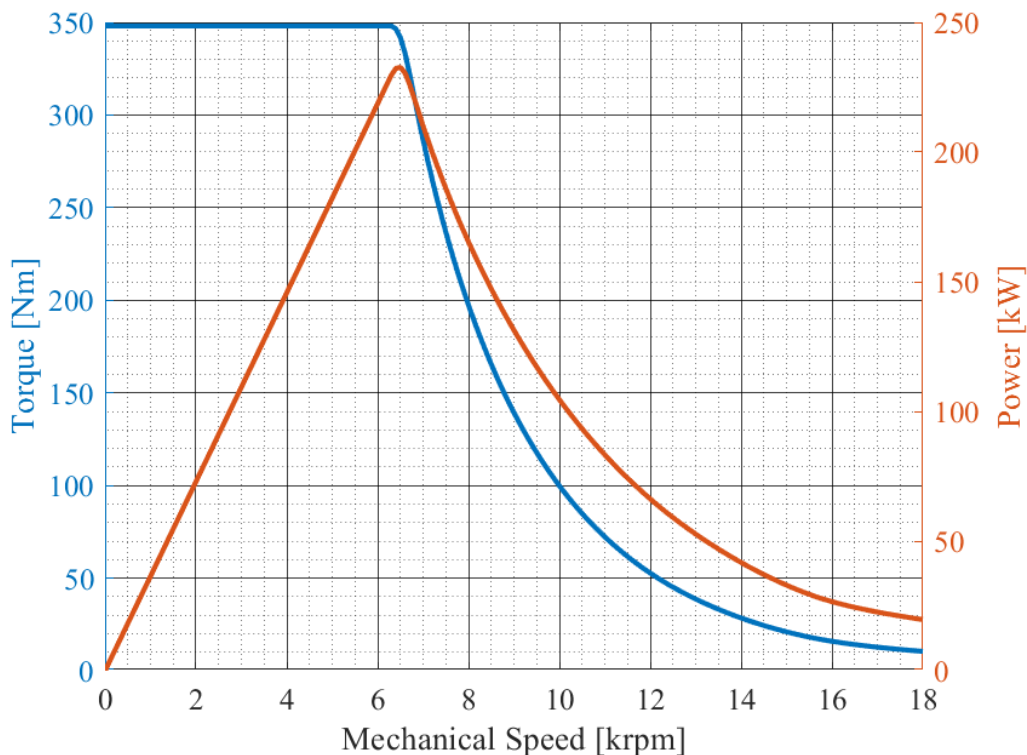


Figure 7.5: Maximum torque and power over the speed range of the rotor with radial ribs.

For these reasons, a new approach to reduce, as much as possible, the effect of the introduction of radial ribs must be evaluated: the first alternative, which does not modify the manufacturing process, consists in changing the position and the number of the inner ribs. This alternative is discussed in the next subchapter.

7.2 Topology Optimization

In order to minimize the impact of the inner rib introduction, the first approach includes the use of a magneto-structural optimization where the number of the inner ribs for each barrier is a design variable. This solution complicates the structure of the optimization algorithm and it requires a very high computational burden. Regarding the ribs, the values of the number, of a preliminary width and of the angle must be evaluated in an alternative way and, after that, it is possible to carry out the magneto-structural optimization. This preliminary evaluation has to be made with the aim to minimize the mass of the additional inner ribs while guaranteeing the mechanical integrity of the rotor at high speeds; this requirement seems to match the capabilities of the class of algorithms referred to as “Topology Optimizers” in mechanics [83]-[84].

In literature, there are a few examples that use the Topology Optimization (TO) for the design of SynRels. Watanabe in [85] uses an ON/OFF TO with a focus on the minimization of the torque ripple considering only the electromagnetic performance. Sato in [86] considers the integration of the TO with a normalized Gaussian network, but only the average torque and the steel losses are considered in this work. Considering other typologies of machines, there are even more works: Garibaldi in [87] applies the principle of the mechanical TO in the multiphysics design of a Surface Mounted PM motor, neglecting the torque ripple of the machine; however, thanks to the considerations on the magnetic energy aspect, he is able to integrate a magnetic and a mechanical characteristic in the objective function of the TO. In this way, it is possible to optimize the shape of the electrical steel of the rotor for the maximization of the performance while guaranteeing the mechanical integrity at high speeds. Lee in [88] applies the principles of the TO for the refinement of the electromagnetic performance of a Switched Reluctance motor considering the voltage supply, the inductance and the behavior of the current during the supply. The main limit of this method consists in the possibility to use only linear materials since the saturation effect is neglected.

Further studies are needed for the application of a magneto-structural TO for the SynRel in order to consider the non-linearity of the materials, the evaluation of the torque ripple and the maximum stress in the steel.

In this subchapter, a TO combined with FE analyses has been applied to investigate the optimal number of ribs for each barrier, the rib starting positions and the rib widths for a further magneto-structural optimization. The imposed constraints are the same of the previous subchapter.

Between the different TO methodologies, in this thesis the Solid Isotropic Microstructural (or Material) with Penalization for intermediate densities (SIMP) has been adopted. This is one of the most common methods for the TO and it is available in commercial tools. It is sometimes called “material interpolation”, “artificial material”, “power law” or “density method” due to its particular manipulations on the elements.

This method starts with the realization of the mesh: the solid part is decomposed in a finite number of elements, referred to as microstructures. The properties of each element are manipulated based on a properly defined density ρ [84]. Fixing the density of the element equal to one, it will have the same properties in terms of Young modulus and mass density of the solid element; when the density is zero, the element will have the properties of the air. If the element has a density in the range $0 < \rho < 1$, its mechanical properties are between the ones of the electrical steel and the ones of the air. In the first iteration, the method assigns the same density to all the elements (equal to one) and performs the mechanical analysis in order to compute the stain-stress matrix and, from this matrix, to evaluate the sensitivity of the density of each element respect to the objective function. Based on this analysis, the algorithm modifies the element densities that guarantee an improvement in the objective function and it repeats these iterations until it reaches the convergence.

When the algorithm converges, it should return only the elements with a density $\rho = 0$ (empty or air elements) or $\rho = 1$ (solid or electrical steel elements). Typically, the optimal solution from a mechanical point of view consists in most of the elements with a density $0 < \rho < 1$, which are called “grey” elements, but they are not feasible in practice.

In order to reduce the number of grey elements, these elements have to be penalized through a penalty coefficient γ , which affects the mechanical properties of the elements without affecting the mass density of the element, which is proportional to the mass density of the electrical steel according to the density ρ . The application of the penalty coefficient related to the Young modulus is reported as an example:

$$E(\rho) = E_0 \rho^\gamma \quad (7.1)$$

where $E(\rho)$ is the Young modulus of the element and E_0 is the Young modulus of the adopted electrical steel.

The higher the value of the penalty coefficient, the higher the probability that the solution will not have grey elements; however, the convergence of the solution might not be reached. A typical value of the penalty coefficient ranges from 3 to 9.

Figure 7.6 reports the different iterations of the topology optimization algorithm, showing how the TO modifies the density of the elements trying to adopt only empty and solid elements to distribute the stress while minimizing the mass.

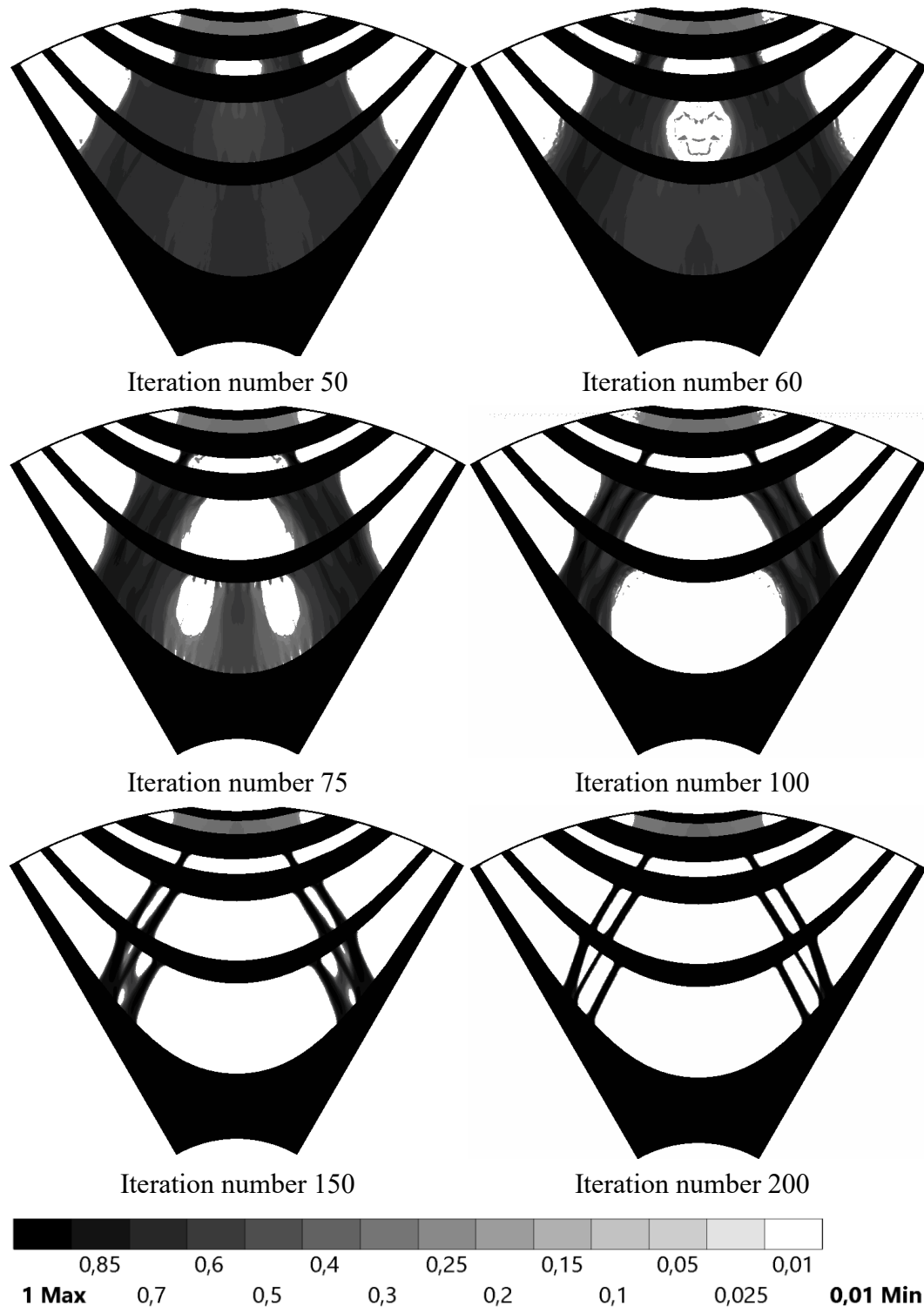


Figure 7.6: Evolution of the geometry obtained by the topology optimization. Empty elements are in white, “grey” elements are in grey and solid elements are in black.

The final geometry shows a reduction in the width of each inner rib and an increase in the rib number; the TO has found a promising but unusual shape, for which further refinements are needed:

- the final shape of the rotor has been optimized only minimizing the mass of the inner ribs to counteract the centrifugal forces, but the electromagnetic performance of the machine has not been considered;
- the last barrier is almost entirely composed by “grey” elements, which are not manufacturable;
- the first barrier has 6 inner ribs, but two of them are too thin for being manufactured; for this reason, the number of inner ribs needs to be reduced to 4.

The final design can be used as a useful guideline for the preliminary design of the inner ribs in terms of inner rib number for each barrier, rib positioning, inclination and width. Therefore, a suitable parametric model has been built up for a further magneto-structural optimization.

Considering a symmetric machine, the variable number that describes the model is seven for each inner rib: one for the position, one for the inclination, one for the width and four for the fillets. The last barrier, which is composed only by “grey” elements, has been modeled with a single radial rib. For this last rib, only the width and the two fillets are necessary for its definition. For the radial ribs only, the fillets are used as design variables. In this way, the model reaches a total of 45 variables: since this number is very high together with the number of iterations, it could be too much in terms of computational burden. From the TO, the fillets seem to have the same radius in the inner ribs; therefore, the radius of all the fillets of the inner ribs is considered equal and defined by only one variable. In this way, the total number of design variables is 26, close to the one in the previous subchapter.

In this case, since the stress inside the ribs is uniform, the maximum admitted stress in the steel has been imposed equal to 360 *MPa* with a safety coefficient of 1.6.

The whole design procedure has led to a new rotor layout, which is similar to the one obtained by the TO, characterized by multiple ribs in different positions respect to the flux barriers: the final rotor shape is shown in Figure 7.7. The solution is quite original compared to the ones found in literature.

The magneto-structural optimization further improves the electromagnetic performance obtained by the TO result; moreover, the position of the ribs is closer to the q -axis with a lower width and a higher length. The total mass is higher than the one of the TO but, with thinner ribs, the electromagnetic performance has been

improved. The mechanical equivalent von Mises stress map at maximum speed is shown in Figure 7.8. The solution satisfies the constraint of the maximum stress.

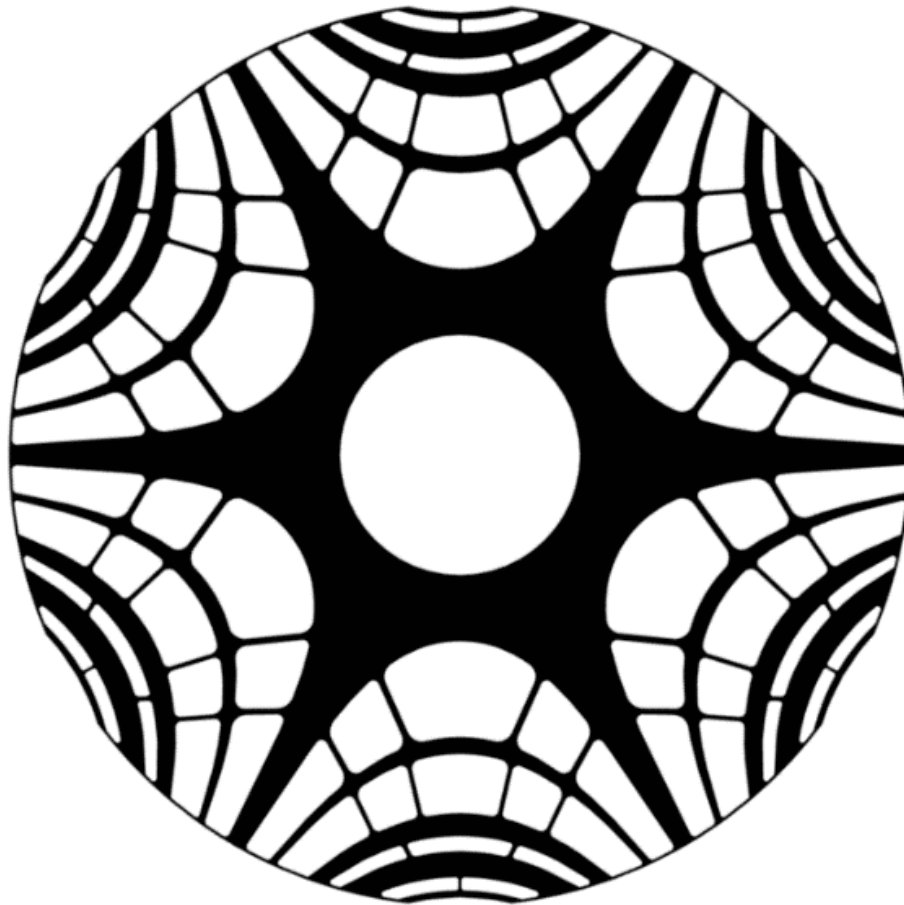


Figure 7.7: Optimized topology rotor shape.

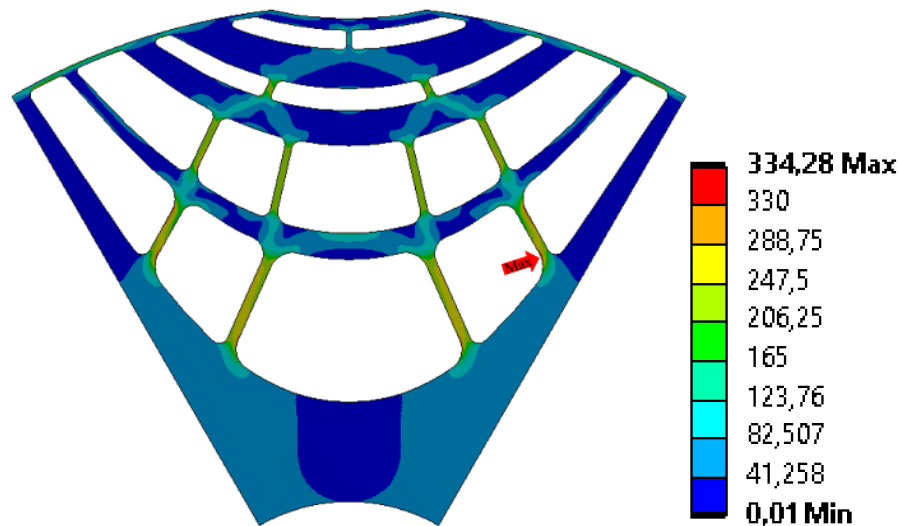


Figure 7.8: Equivalent von Mises stress [MPa] of the optimized topology rotor.

The design steps carried out to achieve the final design of high-speed SynRels with the aid of the TO are summarized in Figure 7.9.

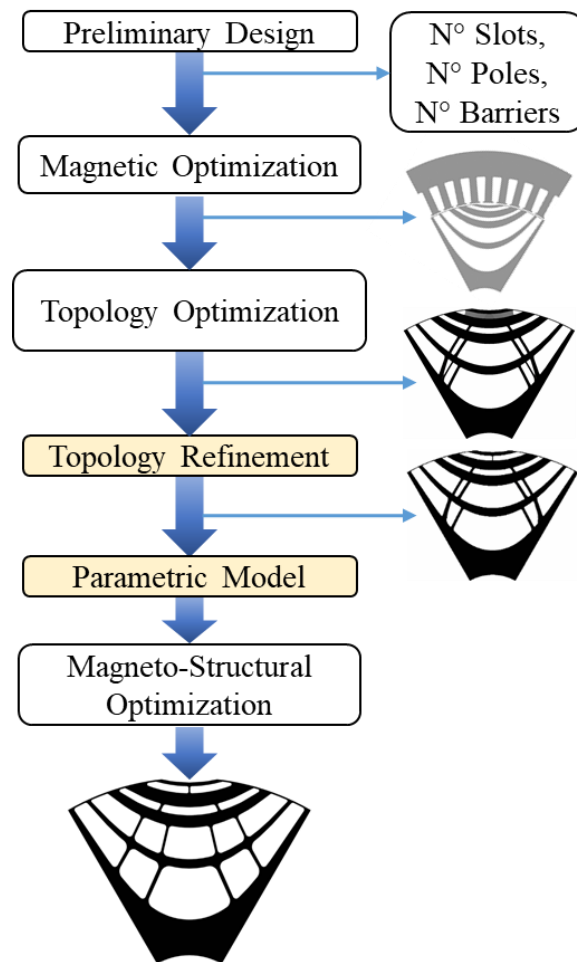


Figure 7.9: Design flow involving the adoption of the Topology Optimization.

Figure 7.10 reports the rotor deformations close to the airgap: the maximum deformation of the notch at the airgap is $48 \mu m$, value that is similar to the one obtained by the radial rib solution; therefore, it is acceptable for this application. Figure 7.11 shows the direct and quadrature inductances and the saliency ratio over the speed range in the maximum torque points. Up to the base speed, the d - and q -inductances have a low value due to the saturation, together with the saliency ratio: this behavior is very similar to the one of the radial rib solution, but the saliency ratio has a higher value. Figure 7.12 reports the performance of the motor over the speed range in terms of maximum torque and power. Compared to the radial rib design, the torques at base speed and maximum speed have been improved. The peak torque at base speed moves from a value of $350 Nm$ to $380 Nm$, with an improvement of 8.5%, while the maximum power at maximum speed has been increased of about 200%, passing from $20 kW$ to $60 kW$.

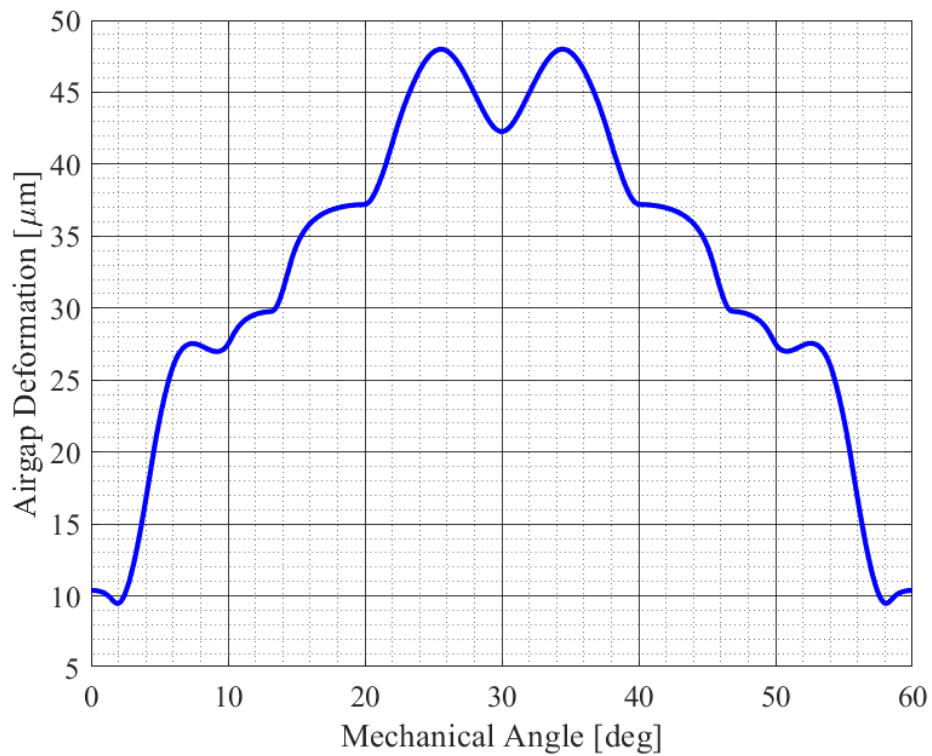


Figure 7.10: Airgap deformations [μm] of the optimized topology rotor.

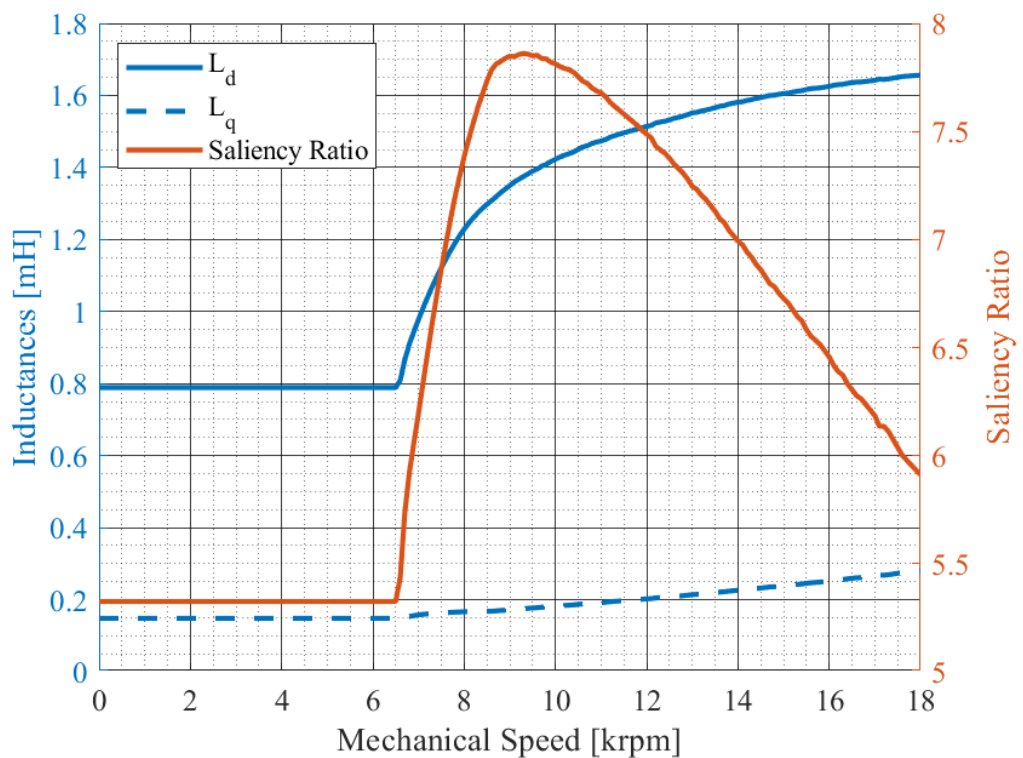


Figure 7.11: d- and q-axis inductances and saliency ratio over the speed range of the optimized topology rotor.

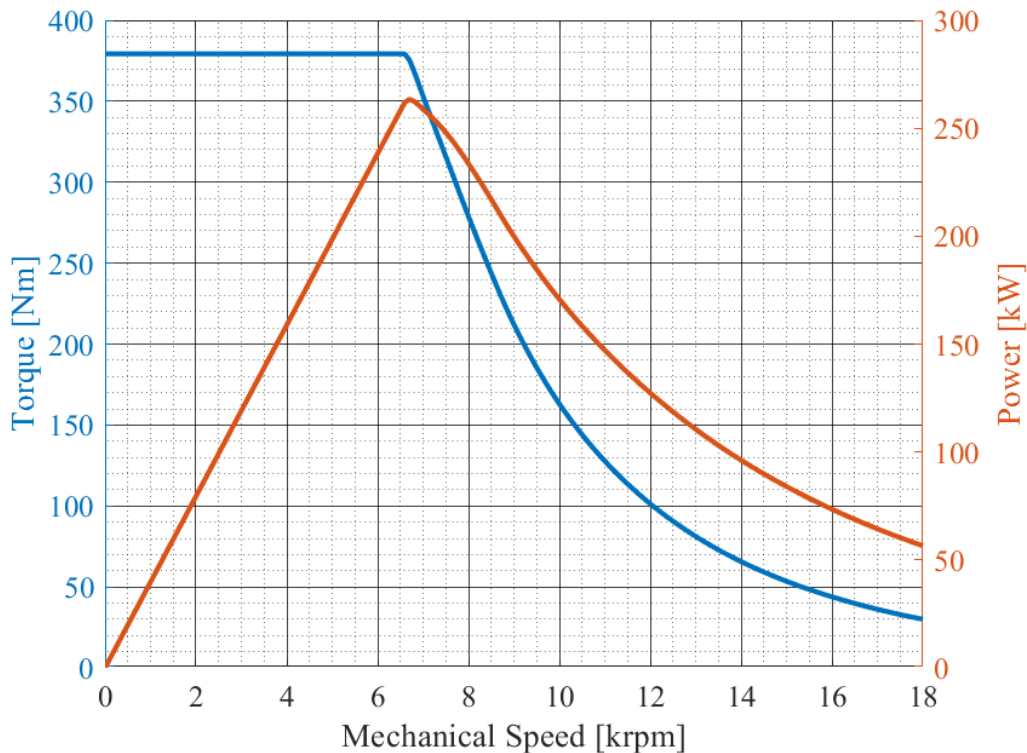


Figure 7.12: Maximum torque and power over the speed range of the optimized topology rotor.

7.3 Adhesive Epoxy Resin

The last solution that can guarantee the mechanical integrity consists in the adoption of the adhesive epoxy resin: with this solution, the shape of the machine is not modified and the maximum performance can be obtained.

Epoxy resins are used in a wide area of engineering: in fact, they are used for adhesives, aerospace coatings and composite matrices thanks to their high mechanical performance. Epoxy resins present a high tensile strength, a high stiffness, a good chemical resistance and very good adhesive properties. It is possible to modify the mechanical and thermal properties of the resins by combining different types of additives [89]. The Young modulus and the tensile strength vary over 100% modifying the filler fraction as well as the adhesive strength [90]-[91].

The use of the epoxy resin in the electrical machine field is limited to:

- the impregnation of the AC rotors and stators (according to the motor typology) for a secondary insulation [92];
- the retainment of some mechanical parts, such as the rotor ring of an Axial-Flux Switched Reluctance Motor [93]-[94];

- the potting of the stator end-windings for a better heat exchange, thus reducing the maximum temperature [95];
- the realization of Soft Magnetic Composites by mixing the resin with iron powders [96]-[97];
- the improvement in the flux magnetic density of bonded NdFeB [98].

The adhesion properties can significantly change with the temperature variation; therefore, it is important to know the maximum operative temperature of the adhesive resin and the one reached by the motor in the specific application.

The literature shows that the thermal and adhesive properties of the resin can change along with the use of different epoxy matrices and fillers, up to certain limits. From the online datasheet of the material properties [99], it is worth noting that the values of the mechanical properties are quite different between the different resins. Therefore, in this subchapter, the best material properties are identified for the application of the high speed SynRel in electric vehicles.

The use of the epoxy resin does not require the use of complex optimization procedures because the barriers of the motor do not change. The study that must be carried out consists in a parametric evaluation of the properties of the resin in order to guarantee the rotor integrity at the maximum speed. For this reason, the mechanical analyses have been carried out on the rotor that presents a double asymmetry, but they are also valid for other solutions. The electromagnetic performance, at the end of this study, regards the symmetric rotor for a better comparison with the other proposed solutions.

The flux barriers have to be filled with adhesive epoxy resin in order to improve the mechanical strength of the rotor. As discussed before, the mechanical properties of the epoxy resin can be changed and, therefore, it is possible to “create” a custom resin for this application. From the available data, the Young modulus of the resin and its mass density can be varied in the range of $[750 \div 4500] \text{ kg/m}^3$ and $[1 \div 10] \text{ GPa}$, respectively. The presented results have been computed considering that the maximum speed of the rotor is equal to 16000 *rpm*, slightly lower than the one of the other designs since the constraints are too stringent.

Figure 7.13 reports the equivalent von Mises stress in the electrical steel in function of the Young modulus of the generic resin and parametrized respect to the mass density. It has been considered a maximum admitted steel stress equal to 360 *MPa* with a safety coefficient of 1.5. The lower the resin density, the lower the stress of the steel; on the other hand, increasing the Young modulus of the resin, the maximum stress of the steel is reduced. The constraint of the maximum admitted

stress in the steel (360 MPa) is satisfied for all the values of the density if the Young modulus is higher than 7 GPa.

With lower values of resin density, it is possible to reduce the Young modulus in order to satisfy the constraint.

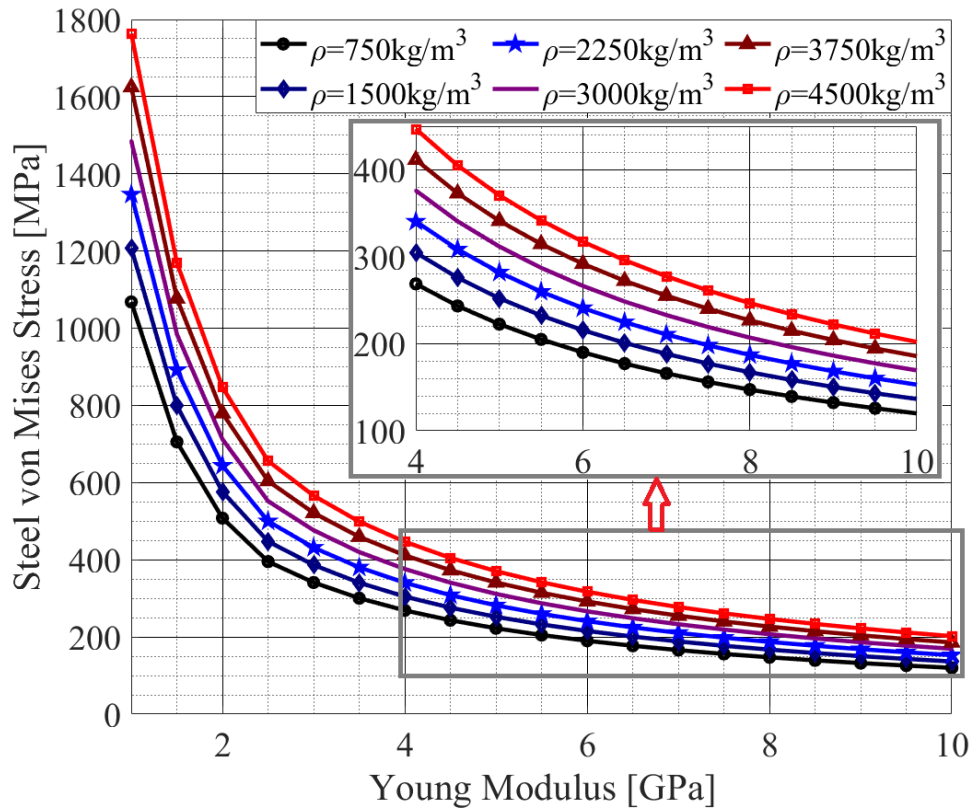


Figure 7.13: Equivalent von Mises stress in the electrical steel.

Figure 7.14 shows the equivalent von Mises stress in the resin in function of the Young modulus of the generic resin and parametrized respect to the density.

The resin stress is maximum for the highest value of the density and for the lowest value of the Young modulus. For the resin stress, the worst possible case that satisfies the constraint requires a density equal to 4500 kg/m³ (the maximum evaluated value) and a Young modulus equal to 7 GPa (the minimum value that satisfies the constraint). In this conditions, the maximum stress inside the resin is equal to 13.5 MPa.

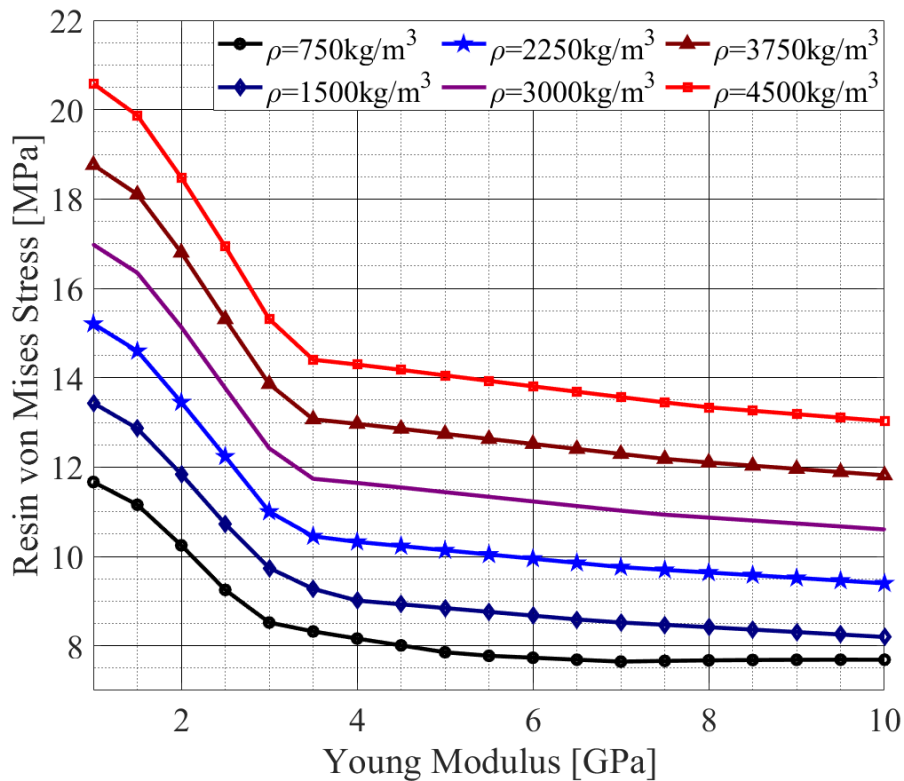


Figure 7.14: Equivalent von Mises stress in the resin.

Figure 7.15 shows the contact pressure between the resin and the electrical steel in function of the Young modulus of the generic resin and parametrized respect to the density. The adhesion of the resin is one of the most critical aspects, especially when the resin is used for both adhesive and structural elements of the motor and when it is used for large sections (as filler of the rotor barriers). In order to easier satisfy the requirements of the resin, the required adhesive strength of the resin should be the minimum possible. From the following figure, it is worth noting that for this parameter, the higher the mass density and the young modulus of the resin, the higher the contact pressure. Considering the maximum mass density value of the resin (4500 kg/m^3), the best condition is verified for the minimum Young modulus value, which is equal to 7 GPa , in order to satisfy the requirement. In this condition, the minimum adhesive strength needed to guarantee the adhesion is equal to 25 MPa .

Figure 7.16 shows the maximum steel deformation near the airgap in function of the Young modulus of the generic resin and parametrized respect to the density. The behavior of this result is the same of the equivalent von Mises stress in the steel and, considering the same critical conditions, the maximum airgap deformation is equal to $45 \mu\text{m}$ (which is about 7% of the airgap itself).

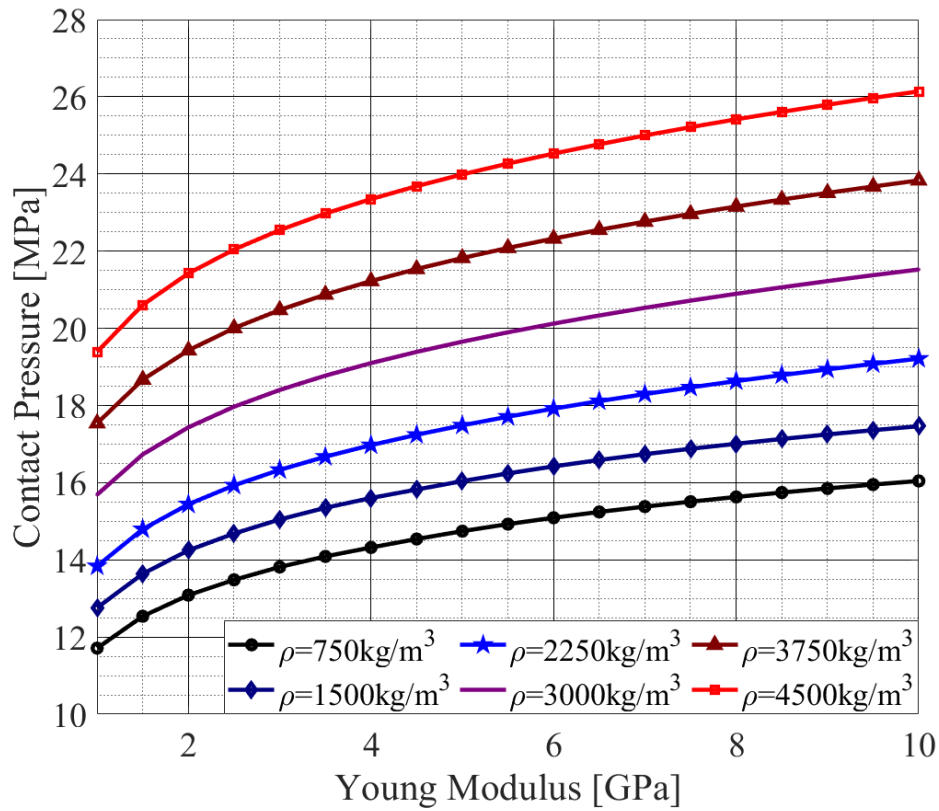


Figure 7.15: Contact pressure between the resin and the electrical steel.

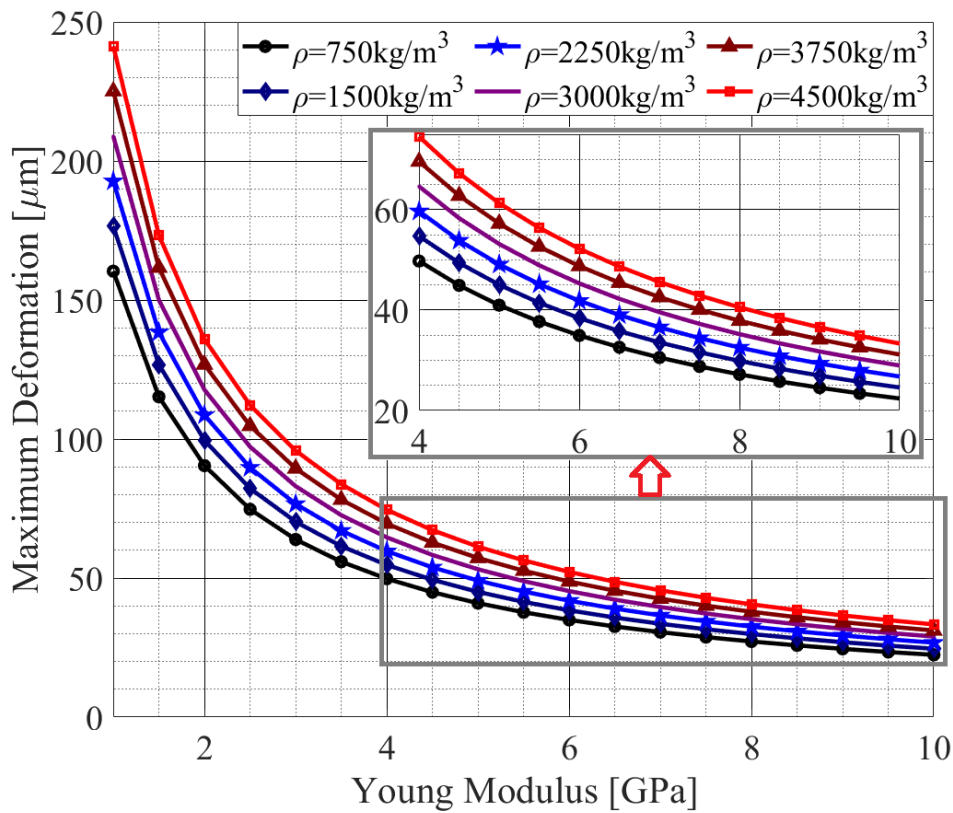


Figure 7.16: Maximum steel deformation near the airgap.

From the presented results, it is possible to calculate, in function of the resin mass density, the minimum Young modulus of the resin that satisfies the constraints imposed by the electrical steel, which are reported in Table 7.1. The minimum Young modulus has been chosen in order to minimize the required adhesion force. All these properties have to be maintained up to the maximum temperature reached by the resin, that for the S1 condition could be similar to the one reached by the windings (over than 100°C).

Table 7.1: Mechanical results.

Density [kg/m ³]	Young modulus [GPa]	Steel stress [MPa]	Resin stress [MPa]	Contact pressure [MPa]	Airgap Def. [μm]
750	2.6422	380	9.044	13.575	71.658
1500	3.0713	380	9.676	15.088	69.015
2250	3.5058	380	10.449	16.675	66.965
3000	3.9562	380	11.653	19.069	65.340
3750	4.4090	380	12.878	21.479	64.014
4500	4.8635	380	14.086	23.904	62.916
750	2.6422	380	9.044	13.575	71.658
1500	3.0713	380	9.676	15.088	69.015

As an example, a further stress analysis has been carried out on the resin with a density of 1500 kg/m³ (one of the most frequent values) and with the best Young modulus value to minimize the contact pressure, as shown in Table 7.1.

Figure 7.17 shows the equivalent von Mises stress in the electrical steel, the details of the most critical parts and the mesh used for the rotor. The maximum stress can be found in the fillet of the radial ribs; the distributions for the other values of density and Young modulus of the resin are quite similar.

Figure 7.18 reports the equivalent von Mises stress in the resin, the details of the most critical parts and the mesh used for the resin. This last one is finer than the mesh used for the rotor in order to obtain a correct computation of the contact pressure between the steel and the resin, which is presented in Figure 7.19. The negative values indicate a force that tries to separate the bodies and these forces are critical to be analyzed. For this reason, the values reported in Table 7.1 are the minimum ones.

Figure 7.20 shows the deformations of the electrical steel; the maximum values can be found near the airgap in correspondence of the q -axis but, there, the mechanical airgap is increased due to the presence of the notch, hence avoiding possible contacts between the stator and the rotor. Therefore, in Table 7.1 and in Figure 7.16, the maximum airgap reduction is reported.

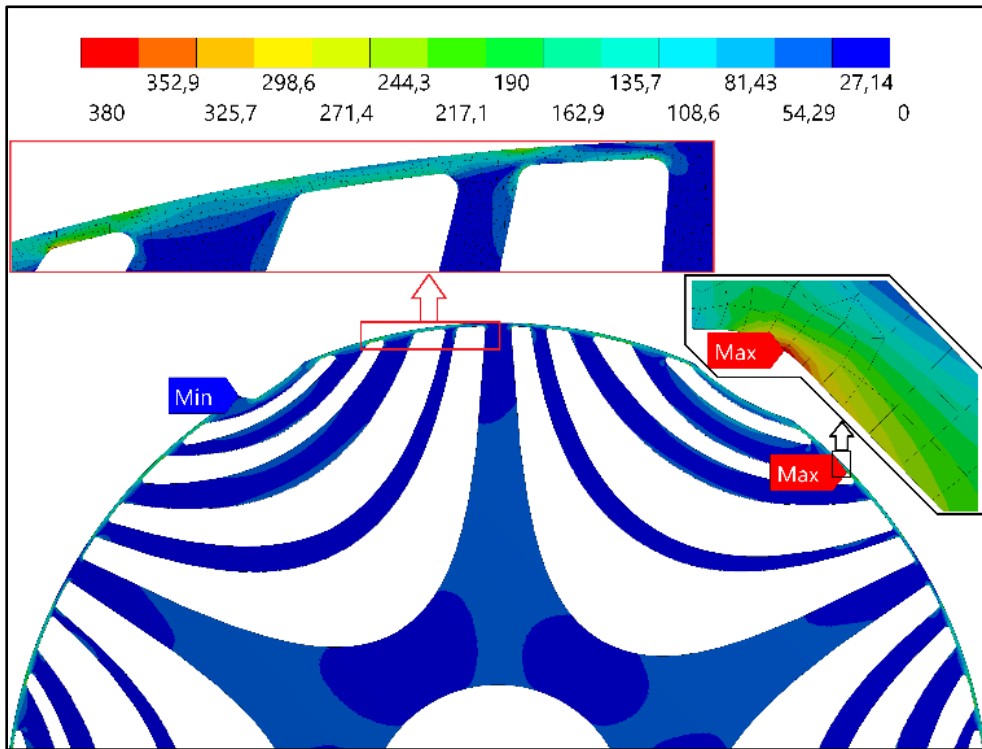


Figure 7.17: Equivalent von Mises Stress in the electrical steel in MPa.

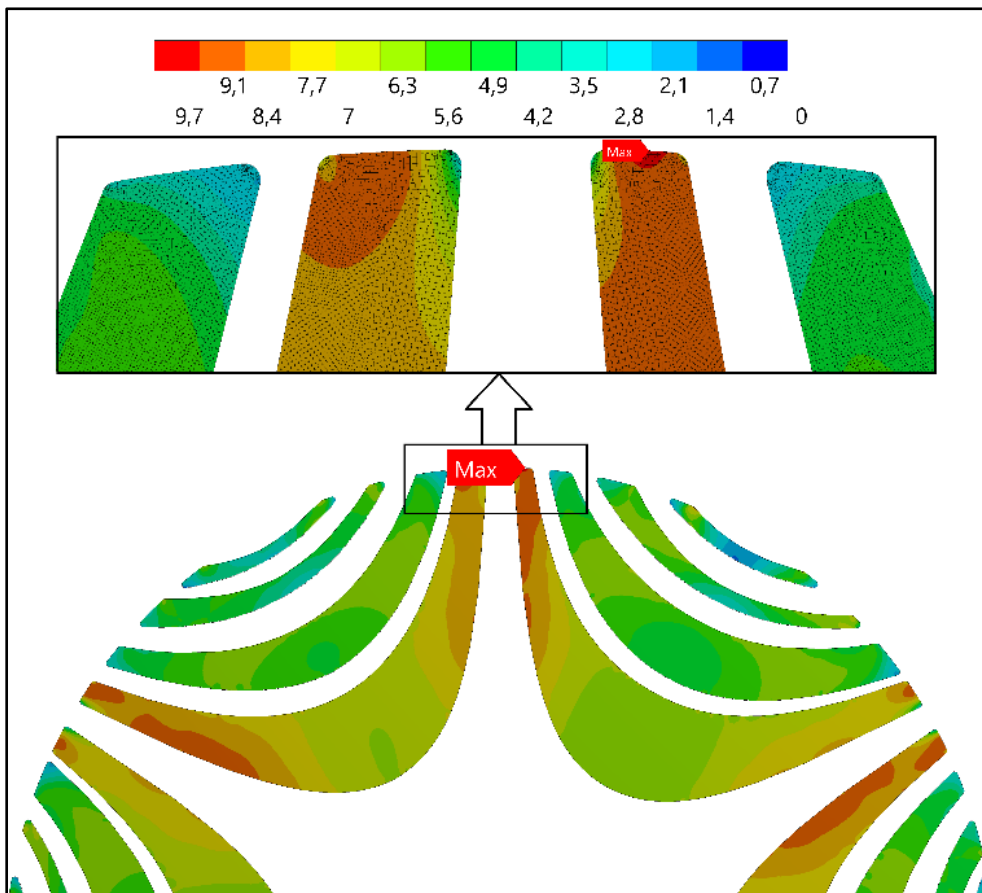


Figure 7.18: Equivalent von Mises Stress in the resin in MPa.

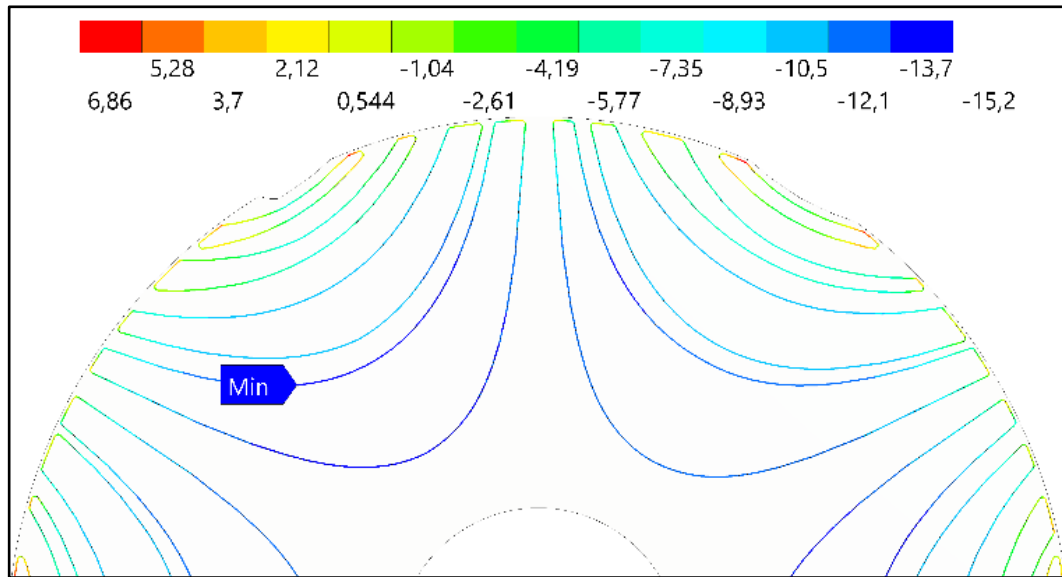


Figure 7.19: Contact pressure between the resin and the electrical steel in MPa.

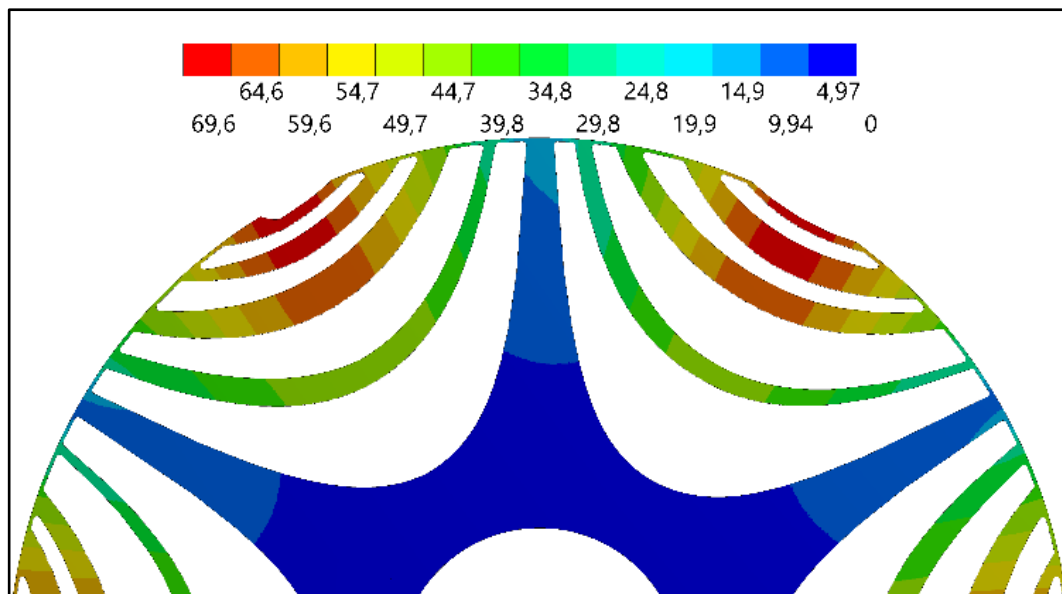


Figure 7.20: Electrical steel deformations in μm .

Figure 7.21 reports the rotor deformations near the airgap: the maximum deformation for the notch at the airgap is of $51 \mu\text{m}$, slightly higher than the ones obtained by the radial rib and the optimized topology solutions but acceptable for this type of application. Figure 7.22 shows the direct and quadrature inductances and the saliency ratio over the speed range in the maximum torque points. Up to the base speed, the d - and q -inductances have low values due to the saturation, together with the saliency ratio; over the base speed, the d -inductance increases because there is a lower saturation, but the q -inductance maintains the same value because the tangential ribs reach the saturation condition also with a low current.

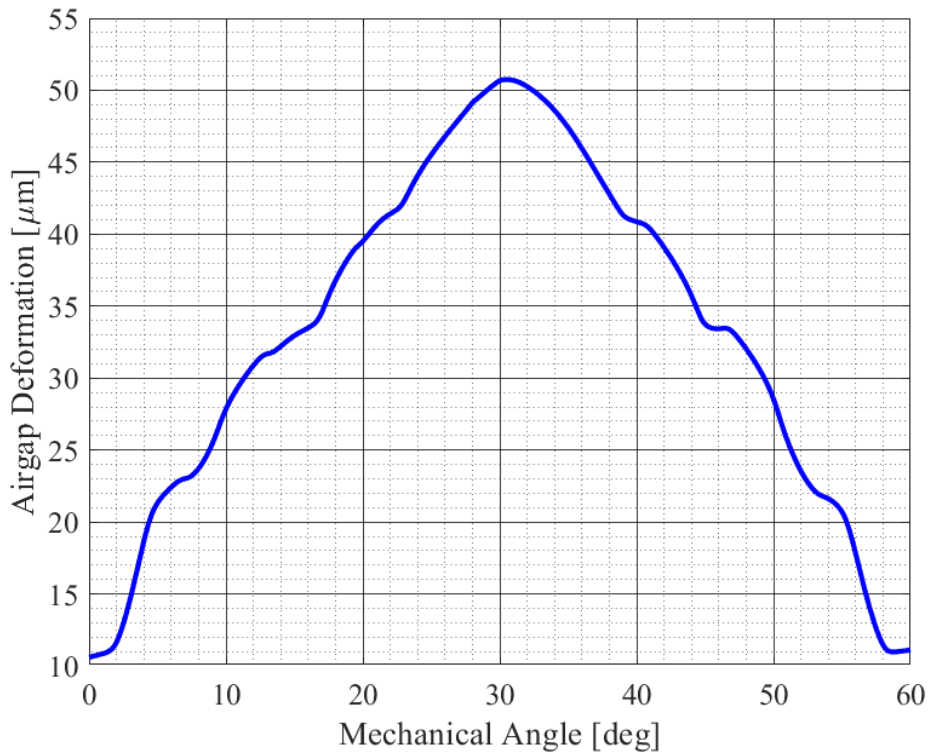


Figure 7.21: Airgap deformations [μm] of the epoxy resin filled rotor.

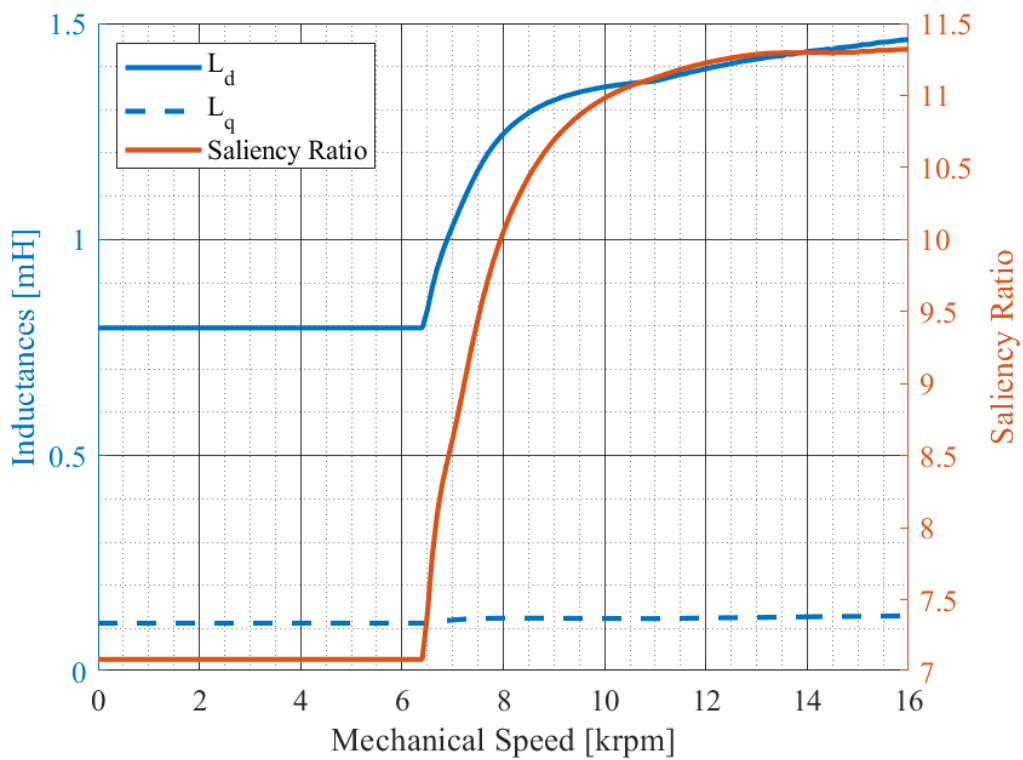


Figure 7.22: d - and q -axis inductances and saliency ratio over the speed range of the epoxy resin filled rotor.

Figure 7.23 reports the performance of the motor over the speed range in terms of maximum torque and power. Compared to the radial rib design and to the optimized topology solution, the torque at base speed has been improved and the power at maximum speed is much higher. Considering the electric vehicle application, due to the rotor impossibility of reaching the maximum speed of 18000 *rpm*, a different gear ratio has to be used, thus reducing the equivalent torque but increasing the speed. The peak torque at base speed moves from a value of 350 *Nm* to 386 *Nm*, with an improvement of 10.3%, while the maximum power at maximum speed has an increase of about 700%, passing from 20 *kW* to 140 *kW*; the base speed moves from 6300 *rpm* to 7200 *rpm*. Another advantage of this solution is an improvement in the efficiency of the mechanical transmission because it uses a lower gear ratio.

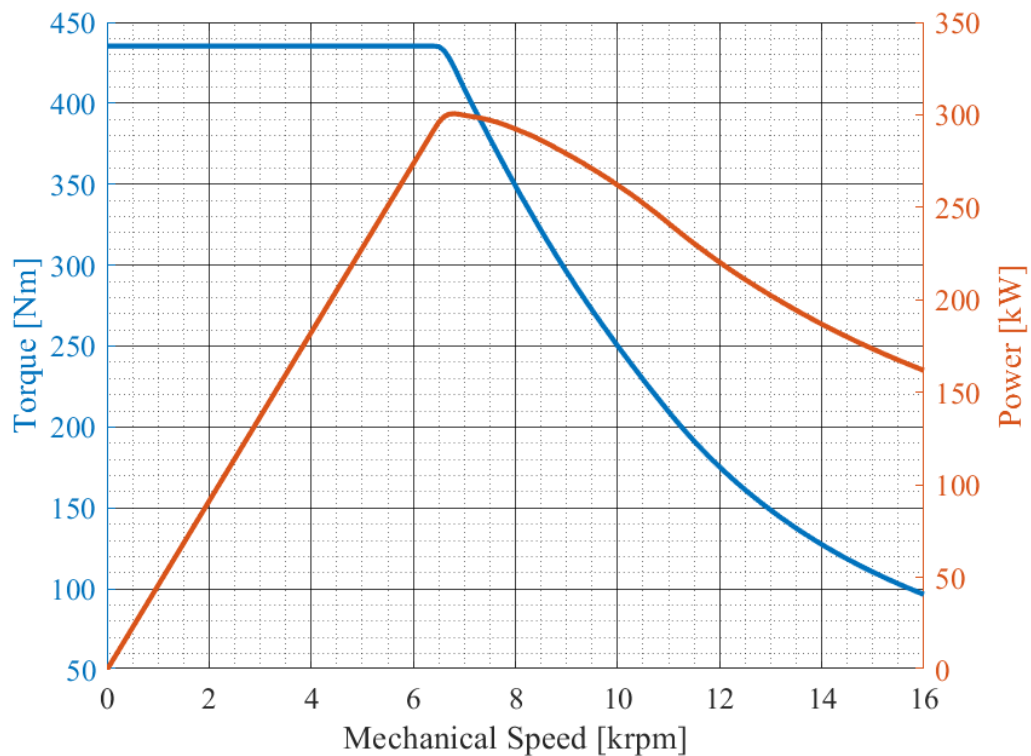


Figure 7.23: Maximum torque and power over the speed range of the epoxy resin filled rotor.

7.4 Comparison of the proposed solutions

This subchapter provides a brief comparison between the different solutions in order to evaluate the improvement due to a novel approach for the optimization and to the use of innovative materials and technologies. For this comparison, the values of the epoxy resin filled rotor have been reported to the same maximum speed considering a different gear ratio.

Figure 7.24 shows the deformations of the rotor at the airgap for each proposed solution at their maximum speed. In each design, the deformation is under 10% of the airgap, as imposed by the constraint and with a good margin to avoid the contact between the rotor and the stator. The deformations have similar values as well as the stress inside the steel for the different solutions.

Figure 7.25 reports the saliency ratio over the equivalent speed range (as discussed in the previous subchapter, the maximum speed of the epoxy resin filled rotor is different). From the figure, it is clear how the epoxy resin filled rotor is able to reach the best performance: in fact, the saliency ratio of this solution, past the base speed, never decreases, hence guaranteeing the best performance in the flux-weakening region; moreover, its value at the base speed is higher than the other solution ones. The optimized topology rotor has a higher value compared to the radial rib one: at the maximum speed, the saliency ratio has a double value, showing better flux-weakening capabilities. The lower widths of the rotor ribs allow to reach the saturation with lower currents.

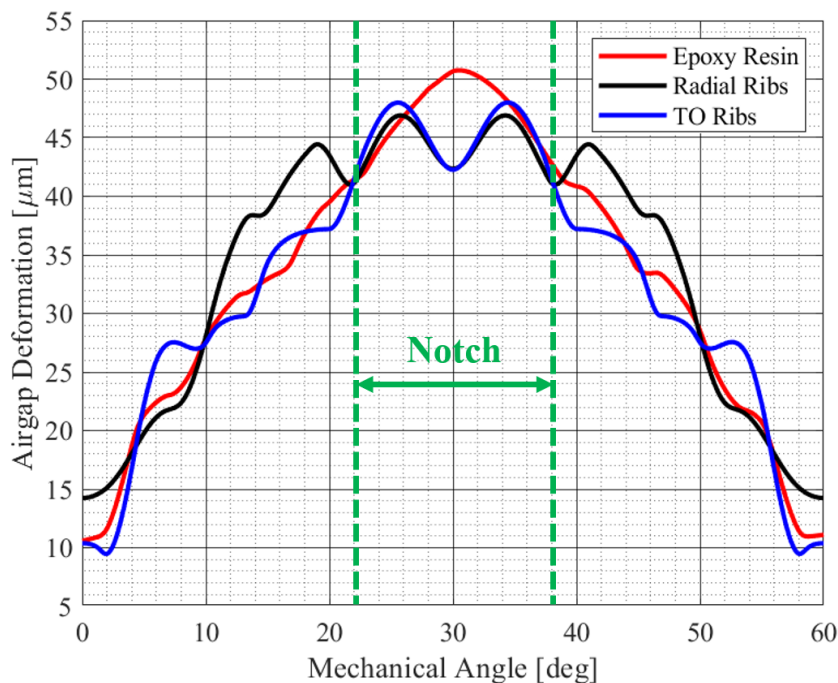


Figure 7.24: Deformations at the airgap of the proposed SynRel solutions.

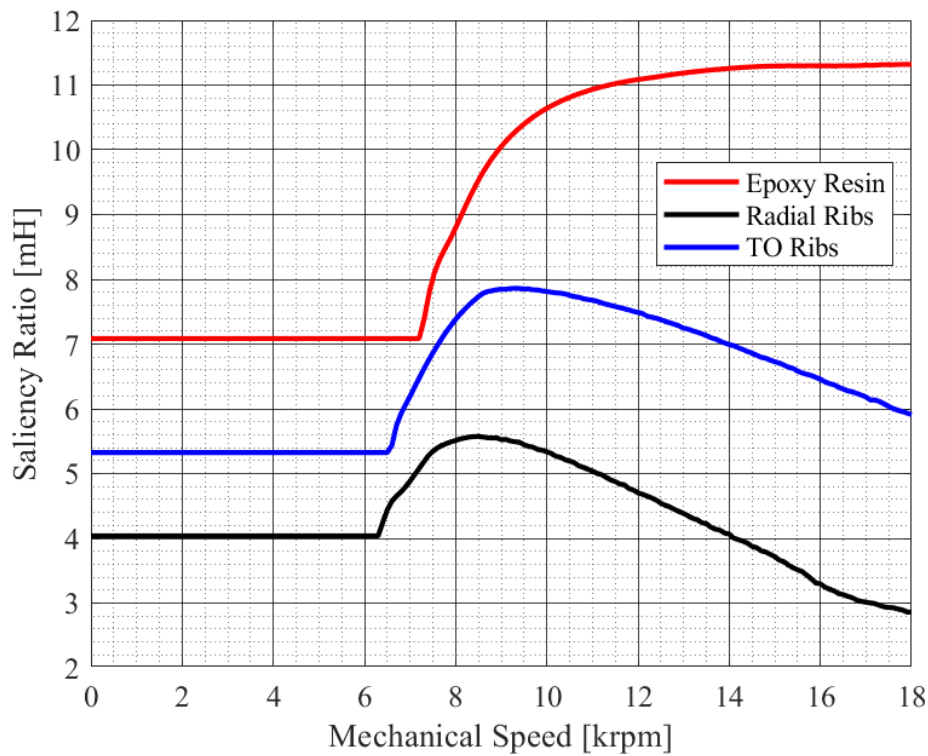


Figure 7.25: Saliency ratios over the equivalent speed range of the proposed SynRel solutions.

Figure 7.26 and Figure 7.27 present the behaviors of the d -axis and q -axis inductances of the proposed solutions over the equivalent speed range. The radial rib solution shows a higher direct inductance: this is due to the cross coupling introduced by the radial ribs since the flux has a higher part of steel, thus reducing the reluctance and increasing the inductance. This effect is the same for the q -axis with a similar increase of the inductance, thus reducing the saliency ratio, as shown in the previous figure3. The increase of the axis inductances means an increase of the motional term of the voltage, with a consequent reduction of the flux-weakening capability of the machine. The optimized topology rotor shows a behavior that is in the middle of the epoxy resin filled rotor and the radial rib one.

Figure 7.28 and Figure 7.29 show the electromagnetic torque and power of the motor over the speed range for the proposed solutions. The optimized topology rotor allows to gain up to 200% more power at maximum speed respect to the solution with radial ribs, but the epoxy resin filled rotor guarantees the best performance with a power at maximum speed that is three times the one of the optimized topology rotor and eight times the one of the radial rib solution.

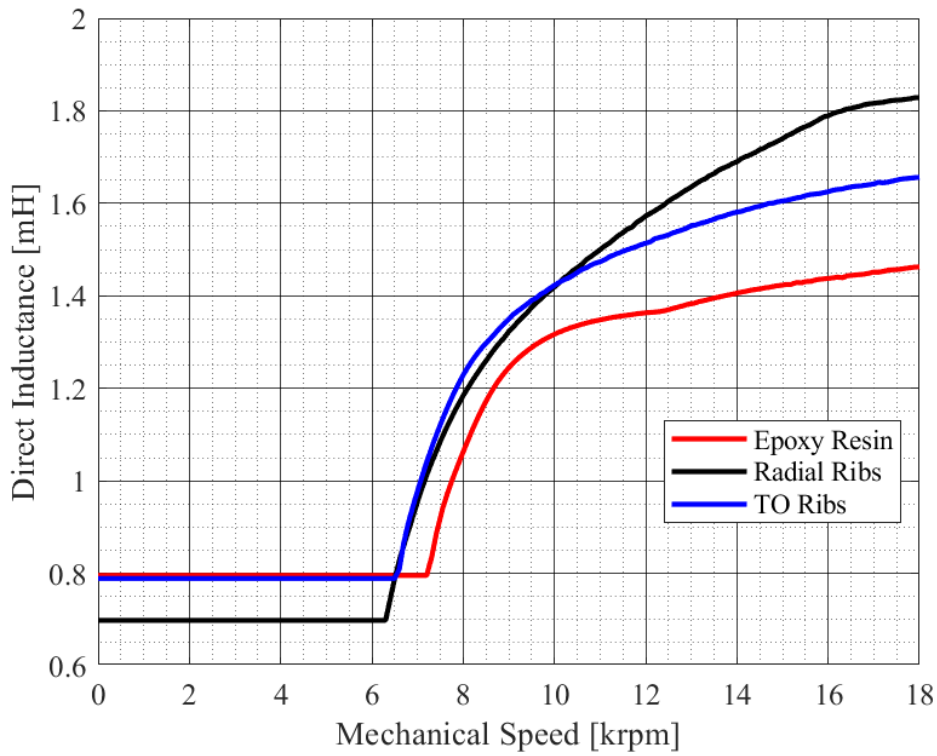


Figure 7.26: d -inductance over the equivalent speed range of the proposed SynRel solutions.

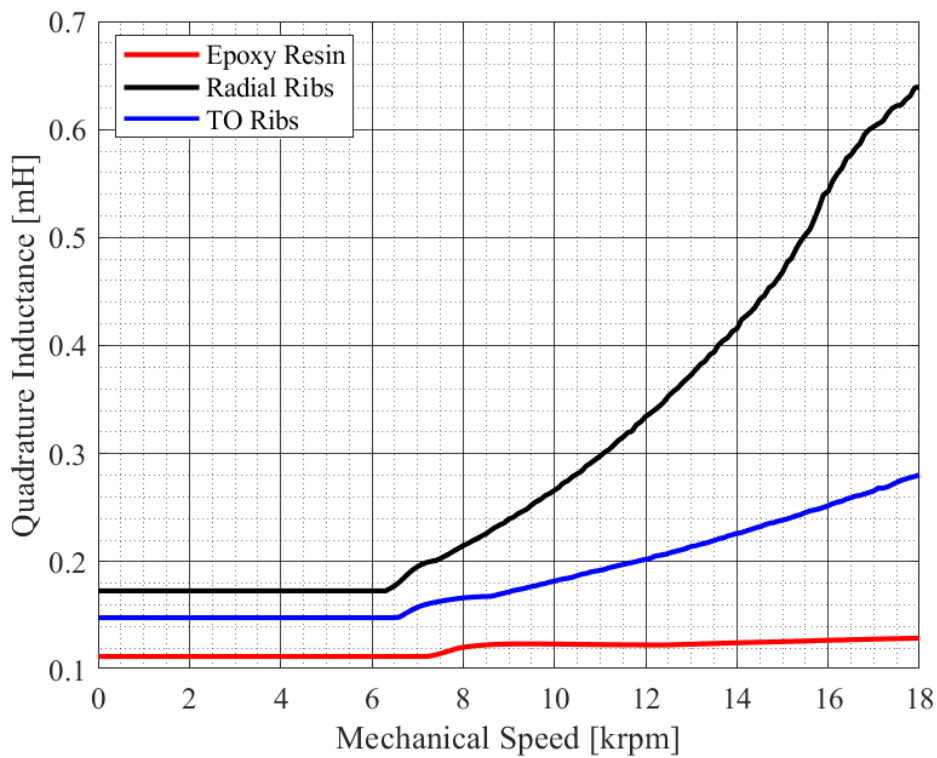


Figure 7.27: q -inductance over the equivalent speed range of the proposed SynRel solutions.

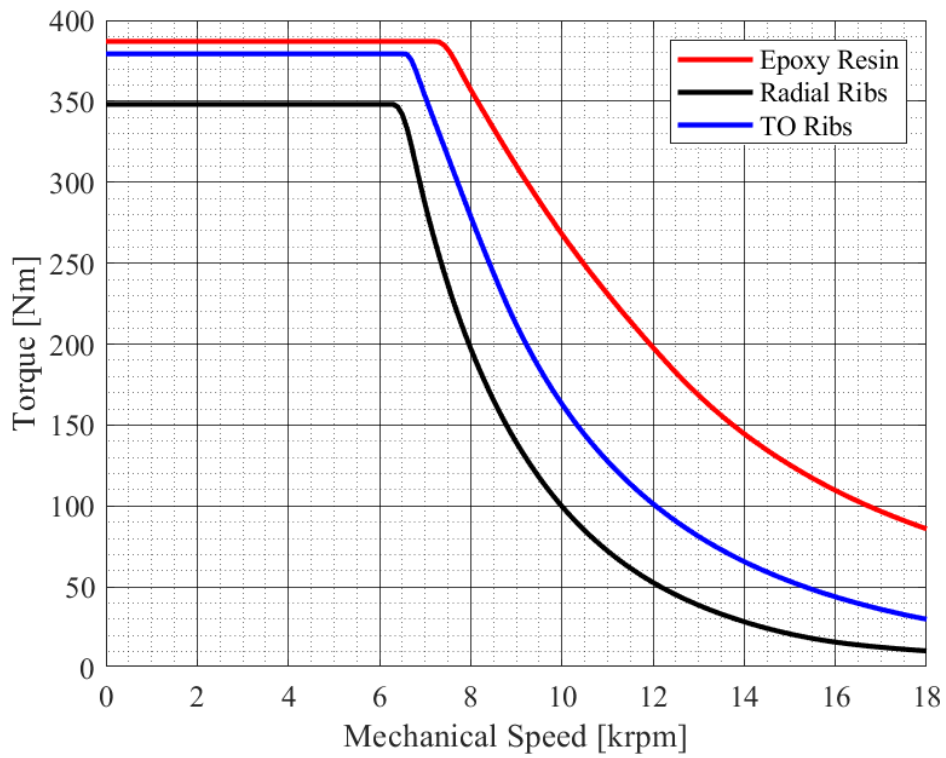


Figure 7.28: Torque over the equivalent speed range of the proposed SynRel solutions.

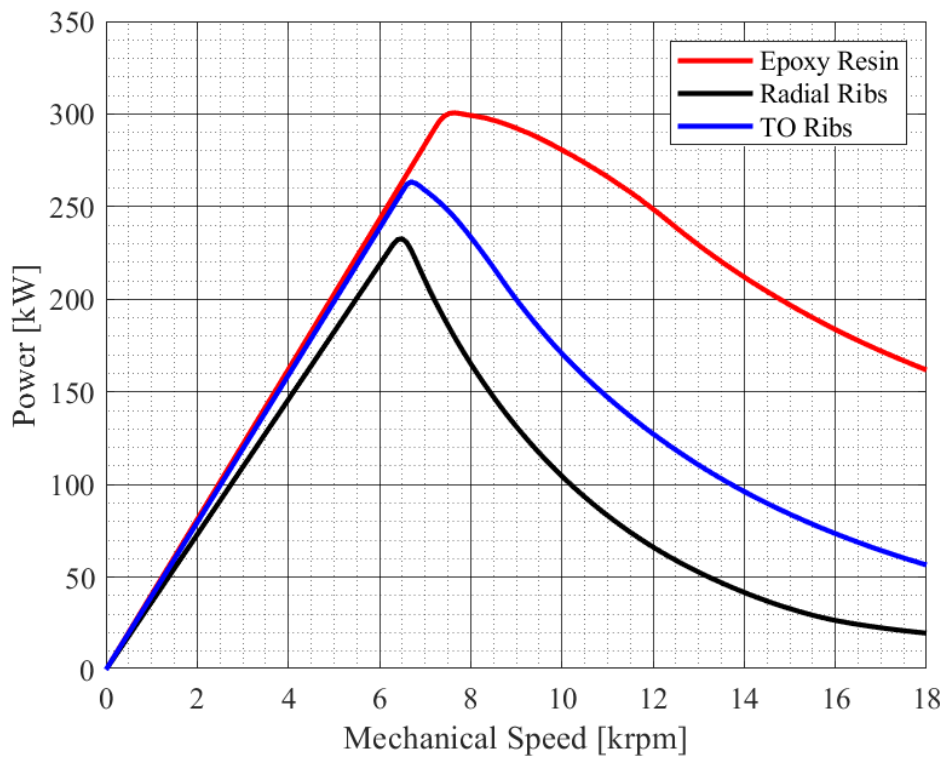


Figure 7.29: Power over the equivalent speed range of the proposed SynRel solutions.

Table 7.2: Comparison of the proposed solutions.

Performance	Unit	Epoxy Resin	Radial Ribs	Optimized Topology
Peak Torque	<i>Nm</i>	390	350	380
Peak Power	<i>kW</i>	300	230	260
Power @ Max Speed	<i>kW</i>	160	20	54
Power Factor @ Peak Power		0.64	0.46	0.51
Power Factor @ Max. Speed		0.61	0.41	0.46
Peak Efficiency	%	97.6	96.9	97.1
Torque Ripple	%	20	30	25
Max Airgap Deformation	%	5.8	6.3	5.8

The epoxy resin filled rotor is the best solution for each performance, but its use is critical due to the required properties of the epoxy resin (no commercial resin is available) and to the high range of the resin. Further studies on the resin have been carried out in order to define the composite matrix and filler that guarantee all the needed properties. For these reasons, in the next chapter, the epoxy resin filled rotor will not be considered for the design and for the manufacturing.

The optimized topology rotor is able to improve the performance respect to the radial rib one, despite the complexity of its geometry, since no additional costs or manufacturing concerns are expected: in fact, this solution is a good candidate for the design and the prototyping of ReFreeDrive motors, which will be presented in the next chapter.

Chapter 8

Two Case Studies: 200 and 75 kW SynRel Designs

This chapter applies the concepts illustrated in the previous chapters for the design of two sizes of SynRel motors (200 kW and 75 kW of peak powers, respectively) as part of the ReFreeDrive project (explained in section 2.3.1). The design of these motors can be used as a case study, which is useful for the evaluation of the sizing procedure for high speed SynRels.

In subchapter 8.1, the requirements of the project, that directly come from the initial project aim, are presented. Subchapter 8.2 summarizes the used design procedure; the rotor skewing is discussed in subchapter 8.3 as a method for a further reduction of the torque ripple, then its main advantages and drawbacks are illustrated.

Subchapter 8.4 presents the performance of the 75 kW motor design.

Subchapter 8.5 and subchapter 8.6 show the prototyping steps and the experimental results.

8.1 Requirements

The requirements of the European Project H2020 ReFreeDrive have been imposed on the basis of a reference vehicle motor (IM of the Tesla Model S60, 2012): in particular, they were seeking a 30% increment in the specific power and a 50% reduction in the motor losses. In addition to that, a partner of the project (Jaguar - Land Rover) has imposed additional constraints in order to guarantee the maximum speed and acceleration performance of the vehicle.

The requirements for the motors of 200 kW and of 75 kW are shown in Table 8.1 and Table 8.2, respectively. The two motors must have the same shape for scalability reasons.

Table 8.1: Requirements of the 200 kW ReFreeDrive SynRel motor.

Requirements	Unit	Value	Requirements	Unit	Value
DC Voltage	V	800	Torque @ Base Speed	Nm	≥ 360
Phase Current	A	≤ 820	Base Speed	rpm	≥ 5300
Specific Peak Power	kW/kg	≥ 4.3	Power @ Base Speed	kW	≥ 200
Peak Power Density	kW/l	≥ 8.0	Torque Ripple @ Base S.	%	≤ 15
Specific Peak Torque	Nm/kg	≥ 8.2	Power @ Max. Speed	kW	≥ 75
Peak Torque Density	Nm/l	≥ 15.4	Maximum Speed	rpm	18000
Stack Length	mm	≤ 202	Torque @ Max. Speed	Nm	≥ 32
Outer Stator Diameter	mm	≤ 220	Torque Ripple @ Max S.	%	≤ 20
Active Parts Weight	kg	≤ 47	Peak Efficiency	%	≥ 96

Table 8.2: Requirements of the 75 kW ReFreeDrive SynRel motor.

Requirements	Unit	Value	Requirements	Unit	Value
DC Voltage	V	350	Torque @ Base Speed	Nm	≥ 170
Phase Current	A	≤ 620	Base Speed	rpm	≥ 4200
Specific Peak Power	kW/kg	≥ 1.6	Power @ Base Speed	kW	≥ 75
Peak Power Density	kW/l	≥ 3.0	Power @ Max. Speed	kW	≥ 25
Specific Peak Torque	Nm/kg	≥ 3.0	Maximum Speed	rpm	12000
Peak Torque Density	Nm/l	≥ 6.0	Torque @ Max. Speed	Nm	≥ 20
Stack Length	mm	≤ 100	Peak Efficiency	%	≥ 94

Since the requirements have been imposed in terms of peak torque at base speed and maximum power at maximum speed, it is not necessary to use the model of the vehicle and its requirements in terms of acceleration (0-100 km/h) and maximum speed. Considering the requirements of the 200 kW motor (Table 8.1), it is possible to understand that the application of destination for this electric motor is a high performance vehicle with low acceleration time (less than 4 seconds) and high driving speeds (over 230 km/h).

8.2 The Design Procedure

The design procedure has focused its attention on the 200 kW size since it has stricter requirements; the 75 kW design will therefore be obtained by modifying the stack length and the number of turns of the first motor design.

The design procedure starts with the preliminary design; in this case, there are no constraints for the choice of the number of poles, slots, and barriers. Therefore, several preliminary designs carried out using the equations presented in subchapter 4.1 have been analyzed just varying the number of poles, slots, and barriers. From these first evaluations, three solutions have been identified and chosen for a further optimization. The candidates have the following combinations:

- 4 poles, 36 slots, and 4 barriers plus a notch.
- 6 poles, 54 slots, and 4 barriers plus a notch.
- 8 poles, 75 slots, and 4 barriers plus a notch.

Starting from these designs, the optimizations of the machines (including the stator and rotor variables) have been carried out in order to find the best solution. Considering that these preliminary optimizations do not take into account the effects of the inner rib insertion, the constraints have been slightly increased respect to the ones imposed by the initial requirements. Thereafter, the Topology Optimization has been carried out on the best candidate with the aim of identifying the following best parameters for the inner ribs of each air barrier: the number, the starting position, the width, and the inclination.

For this analysis, four simulation points have been considered: the peak torque at base speed (P1), the maximum power at maximum speed (P2), the estimated maximum efficiency point (considered in correspondence of 33% of the maximum torque and of 50% of the maximum speed, P3), and the last point characterized by a low torque and a low speed to try to represent the WLTP cycle 3 (P4).

The constraints, the objective function and the design variables that have been used are reported in Table 8.3 (where DV stands for Design Variables), whose symbolism has been explained in Table 5.2. The constraints regarding the torque ripple have been chosen equal to the ones of the requirements since the introduction of the inner ribs could increase it but, in order to further reduce the torque ripple, asymmetric solutions can be adopted (Chapter 6). The constraint about the efficiency in P3 has been increased, as well as the ones of the peak torque at base speed and the base speed itself. In this way, once that the inner ribs are inserted in the flux barriers, there will be sufficient margin to satisfy the requirements. For the objective function, it has been decided to use the maximum torque at maximum

speed because this one is the performance mainly affected by the inner ribs: in fact, the maximum torque at maximum speed is the most critical value.

Table 8.3: Design Variables and Constraints.

DV	DV	DV	Constraints	Unit	Value	Constraints	Unit	Value
O_{RD}	X_3	$\varepsilon @ P1$	Torque @ P1	Nm	≥ 410	Ripple @ P1	%	≤ 15
S_W	R_3	$I_{ph} @ P2$	Speed @ P1	rpm	5500	Ripple @ P2	%	≤ 20
S_H	X_4	$\varepsilon @ P2$	Speed @ P2	rpm	18000	Efficiency @ P3	%	≥ 97
X_1	R_4	$I_{ph} @ P3$	Torque @ P3	Nm	≈ 140	Efficiency @ P4	%	≥ 95
R_1	X_5	$\varepsilon @ P3$	Speed @ P3	rpm	9000	$V_{ph} @ \text{All Ps}$	V	≤ 400
X_2	T_{TA}	$I_{ph} @ P4$	Torque @ P4	Nm	≈ 20	Objective Function		
R_2	$I_{ph} @ P1$	$\varepsilon @ P4$	Speed @ P4	rpm	2000	Maximization of Torque @ P2		

The results of the optimization in terms of stator and rotor shapes are shown in Figure 8.1, Figure 8.2, and Figure 8.3, while the performance of these three solutions are listed in Table 8.4.

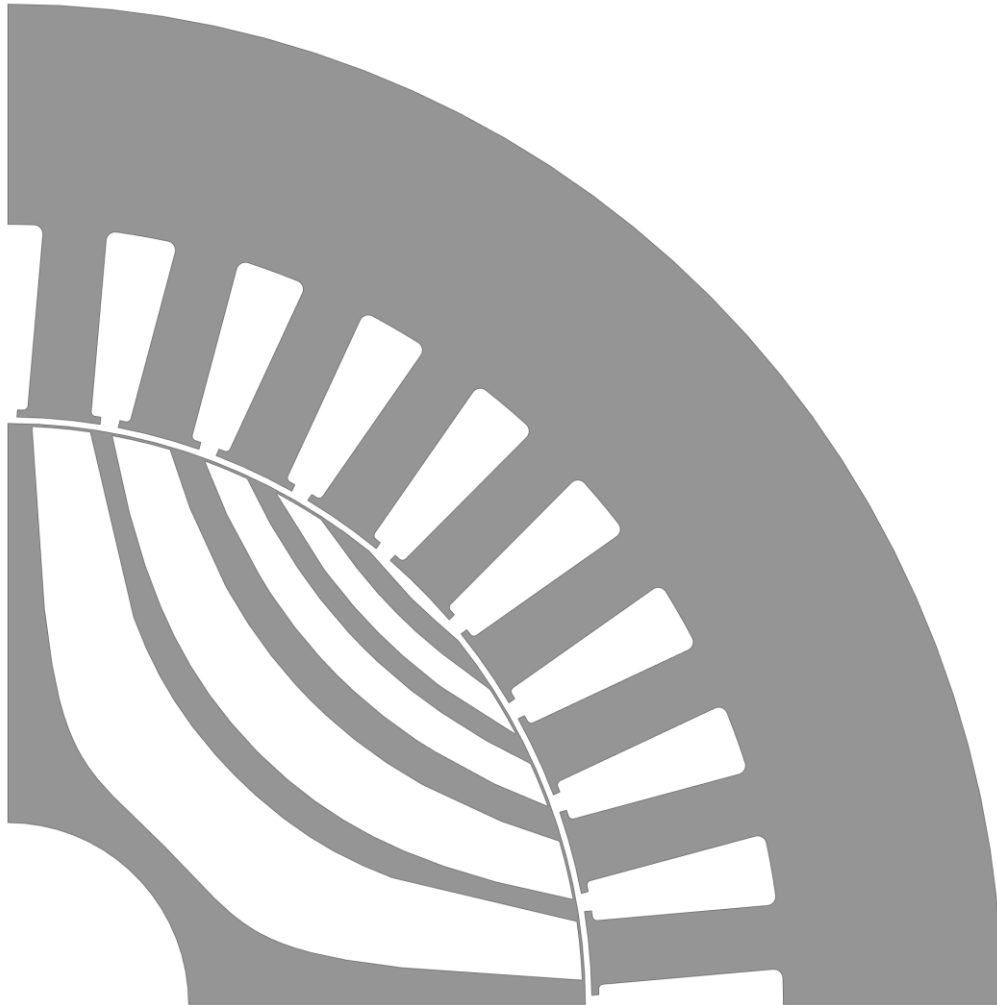


Figure 8.1: Stator and rotor cross section of the optimized 4-pole design.



Figure 8.2: Stator and rotor cross section of the optimized 6-pole design.



Figure 8.3: Stator and rotor cross section of the optimized 8-pole design.

Table 8.4: Comparison between the optimized solutions.

Performance	Unit	4-pole design	6-pole design	8-pole design
Torque @ P1	<i>Nm</i>	410	410	410
Torque @ P2	<i>Nm</i>	94	110	78
Torque @ P3	<i>Nm</i>	139	139	141
Torque @ P4	<i>Nm</i>	20	21	21
Ripple @ P1	%	14	15	14
Ripple @ P2	%	20	20	20
Efficiency @ P3	%	97.3	97.2	97.1
Efficiency @ P4	%	95	95	95

The solution with the highest number of poles is able to adopt a greater shaft diameter, meanwhile the other two solutions are forced to use the minimum shaft diameter possible, which is imposed by their mechanical limits. If the minimum shaft diameter were greater than the considered one (40 mm), the obtained results could be different, hence making the 8-pole solution the best one.

The three solutions have similar results in terms of torque in P1 and of torque ripples; the 4-pole design presents the best efficiency in P3, but the 6-pole one has the highest torque production at maximum speed. Since this last performance is the most critical one, the 6-pole solution has been chosen for further optimizations.

The next step consists in the insertion of the inner ribs (with the aid of the TO) within the symmetric structure, as it has been done in subchapter 7.2. The rotor structure is quite similar to the one obtained in that subchapter and the results are the same: in the first and in the second barrier there are 4 ribs, in the third barrier there are 2 ribs and in the fourth barrier there is only one rib.

Therefore, a further magneto-structural optimization has been carried out for further improvements of the machine performance. The optimization uses the same variables employed in the optimization of subchapter 7.2: with those variables, it has been possible to obtain a similar final shape. The constraints of this optimization are equal to the requirements in Table 8.1, with the addition of the maximum equivalent von-Mises stress in the rotor, which is equal to 360 MPa with a safety coefficient of 1.6 (the ultimate tensile strength of the selected electrical steel is 540 MPa). The performance of this optimized shape is shown in Table 8.5.

Table 8.5: Performance of the optimized topology solution.

Requirements	Unit	Value	Requirements	Unit	Value
Torque @ P1	<i>Nm</i>	355	Ripple @ P1	%	30
Torque @ P2	<i>Nm</i>	44	Ripple @ P2	%	40
Torque @ P3	<i>Nm</i>	139	Efficiency @ P3	%	95.8
Torque @ P4	<i>Nm</i>	21	Efficiency @ P4	%	90.9

The new solution has a lower performance compared to the one of the same design without inner ribs; in addition, it does not satisfy the requirements (the unsatisfactory values are in bold in the table). Since the torque ripple values are not satisfied, it is possible to apply the asymmetry principles discussed in Chapter 6. The adoption of the asymmetry can reduce the torque ripple while improving the torque for the main direction of rotation; therefore, it can be possible to satisfy the requirements. In the first step, the asymmetry solution discussed in subchapter 6.2 combined to the results of the topology optimization has been adopted for the reduction of the torque ripple. The solution includes an asymmetry inside the pole, which can be defined by 9 variables, while the position, the width and the inclination of the inner ribs can be defined by 17 variables: 6 variables for the inner ribs of the first barrier; 6 variables for the inner ribs of the second barrier; 3 variables for the inner ribs of the third barrier; 1 variable for the inner rib of the fourth barrier; 1 variable for the fillets of each inner rib. The fillets of the tangential ribs have been fixed according to the results obtained during the study of the topology optimization for the symmetric solution. The total variable number for the magneto-structural optimization is 26. The new rotor shape is shown in Figure 8.4, while its performance has been displayed in Table 8.6.

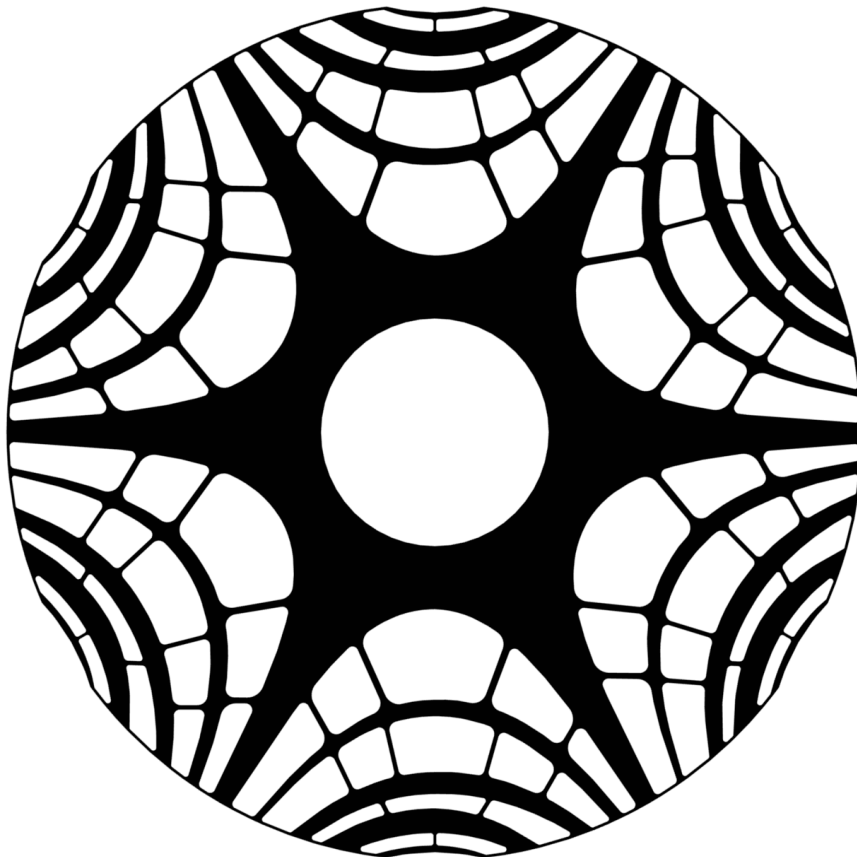


Figure 8.4: Rotor shape of the solution with inner ribs and an asymmetry in the pole.

Table 8.6: Performance of the optimized topology solution with an asymmetry in the pole.

Requirements	Unit	Value	Requirements	Unit	Value
Torque @ P1	Nm	384	Ripple @ P1	%	32
Torque @ P2	Nm	47	Ripple @ P2	%	28
Torque @ P3	Nm	139	Efficiency @ P3	%	95.9
Torque @ P4	Nm	21	Efficiency @ P4	%	90.9

The adoption of an asymmetric rotor allows to satisfy the requirement of the peak torque at base speed, but the efficiency in P3 and the torque ripple are not yet satisfied. According to the procedure that can be found in Chapter 6, a new asymmetry has been introduced: the rotor has been designed with adjacent different poles (subchapter 6.3). Then, the first rotor pole is the same of the symmetric solution while the second rotor pole is obtained through a new optimization. The new pole can be defined by nine variables, which can be used to design the flux barriers and the notch; likewise, the number of variables used for the inner ribs is the same of the previous optimizations. Therefore, the total number of variables is equal to 26. This further step is useful to define the geometry of the new pole; thereafter, it is possible to introduce the last asymmetry to reach the best performance possible. The new rotor shape is shown in Figure 8.5, while its performance is indicated in Table 8.7.

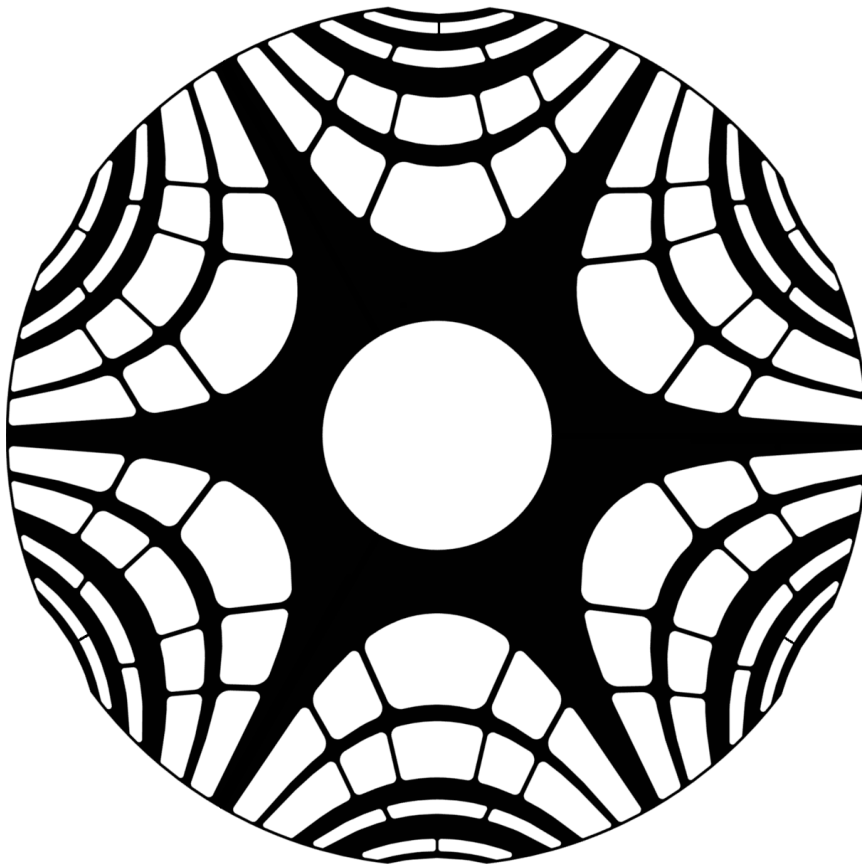
**Figure 8.5: Rotor shape of the solution with inner ribs and different adjacent poles.**

Table 8.7: Performance of the optimized topology solution with different adjacent poles.

Requirements	Unit	Value	Requirements	Unit	Value
Torque @ P1	Nm	359	Ripple @ P1	%	9
Torque @ P2	Nm	46	Ripple @ P2	%	30
Torque @ P3	Nm	139	Efficiency @ P3	%	95.8
Torque @ P4	Nm	21	Efficiency @ P4	%	90.9

With this asymmetry, it is possible to satisfy the torque ripple requirement in P1, but the peak torque at base speed is slightly lower than the one demanded by the requirements.

In order to improve the performance of the peak power at base speed and to reduce the torque ripple at maximum torque and speed, the two asymmetries have to be combined as it has been made in subchapter 6.4.

The first pole is the same of the one obtained in the first asymmetry case (Figure 8.4) while half of the second pole has been obtained by different poles of the second asymmetry (Figure 8.5). The last half of the pole has been obtained through an optimization that used the same variables of the first asymmetry case. The final rotor shape is shown in Figure 8.6, while its performance is listed in Table 8.8.

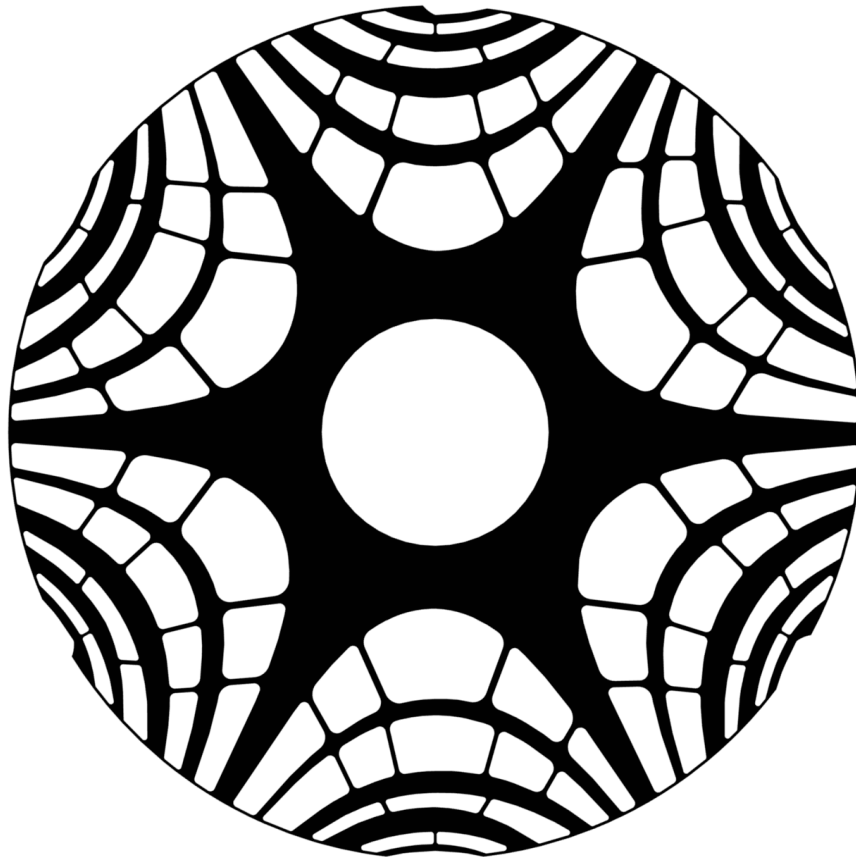
**Figure 8.6: Rotor shape of the solution with inner ribs and double asymmetry.**

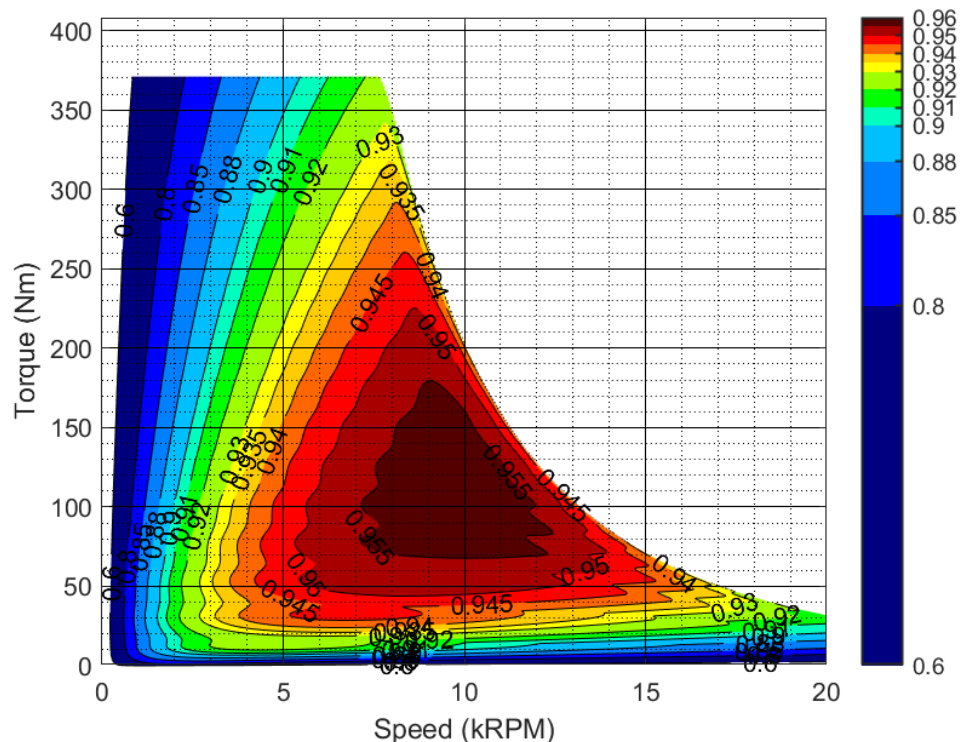
Table 8.8: Performance of the optimized topology solution with double asymmetry.

Requirements	Unit	Value	Requirements	Unit	Value
Torque @ P1	Nm	371	Ripple @ P1	%	10
Torque @ P2	Nm	47	Ripple @ P2	%	19.8
Torque @ P3	Nm	140	Efficiency @ P3	%	96.04
Torque @ P4	Nm	20	Efficiency @ P4	%	91

Proceeding with an asymmetry at a time, each optimization has adopted 26 variables, while the full optimization, which should require a very high number of variables, has used more than 100 variables. The total computational burden of the sub-optimizations solved separately is much lower than the one of the single optimization with all the variables (considering about an order of magnitude).

The final machine is able to satisfy all the performance for the torque values, for the ripple values and for the efficiency ones.

On this last geometry, a further magnetic analysis has been carried out in order to compute the efficiency map and the torque ripple map to better evaluate the performance of the machine. If the maximum speed is rarely reached, the machine could work in over speed conditions, up to 20000 *rpm*, while maintaining a safety coefficient equal to 1.2 (the maximum stress at 20000 *rpm* is equal to 444 *MPa*); therefore, the maps have been computed up to that speed.

**Figure 8.7: Double asymmetric optimized topology design: Efficiency map [p.u.].**

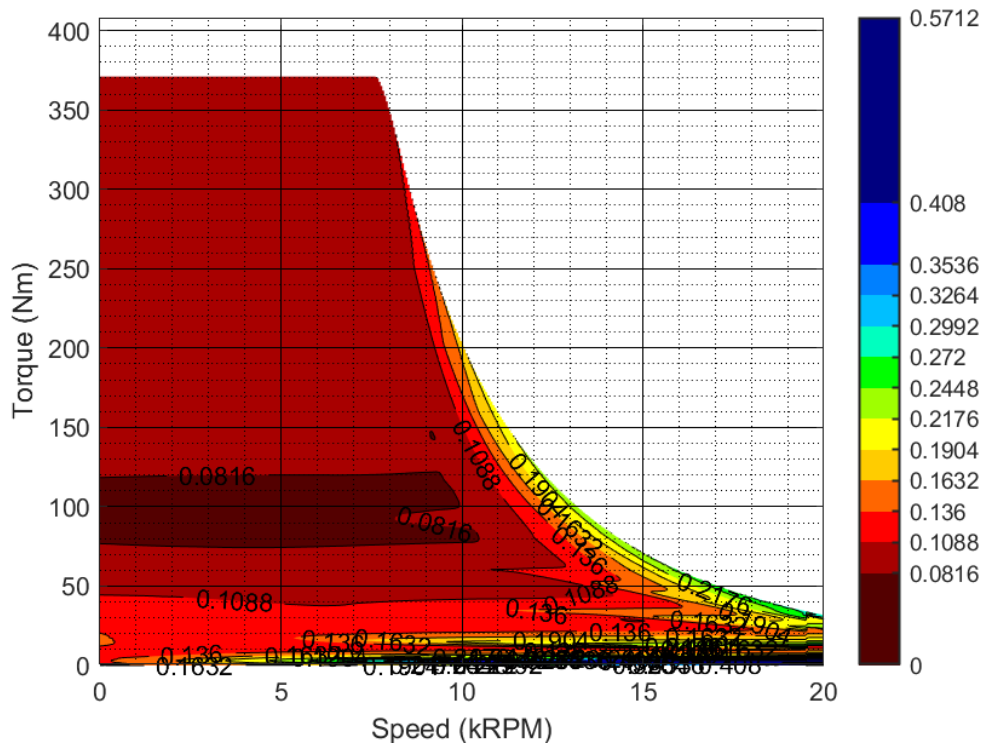


Figure 8.8: Double asymmetric optimized topology design: Torque ripple map [p.u.].

The motor shows a good efficiency performance: in fact, there is a wide area characterized by an efficiency value higher than 95%. The peak torque at base speed and its respective ripple, together with the maximum torque at 18000 rpm and its corresponding ripple, satisfy the initial requirements. The base speed is higher than the one of the requirements (7600 rpm vs 5500 rpm) and, as a consequence, the peak power is over 200 kW. This means that the machine needs to be oversized in terms of peak power to satisfy all the requirements. This is one of the most critical aspects when a SynRel motor is used for electric vehicle applications; the machine oversizing is needed because of the low flux-weakening capability of this machine once that the inner ribs are introduced.

8.3 Rotor Skewing

Applying the principles of the robust design discussed in Chapter 5 and, in particular, the statistical performance analysis of subchapter 5.3, it is possible to compute the guaranteed performance with a Degree of Confidence (*DoC*) equal to 99.7%. The number of laminations in this case is equal to 565 because the stack length is equal to 202 mm, the thickness of each lamination is 0.35 mm and the stacking factor is of 0.98. Due to the high number of laminations, the averaging effect is dominant and the distribution becomes equal to its mean value. However, as discussed earlier, the mean value can be different from the rated one. In this case,

the torques are very similar to the rated ones while their ripples have increased, moving from 10% in P1 to 13% and from 19.8% in P2 to 30%. With these new values, the motor does not satisfy the requirements in terms of torque ripple. At this optimization step, it is hard to consider also the robust design aspects, because all the steps to obtain the final solution must consider a statistical performance analysis: this can require a lot of computational time. For this reason, to meet the initial requirements, it is possible to proceed with the rotor skewing in order to reduce the torque ripple whilst admitting a slight reduction of the average values of the torque.

Many angles for the rotor skewing have been tested in order to use the best possible one; the conclusion is that the best angle is equal to 6.66° , which corresponds to the slot pitch. Figure 8.9 and Figure 8.10 report the new efficiency map and the torque ripple map, respectively, with the best angle for rotor skewing.

The peak torque at base speed and the maximum torque at 18000 rpm are slightly lower (366 Nm and 40 Nm, respectively), but their values still satisfy the requirements; the efficiency is also reduced, but the difference with the non-skewed solution is so little that does not have any impact on the performance.

The torque ripple has been strongly reduced in all the points of the map: in particular, the ripple of the peak torque at base speed is under 5% and the ripple of the maximum torque at 18000 rpm is under 12%. These values are low if compared to their respective ones of the non-skewed solution, which are 10% and 20%.

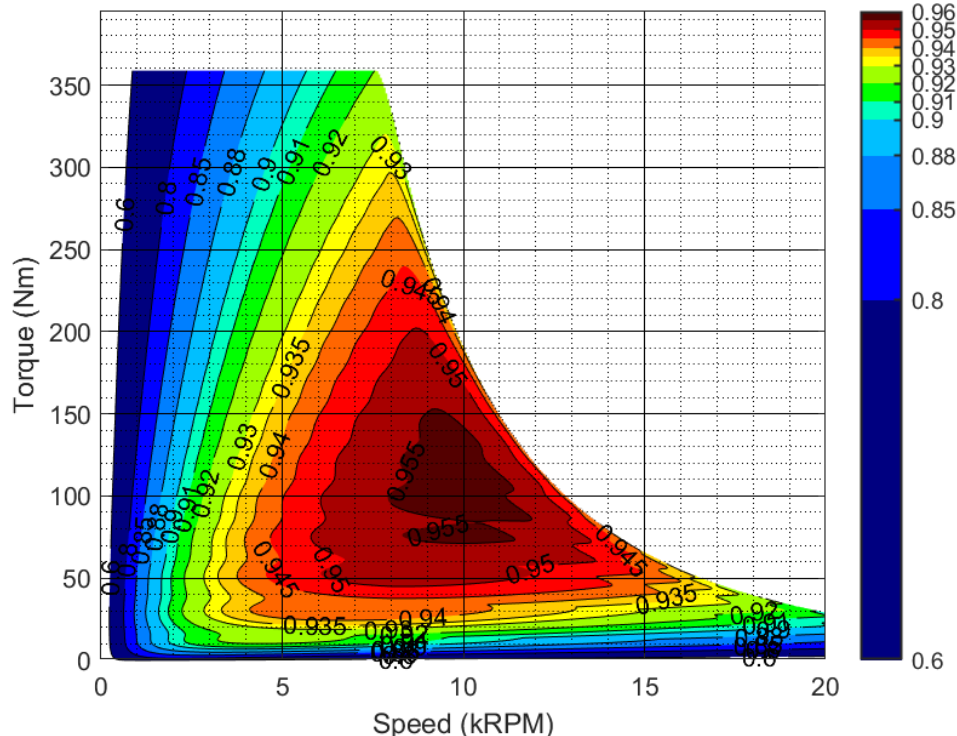


Figure 8.9: Double asymmetric optimized topology design with the skewed rotor (slot pitch): Efficiency map [p.u.].

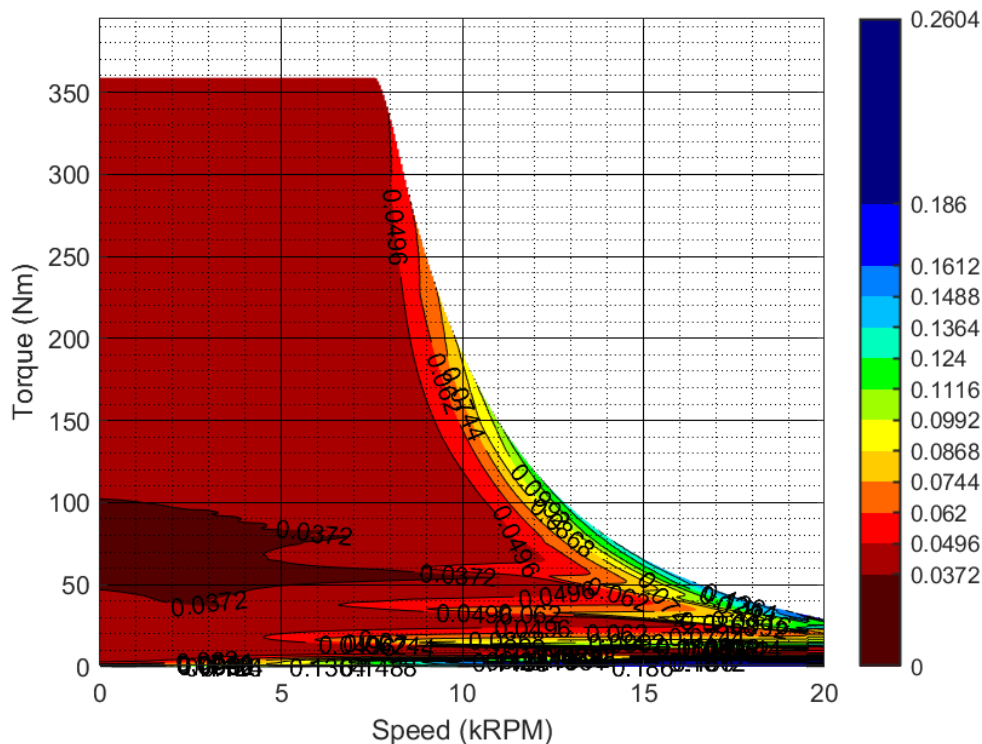


Figure 8.10: Double asymmetric optimized topology design with the skewed rotor (slot pitch): Torque ripple map [p.u.].

By carrying out the statistical performance analysis on the skewed motor, the torque ripples of the peak torque at base speed and of the maximum torque at 18000 rpm become 6% (from 5%) and 18.5% (from 12%), satisfying all the requirements.

The rotor skewing introduces another important advantage, which is the reduction of the flux harmonics inside the machine. In the efficiency and torque ripple maps, only the first harmonics of the flux and of the voltage have been considered but, in order to have a sinusoidal current, the voltage (due to flux harmonics) is not sinusoidal and the maximum linked-voltage is equal to the DC bus one multiplied by the maximum modulation index. By accepting non-sinusoidal currents (also neglecting the PWM effects), it is possible to exploit the available voltage and to guarantee the values illustrated by the maps, but with non-sinusoidal currents the torque ripple increases as well as the losses. Considering only sinusoidal currents, the maximum available torque in the flux-weakening region and the base speed are reduced: hence, the requirements may no longer be satisfied.

In order to evaluate these reductions, the efficiency maps have been recalculated for each solution imposing as maximum linked-voltage at any time (and not the magnitude of the first harmonic) the 98% of the DC bus voltage (a maximum modulation index of 0.98 has been considered). The efficiency maps for the non-skewed solution and for the skewed one are displayed in Figure 8.11 and in Figure 8.12, respectively.

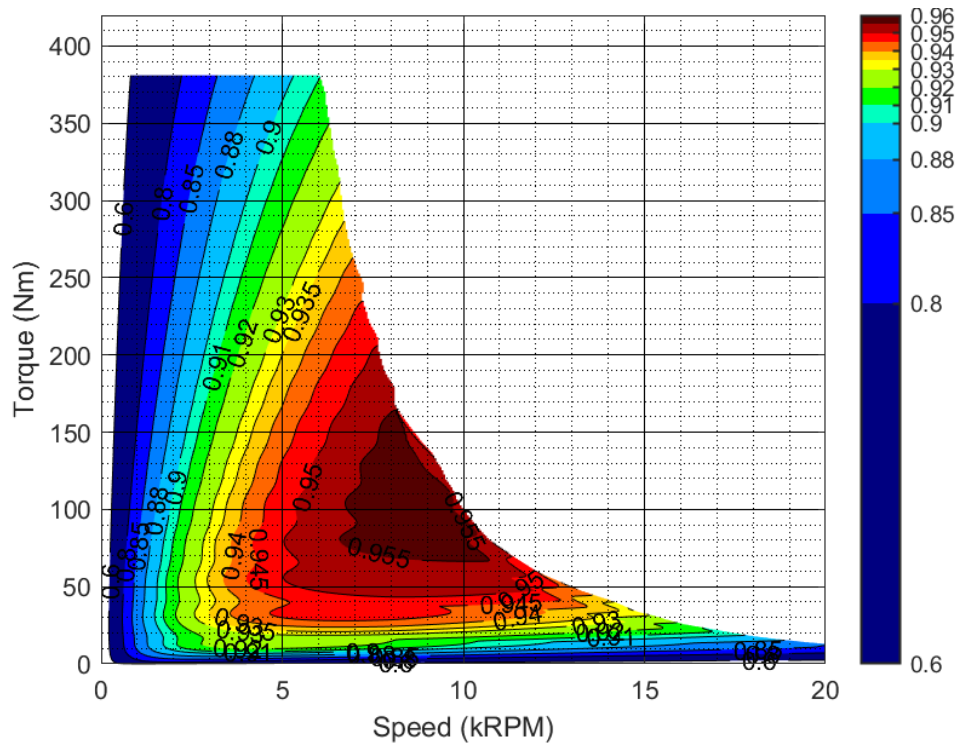


Figure 8.11: Double asymmetric optimized topology design with the non-skewed rotor: Efficiency map [p.u.] considering the flux harmonics.

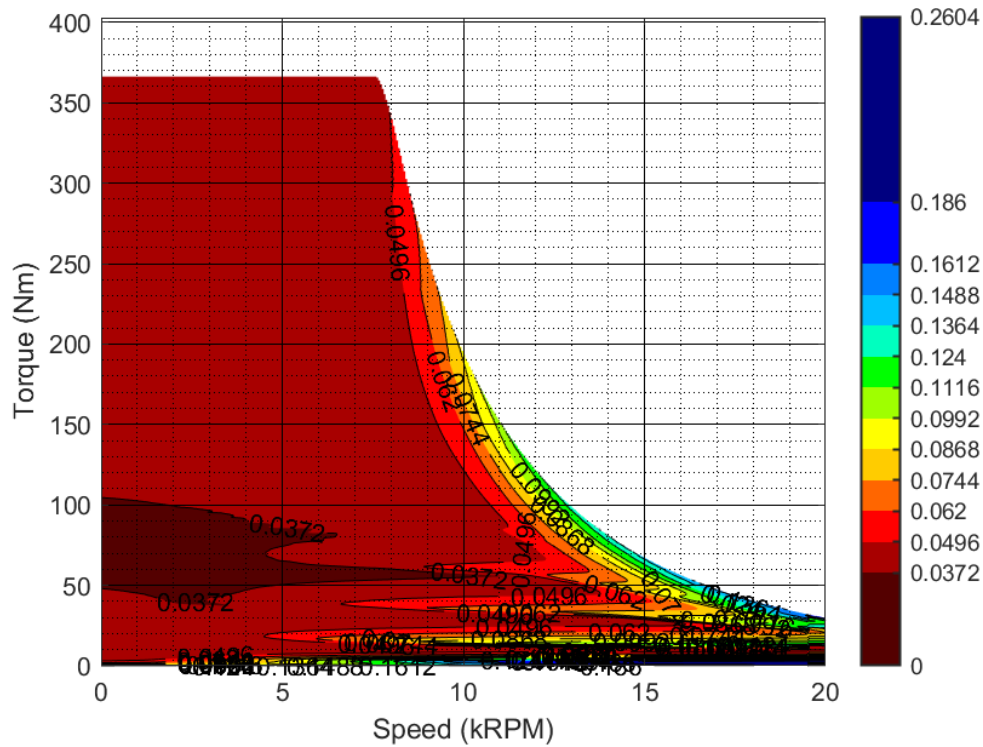


Figure 8.12: Double asymmetric optimized topology design with the skewed rotor (slot pitch): Torque ripple map [p.u.] considering the flux harmonics.

The motor with the skewed rotor can guarantee higher values of torque in the flux-weakening region and a higher base speed while maintaining a sinusoidal current. After those torque values, the control might be harder due to the impossibility of maintaining a sinusoidal current. Therefore, with the skewed rotor it is possible to simplify the control.

8.4 The 75 kW Design

The 75 kW design has been obtained by scaling the final solution discussed in the previous subchapter. Therefore, the stator and rotor shapes are the same of the analyzed ones, while the stack length has been reduced to 95 mm and the number of conductors in the slots has been increased. For this solution, only the efficiency map is presented for further comparisons of the experimental tests. All the other aspects are equal to the ones discussed in the previous subchapter; the differences consist in the values of the peak torque, the base speed, the torque in the flux-weakening region and the maximum speed: all these values are visible in the efficiency map reported in Figure 8.13.

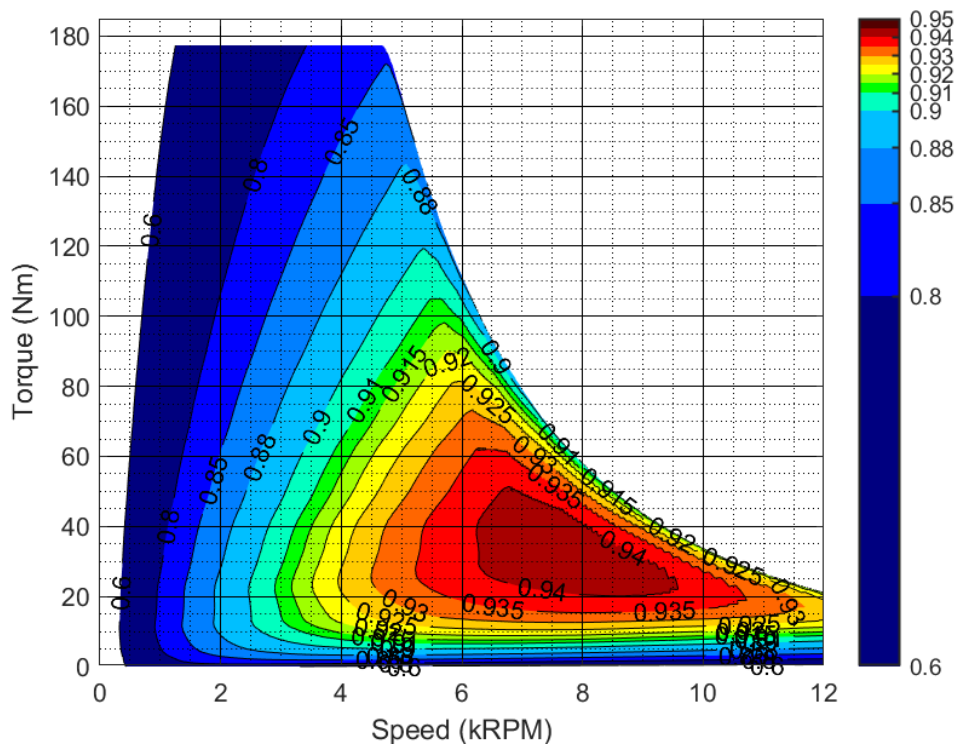


Figure 8.13: Scaled version of the double asymmetric optimized topology design: Efficiency map [p.u.].

The presented motor is able to satisfy all the requirements listed in Table 8.2 in terms of torque (the peak torque is equal to 177 Nm vs 170 Nm) and power (the peak power is equal to 80 kW vs 75 kW and the power at maximum speed is 26 kW vs 25 kW).

8.5 Prototyping

Starting from the design data of the optimized designs, two 200 kW prototypes (one with and one without the skewing of the rotor) and a 75 kW prototype with the non-skewed rotor have been manufactured.

Firstly, the stator core has been realized with a resin 3D-printer in order to evaluate the overall length, including the end-windings. The 3D-printed stator core together with the windings is shown in Figure 8.14.



Figure 8.14: Resin stator core with the windings (200 kW machine).

The electrical steel has been laser-cut for the prototypes and subsequently assembled in the stacked core with the back-lack technique. For mass production, the manufacturing process is realized with the punching technique, which reduces the manufacturing effects improving the overall performance. Some pictures of the stacked cores are shown in Figure 8.15, Figure 8.16, and Figure 8.17.

After cutting and assembling the electrical steel, the next step has been the insertion of the stator winding. The stator winding has been realized with round wires for the prototypes. The hairpin winding can also be adopted, but this choice requires the redesign of the stator slots. Some pictures of the wound stator cores are shown in Figure 8.18 and Figure 8.19. Figure 8.20 shows both the wound stator core and the rotor core of the 75 kW and of the 200 kW machines.

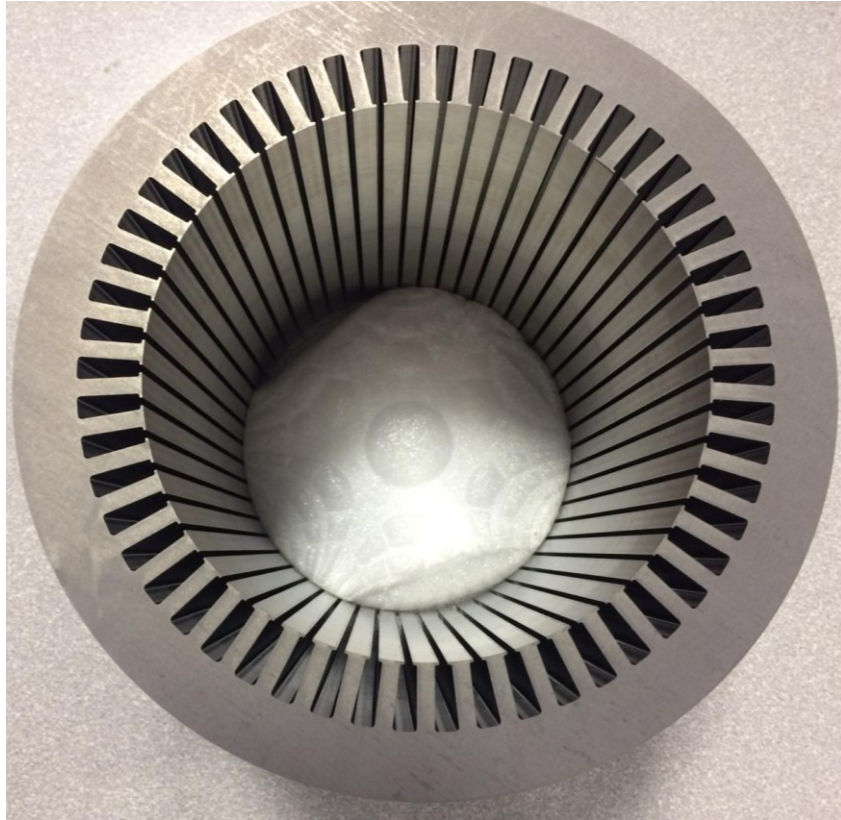


Figure 8.15: Stator core of the 200 kW prototype.



Figure 8.16: Rotor core of the 200 kW prototype.

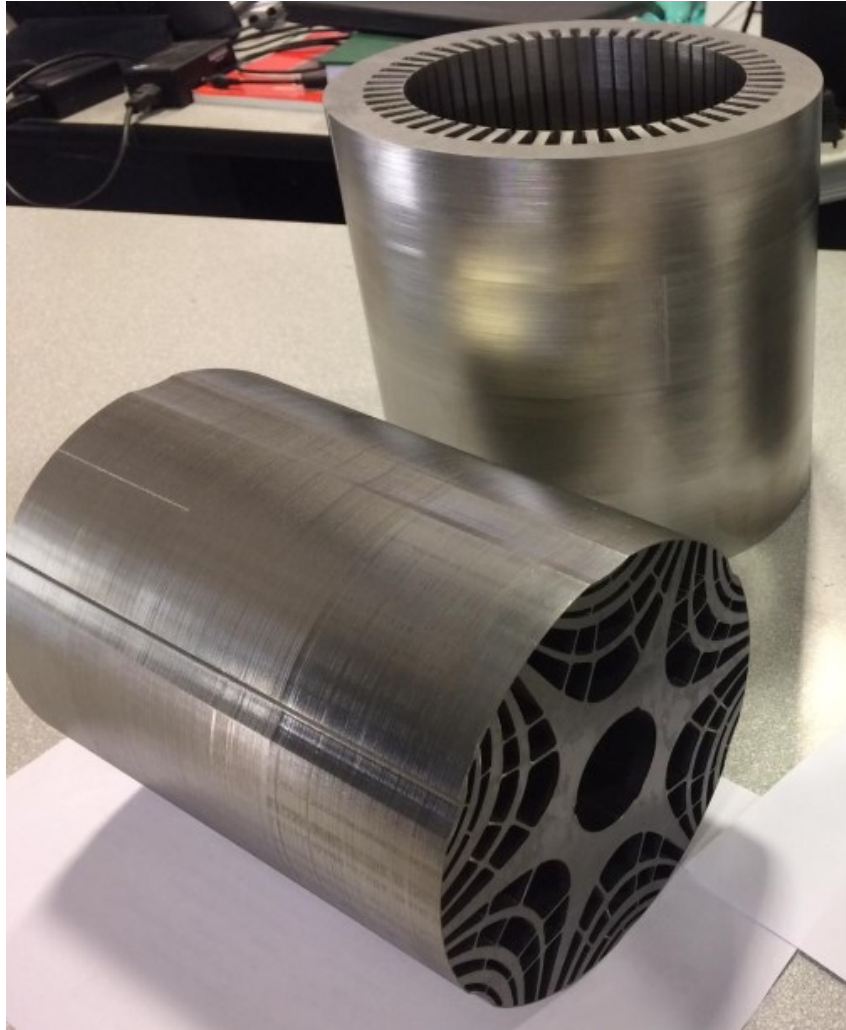


Figure 8.17: Stator and rotor cores of the 200 kW prototype.

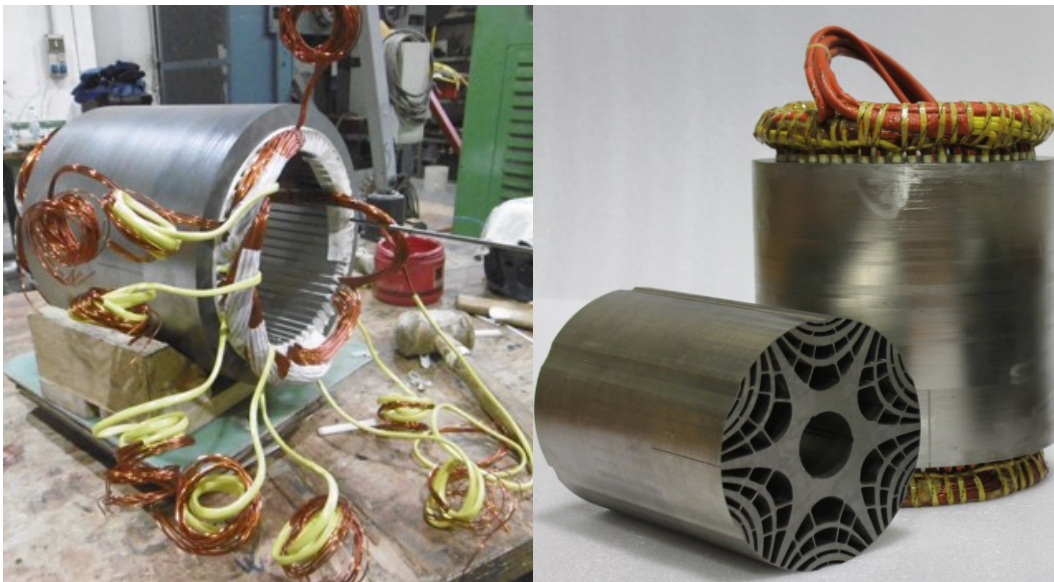


Figure 8.18: Manufacturing process of the stator winding (on the left), wound stator core and rotor core (on the right) - 200 kW machine.



Figure 8.19: Wound stator core with sensors - 200 kW machine.



Figure 8.20: Wound stator cores and rotor cores of the 75 kW (on the right) and of the 200 kW machines (on the left).

The motor is liquid cooled in order to improve the power density: therefore, the following step in the prototyping has been the manufacturing of the cooling jacket, which is shown in Figure 8.21.



Figure 8.21: Cooling jacket.

The final steps have consisted in the insertion of the shaft in the rotor core, the insertion of the wound stator core in the cooling jacket system and, finally, the motor assembly.

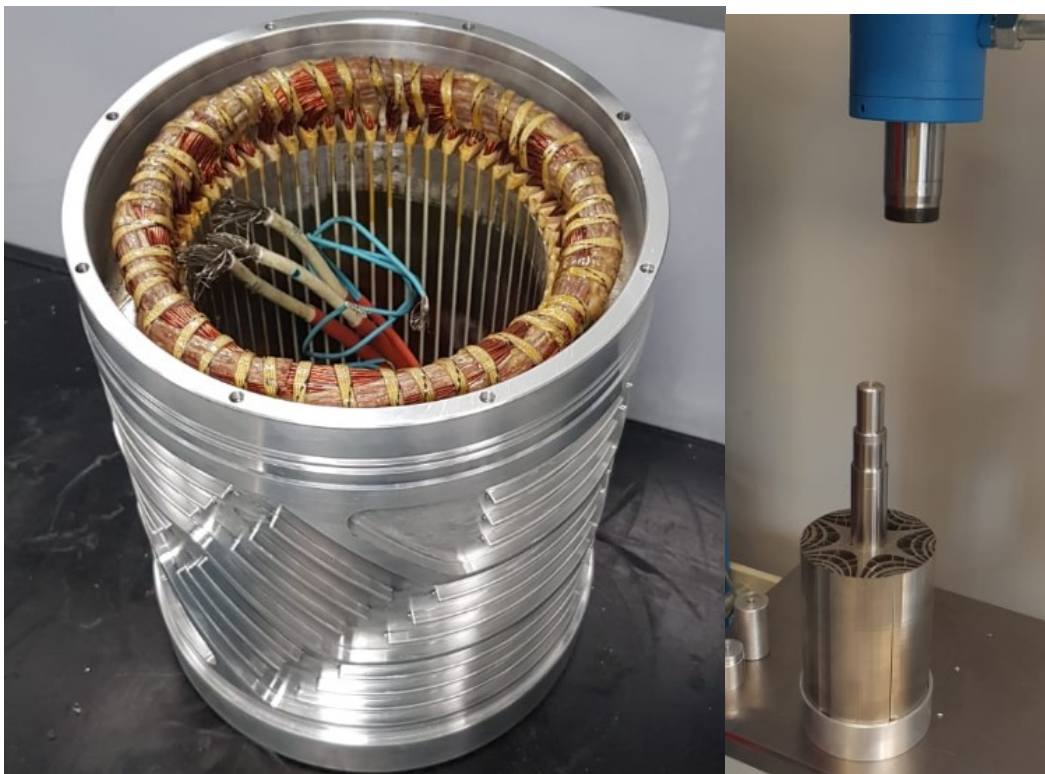


Figure 8.22: Wound stator core insertion in the cooling jacket system (on the left) and insertion of the shaft in the rotor core (on the right).

After the motor assembly, the integrated power electronics has also been assembled.

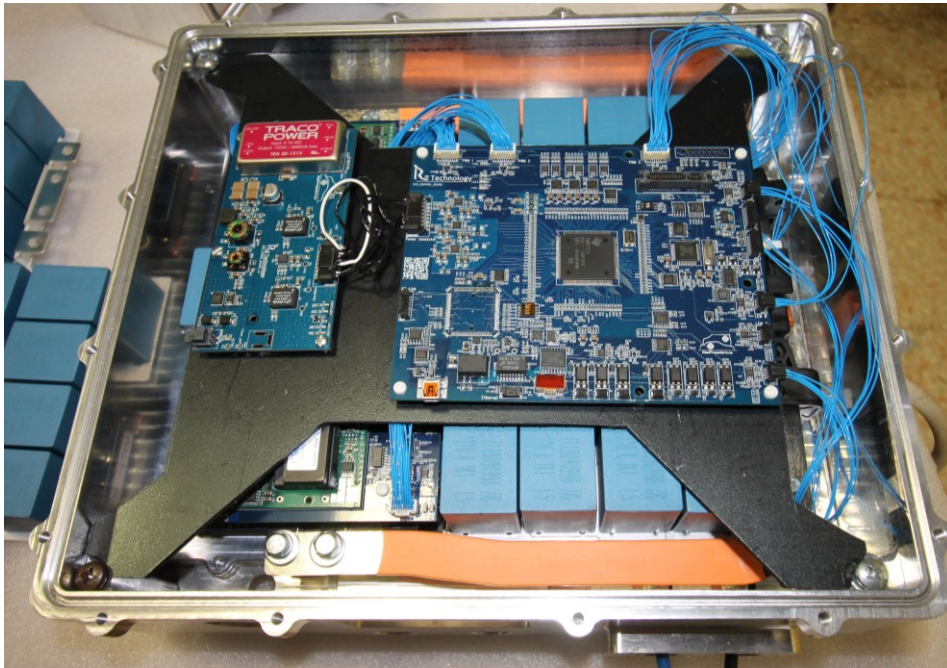


Figure 8.23: Power electronics.

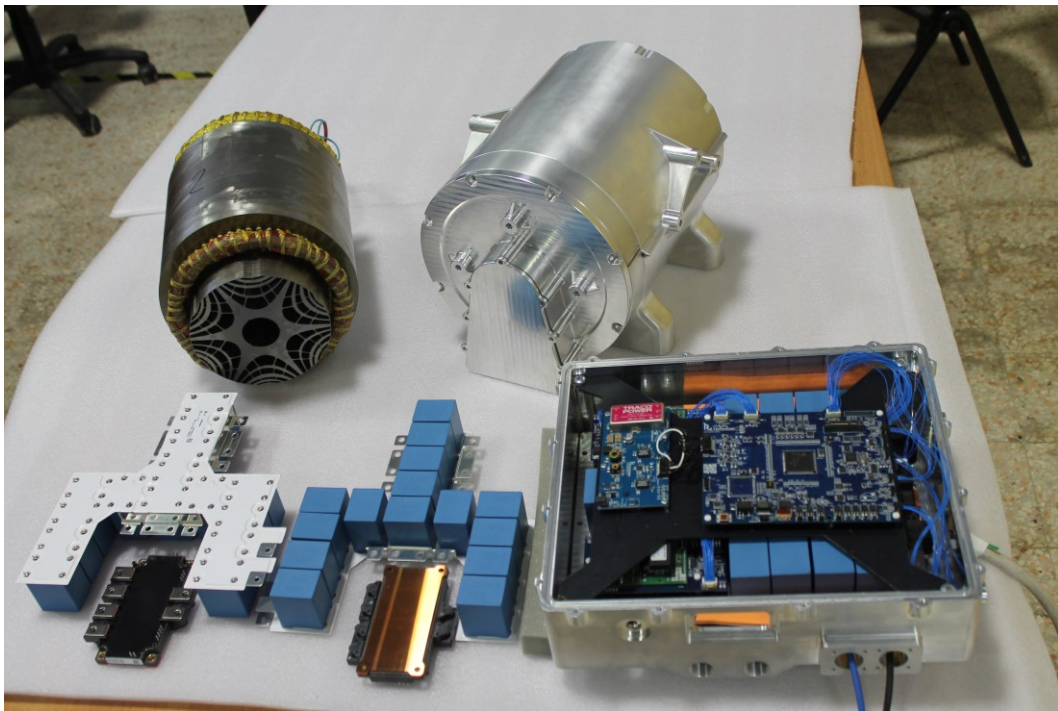


Figure 8.24: Power electronics, stator and rotor cores and housing.

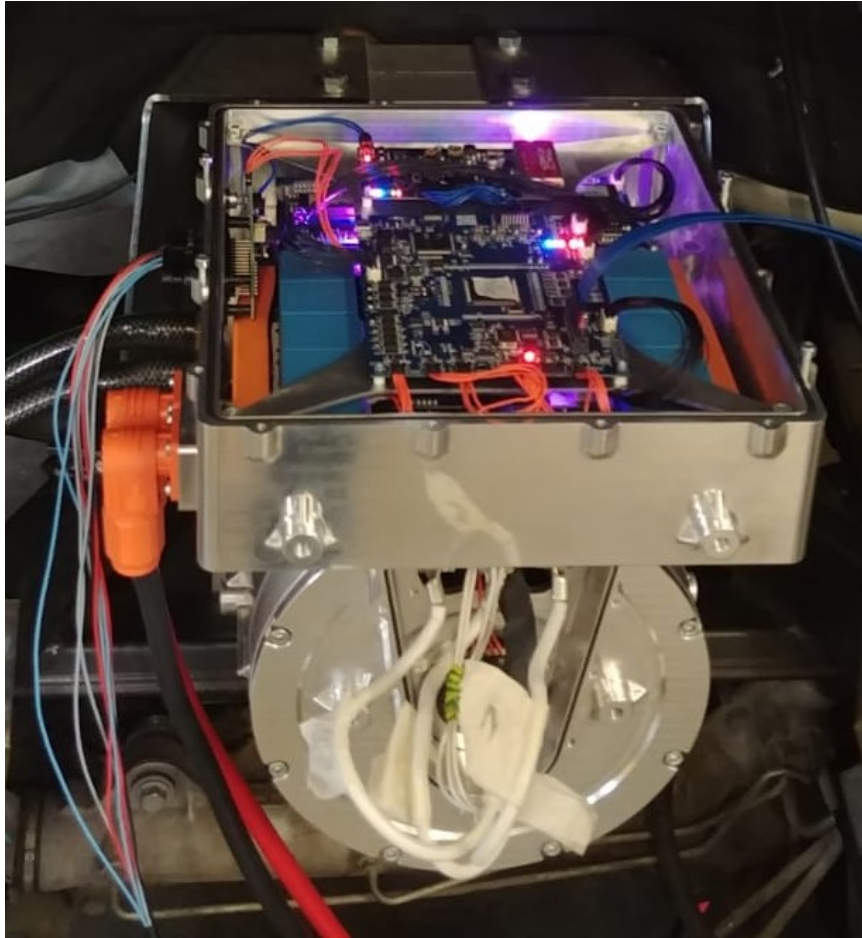


Figure 8.25: Assembled motor.

8.6 Experimental tests

The preliminary test, made at the laboratory of the University of L'Aquila, has been the bearing running-in, which is necessary for the correct motor operation when it has to work at high speeds.

8.6.1 Maximum speed tests

After the bearing running-in, the motor has been tested at the maximum speed (18000 rpm) for a long time in order to verify its noise and vibration levels while evaluating the motor capabilities to maintain high speeds. After these tests, the motor has been stressed with rapid accelerations and decelerations from 0 to the maximum speed.

The results of this repeated stress test are shown in Figure 8.26 in terms of measured and reference speed and of reference torque; in Figure 8.27, the results are displayed in terms of measured and reference axis currents and of current

control angle; in Figure 8.28, the results are presented in terms of reference axis voltages.

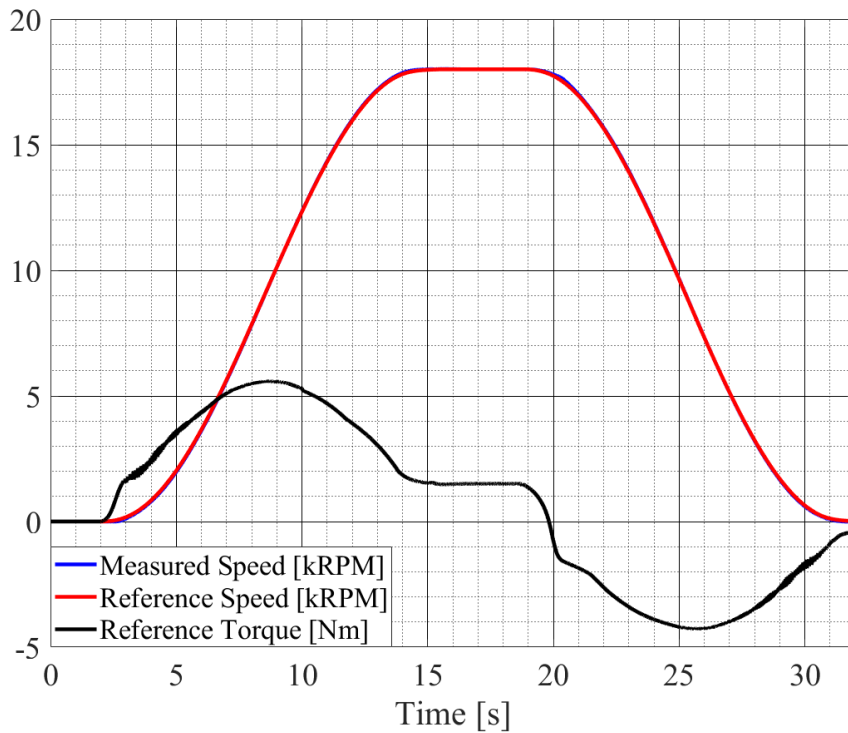


Figure 8.26: Measured and reference speed and reference torque during the stress test.

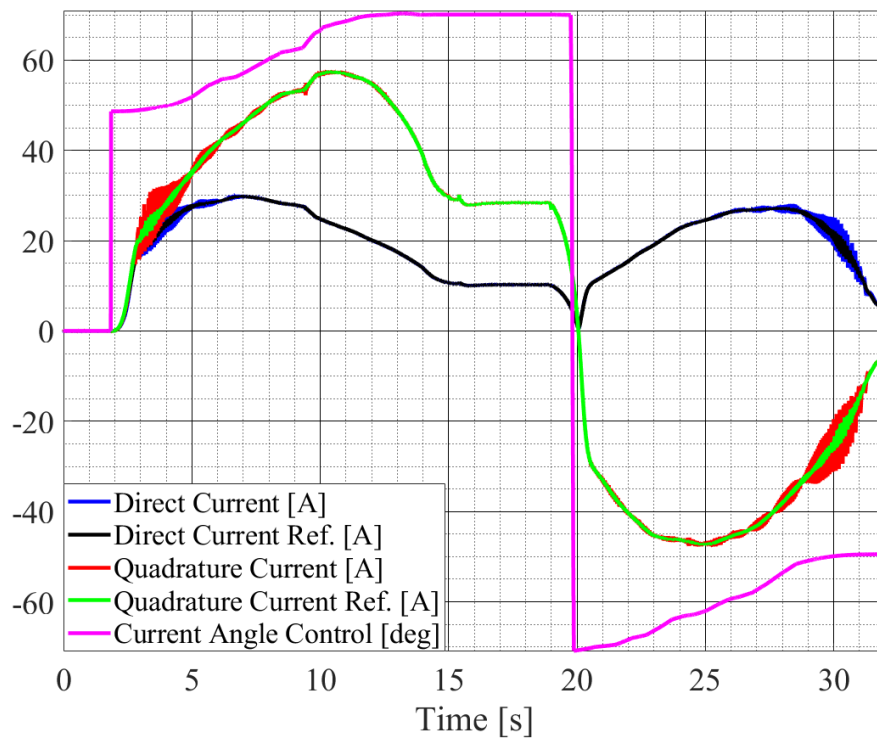


Figure 8.27: Measured and reference axis currents and current control angle.

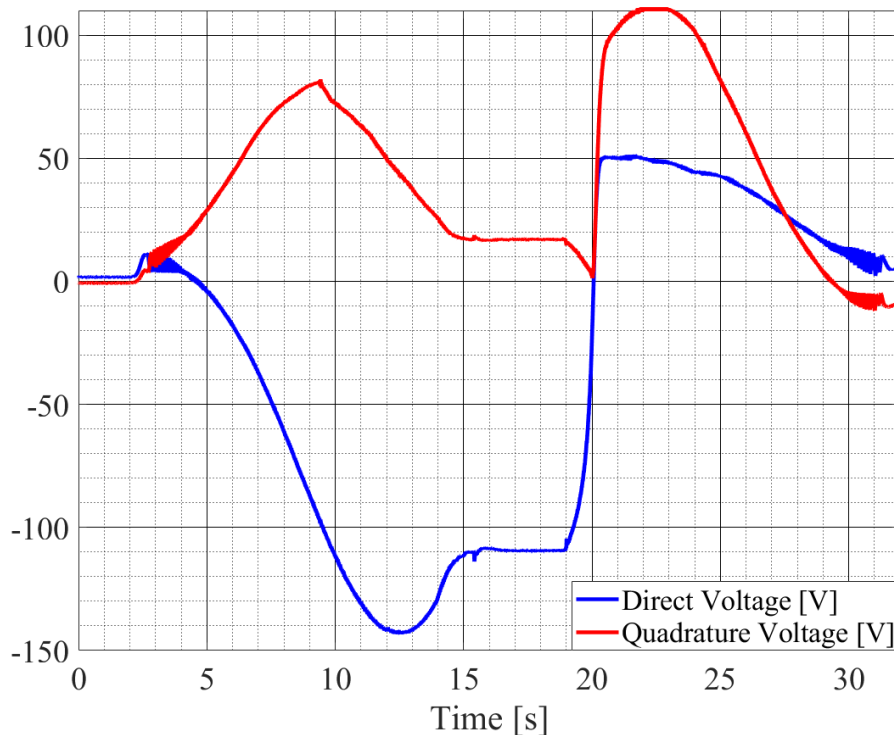


Figure 8.28: Reference axis voltages.

This stress tests demonstrate that the rotor is able to reach and maintain the maximum speed, according to the mechanical simulations. These tests have been realized at no load conditions: this can be noticed from the torque low value. The current angle has been varied according to the MTPA curve and to the flux-weakening law. With low torque values, the best angle at maximum speed is around 70° , while the one for the maximum torque condition is equal to 82° (obtained from simulations).

8.6.2 Full load tests on the 200 kW machine

The next step has involved the full tests of the motor and has been realized at the laboratory of IFP Energies Nouvelles, a partner of the ReFreeDrive project. A picture of the test bench is shown in Figure 8.29. The SiC inverter has been designed and manufactured by other partners of the ReFreeDrive project: IFP Energies Nouvelles and R13 Technology, a spin-off company of the University of L'Aquila.

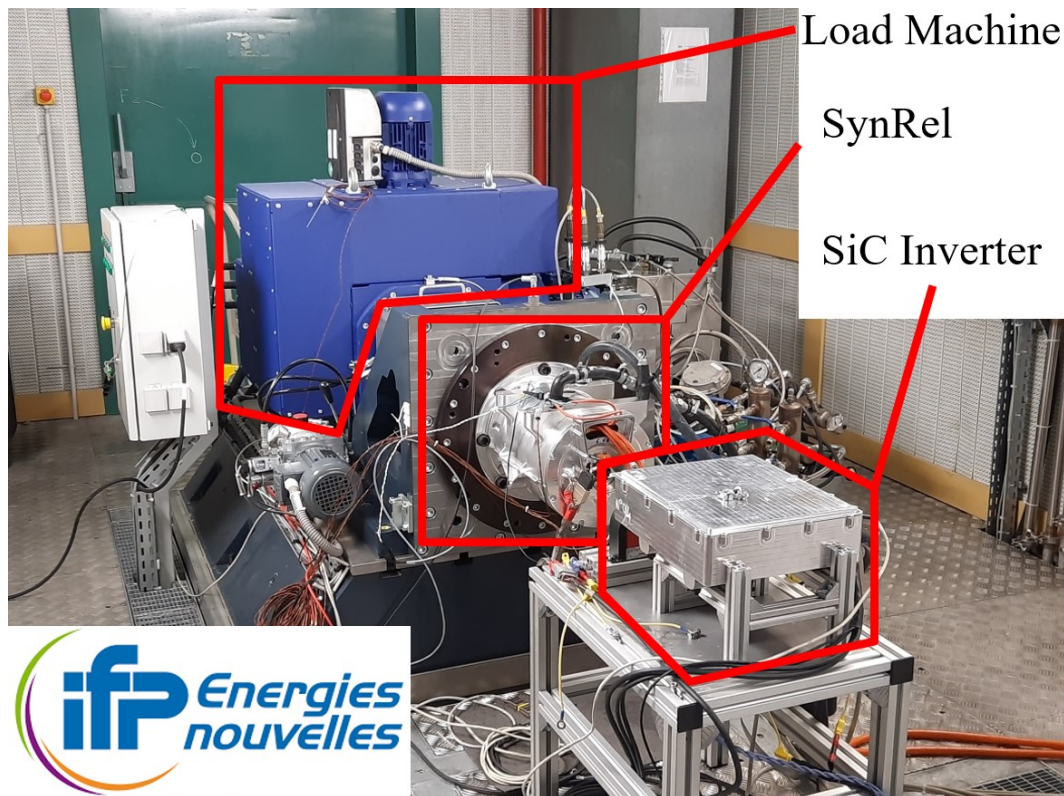


Figure 8.29: Test Bench in the laboratory of IFP Energies Nouvelles.

The testing procedures have been scheduled for the period of September/October but, due to the Covid-19 pandemic, the period has been significantly reduced to just a few days, hence it has not been possible to test all the motor working points. Moreover, it has not been possible to attend the testing procedures and, therefore, to provide direct support for the control setup. Then, additional tests on the motor had to be organized. Nevertheless, the tested points are in good agreement with the simulated ones, confirming the goodness of the design procedure. Figure 8.30 shows the experimental efficiency map for the 200 kW motor. The maximum torque of the motor, computed by the FE analysis, is equal to 360 Nm, while the experimental one is around 300 Nm. This difference is due to the maximum phase current used for the tests that has been set to 675 A, while in the simulation is 820 A. The tests have been carried out with the liquid cooling system, which operates with an inverter inlet temperature of 65°C (the maximum one reached during this application operation). In such derated conditions, the modules of the power electronics reach a temperature of 130°C, but from the datasheet they are able to stand higher temperatures. Since the replacement of the modules would require several months (due to the lack of spare parts and to long times of supplying), it has been preferred to avoid any inconvenience by choosing to work with low temperatures. At the maximum speed of 18000 rpm, but also over that speed (in the

flux-weakening region), the generated torque is lower than the one obtained by the FE analysis. This difference can be explained by noting that a different current control angle (the value used during the test is of 72° , while the best control angle according to the MTPV curve is equal to 82°) and a different bus DC voltage (750 V) have been used. This choice has been made because adopting higher values of the control angle there have been some issues due to an unexpected additional vibration of the motor: the reason of this problem can be addressed to higher torque and torque ripple using the corresponding correct angle (according to Figure 8.10); in fact, during this test, the incorrect balance of the rotor has caused vibrations at high speed, even when the load torque was equal to zero.

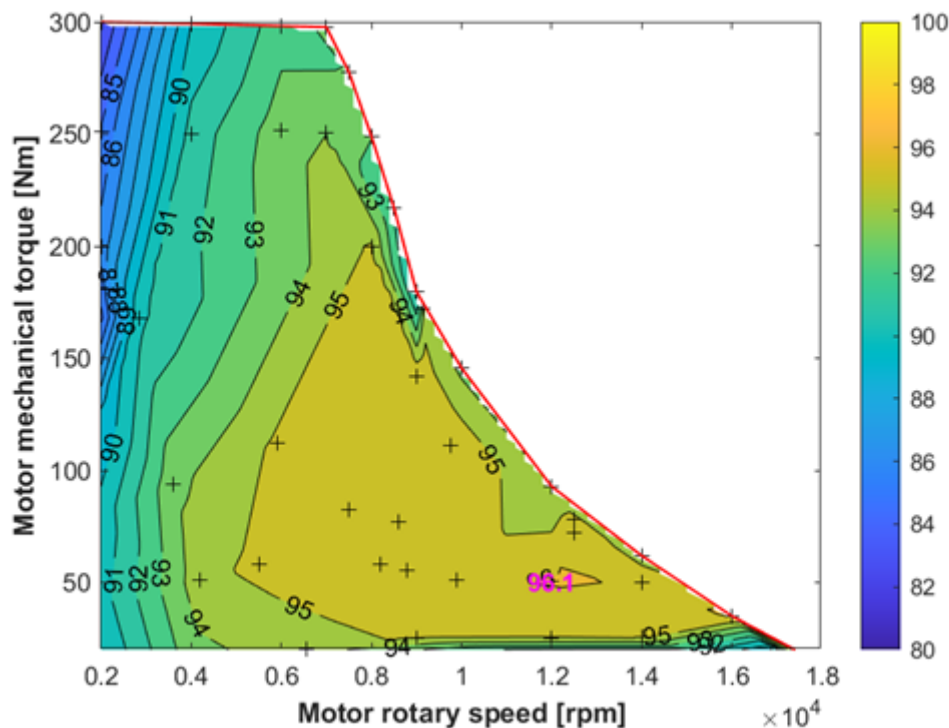


Figure 8.30: Experimental Efficiency Map of the 200 kW solution.

These problems may be solved with a correct balance of the rotor and with an optimization of the motor control: these will represent two future activities that must be carried out to correctly evaluate the differences between the experimental results and the simulation ones.

8.6.3 Full load tests on the 75 kW machine

The 75 kW motor, after being tested, has shown very encouraging results with a good match between the experimental results and the simulation ones; the experimental efficiency map is shown in Figure 8.31.

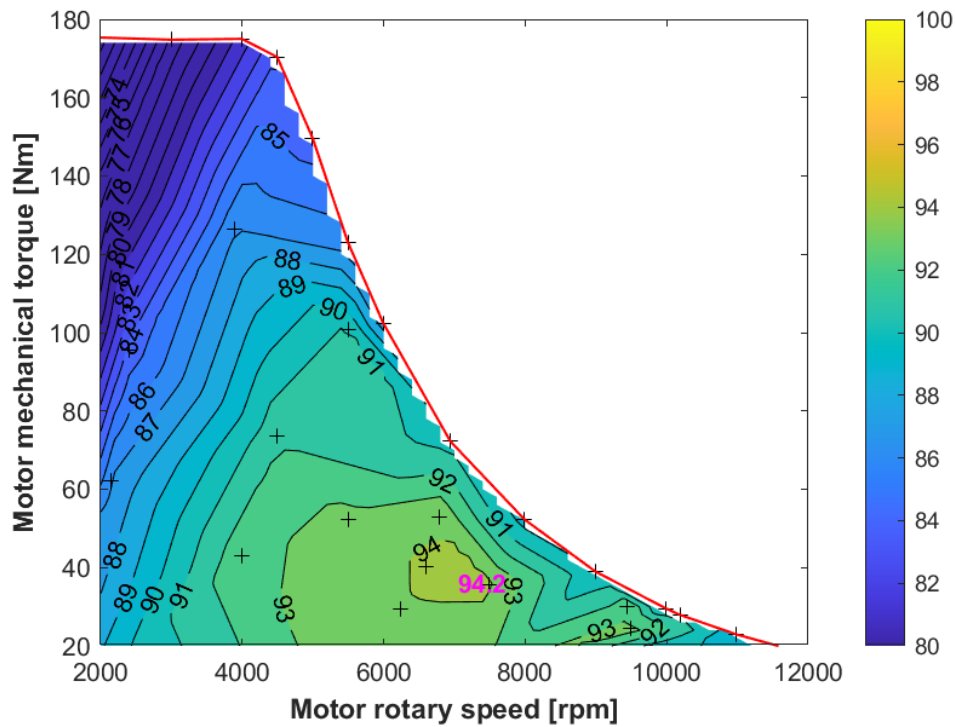


Figure 8.31: Experimental Efficiency Map of the 75 kW solution.

The maximum torque obtained by the experimental test is equal to 176 Nm, nearly equal to 177 Nm of the simulations. The base speed of the experiments is 4300 rpm, while the one obtained by the simulations is 4600 rpm. The main difference consists in the maximum torque during flux-weakening operations: at maximum speed (12000 rpm), the maximum torque produced during the test is equal to 18 Nm (versus 20.5 Nm of the FE analysis) with a mechanical power of 22.6 kW (versus 26 kW). This difference is due to the use of the first flux harmonic for the computation of the efficiency map considering the phase voltages (but a margin of 10% has been imposed to consider the impact of the harmonics) and to the use of a non-skewed rotor.

Chapter 9

Conclusions and Future Developments

The research carried out throughout this thesis project has been focusing on the design of high performance and high speed Synchronous Reluctance machines for electric vehicles. After an introductory section about the market of electric cars and the uncertainty related to Rare Earth material supply, the Synchronous Reluctance machine has been introduced and reviewed in the first part of the thesis.

The second part of the thesis has covered the design procedure of the synchronous reluctance machine, starting from its preliminary design. Thereafter, the optimization procedure has been discussed: in particular, a multi-objective derivative free algorithm has been presented as a suitable solution for the electric motor design and some considerations have been added regarding the use of a local optimization instead of a global one in order to reduce the computational burden. Afterwards, to improve the degree of confidence (*DoC*) of the manufactured machine, a method to carry out a robust design optimization has been presented. The mentioned procedure involves the simulated annealing algorithm for the identification of the candidates, the adoption of statical tools and the worst-case analysis to identify the most robust design.

The third part of the thesis has been focusing on the adoption of innovative solutions for the rotor mechanical integrity at high speeds. Firstly, the radial ribs have been introduced in correspondence of the q -axis in order to analyze the solution that is most used in literature; and secondly, two innovative solutions have been proposed, analyzed and compared. The first solution has been derived from the adoption of the Topology Optimization for the definition of the best combination in terms of number of the inner ribs for each barrier, position of the inner ribs, their width and inclination. After the definition of the model, a magneto-structural optimization has been carried out for further refinements concerning the performance of the machine. The second solution involved the

filling of the flux barriers with adhesive epoxy resin to sustain the rotor yokes, upon which the centrifugal force acts.

Lastly, two case studies that are part of the European H2020 ReFreeDrive project have been presented and discussed. The imposed motor requirements are fully satisfied thanks to the sizing procedures discussed in the thesis project. Finally, two prototypes have been realized and tested at the IFP Energies Nouvelles laboratory in France. The tests, despite the limited days for the test implementation and the few tested points, have confirmed a good correspondence between the simulation results and the experimental ones in terms of torque, power and efficiency.

The remaining open activities for future research developments can be summarized in the following points:

- The number of experimental points might be increased, especially for the 200 kW motor, to verify the effective maximum torque in the flux-weakening region;
- The motor should be tested for both the operating directions to check the effect of the adoption of an asymmetric rotor in terms of efficiency, maximum torque, noise and vibrations;
- The control parameters could be modified or a multivariable Proportional Integral control could be adopted in order to improve the maximum torque of the 75 kW motor in the flux-weakening region and to verify if it is possible to reach the simulated performance;
- The non-skewed solution of the 200 kW motor might be tested in order to better evaluate the effect of the skewing on the machine;
- A model refinement of the rotor filled with adhesive epoxy resin can be realized with the support of experimental tests in order to verify the actual limits of the resin properties and, hence, to guarantee the integrity of the rotor at high speeds. After that, a comprehensive research on the market would be necessary to evaluate and find a proper resin for the application; if a commercial resin is not available, further studies for the development of a specific resin will be carried out. Finally, a prototype characterized by an epoxy resin filled rotor can be manufactured and tested.

List of Figures

Figure 2.1: Global electric car sales trends.....	4
Figure 2.2: Private electric vehicle slow-chargers, 2019.....	5
Figure 2.3: Public electric vehicle slow-chargers, 2019.....	6
Figure 2.4: Public electric vehicle fast-chargers, 2019.....	7
Figure 2.5: World mine production of Rare Earth materials over the last decade in tons.....	8
Figure 2.6: World mine reserves of Rare Earth materials over the last decade in ktons.....	9
Figure 2.7: Neodymium price over the last decade in US\$ per kg.....	9
Figure 2.8: Wheel-road kinematic pair in stationary conditions.....	14
Figure 2.9: Friction between the spindle and the bearing.....	15
Figure 2.10: Rolling friction between the wheel and the road.....	16
Figure 2.11: Gradient resistive force.....	17
Figure 2.12: Torque (blue) and power (red) vs speed.....	22
Figure 2.13: WLTP cycle 3.....	22
Figure 2.14: Torque and speed during the WLTP cycle 3.....	23
Figure 2.15: Torque-speed points (green) in the WLTP cycle 3 and their limits (blue and red).....	24
Figure 2.16: Example of an efficiency map.....	24
Figure 2.17: Torque-speed points (green) in the WLTP cycle 3 and their limits (blue and red) for the LDV segment A.....	26
Figure 2.18: Torque-speed points (green) in the WLTP cycle 3 and their limits (blue and red) for the LDV segment B.....	26
Figure 2.19: Torque-speed points (green) in the WLTP cycle 3 and their limits (blue and red) for the LDV segment C.....	27
Figure 2.20: Torque-speed points (green) in the WLTP cycle 3 and their limits (blue and red) for the LDV segment D.....	27
Figure 2.21: Torque-speed points (green) in the WLTP cycle 3 and their limits (blue and red) for the LDV segment E.....	28
Figure 2.22: Torque-speed points (green) in the WLTP cycle 3 and their limits (blue and red) for the LDV segment J.....	28
Figure 2.23: Induction Motor: examples of squirrel cage rotors.....	29
Figure 2.24: Permanent Magnet-assisted-Synchronous Reluctance motor: one rotor pole.....	31
Figure 2.25: Pure Synchronous Reluctance motors.....	32
Figure 3.1: Direct-axis flux vs d-q currents in p.u.....	41
Figure 3.2: Quadrature-axis flux vs d-q currents in p.u.....	41
Figure 3.3: Constant Torque loci vs d-q currents.....	42
Figure 3.4: 4-pole axially-laminated rotor [23].....	43
Figure 3.5: 4-pole transversally-laminated rotor (U-shaped).....	44
Figure 3.6: 4-pole transversally-laminated rotor (Circular Shape).....	45
Figure 3.7: Flow around a cylinder.....	46
Figure 3.8: Flux lines of 4-pole, 6-pole, 8-pole and 10-pole machines.....	49
Figure 3.9: Variables of a fluid shaped rotor.....	50
Figure 3.10: Comparison between the circular (red dotted line) and the fluid (black line) shapes in a 4-pole machine.....	51
Figure 3.11: Comparison between the circular (red dotted line) and the fluid (black line) shapes in a 6-pole machine.....	52
Figure 4.1: Simplified scheme of the DFL algorithm.....	60
Figure 4.2: Division of the cycle in working areas (Case 1).....	62
Figure 4.3: Division of the cycle in working areas (Case 2).....	62
Figure 4.4: Duty cycle in terms of torque and speed.....	64
Figure 4.5: Stator and rotor shapes of the preliminary design.....	65
Figure 4.6: Behavior of the objective function (efficiency during the cycle) in the optimization OPT1.....	67
Figure 4.7: Behavior of the objective function (efficiency in P2) in the optimization OPT2.....	68
Figure 4.8: Behavior of the objective function (efficiency in P3) in the optimization OPT3.....	68
Figure 4.9: Stator and rotor geometries of the Preliminary Design (PrD) and of the optimizations during the cycle (OPT1), in P2 (OPT2), and in P3 (OPT3).....	70
Figure 4.10: Magnetic flux density [T] for the working point P1 of the Preliminary Design (PrD) and of the optimizations during the cycle (OPT1), in P2 (OPT2), and in P3 (OPT3).....	71
Figure 4.11: Magnetic flux density [T] for the working point P2 of the Preliminary Design (PrD) and of the optimizations during the cycle (OPT1), in P2 (OPT2), and in P3 (OPT3).....	71
Figure 4.12: Magnetic flux density [T] for the working point P3 of the Preliminary Design (PrD) and of the optimizations during the cycle (OPT1), in P2 (OPT2), and in P3 (OPT3).....	72

Figure 4.13: Magnetic flux density [T] for the working point P4 of the Preliminary Design (PrD) and of the optimizations during the cycle (OPT1), in P2 (OPT2), and in P3 (OPT3).....	72
Figure 4.14: Behavior of the torque in relation to the mechanical angle for all the working points of the project OPT1.	74
Figure 4.15: Behavior of the torque in relation to the mechanical angle for all the working points of the project OPT2.	75
Figure 4.16: Behavior of the torque in relation to the mechanical angle for all the working points of the project OPT3.	75
Figure 5.1: Effect of the MTs on the machine output performance P for the BLM design and for one LM design: design performance (P), distribution due to MTs (D) and worst-case due to MTs (W).	80
Figure 5.2: Stator slot geometry and related design variables.	81
Figure 5.3: Sensitivity analysis on the airgap length (left) and the rotor outer diameter (right).....	82
Figure 5.4: Sensitivity analysis on the ribs of the first (left) and of the second (right) barrier.	82
Figure 5.5: Sensitivity analysis on the ribs of the third (left) and of the fourth (right) barrier.	83
Figure 5.6: Sensitivity analysis on the lower (left) and on the upper (right) fillet of the first barrier.	83
Figure 5.7: Sensitivity analysis on the lower (left) and on the upper (right) fillet of the second barrier.	83
Figure 5.8: Sensitivity analysis on the lower (left) and on the upper (right) fillet of the third barrier.	84
Figure 5.9: Sensitivity analysis on the lower (left) and on the upper (right) fillet of the fourth barrier.	84
Figure 5.10: Sensitivity analysis on the position of the first (left) and of the second (right) barrier.	84
Figure 5.11: Sensitivity analysis on the position of the third (left) and of the fourth (right) barrier.	85
Figure 5.12: Sensitivity analysis on the width of the first (left) and of the second (right) barrier.	85
Figure 5.13: Sensitivity analysis on the width of the third (left) and of the fourth (right) barrier.	85
Figure 5.14: Sensitivity analysis on the width of the notch (left) and on the slot opening (right).....	86
Figure 5.15: Sensitivity analysis on the slot width (left) and on the slot height (right).....	86
Figure 5.16: Sensitivity analysis on the tooth tip angle (left) and on the tooth tip depth (right).	86
Figure 5.17: Sensitivity analysis on the stator outer diameter (left) and on the lower slot fillet (right).	87
Figure 5.18: Sensitivity analysis on the upper slot fillet (left) and on the control angle (right).....	87
Figure 5.19: Sensitivity analysis on the manufacturing factor (left) and on the shaft radius (right).	87
Figure 5.20: Shape and magnetic flux density [T] at the rated power of the preliminary design.	91
Figure 5.21: Shape and magnetic flux density [T] at the rated power of the BLM.	91
Figure 5.22: Comparison between the preliminary design (PD), the BLM design and the six LM designs (LM1, LM2, LM3, LM4, LM5, LM6).	92
Figure 5.23: Statistical distribution of the torque ripple of the BLM design affected by the MTs in a lamination and the averaging effect of the stacked core.	94
Figure 5.24: Statistical distribution of the torque ripple of the Best Local Minimum (BLM) and of the six Local Minimums (LMs) considering the stacked machine affected by the MTs.	95
Figure 5.25: Statistical distribution of the average torque of the Best Local Minimum (BLM) and of the six Local Minimums (LMs) considering the stacked machine affected by the MTs.	95
Figure 5.26: Statistical distribution of the phase voltage of the Best Local Minimum (BLM) and of the six Local Minimums (LMs) considering the stacked machine affected by the MTs.	96
Figure 5.27: Cumulative distribution of the torque ripple of the Best Local Minimum (BLM) and of the six Local Minimums (LMs) considering the stacked machine affected by the MTs.	97
Figure 5.28: Cumulative distribution of the average torque of the Best Local Minimum (BLM) and of the six Local Minimums (LMs) considering the stacked machine affected by the MTs.	97
Figure 5.29: Cumulative distribution of the phase voltage of the Best Local Minimum (BLM) and of the six Local Minimums (LMs) considering the stacked machine affected by the MTs.	98
Figure 5.30: Proposed flow for the robust design selection.	102
Figure 6.1: Cross section of the stator.	105
Figure 6.2: M1 design: cross section of the symmetric rotor (2 poles).	106
Figure 6.3: M1 design: Torque vs Electrical rotor position for peak torque and base speed (upper) and maximum torque and maximum speed (lower) operations.	107
Figure 6.4: M2 design: cross section of the asymmetric rotor (2 poles).	108
Figure 6.5: M2 design: Torque vs Electrical rotor position for peak torque and base speed (upper) and maximum torque and maximum speed (lower) operations.	109
Figure 6.6: M3 design: cross section of the asymmetric rotor (2 poles).	110
Figure 6.7: M3 design: Torque vs Electrical rotor position for peak torque and base speed (upper) and maximum torque and maximum speed (lower) operations.	110
Figure 6.8: M4 design: cross section of the asymmetric rotor (2 poles).	111
Figure 6.9: M4 design: Torque vs Electrical rotor position for peak torque and base speed (upper) and maximum torque and maximum speed (lower) operations.	112

Figure 6.10: M4 design: Torque ripple map.....	114
Figure 7.1: Radial rib solution shape.....	117
Figure 7.2: Equivalent von Mises stress [MPa] of the rotor with radial ribs.	118
Figure 7.3: Airgap deformations [μm] of the rotor with radial ribs.	119
Figure 7.4: d- and q-axis inductances and saliency ratio over the speed range of the rotor with radial ribs.	119
Figure 7.5: Maximum torque and power over the speed range of the rotor with radial ribs.	120
Figure 7.6: Evolution of the geometry obtained by the topology optimization. Empty elements are in white, “grey” elements are in grey and solid elements are in black.....	123
Figure 7.7: Optimized topology rotor shape.....	125
Figure 7.8: Equivalent von Mises stress [MPa] of the optimized topology rotor.....	125
Figure 7.9: Design flow involving the adoption of the Topology Optimization.	126
Figure 7.10: Airgap deformations [μm] of the optimized topology rotor.	127
Figure 7.11: d- and q-axis inductances and saliency ratio over the speed range of the optimized topology rotor.....	127
Figure 7.12: Maximum torque and power over the speed range of the optimized topology rotor.	128
Figure 7.13: Equivalent von Mises stress in the electrical steel.	130
Figure 7.14: Equivalent von Mises stress in the resin.	131
Figure 7.15: Contact pressure between the resin and the electrical steel.	132
Figure 7.16: Maximum steel deformation near the airgap.....	132
Figure 7.17: Equivalent von Mises Stress in the electrical steel in MPa.	134
Figure 7.18: Equivalent von Mises Stress in the resin in MPa.	134
Figure 7.19: Contact pressure between the resin and the electrical steel in MPa.....	135
Figure 7.20: Electrical steel deformations in μm	135
Figure 7.21: Airgap deformations [μm] of the epoxy resin filled rotor.	136
Figure 7.22: d- and q-axis inductances and saliency ratio over the speed range of the epoxy resin filled rotor.....	136
Figure 7.23: Maximum torque and power over the speed range of the epoxy resin filled rotor.....	137
Figure 7.24: Deformations at the airgap of the proposed SynRel solutions.....	138
Figure 7.25: Saliency ratios over the equivalent speed range of the proposed SynRel solutions.	139
Figure 7.26: d-inductance over the equivalent speed range of the proposed SynRel solutions.....	140
Figure 7.27: q-inductance over the equivalent speed range of the proposed SynRel solutions.....	140
Figure 7.28: Torque over the equivalent speed range of the proposed SynRel solutions.....	141
Figure 7.29: Power over the equivalent speed range of the proposed SynRel solutions.	141
Figure 8.1: Stator and rotor cross section of the optimized 4-pole design.	146
Figure 8.2: Stator and rotor cross section of the optimized 6-pole design.	147
Figure 8.3: Stator and rotor cross section of the optimized 8-pole design.	147
Figure 8.4: Rotor shape of the solution with inner ribs and an asymmetry in the pole.	149
Figure 8.5: Rotor shape of the solution with inner ribs and different adjacent poles.....	150
Figure 8.6: Rotor shape of the solution with inner ribs and double asymmetry.....	151
Figure 8.7: Double asymmetric optimized topology design: Efficiency map [p.u.]	152
Figure 8.8: Double asymmetric optimized topology design: Torque ripple map [p.u.].....	153
Figure 8.9: Double asymmetric optimized topology design with the skewed rotor (slot pitch): Efficiency map [p.u.].....	154
Figure 8.10: Double asymmetric optimized topology design with the skewed rotor (slot pitch): Torque ripple map [p.u.].....	155
Figure 8.11: Double asymmetric optimized topology design with the non-skewed rotor: Efficiency map [p.u.] considering the flux harmonics.	156
Figure 8.12: Double asymmetric optimized topology design with the skewed rotor (slot pitch): Torque ripple map [p.u.] considering the flux harmonics.	156
Figure 8.13: Scaled version of the double asymmetric optimized topology design: Efficiency map [p.u.].....	157
Figure 8.14: Resin stator core with the windings (200 kW machine).....	158
Figure 8.15: Stator core of the 200 kW prototype.	159
Figure 8.16: Rotor core of the 200 kW prototype.	159
Figure 8.17: Stator and rotor cores of the 200 kW prototype.	160
Figure 8.18: Manufacturing process of the stator winding (on the left), wound stator core and rotor core (on the right) - 200 kW machine.....	160
Figure 8.19: Wound stator core with sensors - 200 kW machine.	161
Figure 8.20: Wound stator cores and rotor cores of the 75 kW (on the right) and of the 200 kW machines (on the left). ...	161
Figure 8.21: Cooling jacket.....	162
Figure 8.22: Wound stator core insertion in the cooling jacket system (on the left) and insertion of the shaft in the rotor core (on the right).	162

Figure 8.23: Power electronics.....163
Figure 8.24: Power electronics, stator and rotor cores and housing.....163
Figure 8.25: Assembled motor.164
Figure 8.26: Measured and reference speed and reference torque during the stress test.165
Figure 8.27: Measured and reference axis currents and current control angle.165
Figure 8.28: Reference axis voltages.....166
Figure 8.29: Test Bench in the laboratory of IFP Energies Nouvelles.....167
Figure 8.30: Experimental Efficiency Map of the 200 kW solution.168
Figure 8.31: Experimental Efficiency Map of the 75 kW solution.169

List of Tables

Table 2.1: Traction motors for electric vehicles (2018-2019) [21].	11
Table 2.2: Vehicle parameters and performance.	19
Table 2.3: European Light Drive Vehicle (LDV) categories and parameters.	25
Table 2.4: Electric machines performance in the different LDV segments.	25
Table 3.1: The commercial SynRel parameters.	40
Table 4.1: Comparison between the representative points.	63
Table 4.2: Design variables, constraints and objective functions.	66
Table 4.3: Performance of the preliminary design and of the optimized ones.	73
Table 5.1: Main motor requirements and data (Base values).	80
Table 5.2: Independent design variables of the Preliminary Design (Base values).	81
Table 5.3: Preliminary design performance (Base values).	81
Table 5.4: Summary of the sensitivity analysis.	89
Table 5.5: Design Variables and Constraints (p.u.).	90
Table 5.6: Constraints and Objective Function for the different projects (p.u.).	91
Table 5.7: Results of the Statistical Tolerance Analysis of the different projects (p.u.).	98
Table 5.8: Variables used in the search of the worst case and their limits.	99
Table 5.9: Results of the Worst-case Analysis of the different projects (p.u.).	100
Table 5.10: Results from all the design steps (p.u.).	101
Table 6.1: Main motor requirements and data.	106
Table 6.2: Optimized design comparison.	113
Table 7.1: Mechanical results.	133
Table 7.2: Comparison of the proposed solutions.	142
Table 8.1: Requirements of the 200 kW ReFreeDrive SynRel motor.	144
Table 8.2: Requirements of the 75 kW ReFreeDrive SynRel motor.	144
Table 8.3: Design Variables and Constraints.	146
Table 8.4: Comparison between the optimized solutions.	148
Table 8.5: Performance of the optimized topology solution.	148
Table 8.6: Performance of the optimized topology solution with an asymmetry in the pole.	150
Table 8.7: Performance of the optimized topology solution with different adjacent poles.	151
Table 8.8: Performance of the optimized topology solution with double asymmetry.	152

References

- [1] M. Tursini, M. Villani, G. Fabri, S. Paolini, A. Credo and A. Fioravanti, "Sensorless control of a synchronous reluctance motor by finite elements model results," *2017 IEEE International Symposium on Sensorless Control for Electrical Drives (SLED)*, Catania, 2017, pp. 19-24, DOI: 10.1109/SLED.2017.8078424.
- [2] M. Tursini, M. Villani, G. Fabri, A. Credo, F. Parasiliti and A. Abdelli, "Synchronous Reluctance Motor: Design, Optimization and Validation," *2018 International Symposium on Power Electronics, Electrical Drives, Automation and Motion (SPEEDAM)*, Amalfi, 2018, pp. 1297-1302, DOI: 10.1109/SPEEDAM.2018.8445304.
- [3] M. Villani, M. Tursini, M. Popescu, G. Fabri, A. Credo and L. Di Leonardo, "Experimental Comparison Between Induction and Synchronous Reluctance Motor-Drives," *2018 XIII International Conference on Electrical Machines (ICEM)*, Alexandroupoli, 2018, pp. 1188-1194, DOI: 10.1109/ICELMACH.2018.8506983.
- [4] A. Credo et al., "Design Optimization of Synchronous Reluctance Motor for Low Torque Ripple", *AIRO Springer Series*, pp. 53-69, 2019. DOI: 10.1007/978-3-030-25842-9_5.
- [5] A. Credo, G. Fabri, M. Villani and M. Popescu, "High Speed Synchronous Reluctance Motors for Electric Vehicles: a Focus on Rotor Mechanical Design," *2019 IEEE International Electric Machines & Drives Conference (IEMDC)*, San Diego, CA, USA, 2019, pp. 165-171, DOI: 10.1109/IEMDC.2019.8785083.
- [6] A. Credo, M. Paletta, S. Paolini and M. Tursini, "An Open-Loop Starting Procedure for Sensorless Control of Synchronous Reluctance Motors," *2019 IEEE 10th International Symposium on Sensorless Control for Electrical Drives (SLED)*, Turin, Italy, 2019, pp. 1-6, DOI: 10.1109/SLED.2019.8896287.
- [7] A. Credo, M. Villani, M. Popescu and N. Riviere, "Synchronous reluctance motors with asymmetric rotor shapes and epoxy resin for electric vehicles," *2019 IEEE Energy Conversion Congress and Exposition (ECCE)*, Baltimore, MD, USA, 2019, pp. 4463-4469, DOI: 10.1109/ECCE.2019.8912668.
- [8] A. Credo, G. Fabri, M. Villani and M. Popescu, "Adopting the Topology Optimization in the Design of High-Speed Synchronous Reluctance Motors for Electric Vehicles," in *IEEE Transactions on Industry Applications*, vol. 56, no. 5, pp. 5429-5438, Sept.-Oct. 2020, DOI: 10.1109/TIA.2020.3007366.

-
- [9] A. Credo, L. di Leonardo, F. P. Collazzo, M. Tursini and M. Villani, "Optimum Wave Energy Conversion of a Point Absorber with Direct Electrical Power Take-Off," *2020 International Symposium on Power Electronics, Electrical Drives, Automation and Motion*, Sorrento, Italy, 2020, pp. 71-76, DOI: 10.1109/SPEEDAM48782.2020.9161928.
- [10] A. Credo, G. Fabri, M. Villani and M. Popescu, "A Robust Design Methodology for Synchronous Reluctance Motors," in *IEEE Transactions on Energy Conversion*, vol. 35, no. 4, pp. 2095-2105, Dec. 2020, DOI: 10.1109/TEC.2020.3016567.
- [11] A. Credo and P. Pescetto, "Design Optimization of a Synchronous Reluctance Motor Based on Operating Cycle," *2020 International Conference on Electrical Machines (ICEM)*, Gothenburg, 2020, pp. 2486-2492, DOI: 10.1109/ICEM49940.2020.9271012.
- [12] A. Credo, M. Villani, M. Popescu and N.Riviere, "Application of Epoxy Resin in Synchronous Reluctance motors with fluid-shaped barriers for e-mobility," in *IEEE Transactions on Industry Applications*, **(Under review)**
- [13] "Emission Standards: Europe: Cars and Light Trucks", *Dieselnet.com*, 2021. [Online]. Available: <https://dieselnet.com/standards/eu/ld.php>.
- [14] J. Buekers, M. Van Holderbeke, J. Bierkens and L. Int Panis, "Health and environmental benefits related to electric vehicle introduction in EU countries", *Transportation Research Part D: Transport and Environment*, vol. 33, pp. 26-38, 2014. DOI: 10.1016/j.trd.2014.09.002.
- [15] IEA (2020), *Global EV Outlook 2020*, IEA, Paris <https://www.iea.org/reports/global-ev-outlook-2020>
- [16] "Rare Earths Statistics and Information", *Usgs.gov*, 2021. [Online]. Available: <https://www.usgs.gov/centers/nmic/rare-earths-statistics-and-information>.
- [17] "TRADING ECONOMICS | 20 million INDICATORS FROM 196 COUNTRIES", *Tradingeconomics.com*, 2021. [Online]. Available: <https://tradingeconomics.com/>.
- [18] M. Schmid, "Rare Earths in the Trade Dispute Between the US and China: A Deja Vu", *Intereconomics*, 2021. [Online]. Available: <https://www.intereconomics.eu/contents/year/2019/number/6/article/rare-earths-in-the-trade-dispute-between-the-us-and-china-a-deja-vu.html>.
- [19] "Materials: a potential bottleneck to deployment of low-carbon technologies in the EU? - EU Science Hub - European Commission", *EU Science Hub - European Commission*, 2021. [Online]. Available: <https://ec.europa.eu/jrc/en/news/materials-potential-bottleneck-deployment-low-carbon-technologies->
-

- eu.<https://ec.europa.eu/jrc/en/news/materials-potential-bottleneck-deployment-low-carbon-technologies-eu>
- [20] E. A. Grunditz and T. Thiringer, "Performance Analysis of Current BEVs Based on a Comprehensive Review of Specifications," in *IEEE Transactions on Transportation Electrification*, vol. 2, no. 3, pp. 270-289, Sept. 2016, DOI: 10.1109/TTE.2016.2571783.
- [21] "EVSpecifications - Electric vehicle specifications, electric car news, EV comparisons", *EVSpecifications*, 2021. [Online]. Available: <https://www.evspecifications.com/>.
- [22] I. Boldea, L. N. Tutelea, L. Parsa and D. Dorrell, "Automotive Electric Propulsion Systems With Reduced or No Permanent Magnets: An Overview," in *IEEE Transactions on Industrial Electronics*, vol. 61, no. 10, pp. 5696-5711, Oct. 2014, DOI: 10.1109/TIE.2014.2301754.
- [23] J. Kolehmainen, "Synchronous Reluctance Motor With Form Blocked Rotor," in *IEEE Transactions on Energy Conversion*, vol. 25, no. 2, pp. 450-456, June 2010, DOI: 10.1109/TEC.2009.2038579.
- [24] J. Widmer, R. Martin and M. Kimiabeigi, "Electric vehicle traction motors without rare earth magnets", *Sustainable Materials and Technologies*, vol. 3, pp. 7-13, 2015. DOI: 10.1016/j.susmat.2015.02.001.
- [25] "Rare Earths: BMW's fifth-generation REE-free electric drivetrain — Roskill", *Roskill*, 2021. [Online]. Available: <https://roskill.com/news/rare-earths-bmws-fifth-generation-ree-free-electric-drivetrain/>.
- [26] "refreedrive – Rare Earth Free e-drives featuring low cost manufacturing", *Refreedrive.eu*, 2021. [Online]. Available: <http://www.refreedrive.eu/>.
- [27] Y. Wang and H. Fujimoto, "Dynamics Control for EVs", *Modeling, Dynamics and Control of Electrified Vehicles*, pp. 309-337, 2018. DOI: 10.1016/b978-0-12-812786-5.00009-4
- [28] Jörg Kühlwein (2016) *Driving resistances of light duty vehicles in Europe: present situation, trends, and scenarios for 2025* [White paper]. The International Council on Clean Transportation. https://theicct.org/sites/default/files/publications/ICCT_LDV-Driving-Resistances-EU_121516.pdf
- [29] J.R. Hendershot, "Electric traction machine choices for hybrid & electric vehicles" Florida International University, 2012.
- [30] G. Pellegrino, F. Cupertino and C. Gerada, "Automatic Design of Synchronous Reluctance Motors Focusing on Barrier Shape Optimization," in *IEEE Transactions on Industry Applications*, vol. 51, no. 2, pp. 1465-1474, March-April 2015, DOI: 10.1109/TIA.2014.2345953.

-
- [31] "Flow of a Uniform Incompressible Viscous Fluid", *An Introduction to Fluid Dynamics*, pp. 174-263, 2000. DOI: 10.1017/cbo9780511800955.006 [Accessed 31 January 2021].
- [32] P. J. Olver. (2020) *Complex Analysis and Conformal Mapping* [Online]. Available: https://www-users.math.umn.edu/~olver/ln_/cml.pdf
- [33] I. Boldea and S. Nasar, "The Induction Machines Design Handbook", pp. 423-446, 2009. DOI: 10.1201/9781315222592.
- [34] I. Boldea, *Reluctance synchronous machines and drives*. Oxford: Clarendon Press, 1996.
- [35] R. Moghaddam and F. Gyllensten, "Novel High-Performance SynRM Design Method: An Easy Approach for A Complicated Rotor Topology," in *IEEE Transactions on Industrial Electronics*, vol. 61, no. 9, pp. 5058-5065, Sept. 2014, DOI: 10.1109/TIE.2013.2271601.
- [36] T. A. Lipo, T. J. E. Miller, A. Vagati, I. Boldea, L. Malesani, and T. Fukao, "Synchronous reluctance drives," in *Conf. Rec. IEEE IAS Annual Meeting*, Oct. 1994.
- [37] N. Bianchi, S. Bolognani, A. Consoli, T. M. Jahns, R. D. Lorenz, E. C. Lovelace, S. Morimoto, and A. Vagati, "Design analysis and control of interior PM synchronous machines," in *Conf. Rec. IEEE IAS Annu. Meeting*, Oct. 2004.
- [38] A. Vagati, G. Franceschini, I. Marongiu and G. P. Troglia, "Design criteria of high performance synchronous reluctance motors," *Conference Record of the 1992 IEEE Industry Applications Society Annual Meeting*, Houston, TX, USA, 1992, pp. 66-73 vol.1, DOI: 10.1109/IAS.1992.244463.
- [39] I. Boldea, S. A. Nasar, "The induction machines design handbook", *CRC Press, Taylor & Francis Group*, 2010.
- [40] J. Pyrhönen, T. Jokinen, V. Hrabovcová, "Design of rotating electrical machines", *John Wiley & Son, Ltd*, 2009.
- [41] S. Ferrari and G. Pellegrino, "FEAfix: FEA Refinement of Design Equations for Synchronous Reluctance Machines," in *IEEE Transactions on Industry Applications*, vol. 56, no. 1, pp. 256-266, Jan.-Feb. 2020, DOI: 10.1109/TIA.2019.2954797.
- [42] A. Custódio, J. Madeira, A. Vaz and L. Vicente, "Direct Multisearch for Multiobjective Optimization", *SIAM Journal on Optimization*, vol. 21, no. 3, pp. 1109-1140, 2011. DOI: 10.1137/10079731x
- [43] G. Liuzzi, S. Lucidi and F. Rinaldi, "A Derivative-Free Approach to Constrained Multiobjective Nonsmooth Optimization", *SIAM Journal on Optimization*, vol. 26, no. 4, pp. 2744-2774, 2016. DOI: 10.1137/15m1037810.
-

-
- [44] G. Liuzzi, S. Lucidi and F. Rinaldi, "Derivative-Free Methods for Mixed-Integer Constrained Optimization Problems", *Journal of Optimization Theory and Applications*, vol. 164, no. 3, pp. 933-965, 2014. DOI: 10.1007/s10957-014-0617-4.
- [45] M. Palmieri, M. Perta, F. Cupertino and G. Pellegrino, "Effect of the numbers of slots and barriers on the optimal design of synchronous reluctance machines," *2014 International Conference on Optimization of Electrical and Electronic Equipment (OPTIM)*, Bran, 2014, pp. 260-267, DOI: 10.1109/OPTIM.2014.6850947.
- [46] N. Taran, V. Rallabandi, D. M. Ionel and P. Zhou, "On the effect of design tolerances on the performance of synchronous PM machines evaluated according to the IEEE Std 1812," *2017 IEEE International Electric Machines and Drives Conference (IEMDC)*, Miami, FL, 2017, pp. 1-7, DOI: 10.1109/IEMDC.2017.8002387.
- [47] R. Siebert, J. Schneider and E. Beyer, "Laser Cutting and Mechanical Cutting of Electrical Steels and its Effect on the Magnetic Properties," in *IEEE Transactions on Magnetics*, vol. 50, no. 4, pp. 1-4, April 2014, Art no. 2001904, DOI: 10.1109/TMAG.2013.2285256.
- [48] M. Balluff, H. Naumoski and K. Hameyer, "Sensitivity analysis on tolerance induced torque fluctuation of a synchronous machine," *2016 6th International Electric Drives Production Conference (EDPC)*, Nuremberg, 2016, pp. 128-134, DOI: 10.1109/EDPC.2016.7851324.
- [49] H. Khreis, A. Deflorio, K. Voelz and B. Schmuelling, "Sensitivity analysis on electrical parameters for Permanent Magnet Synchronous Machine manufacturing tolerances in EV and HEV," *2016 IEEE Transportation Electrification Conference and Expo (ITEC)*, Dearborn, MI, 2016, pp. 1-5, DOI: 10.1109/ITEC.2016.7520221.
- [50] T. Kim, M. Chowdhury, M. Islam, A. Gebregergis and T. Sebastian, "Tolerance study to forecast performances of permanent magnet synchronous machines using segmented stator for mass production," *2016 IEEE Energy Conversion Congress and Exposition (ECCE)*, Milwaukee, WI, 2016, pp. 1-6, DOI: 10.1109/ECCE.2016.7855525.
- [51] C. Jun, B. Kwon and O. Kwon, "Tolerance Sensitivity Analysis and Robust Optimal Design Method of a Surface-Mounted Permanent Magnet Motor by Using a Hybrid Response Surface Method Considering Manufacturing Tolerances", *Energies*, vol. 11, no. 5, p. 1159, 2018. DOI: 10.3390/en11051159.
- [52] G. Bramerdorfer, "A General Investigation of the Sensitiveness of Brushless Permanent Magnet Synchronous Machines Considering Magnet Tolerances," in *IEEE Transactions on Magnetics*, vol. 56, no. 1, pp. 1-9, Jan. 2020, Art no. 8100109, DOI: 10.1109/TMAG.2019.2948593.
-

-
- [53] S. Lee, K. Kim, S. Cho, J. Jang, T. Lee and J. Hong, "Optimal design of interior permanent magnet synchronous motor considering the manufacturing tolerances using Taguchi robust design," in *IET Electric Power Applications*, vol. 8, no. 1, pp. 23-28, January 2014, DOI: 10.1049/iet-epa.2013.0109.
- [54] N. Bianchi, M. Degano and E. Fornasiero, "Sensitivity Analysis of Torque Ripple Reduction of Synchronous Reluctance and Interior PM Motors," in *IEEE Transactions on Industry Applications*, vol. 51, no. 1, pp. 187-195, Jan.-Feb. 2015, DOI: 10.1109/TIA.2014.2327143.
- [55] N. Bianchi, M. Degano and E. Fornasiero, "Sensitivity analysis of torque ripple reduction of synchronous reluctance and interior PM motors," *2013 IEEE Energy Conversion Congress and Exposition*, Denver, CO, 2013, pp. 1842-1849, DOI: 10.1109/ECCE.2013.6646932.
- [56] Z. Xinchao, "Simulated annealing algorithm with adaptive neighborhood", *Applied Soft Computing*, vol. 11, no. 2, pp. 1827-1836, 2011. DOI: 10.1016/j.asoc.2010.05.029.
- [57] Y. K. Kim, J. P. Hong, and J. Hur, "Robust optimization of electric machine using stochastic finite element method," *J. Elect. Eng.*, vol. 1/2001, no. 1, pp. 69-72, Jan. 2001.
- [58] I. Ion et al., "Robust shape optimization of electric devices based on deterministic optimization methods and finite-element analysis with affine parametrization and design elements", *Electrical Engineering*, vol. 100, no. 4, pp. 2635-2647, 2018. DOI: 10.1007/s00202-018-0716-6.
- [59] Z. Bontinck, O. Lass, S. Schöps, H. De Gersem, S. Ulbrich and O. Rain, "Robust optimisation formulations for the design of an electric machine," in *IET Science, Measurement & Technology*, vol. 12, no. 8, pp. 939-948, 11 2018, DOI: 10.1049/iet-smt.2018.5235.
- [60] G. Bramerdorfer, "Tolerance Analysis for Electric Machine Design Optimization: Classification, Modeling and Evaluation, and Example," in *IEEE Transactions on Magnetics*, vol. 55, no. 8, pp. 1-9, Aug. 2019, Art no. 8106809, DOI: 10.1109/TMAG.2019.2903029.
- [61] Y. Hong and T. Chang, "A comprehensive review of tolerancing research", *International Journal of Production Research*, vol. 40, no. 11, pp. 2425-2459, 2002. DOI: 10.1080/00207540210128242.
- [62] Douglas C. Montgomery, George C. Runger, "Applied Statistics and Probability for Engineers", *John Wiley & Sons*, 2011.
- [63] S. Raychaudhuri, "Introduction to Monte Carlo simulation", *Winter Simulation Conference*, 2008.
- [64] A. Vagati, M. Pastorelli, G. Francheschini and S. C. Petrache, "Design of low-torque-ripple synchronous reluctance motors," in *IEEE Transactions*
-

- on *Industry Applications*, vol. 34, no. 4, pp. 758-765, July-Aug. 1998, DOI: 10.1109/28.703969.
- [65] N. Bianchi, S. Bolognani, D. Bon and M. D. Pre, "Rotor flux-barrier design for torque ripple reduction in synchronous reluctance motors," *Conference Record of the 2006 IEEE Industry Applications Conference Forty-First IAS Annual Meeting*, Tampa, FL, 2006, pp. 1193-1200, DOI: 10.1109/IAS.2006.256683.
- [66] S. Ferrari, G. Pellegrino, M. Davoli and C. Bianchini, "Reduction of Torque Ripple in Synchronous Reluctance Machines through Flux Barrier Shift," *2018 XIII International Conference on Electrical Machines (ICEM)*, Alexandroupoli, 2018, pp. 2290-2296, DOI: 10.1109/ICELMACH.2018.8507223.
- [67] N. Bianchi, S. Bolognani, D. Bon and M. Dai Pre, "Rotor Flux-Barrier Design for Torque Ripple Reduction in Synchronous Reluctance and PM-Assisted Synchronous Reluctance Motors," in *IEEE Transactions on Industry Applications*, vol. 45, no. 3, pp. 921-928, May-june 2009, DOI: 10.1109/TIA.2009.2018960.
- [68] P. Alotto, M. Barcaro, N. Bianchi and M. Guarnieri, "Optimization of Interior PM Motors With Machaon Rotor Flux Barriers," in *IEEE Transactions on Magnetics*, vol. 47, no. 5, pp. 958-961, May 2011, DOI: 10.1109/TMAG.2010.2073450.
- [69] D. Gerada, A. Mebarki, N. L. Brown, C. Gerada, A. Cavagnino and A. Boglietti, "High-Speed Electrical Machines: Technologies, Trends, and Developments," in *IEEE Transactions on Industrial Electronics*, vol. 61, no. 6, pp. 2946-2959, June 2014, DOI: 10.1109/TIE.2013.2286777.
- [70] K. Grace, S. Galioto, K. Bodla and A. El-Refaie, "Carbon-fiber-wrapped synchronous reluctance traction motor," *2017 IEEE Energy Conversion Congress and Exposition (ECCE)*, Cincinnati, OH, 2017, pp. 3913-3920, DOI: 10.1109/ECCE.2017.8096687.
- [71] K. Grace, S. Galioto, K. Bodla and A. M. El-Refaie, "Design and Testing of a Carbon-Fiber-Wrapped Synchronous Reluctance Traction Motor," in *IEEE Transactions on Industry Applications*, vol. 54, no. 5, pp. 4207-4217, Sept.-Oct. 2018, DOI: 10.1109/TIA.2018.2836966.
- [72] J. Ikäheimo, J. Kolehmainen, T. Käsäkangas, V. Kivelä and R. R. Moghaddam, "Synchronous High-Speed Reluctance Machine With Novel Rotor Construction," in *IEEE Transactions on Industrial Electronics*, vol. 61, no. 6, pp. 2969-2975, June 2014, DOI: 10.1109/TIE.2013.2253077.
- [73] J. Kolehmainen, "Optimal Dovetail Permanent Magnet Rotor Solutions for Various Pole Numbers," in *IEEE Transactions on Industrial Electronics*, vol. 57, no. 1, pp. 70-77, Jan. 2010, DOI: 10.1109/TIE.2009.2029590.

-
- [74] M. D. Nardo, G. L. Calzo, M. Galea and C. Gerada, "Design Optimization of a High-Speed Synchronous Reluctance Machine," in *IEEE Transactions on Industry Applications*, vol. 54, no. 1, pp. 233-243, Jan.-Feb. 2018, DOI: 10.1109/TIA.2017.2758759.
- [75] K. Chen, W. Yu and C. Wen, "Rotor optimization for synchronous reluctance motors," in *CES Transactions on Electrical Machines and Systems*, vol. 3, no. 3, pp. 279-284, Sept. 2019, DOI: 10.30941/CESTEMS.2019.00036.
- [76] E. C. Lovelace, T. M. Jahns, T. A. Keim and J. H. Lang, "Mechanical design considerations for conventionally laminated, high-speed, interior PM synchronous machine rotors," in *IEEE Transactions on Industry Applications*, vol. 40, no. 3, pp. 806-812, May-June 2004, DOI: 10.1109/TIA.2004.827440.
- [77] C. Babetto, G. Bacco and N. Bianchi, "Analytical approach to determine the power limit of high-speed synchronous reluctance machines," *2017 IEEE International Electric Machines and Drives Conference (IEMDC)*, Miami, FL, 2017, pp. 1-7, DOI: 10.1109/IEMDC.2017.8002316.
- [78] C. Babetto, G. Bacco and N. Bianchi, "Analytical Power Limits Curves of High-Speed Synchronous Reluctance Machines," in *IEEE Transactions on Industry Applications*, vol. 55, no. 2, pp. 1342-1350, March-April 2019, DOI: 10.1109/TIA.2018.2875663.
- [79] P. B. Reddy *et al.*, "Performance testing and analysis of synchronous reluctance motor utilizing dual-phase magnetic material," *2017 IEEE International Electric Machines and Drives Conference (IEMDC)*, Miami, FL, 2017, pp. 1-8, DOI: 10.1109/IEMDC.2017.8002024.
- [80] P. B. Reddy *et al.*, "Performance Testing and Analysis of Synchronous Reluctance Motor Utilizing Dual-Phase Magnetic Material," in *IEEE Transactions on Industry Applications*, vol. 54, no. 3, pp. 2193-2201, May-June 2018, DOI: 10.1109/TIA.2018.2801264.
- [81] S. Panda and R. Keshiri, "Reduced Rib Synchronous Reluctance Motor for Traction Applications", *Advances in Electrical and Computer Engineering*, vol. 19, no. 4, pp. 83-90, 2019. DOI: 10.4316/aece.2019.04010.
- [82] S. Panda, R. K. Keshri, A. Tassarolo, G. Tiwari and M. Mezzarobba, "Design refinements of synchronous reluctance motor utilising non-magnetic radial ribs for traction applications," in *IET Electric Power Applications*, vol. 14, no. 12, pp. 2480-2489, 12 2020, DOI: 10.1049/iet-epa.2020.0199.
- [83] H. Eschenauer and N. Olhoff, "Topology optimization of continuum structures: A review", *Applied Mechanics Reviews*, vol. 54, no. 4, pp. 331-390, 2001. DOI: 10.1115/1.1388075.
-

-
- [84] G. Rozvany, "A critical review of established methods of structural topology optimization", *Structural and Multidisciplinary Optimization*, vol. 37, no. 3, pp. 217-237, 2008. DOI: 10.1007/s00158-007-0217-0.
- [85] K. Watanabe, T. Suga and S. Kitabatake, "Topology Optimization Based on the ON/OFF Method for Synchronous Motor," in *IEEE Transactions on Magnetics*, vol. 54, no. 3, pp. 1-4, March 2018, Art no. 7201104, DOI: 10.1109/TMAG.2017.2751653.
- [86] S. Sato, T. Sato and H. Igarashi, "Topology Optimization of Synchronous Reluctance Motor Using Normalized Gaussian Network," in *IEEE Transactions on Magnetics*, vol. 51, no. 3, pp. 1-4, March 2015, Art no. 8200904, DOI: 10.1109/TMAG.2014.2359679.
- [87] M. Garibaldi, C. Gerada, I. Ashcroft and R. Hague, "Free-Form Design of Electrical Machine Rotor Cores for Production Using Additive Manufacturing", *Journal of Mechanical Design*, vol. 141, no. 7, 2019. DOI: 10.1115/1.4042621.
- [88] J. Lee, J. Seo and N. Kikuchi, "Topology optimization of switched reluctance motors for the desired torque profile", *Structural and Multidisciplinary Optimization*, vol. 42, no. 5, pp. 783-796, 2010. DOI: 10.1007/s00158-010-0547-1.
- [89] Z. Ahmadi, "Nanostructured epoxy adhesives: A review", *Progress in Organic Coatings*, vol. 135, pp. 449-453, 2019. DOI: 10.1016/j.porgcoat.2019.06.028.
- [90] S. Han, Q. Meng, S. Araby, T. Liu and M. Demiral, "Mechanical and electrical properties of graphene and carbon nanotube reinforced epoxy adhesives: Experimental and numerical analysis", *Composites Part A: Applied Science and Manufacturing*, vol. 120, pp. 116-126, 2019. DOI: 10.1016/j.compositesa.2019.02.027.
- [91] C. Salom, M. Prolongo, A. Toribio, A. Martínez-Martínez, I. de Cárcer and S. Prolongo, "Mechanical properties and adhesive behavior of epoxy-graphene nanocomposites", *International Journal of Adhesion and Adhesives*, vol. 84, pp. 119-125, 2018. DOI: 10.1016/j.ijadhadh.2017.12.004.
- [92] A. Burkanudeen and P. Ramesh, "Novel latent epoxy curing agent for secondary insulation in electrical rotors and stators," in *IEEE Transactions on Dielectrics and Electrical Insulation*, vol. 19, no. 5, pp. 1791-1798, October 2012, DOI: 10.1109/TDEI.2012.6311529.
- [93] J. Ma, R. Qu and J. Li, "Optimal design of an axial flux switched reluctance motor with grain oriented electrical steel," *2015 18th International Conference on Electrical Machines and Systems (ICEMS)*, Pattaya, 2015, pp. 2071-2077, DOI: 10.1109/ICEMS.2015.7385381.
-

-
- [94] J. Ma *et al.*, "Optimal Design of an Axial-Flux Switched Reluctance Motor With Grain-Oriented Electrical Steel," in *IEEE Transactions on Industry Applications*, vol. 53, no. 6, pp. 5327-5337, Nov.-Dec. 2017, DOI: 10.1109/TIA.2017.2727438.
- [95] S. Nategh, A. Boglietti, D. Barber, Y. Liu and R. Brammer, "Thermal and Manufacturing Aspects of Traction Motors Potting: A Deep Experimental Evaluation," in *IEEE Transactions on Energy Conversion*, vol. 35, no. 2, pp. 1026-1035, June 2020, DOI: 10.1109/TEC.2020.2966606.
- [96] M. A. Grande, L. Ferraris, F. Franchini and E. Pošković, "New SMC Materials for Small Electrical Machine With Very Good Mechanical Properties," in *IEEE Transactions on Industry Applications*, vol. 54, no. 1, pp. 195-203, Jan.-Feb. 2018, DOI: 10.1109/TIA.2017.2756593.
- [97] R. Kolano, K. Krykowski, A. Kolano-Burian, M. Polak, J. Szynowski and P. Zackiewicz, "Amorphous Soft Magnetic Materials for the Stator of a Novel High-Speed PMSM Motor," in *IEEE Transactions on Magnetics*, vol. 49, no. 4, pp. 1367-1371, April 2013, DOI: 10.1109/TMAG.2012.2234757.
- [98] N. Rusnaeni, P. Sarjono, Muljadi and N. Noer, "The epoxy resin variation effect on microstructure and physical properties to improve bonded NdFeB flux magnetic density", *Journal of Physics: Conference Series*, vol. 776, p. 012025, 2016. DOI: 10.1088/1742-6596/776/1/012025.
- [99] "Online Materials Information Resource - MatWeb", *Matweb.com*, 2021. [Online]. Available: <http://www.matweb.com/>.

